Geophys. J. Int. (2010) **181,** 1–80 doi: 10.1111/j.1365-246X.2009.04491.x

Geologically current plate motions

Charles DeMets,[1] Richard G. Gordon[2] and Donald F. Argus[3]

[1]*Department of Geoscience, University of Wisconsin-Madison, Madison, WI* 53706*, USA. E-mail: chuck@geology.wisc.edu*
[2]*Department of Earth Science, Rice University, Houston, TX* 77005*, USA*
[3]*Jet Propulsion Laboratory, California Institute of Technology, Pasadena, CA* 91109*, USA*

Accepted 2009 December 17. Received 2009 December 16; in original form 2009 March 30

SUMMARY

We describe best-fitting angular velocities and MORVEL, a new closure-enforced set of angular velocities for the geologically current motions of 25 tectonic plates that collectively occupy 97 per cent of Earth's surface. Seafloor spreading rates and fault azimuths are used to determine the motions of 19 plates bordered by mid-ocean ridges, including all the major plates. Six smaller plates with little or no connection to the mid-ocean ridges are linked to MORVEL with GPS station velocities and azimuthal data. By design, almost no kinematic information is exchanged between the geologically determined and geodetically constrained subsets of the global circuit—MORVEL thus averages motion over geological intervals for all the major plates. Plate geometry changes relative to NUVEL-1A include the incorporation of Nubia, Lwandle and Somalia plates for the former Africa plate, Capricorn, Australia and Macquarie plates for the former Australia plate, and Sur and South America plates for the former South America plate. MORVEL also includes Amur, Philippine Sea, Sundaland and Yangtze plates, making it more useful than NUVEL-1A for studies of deformation in Asia and the western Pacific. Seafloor spreading rates are estimated over the past 0.78 Myr for intermediate and fast spreading centres and since 3.16 Ma for slow and ultraslow spreading centres. Rates are adjusted downward by 0.6–2.6 mm yr^{-1} to compensate for the several kilometre width of magnetic reversal zones. Nearly all the NUVEL-1A angular velocities differ significantly from the MORVEL angular velocities. The many new data, revised plate geometries, and correction for outward displacement thus significantly modify our knowledge of geologically current plate motions. MORVEL indicates significantly slower 0.78-Myr-average motion across the Nazca–Antarctic and Nazca–Pacific boundaries than does NUVEL-1A, consistent with a progressive slowdown in the eastward component of Nazca plate motion since 3.16 Ma. It also indicates that motions across the Caribbean–North America and Caribbean–South America plate boundaries are twice as fast as given by NUVEL-1A. Summed, least-squares differences between angular velocities estimated from GPS and those for MORVEL, NUVEL-1 and NUVEL-1A are, respectively, 260 per cent larger for NUVEL-1 and 50 per cent larger for NUVEL-1A than for MORVEL, suggesting that MORVEL more accurately describes historically current plate motions. Significant differences between geological and GPS estimates of Nazca plate motion and Arabia–Eurasia and India–Eurasia motion are reduced but not eliminated when using MORVEL instead of NUVEL-1A, possibly indicating that changes have occurred in those plate motions since 3.16 Ma. The MORVEL and GPS estimates of Pacific–North America plate motion in western North America differ by only 2.6 $\pm$ 1.7 mm yr^{-1}, $\approx$25 per cent smaller than for NUVEL-1A. The remaining difference for this plate pair, assuming there are no unrecognized systematic errors and no measurable change in Pacific–North America motion over the past 1–3 Myr, indicates deformation of one or more plates in the global circuit. Tests for closure of six three-plate circuits indicate that two, Pacific–Cocos–Nazca and Sur–Nubia–Antarctic, fail closure, with respective linear velocities of non-closure of 14 $\pm$ 5 and 3 $\pm$ 1 mm yr^{-1} (95 per cent confidence limits) at their triple junctions. We conclude that the rigid plate approximation continues to be tremendously useful, but—absent any unrecognized systematic errors—the plates deform measurably, possibly by thermal contraction and wide plate boundaries with deformation rates near or beneath the level of noise in plate kinematic data.

Key words: Plate motions; Planetary tectonics.

CONTENTS

1 Introduction 3
2 Assumptions 5
2.1 Global plate geometry 5
2.2 Changes in global plate circuit closure constraints 6
2.3 Averaging intervals for kinematic data 6
3 Data overview 7
3.1 Magnetic and bathymetric data 7
3.2 Earthquake data 8
3.3 GPS data 9
4 Methods 9
4.1 Overview 9
4.2 Seafloor spreading rates 11
4.2.1 Cross-correlation technique for spreading rate determination 11
4.2.2 Correction for outward displacement 12
4.2.3 Determination of uncertainties 13
4.3 Plate motion directions from transform fault azimuths 14
4.4 Site velocities from GPS data 14
4.4.1 Raw GPS data analysis 14
4.4.2 Velocity transformation to plate-based reference frames 15
4.5 Estimation of angular velocities and their uncertainties 15
4.6 Statistical comparisons of angular velocities 16
5 Data and results: Best-fitting and MORVEL plate motion estimates 16
5.1 Spreading rate, transform fault, and GPS site velocity RMS misfits 17
5.2 MORVEL summary 17
5.2.1 Best-fitting and global angular velocity information 17
5.2.2 Overview of data misfits 19
5.2.3 Data importances 19
5.2.4 Influence of GPS velocities 20
5.3 Arctic and Atlantic Ocean basins 21
5.3.1 Data from the Arctic and northern Atlantic 21
5.3.2 Data from the equatorial and southern Atlantic 22
5.3.3 Eurasia–North America plate motion 23
5.3.4 The Azores microplate 24
5.3.5 Nubia–Eurasia plate motion from the Azores to Gibraltar 25
5.3.6 Boundary between the North and South America plates 26
5.3.7 Nubia–North America plate motion 27
5.3.8 Nubia–South America plate motion 29
5.3.9 Motion between the North and South America plates 30
5.3.10 Antarctic–Sur plate motion and evidence for a Sur microplate 32
5.4 The Scotia Sea 34
5.4.1 Data description 34
5.4.2 Scotia and Sandwich plate motions 35
5.5 Indian Ocean basin 36
5.5.1 Data from the Southwest Indian ridge 36
5.5.2 Southwest Indian ridge plate motions 38
5.5.3 Lwandle plate motions 39
5.5.4 Data from the Southeast Indian ridge 39
5.5.5 Capricorn–Australia plate boundary location 40
5.5.6 Macquarie–Australia plate boundary location 42
5.5.7 Capricorn–Antarctic plate motion 42
5.5.8 Australia–Antarctic plate motion 43
5.5.9 Macquarie–Antarctic plate motion 43
5.5.10 Australia–Capricorn plate motion 43
5.5.11 Australia–Macquarie–Pacific plate motion 43
5.5.12 Data from the central and northern Indian basin, Gulf of Aden and Red Sea 43
5.5.13 Capricorn–Somalia plate motion 45
5.5.14 India–Somalia plate motion 45
5.5.15 Arabia–India plate motion 46
5.5.16 Arabia–Somalia plate motion in the Gulf of Aden 47
5.5.17 Nubia–Arabia plate motion in the Red Sea 48
5.6 Pacific Ocean basin 48
5.6.1 Data description 48
5.6.2 Pacific–Antarctic plate motion 50
5.6.3 Nazca–Antarctic plate motion 51
5.6.4 Pacific–Nazca plate motion 52
5.6.5 Cocos–Nazca plate motion 52
5.6.6 Pacific–Cocos plate motion 54
5.6.7 Pacific–Rivera plate motion and evidence for Rivera plate break up 54
5.6.8 Pacific–Juan de Fuca plate motion 55
5.7 The western Pacific basin and eastern Asia 55
5.7.1 The Sundaland plate and convergence along the Java–Sumatra trench 55
5.7.2 Yangtze–Sundaland plate motion 57
5.7.3 Amur plate motion: northeast Asia 58
5.7.4 The Philippine Sea plate and subduction in the western Pacific 59
5.8 The Caribbean Sea 61
5.8.1 Data description 61
5.8.2 Caribbean plate motion 61
5.9 PVEL estimates of Cocos, Juan de Fuca and Rivera plate motions 61
6 Plate circuit closures and outward displacement 62
6.1 Methods for determining circuit non-closure 62
6.2 Three-plate circuit non-closures 63
6.2.1 Nubia–Antarctic–Sur plate circuit 63
6.2.2 Pacific–Antarctic–Nazca plate circuit 63
6.2.3 Pacific–Cocos–Nazca plate circuit 64
6.2.4 Capricorn–Somalia–Antarctic plate circuit 64
6.2.5 Nubia–Eurasia–North America and Arabia–India–Somalia plate circuits 64
7 Discussion 65
7.1 Fit to MORVEL data with the NUVEL-1 global plate geometry 65
7.1.1 Effect of single Africa, Australia, and South America plates 65
7.1.2 Baja sliver plate and data from the Gulf of California 65
7.2 NUVEL-1A and MORVEL spreading rate comparison 66
7.3 NUVEL-1A and MORVEL angular velocity comparisons 66
7.4 Comparison of MORVEL and NUVEL-1A to plate velocities from GPS 66
7.4.1 Angular velocity comparisons 68
7.4.2 Linear velocity comparisons for spreading centers and other plate boundaries 69
7.4.3 Evidence for changes since 1–3 Ma in Arabia, India and Nazca plate motions 70
7.5 Test for global circuit closure: Pacific–North America plate motion 70
7.5.1 Effects of local plate circuit closures and outward displacement 71
7.5.2 Comparison to geodetic estimates 72
7.5.3 Influence of the Kane transform fault 72
7.5.4 Plate motion changes or thermal contraction as cause of non-closure 72
7.6 Poles of rotation in diffuse oceanic plate boundaries 73
8 Conclusions 73

1 INTRODUCTION

Four decades after the inception of the theory of plate tectonics, estimates of geologically current plate motions (Chase 1972, 1978; Minster *et al.* 1974; Minster & Jordan 1978; DeMets *et al.* 1990, 1994a) continue to be used broadly for geological, geophysical and geodetic studies. Increased shipboard, airborne and satellite coverage of the mid-ocean ridge system over time has enabled steady improvements in the precision and accuracy of successive estimates of plate angular velocities, making them ever more useful for estimating plate motion, for detecting zones of slow deformation, and for determining the limits to the rigid plate approximation. Since the early 1990s, steady improvements in estimates of instantaneous tectonic plate velocities from Global Positioning System (GPS) and other geodetic data (e.g. Argus & Gordon 1990; Ward 1990; Argus & Heflin 1995; Larson *et al.* 1997; Sella *et al.* 2002; Kreemer *et al.* 2003; Kogan & Steblov 2008; Argus *et al.* 2010) have enabled valuable comparisons between geological and geodetic estimates of current plate motions and have set the stage for efforts to detect and link recent changes in plate motions to the forces that cause those changes.

Herein we review available data that describe geologically current plate motions and present a new closure-enforced set of angular velocities for the motions of 25 tectonic plates (Figs 1 and 2). We also determine best-fitting angular velocities for all plate pairs that share a boundary populated by data. Rates of seafloor spreading and azimuths of oceanic transform faults supply ≈75 per cent of the kinematic information for the new set of angular velocities. We therefore use the name MORVEL (Mid-Ocean Ridge VELocity) for the new set of angular velocities. Unlike its predecessors NUVEL-1 and NUVEL-1A (DeMets *et al.* 1990, 1994a), few earthquake slip directions are used in MORVEL. Moreover, GPS station velocities are used to estimate the motions of six smaller plates with few or no other reliable kinematic data, with care taken to avoid introducing any dependence between plate angular velocities that are determined from geological data and angular velocities that are estimated from geodetic data.

Many new multibeam sonar, side-scan sonar and dense magnetic surveys of the mid-ocean ridges have become available since the publication of NUVEL-1. Some of these surveys occurred in regions where few or no data were available before and thus provide valuable new limits on estimates of plate motions. Whereas many NUVEL-1 spreading rates were estimated from isolated shipboard transits of the mid-ocean ridges, most MORVEL spreading rates are determined from dense ship and airborne surveys. This enhances our ability to identify the present and past locations of ridge-axis offsets that can disrupt an anomaly sequence and corrupt estimates of spreading rates. Nearly all the new spreading rates are estimated

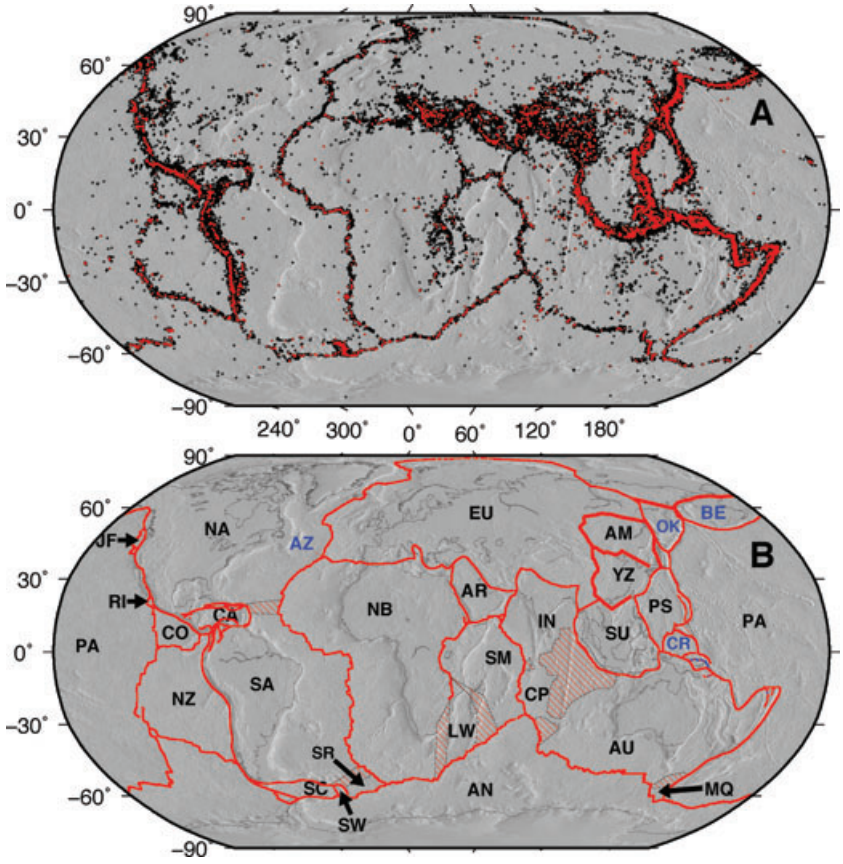

Figure 1. (a) Epicentres for earthquakes with magnitudes equal to or larger than 3.5 (black) and 5.5 (red) and depths shallower than 40 km for the period 1967–2007. Hypocentral information is from the U.S. Geological Survey National Earthquake Information Center files. (b) Plate boundaries and geometries employed for MORVEL. Plate name abbreviations are as follows: AM, Amur; AN, Antarctic; AR, Arabia; AU, Australia; AZ, Azores; BE, Bering; CA, Caribbean; CO, Cocos; CP, Capricorn; CR, Caroline; EU, Eurasia; IN, India; JF, Juan de Fuca; LW, Lwandle; MQ, Macquarie; NA, North America; NB, Nubia; NZ, Nazca; OK, Okhotsk; PA, Pacific; PS, Philippine Sea; RI, Rivera; SA, South America; SC, Scotia; SM, Somalia; SR, Sur; SU, Sundaland; SW, Sandwich; YZ, Yangtze. Blue labels indicate plates not included in MORVEL. Patterned red areas show diffuse plate boundaries.

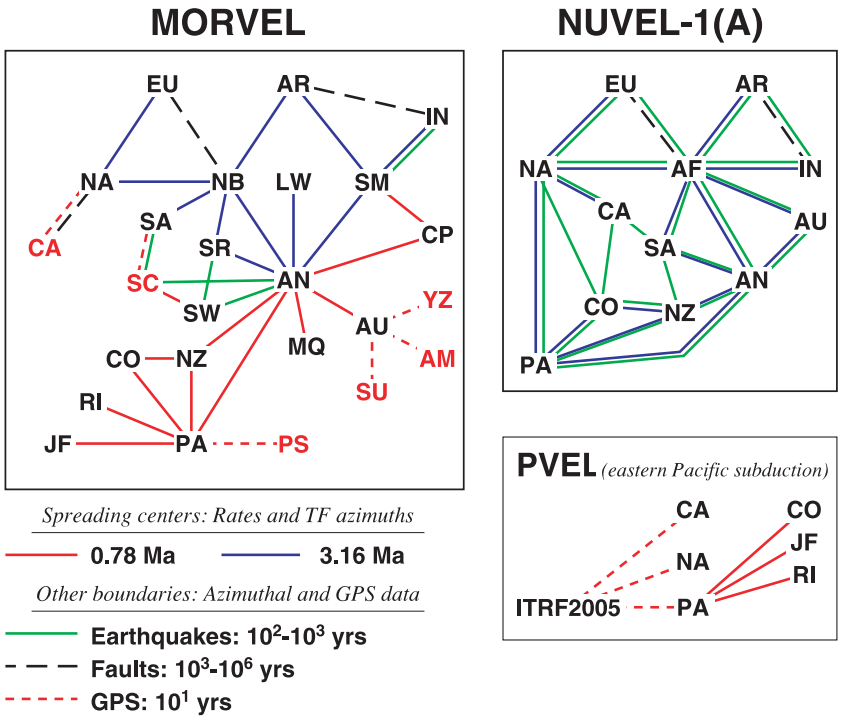

Figure 2. MORVEL, PVEL and NUVEL-1 plate circuits. Plates are represented by two-letter codes defined in the caption to Fig. 1. Plates designated by red letters have motions determined entirely (AM, PS, SU and YZ) or partly (CA and SC) from GPS data. PVEL is an alternative set of angular velocities (Section 5.9 and Table 5) for subduction in the eastern Pacific basin determined from a subset of the MORVEL kinematic data and GPS station velocities. Lines that connect plate pairs represent plate boundaries or plate pairs from which kinematic observations are used to derive relative plate motions. The legend in the lower left-hand corner defines the types of kinematic data and averaging intervals used to determine motion for each plate pair. 'TF' is transform fault.

with an automated procedure for cross-correlating observed and synthetic magnetic profiles, in contrast to the visual matching procedure used for NUVEL-1.

Herein we modify several assumptions that we made in constructing NUVEL-1 and NUVEL-1A. For example, changes in the geometries that were used for several plates in NUVEL-1 are warranted, including a division of the former Africa plate into distinct Nubia, Lwandle and Somalia plates (Jestin *et al.* 1994; Chu & Gordon 1998; Lemaux *et al.* 2002; Horner-Johnson *et al.* 2005; Calais *et al.* 2006a; Horner-Johnson *et al.* 2007), and division of the former Australia plate into distinct Capricorn, Australia and Macquarie plates (Royer & Gordon 1997; Conder & Forsyth 2001; Cande & Stock 2004; Gordon *et al.* 2008). The wide, slowly deforming boundaries that define these plates (Royer & Gordon 1997; Gordon 1998) present special challenges for estimating plate motion because of the difficulty in defining the limits of the diffusely deforming boundaries where they intersect the mid-ocean ridges and because of the slow relative motions that typify these diffuse plate boundaries. Another important assumption of the NUVEL-1 global plate circuit, that motion between the North America and Pacific plates is accurately recorded by seafloor spreading rates and directions from the Gulf of California, has been invalidated by geodetic evidence that the Baja California peninsula moves several millimetre per year relative to the Pacific plate. Herein we also no longer use the homogeneous ≈3 Myr averaging interval that we adopted before for determining seafloor spreading rates. This averaging interval exceeds by an order of magnitude or more the interval over which transform fault azimuths and earthquake slip directions average plate motion, which complicates estimates of plate motion across several Pacific basin spreading centres where changes of plate motion have occurred over the past few million years.

We also correct or eliminate several sources of systematic error that affect NUVEL-1 and NUVEL-1A. For example, it is now clear that the finite-width zone over which new seafloor accretes shifts the midpoints of magnetic reversal transition zones several kilometres outward from the ridge axis relative to their idealized locations, thereby causing a small but significant upward bias in all seafloor spreading rates that are estimated from marine magnetic data (DeMets & Wilson 2008). Thus, all the MORVEL spreading rates are adjusted systematically downward to correct for the effect of outward displacement and the MORVEL uncertainties are modified to include an additional systematic error that accounts for possible errors in these corrections.

Uncertainties in plate angular velocities are also estimated more objectively than before. As described by DeMets *et al.* (1990), the NUVEL-1 angular velocity uncertainties are twice as large as warranted by the rms misfit of NUVEL-1 to its underlying data, reflecting a decision by those authors to assign data uncertainties comparable to those estimated by previous authors. To remedy this, we changed our procedures in two important ways. First, uncertainties in transform fault azimuths are determined from a formula that considers only the insonified width and length of the narrowest zone imaged that contains the zone of active faulting (DeMets *et al.* 1994b). Thus the uncertainties in the azimuths of transform faults are estimated from the appropriate features of the data. No such simple model exists for estimating spreading rate uncertainties, thus their uncertainties are determined from the dispersion of the rates for each plate pair.

The construction of a new set of relative plate angular velocities also provides opportunities for testing the central approximation of plate tectonics—that the plates do not deform internally. When constructing NUVEL-1, DeMets *et al.* (1990) found that two three-plate circuits, the Pacific–Cocos–Nazca (Galapagos triple junction) and Africa–South America–Antarctic (Bouvet triple junction) plate motion circuits, failed tests for circuit closure. While not explicitly discussed by DeMets *et al.* (1990), but as documented herein, the Pacific–Antarctic–Africa–North America circuit also failed closure in NUVEL-1; in NUVEL-1 this is manifested mainly by the large difference between the best-fitting and NUVEL-1 angular velocities for Africa–North America motion. Absent alternative explanations, these results indicate that plates are not rigid as assumed, but instead deform. With the great increase in number and quality of data, these issues are re-examined.

In the following section, we describe in more detail the revised plate geometries that are used here, the justification for excluding data from the Gulf of California from the MORVEL determination of Pacific–North America motion, and our reasons for abandoning a homogeneous 3.16 Myr averaging interval for seafloor spreading rates. We then provide overviews of the marine magnetic, bathymetric, earthquake, and GPS data that are the basis for MORVEL, describe the methods that we use to analyse these data and to assign their uncertainties, and outline the techniques we use to estimate plate angular velocities and their covariances. An extensive description of the MORVEL data and plate motion estimates follows, beginning with an overview of MORVEL and continuing with descriptions of the data and results by geographic region and plate boundary. Finally, we discuss the main tectonic implications and patterns that emerge from our analysis, analyse closure of three-plate and global plate circuits, and compare MORVEL to NUVEL-1A and to plate motions estimated from GPS measurements. Readers are also referred to http://www.geology.wisc.edu/∼chuck/MORVEL for assistance in calculating plate velocities and uncertainties with MORVEL and for additional documentation of the marine magnetic and bathymetric observations that underly this analysis.

2 ASSUMPTIONS

2.1 Global plate geometry

In the most comprehensive description to date of the configuration of active plate boundaries, Bird (2003) defines 14 large and 38 small plates, ranging in size from the Pacific plate, which comprises 20.5 per cent of Earth's surface, to the Manus microplate, which comprises only 0.016 per cent of the surface. The 25 tectonic plates in the MORVEL global plate circuit (Fig. 2) include the 14 largest plates identified by Bird (2003), comprising 95.1 per cent of Earth's surface, and seven of the next nine largest plates, comprising an additional 2.0 per cent of the surface. MORVEL thus describes plate motions for 97 per cent of Earth's surface, albeit only approximately within the zones of diffuse deformation that separate some of the 25 plates.

Relative to NUVEL-1 and NUVEL-1A, MORVEL incorporates more than twice as many plates and covers more of Earth's surface (97.1 per cent versus 92.4 per cent). In addition, different geometries are used for some of those plates. An important difference between the MORVEL and NUVEL-1 plate circuits is our substitution of distinct Nubia, Lwandle and Somalia plates for the African plate of NUVEL-1. The NUVEL-1 plate motion data, especially those in the Red Sea, were insufficient to reliably estimate the motion between the Nubia and Somalia plates. Jestin *et al.* (1994), using two spreading rates from Red Sea magnetic profiles presented by Izzeldin (1987) and a slip rate along the Levant fault, show that Nubia–Arabia motion differs significantly from Somalia–Arabia motion and use this to estimate a Nubia–Somalia angular velocity with large uncertainties.

Chu & Gordon (1998) determine 64 spreading rates from magnetic profiles from the Red Sea, of which 45 record Nubia–Arabia motion and allow more accurate estimates of Nubia–Arabia and Nubia–Somalia angular velocities. From a greatly increased set of spreading rate and transform fault azimuth data along the Southwest Indian Ridge, Chu & Gordon (1999), Lemaux *et al.* (2002) and Horner-Johnson *et al.* (2005) show that northeastern and southwestern portions of the Southwest Indian Ridge record significantly different plate motion and conclude that this difference is caused by relative motion between separate Nubia and Somalia plates north of the Southwest Indian Ridge.

More recently, Horner-Johnson *et al.* (2007) show that a plate geometry with a newly defined Lwandle plate (Hartnady 2002) between the Nubia and Somalia plates along the Southwest Indian Ridge (Fig. 1) results in further significant improvements in the fit to 3.2-Myr average spreading rates along the Southwest Indian Ridge. Their estimates of Nubia–Lwandle–Somalia motion agree well with independent earthquake-mechanism and geodetic observations on the relative motions of these plates. The revised geometry for the former Africa plate significantly changes estimates of plate velocities elsewhere in the Indian and Pacific Ocean basins via propagation of its effects into other plate circuits (Royer *et al.* 2006).

MORVEL also includes distinct Capricorn, Australia and Macquarie plates, which replace the Australia plate of NUVEL-1 (Fig. 1b). Royer & Gordon (1997) show that the existence of a distinct Capricorn plate is required from reconstructions of chron C5n.1o (11 Ma) from the Central Indian, Southwest Indian and Southeast Indian ridges. Their estimate of Capricorn–Australia plate motion is consistent with the locations and focal mechanisms of earthquakes within the diffuse Australia–Capricorn plate boundary north of the Southeast Indian Ridge. From an analysis of Southeast Indian Ridge spreading rates averaged out to the Jaramillo anomaly (1.03 Ma), Conder & Forsyth (2001) confirm the existence of a distinct Capricorn plate and propose that deformation between the Australia and Capricorn plates may be limited to a ≈1200-km-wide zone north of the Southeast Indian Ridge, narrower than proposed by Royer & Gordon (1997). From the many MORVEL data, we corroborate the above results with tighter confidence limits than found before (Section 5.5.5).

DeMets *et al.* (1988) infer the existence of a Macquarie microplate south of Tasmania (Fig. 1b), in a region where a band of diffuse intraplate seismicity between the Macquarie Ridge Complex and Southeast Indian Ridge (Valenzuela & Wysession 1993) appears to define the northern boundary of this oceanic microplate. DeMets *et al.* (1988) found that the slip directions of earthquakes from the Southeast Indian Ridge transform faults that define the western boundary of this microplate tended to lie ≈5° anticlockwise of the direction expected for Australia–Antarctic motion, offering the only kinematic evidence for its existence. The data then available however were insufficient to estimate the motion of this microplate in NUVEL-1.

More recently, Cande & Stock (2004) use well-mapped fracture zone flow lines from the eastern end of the Southeast Indian ridge and crossings of marine magnetic anomalies to show that an

independent Macquarie microplate has existed since ≈6 Ma and has a western limit that coincides with the Tasman fracture zone. From their results and newly available multibeam data that better constrain plate motion in this region, we include the Macquarie microplate in MORVEL.

We also incorporate into MORVEL nine other plates that were omitted or the motions of which were only peripherally investigated for NUVEL-1. In the southern Atlantic, we build on the studies of Pelayo & Wiens (1989), Smalley *et al.* (2003), Thomas *et al.* (2003) and Smalley *et al.* (2007) to estimate the motions of the Scotia and Sandwich plates. We also present kinematic evidence for the existence of a newly named Sur microplate east of the South Sandwich subduction zone and estimate its motion. Farther north in the Atlantic basin, we describe kinematic evidence for the existence and motion of the Azores microplate, but do not estimate angular velocities for this microplate from the sparse observations that are available from its boundaries.

In the eastern Pacific basin, we estimate the motions of the Rivera and Juan de Fuca plates, both of which subduct beneath western North America and pose seismic hazards to onshore regions. For reasons described in the following section, we exclude the geographically small Baja California sliver plate from MORVEL (Dixon *et al.* 2000; Plattner *et al.* 2007), although we use seafloor spreading rates and directions from its eastern boundary in the Gulf of California to confirm geodetic evidence that the Baja California peninsula moves slowly relative to the Pacific plate.

Along the western edge of the Pacific basin and in southeastern Asia, where few or no reliable conventional plate kinematic data can be used to estimate plate motions over geological timescales, we instead use GPS station velocities to estimate angular velocities for the Amur plate (Calais *et al.* 2003; Apel *et al.* 2006; Jin *et al.* 2007), the Philippine Sea plate (Seno *et al.* 1993; Sella *et al.* 2002), the Sundaland plate (Simons *et al.* 2007) and the Yangtze plate (Shen *et al.* 2005; Simons *et al.* 2007).

Omitted from MORVEL are the postulated Bering plate ('BE' in Fig. 1a) (Mackey *et al.* 1997), the slowly moving Okhotsk plate of northeastern Asia (Riegel *et al.* 1993; Seno *et al.* 1993; Takahashi *et al.* 1999; Apel *et al.* 2006), and the North China plate (Wang *et al.* 2001; Jin *et al.* 2007). We also do not estimate the motions of the Victoria or Rovuma microplates in Africa (Calais *et al.* 2006a). We refer readers to the publications cited above for more information about the motions of these slowly moving plates and continental blocks.

The largest oceanic plate excluded from MORVEL is the enigmatic Caroline plate, which is located in the western equatorial Pacific immediately south of the Philippine Sea plate (Fig. 1). Weissel & Anderson (1978) first proposed the existence of this plate and estimated its motions from a synthesis of marine seismic, bathymetric, and seismologic observations from its boundaries with the Pacific and Philippine plates. Uncertainties about the style and rate of present deformation across the poorly understood Caroline plate boundaries and a scarcity of reliable kinematic data for determining Philippine Sea plate motion affect the Weissel & Anderson and subsequent estimates of Pacific–Caroline–Philippine Sea plate angular velocities (Ranken *et al.* 1984; Seno *et al.* 1993; Zang *et al.* 2002). Improved GPS measurements of Philippine plate motion (described herein) reduce the latter source of uncertainty; however, few new kinematic data are available to estimate Caroline plate motion. Absent any unambiguous measurements of Caroline plate motion and any clarity about whether some Caroline plate boundaries are active or relict features, we exclude this slow moving plate from MORVEL.

We also omit the Easter, Juan Fernandez and Galapagos oceanic microplates, which have geometries and plate motions that have evolved rapidly over the past few million years and are better described by studies that document in more detail their evolution with time (e.g. Lonsdale 1988; Naar & Hey 1991; Larson *et al.* 1992; Searle *et al.* 1993; Klein *et al.* 2005). We furthermore omit the many smaller plates and crustal forearc slivers that are situated behind trenches in regions of backarc spreading or oblique subduction.

2.2 Changes in global plate circuit closure constraints

Local plate circuit closures, particularly three-plate circuits about triple junctions, play important roles in constraining both the NUVEL-1A and MORVEL angular velocities. Closures of more extended plate circuits are imposed on the NUVEL-1A angular velocity estimates by two data subsets: subduction zone earthquake slip directions, which link the motions of plate pairs in the Atlantic and Pacific ocean basins (Fig. 2), and data from the Pacific–North America plate boundary, which close the Pacific–Antarctic–Nubia–North America plate circuit. Here we exclude these data to preclude possible biases from influencing the MORVEL angular velocity estimates. Consequently, the MORVEL angular velocities are influenced less by extended plate circuit closures than are those for NUVEL-1A. The MORVEL angular velocities that describe Pacific–North America motion and the motions across all subduction zones except the South Sandwich trench are determined solely from the global plate circuit and constitute pure predictions of the motions for those plate pairs.

Fig. 3 summarizes our reason for excluding seafloor spreading rates and fault azimuths from the Gulf of California east of the Baja California peninsula, which constitute the most critical subset of the NUVEL-1A data that was used to estimate the NUVEL-1A Pacific–North America angular velocity. Three studies of GPS station motions on the Baja California peninsula report that stations from the northern, central, and southern parts of the peninsula move several million years or faster to the southeast relative to the Pacific plate (Dixon *et al.* 2000; Marquez-Azua & DeMets 2003; Plattner *et al.* 2007). Relative to the Pacific plate, the four southernmost sites on the Baja peninsula move to the southeast at 3.5 ± 0.8 mm yr^{-1} (95 per cent) (shown in inset to Fig. 3), consistent with movement of the peninsula as a quasi-rigid or possibly undeforming crustal sliver between the Pacific and North America plates (Dixon *et al.* 2000; Michaud *et al.* 2004; Plattner *et al.* 2007).

Studies of young seafloor spreading magnetic lineations in the Gulf of California also report that spreading rates within the Gulf have been 3–5 mm yr^{-1} lower over the past few million years than expected for Pacific–North America plate motion (DeMets 1995; DeMets & Dixon 1999), consistent with the observed slower-than-expected northwestward motions of GPS stations on the Baja peninsula. Both the geodetic and geological measurements in this region thus indicate that spreading rates in the Gulf of California record motion of the Baja peninsula relative to the North America plate rather than Pacific–North America plate motion.

2.3 Averaging intervals for kinematic data

NUVEL-1A is determined from data that average plate motions over widely different time spans, including earthquake slip directions that average plate directions over decades to centuries, transform fault azimuths that average directions over hundreds of thousands of years or longer, and spreading rates that uniformly average motion since

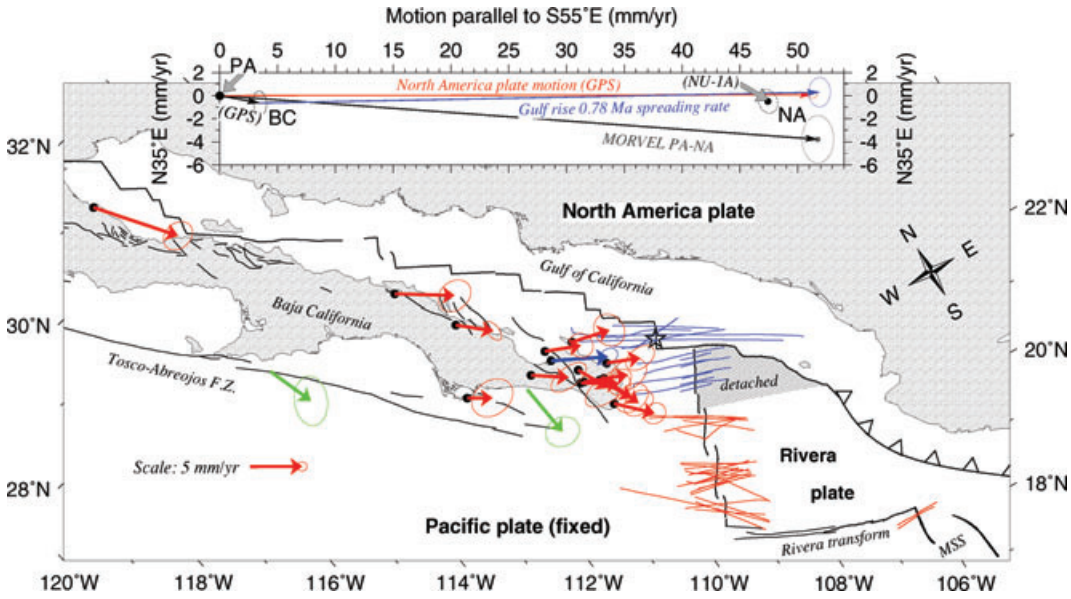

Figure 3. Summary of plate kinematic information from Baja California and the Gulf of California. Ship tracks coloured red indicate magnetic anomaly profiles that are used to determine Pacific–Rivera spreading rates. Ship tracks coloured blue indicate magnetic profiles used to determine spreading rates from the Gulf rise and northernmost segment of the Rivera rise. Red arrows show campaign GPS site velocities relative to the Pacific plate from Plattner *et al.* (2007). Blue arrow shows 1993–2001 motion of continuous GPS station LPAZ (Marquez-Azua & DeMets 2003). Green arrows and ellipses show velocities and uncertainties for Baja peninsula motion relative to the Pacific plate discussed in Section 7.1.2 All ellipses in the map and the velocity diagram inset are 2-D, 1σ. Map is oblique Mercator projection around the Pacific–North America pole of rotation. MSS is Manzanillo spreading segment. Inset: Red and black arrows show velocities predicted at the Gulf Rise (star) for the North America plate (NA) and southern Baja California peninsula (BC) relative to the Pacific plate (PA) from Plattner *et al.* (2007). Blue and black arrows show BC-NA motion calculated from 0.78-Myr-average spreading rates across the Gulf rise and Gulf of California transform fault azimuths and PA-NA motion from MORVEL, respectively. Spreading rates are corrected downward for 2 km of outward displacement. Black circle and ellipse labelled 'NU-1A' show PA-NA motion determined with NUVEL-1A.

3.16 Ma. The NUVEL-1A angular velocity estimates are therefore susceptible to anachronistic inconsistencies along plate boundaries where motion has changed since 3 Ma. This is of particular concern for several Pacific basin spreading centres, along or across which spreading rates or spreading directions or both have changed since 3 Ma (e.g. Macdonald *et al.* 1992; Wilson 1993; Lonsdale 1995; Wilson & Hey 1995; Tebbens *et al.* 1997; DeMets & Traylen 2000; Croon *et al.* 2008).

We attempt to reduce such inconsistencies in two ways. First, we minimize our use of earthquake slip directions, which average motion over a much shorter interval than do the spreading rates and transform fault azimuths. Second, we average spreading rates over the shortest feasible interval wherever possible. For spreading centres with full spreading rates that exceed $\approx$40 mm yr^{-1}, anomaly 1n (i.e. the central anomaly) is always well expressed. Consequently, we use the old edge of anomaly 1n (0.780 Ma) to estimate 0.78-Myr average spreading rates. Along slow and ultraslow spreading centres, where anomaly 1n is often too noisy to estimate spreading rates, we estimate spreading rates from the present out to the anomaly 2A sequence (2.58–3.60 Ma). A further benefit of using anomaly 1n is that it has been crossed in far more locations than has anomaly 2A by the many ships and aeroplanes that target the ridge axis.

Among the seventeen spreading centres considered here, we estimate 3.16-Myr-average spreading rates for seven and 0.78-Myr-average rates for the remaining ten (Fig. 2). Detailed plate reconstructions for the Eurasia–North America (Merkouriev & DeMets 2008), India–Somalia (Merkouriev & DeMets 2006) and Nubia–North America and Nubia–South America (DeMets & Wilson 2008) plate pairs, constituting four of the seven boundaries for which we use a 3.16-Myr-averaging interval, indicate that rates along these boundaries have not changed significantly since 3 Ma. Thus the 3.16-Myr-average rates that we estimate for these plate pairs can be combined with 0.78-Myr-average spreading rates from other plate boundaries without introducing inconsistencies into MORVEL. Similarly detailed studies have not been published for the other three spreading centres where we estimate 3.16-Myr-average rates (Red Sea, Gulf of Aden and the Southwest Indian Ridge).

3 DATA OVERVIEW

Many more data are used herein to estimate plate motions than was the case for NUVEL-1 (Fig. 4), with a six-fold increase in the number of spreading rates (1696 versus 277) and a five-fold increase in the number of transform fault azimuths that are estimated from multibeam or side-scan sonar surveys. Only 15 of the 2203 kinematic data that we use to determine MORVEL, all azimuths of well-mapped transform faults, were previously used to estimate NUVEL-1 and NUVEL-1A.

An overview of the MORVEL data is given in Sections 3.1–3.3, with further details given along with the MORVEL results (Section 5). The data, their sources, fits and formal data importances are documented in Tables S1–S4 of Supporting Information online. More detailed descriptions of the original data are available in the many publications cited in those tables.

3.1 Magnetic and bathymetric data

The magnetic and bathymetric data that we analyse are from many sources including hundreds of cruises and aeromagnetic surveys

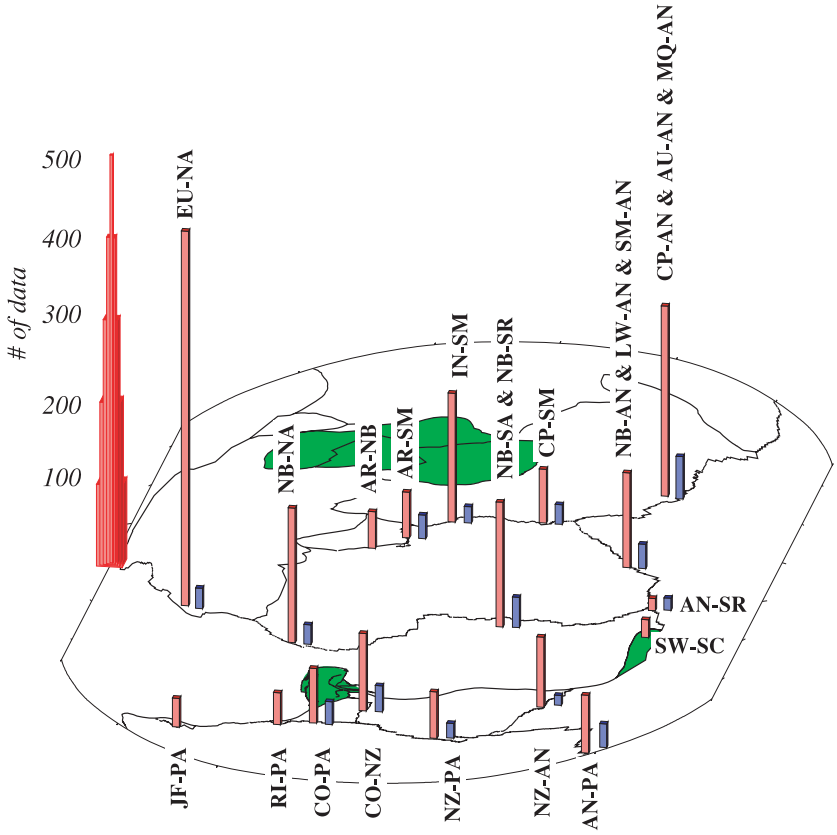

Figure 4. (a) Numbers of spreading rates and transform fault azimuths in the MORVEL (red) and NUVEL-1 (blue) data sets by plate boundary. Plates for which GPS station velocities provide some or all of the information to estimate their motions are shaded green.

that were archived at the U.S. National Geophysical Data Center (NGDC) through January of 2007. We also obtained magnetic data from the U.S. Naval Research Laboratory, the Lamont-Doherty Earth Observatory, and investigators and archives in Canada, France, Great Britain, India, Italy, Japan, the Netherlands, Russia and Spain. The spreading rates that we determined from sources outside the United States constitute ≈45 per cent of the total and greatly improve the geographic coverage of the mid-ocean ridge system relative to NUVEL-1. The track lines for all the magnetic profiles that we use to estimate the MORVEL spreading rates are shown in Figs 3, 16, 17, 29, 35 and 39.

We use many more rates than in NUVEL-1, ranging from a 20-fold increase for the densely surveyed Eurasia–North America plate boundary to an increase of only 25 per cent for the sparsely surveyed American–Antarctic ridge (Fig. 4). All spreading rates and ancillary information are listed in Table S1. Graphics that show the best cross-correlated match between the many magnetic profiles and their corresponding synthetic profiles are available at http://www.geology.wisc.edu/∼chuck/MORVEL.

Many oceanic transform faults that were either unmapped or sparsely surveyed when we assembled the NUVEL-1 data in the 1980s have since been surveyed with high-resolution multibeam or side-scan sonar systems (Table S2). We attempted to identify as many of these data as possible by surveying the literature, soliciting unpublished data from colleagues, and examining multibeam grids and transit-track multibeam swaths that are available through the Marine Geoscience Data System (http://www.marine-geo.org and Carbotte *et al.* 2004). We identified 133 faults that were either completely or partly mapped with multibeam or side-scan sonar or both. For comparison, only 25 fault azimuths were estimated from multibeam or side-scan sonar for NUVEL-1. Graphics that show multibeam images of many of the MORVEL transform faults are available at http://www.geology.wisc.edu/∼chuck/MORVEL.

We also used conventional single-beam sonar surveys to estimate the azimuths of ten faults that had not been mapped in detail as of mid-2007, and we estimated azimuths for twelve other long-offset transform faults from the 1-minute marine gravity grid of Smith & Sandwell (1997). Satellite altimetry lacks the resolution to image either the transform fault zone or principal transform displacement zone. We thus limited our use of altimetric data to unsurveyed transform faults, mainly in the equatorial and southern Atlantic Ocean basin.

3.2 Earthquake data

The 2203 MORVEL data include 56 earthquake slip directions (Table S3), constituting only 2 per cent of the total. These 56 directions help constrain the angular velocities for several plates having directions of motion that are otherwise only weakly constrained. For comparison, the 724 NUVEL-1 earthquake slip directions constitute 65 per cent of the NUVEL-1 data and are used to estimate directions of plate motion along every major plate boundary.

We minimized the use of earthquake slip directions because of evidence that earthquake slip directions give biased estimates of the direction of plate motion. Many studies now document that oblique subduction is almost always partly to completely partitioned into its trench-parallel and trench-orthogonal components,

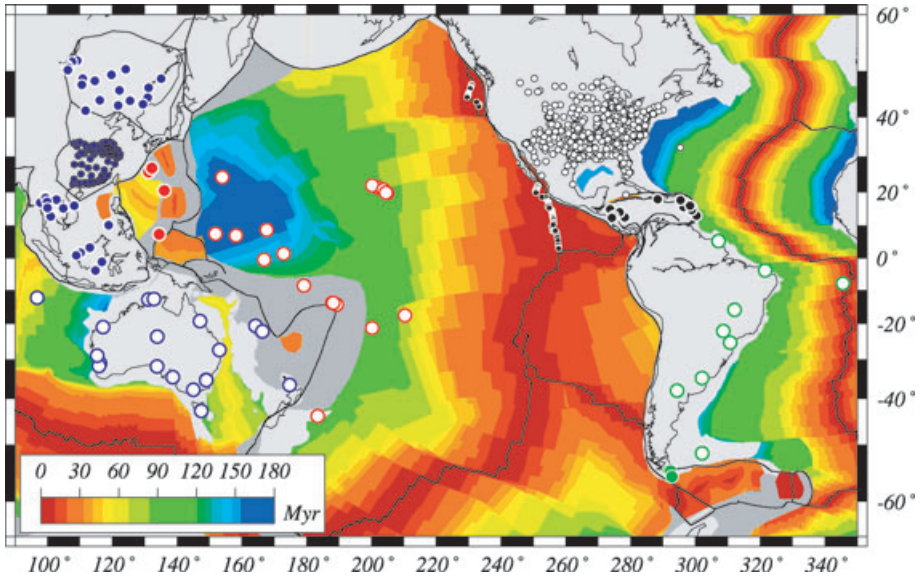

Figure 5. Filled circles show locations of GPS stations having velocities that are used to determine the MORVEL angular velocities for the Amur (medium-sized blue), Caribbean (black), Philippine Sea (red), Scotia (green), Yangtze (small blue) and Sundaland (medium-sized blue) plates (Table S4). Open circles show the locations of the GPS station velocities from the four plates that serve as the geodetic reference frames for the MORVEL GPS site velocities (Table S5), as follows: North America plate (open black), Pacific plate (red), South America plate (green) and Australia plate (blue). Small black circles along the Pacific–Juan de Fuca, Pacific–Rivera and Pacific–Cocos plate boundaries show locations of seafloor spreading rates that are used to estimate the PVEL angular velocities. Seafloor ages are from Müller *et al*. (1997).

resulting in translation and rotation of forearc slivers along faults in the upper plate and orthogonal or nearly orthogonal subduction (e.g. Fitch 1972; Jarrard 1986a,b, DeMets *et al.* 1990; McCaffrey 1992). Where partitioning occurs, the slip directions of shallow-thrust subduction earthquakes are observed to be deflected systematically towards the trench-normal direction with respect to the direction of motion between the subducting and major overlying plate. Where backarc spreading occurs, as is common in the western Pacific basin, shallow-thrust subduction earthquakes also may give incorrect estimates of the relative direction of the subducting plate relative to its major overlying plate.

Argus *et al.* (1989) and DeMets (1993) show that the slip directions of strike-slip earthquakes along oceanic transform faults differ systematically from the azimuths of well-surveyed strike-slip faults in the transform fault valley. The sense of this difference depends on whether the slip along a given transform fault is right-lateral or left-lateral, thereby excluding recent changes in the direction of plate motion as a possible explanation for these still poorly understood differences.

3.3 GPS data

Continuous and campaign GPS measurements at 144 locations are used to extend MORVEL to the Amur, Caribbean, Philippine Sea, Scotia, Sundaland and Yangtze plates (Fig. 5 and Table S4). Except for the Caribbean and Scotia plates, the motions of these plates would otherwise be unconstrained by data from the mid-ocean ridges. All 144 GPS velocities are from sites with three or more years of observations, which reduces the influence of seasonal and other long-period noise in the GPS time-series on the estimated site velocity (Blewitt & Lavallée 2002). Sites with a history of anomalous behaviour are excluded, as are stations near active faults. Further details about the station velocities are given in Sections 4 and 5.

We also use 498 station velocities from the Australia, North America and Pacific plates (Figs 5 and 6) to link the GPS station velocities from the plates listed above to the MORVEL plate circuit. As described in Section 4.4.2, these 498 velocities are not inverted during the estimation of the MORVEL angular velocities, but are instead used prior to the formal MORVEL data inversion to establish plate-centric frames of reference for the 144 velocities from the Amur, Caribbean, Philippine Sea, Scotia, Sundaland and Yangtze plates. These 498 station velocities are listed in Table S5.

Most of the original GPS data that we analysed were obtained from public sources, including the Scripps Orbit and Permanent Array Center archive, the National Geodetic Survey CORS archive, and the UNAVCO data archive. Data for selected stations in the western Pacific were also obtained from Geoscience Australia, the Geographical Survey Institute of Japan, the Japan Association of Surveyors, and from individual investigators for a few sites. The procedures for processing these GPS data are described in Section 4.4.

4 METHODS

4.1 Overview

Data are analysed on four levels to construct the MORVEL angular velocities. On the first level, spreading rates and associated uncertainties are estimated from magnetic data and a correction for outward displacement of reversal boundaries is applied. Azimuths of transform faults and their associated errors are estimated from bathymetric data and to a lesser degree, from ocean depths predicted from satellite altimetry (Smith & Sandwell 1997). Slip directions and associated uncertainties are estimated from published earthquake focal mechanisms. GPS data are processed and site velocities are determined from their coordinate time-series and transformed to

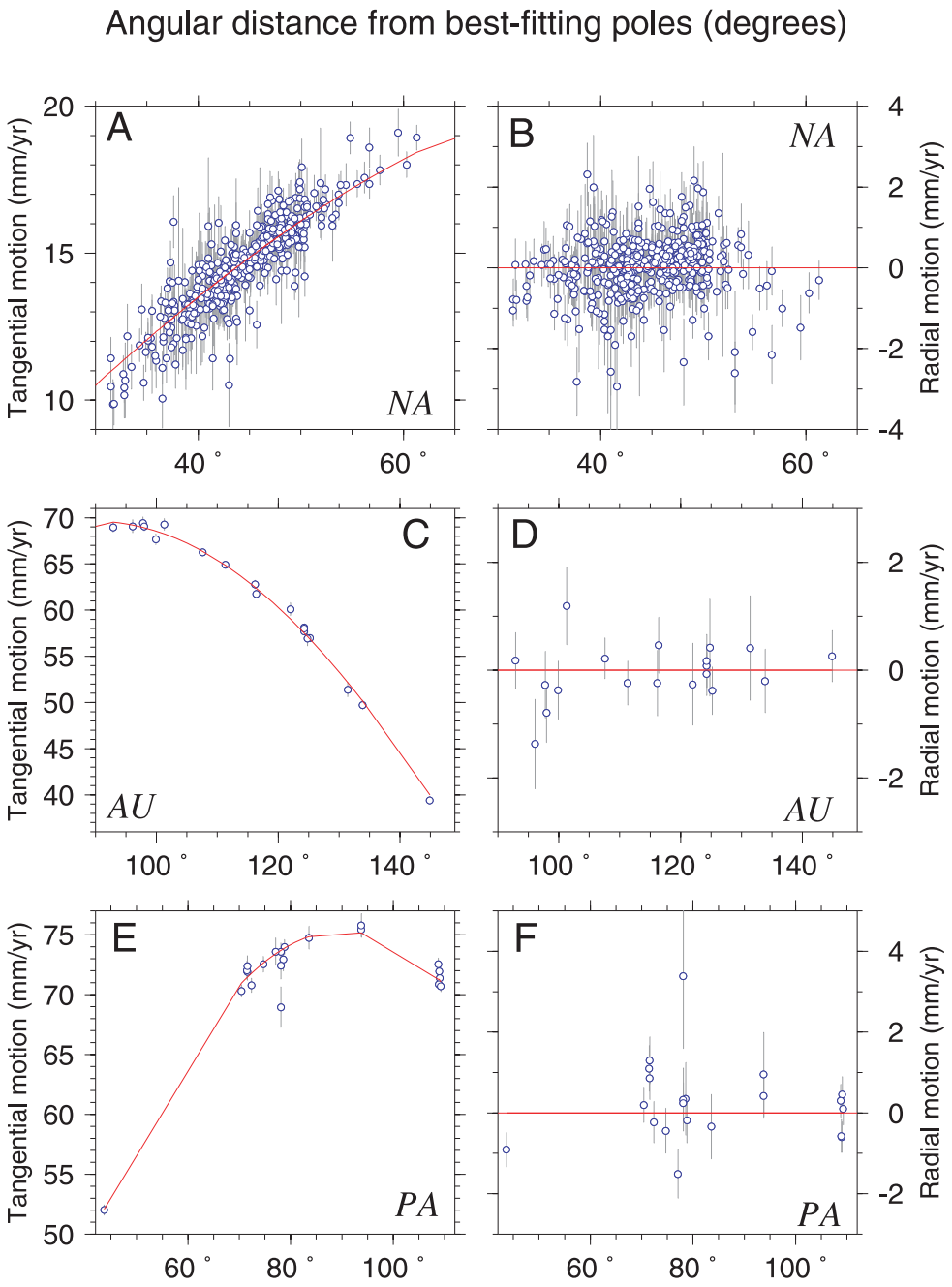

Figure 6. North America (NA), Australia (AU) and Pacific (PA) plate GPS station velocity components (blue circles) and motions calculated from the best-fitting angular velocities in Table 4 (red curves) as a function of angular distance from their best-fitting poles. Station locations are shown in Fig. 5. Australia plate station velocities are relative to ITRF2000. North America and Pacific plate station velocities are relative to ITRF2005. All velocities are corrected for motion of the geocentre, as described in the text. Panels in the left-hand column (a, c, e) show the component of the station motions parallel to small circles around the best-fitting poles. Panels in the right-hand column (b, d, f) show the component of station motions that are orthogonal (radial) to the same small circles. Vertical bars show 1σ uncertainties.

plate-centric frames of reference. On the second level, plate motion data along a single plate boundary or from a single plate are examined, best-fitting angular velocities are determined, and the mutual consistency of data for single plate pairs or plates is tested. Third, closure about local plate circuits is examined by inverting data from circuits of three or more plates (Gordon *et al.* 1987). Fourth, all data are inverted simultaneously to find the set of angular velocities that fit the data best in a least-squares sense, while being constrained to consistency with global plate circuit closure. Plate circuit closure is also examined through comparison of the best-fitting and closure-fitting angular velocities for each plate pair with data along a common boundary. A closure-fitting angular velocity is determined by using all MORVEL data except the data along the shared boundary of a plate pair. Thus a best-fitting angular velocity and a closure-fitting angular velocity are determined from disjoint data sets.

4.2 Seafloor spreading rates

4.2.1 Cross-correlation technique for spreading rate determination

Of the 1696 spreading rates that are used to estimate the MORVEL angular velocities, 1607 (95 per cent) are estimated from digital marine magnetic data via an automated method for cross-correlating observed and synthetic magnetic profiles. For the remaining 5 per cent of the spreading rates, 18 are estimated by Thomas *et al.* (2003) and 71 by Horner-Johnson *et al.* (2005) via visual correlations of synthetic and observed magnetic profiles. Our cross-correlation procedure uses a least-squares fitting criteria to estimate the best-fitting spreading rate and reversal transition width and permits greater precision than visual comparisons. Chu & Gordon (1998) employ a similar technique to estimate 3.16-Myr-average spreading rates in the Red Sea.

Each observed magnetic profile is prepared for cross-correlation by reducing it by its mean residual magnetic intensity, projecting it onto the local ridge-normal direction, and inserting markers into the digital magnetic file to identify the anomaly sequence to be correlated. For plate boundaries with spreading rates higher than 35–40 mm yr^{-1}, the part of the magnetic anomaly sequence that ranges in age from ≈0.6 to 1.0 Ma (pink shaded area in Fig. 7), centred on the Brunhes/Matuyama reversal (0.780 Ma), is chosen for correlation. For slower spreading centres, the entire anomaly 2A sequence, extending from 2.581 to 3.596 Ma (blue shaded area in Fig. 7), is selected for correlation. In places where only part of the anomaly 2A sequence is crossed by a ship or aeroplane track or the sequence is interrupted by ridge propagation, as much of the anomaly as possible was used. The precise averaging interval varies from profile to profile depending on the features of the profile that are fit (Table S1).

Synthetic magnetic anomaly profiles were constructed using reversal ages estimated by Hilgen *et al.* (1995). The age for the Brunhes/Matuyama reversal in the more recent Lourens *et al.* (2004) reversal timescale is 0.781 Ma, 0.1 per cent older than estimated by Hilgen *et al.* (1995). For a 50 mm yr^{-1} plate rate, the implied rate bias of only 0.05 mm yr^{-1} is too small to affect any results or conclusions described below. The maximum difference between the anomaly 2A age estimates from these two timescales is also only 1000 yr, too small to matter herein.

All synthetic magnetic profiles were constructed assuming vertical reversal boundaries in a 500-m-thick magnetic source layer, location-dependent ambient and remanent magnetic field inclinations and declinations, and phase shifts determined from the local strike of the spreading axis. The average depth to the top of the magnetic source layer for ship-board profiles was determined from seafloor depths that were extracted along each profile from the Smith & Sandwell (1997) bathymetric grid. For aeromagnetic profiles, we added 300 m to the average seafloor depth to account for a typical flight altitude of 1000 feet.

For each observed magnetic profile, synthetic magnetic profiles were constructed for a range of trial spreading rates (at increments of 0.2 mm yr^{-1}) and magnetic reversal transition widths (at increments of 0.5 km). For each trial synthetic profile, the synthetic magnetic intensity at the location of each magnetic measurement from the observed profile was calculated, resulting in observed and synthetic profiles with a one-to-one correspondence between the individually measured intensity values and those predicted from the synthetic profile. The amplitude scale of the synthetic was adjusted to match the peak-to-trough amplitude of the observed anomaly. Finally, the summed, squared difference between the synthetic and observed magnetic intensities was determined for all observations that were marked for cross-correlation, resulting in the least-squares misfit between each trial synthetic profile and its observed profile. The

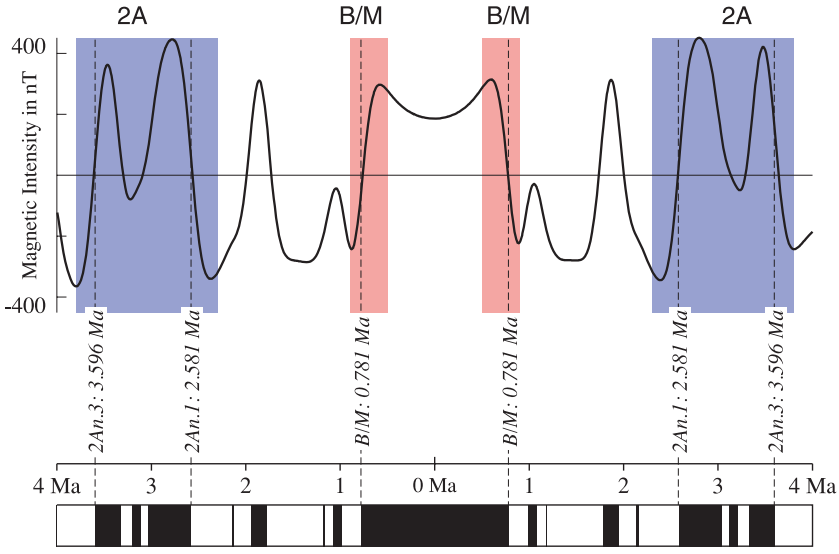

Figure 7. Magnetic anomalies that are used to estimate the MORVEL spreading rates. For plate boundaries with spreading rates that are higher than ≈35 mm yr^{-1}, average opening rates are determined using the width of the central magnetic anomaly, which is bounded on both sides by the Brunhes-Matuyama reversal (BM highlighted in pink on both sides of the ridge). Rates elsewhere are averaged using the anomaly 2A sequence (highlighted in blue), the middle of which has an age of 3.16 Ma. Blue and pink regions show the approximate parts of each observed magnetic profile that are used for cross-correlation with a synthetic magnetic anomaly profile in order to identify the best-fitting opening rate and reversal transition width (see text). The synthetic magnetic profile in the figure (black curve) is calculated for a location near the magnetic north pole and assumes a uniformly magnetized, 500-m-thick layer located 2.5 km below the ocean surface with 1-km-wide polarity transition zones between oppositely magnetized blocks. Reversal ages are from Lourens *et al.* (2004).

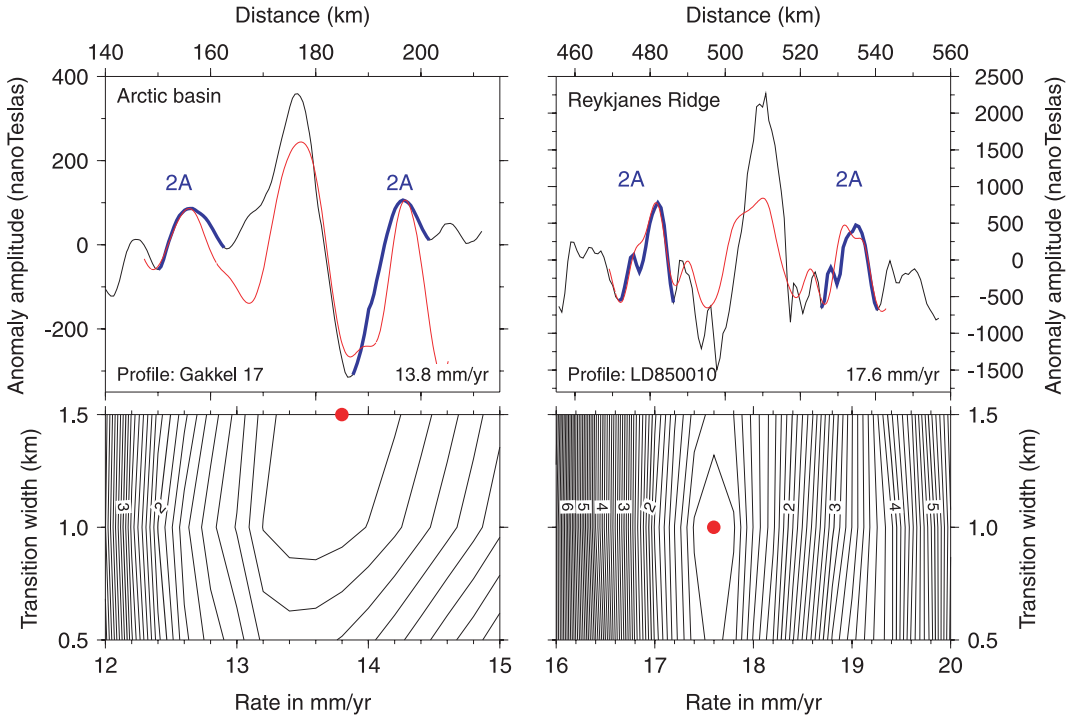

Figure 8. Examples of cross-correlated fits of the anomaly 2A sequence for ridge-normal magnetic profiles across the Gakkel Ridge in the Arctic basin (left-hand panel) and Reykjanes Ridge south of Iceland (right-hand panel). Black and blue curves show observed profile and red curve shows synthetic magnetic profile. Blue curve indicates the part of the observed profile that is anomaly 2A and is cross-correlated with the synthetic profile. Lower diagrams show contours of least-squares misfit normalized by the misfit of the best-fitting least-squares model (red circle) for the suite of spreading rates and anomaly transition widths that were explored during the cross-correlation procedure.

resulting grid of sum-squared errors (Fig. 8) was used to identify the best-fitting spreading rate for each profile, to assess the trade-off in fit as a function of the assumed reversal zone transition widths, and to assess the stability of the best-fitting solution.

Fig. 8 illustrates the best fits to two magnetic profiles, one from the magma-starved, ultraslow-spreading Gakkel Ridge in the Arctic basin, among the poorest-quality magnetic profiles in our data set, and the second from the magma-dominated Reykjanes Ridge south of Iceland, where the magnetic anomaly sequence is excellent despite a spreading rate that is lower than 20 mm yr^{-1}. The Jaramillo anomaly and anomaly 2 are both absent from the Gakkel Ridge profile, as is typical for magma-starved spreading centres, and the profile is well fit by spreading rates that range from ≈12.5 to 15.5 mm yr^{-1}. The wide range of acceptable solutions is attributable to the sloping magnetic anomaly edges and absence of well-resolved short wavelength features in this poor quality profile. In contrast, the Jaramillo anomaly, anomaly 2 and anomaly 2A are all easily recognized in the magnetic profile from the Reykjanes Ridge (right-hand side of Fig. 8). The least-squares fit for this profile changes rapidly as a function of the assumed spreading rate and hence defines a narrower range of acceptable best-fitting spreading rates. Illustrations of the cross-correlated fits to all 1607 spreading rates that were fit with our automated cross-correlation technique are available at http://www.geology.wisc.edu/∼chuck/MORVEL.

Additional magnetic profiles that span the full range of spreading rates sampled in our data are shown in Fig. 9. The biggest challenge in cross-correlation is to match the observed anomaly amplitudes, which vary with location and time as a function of seafloor depth, magnetic mineralogy, departures from 2-D seafloor topography, distance from fracture zones and time variations in the ambient magnetic field, none of which are incorporated in our synthetic modelling. We discarded profiles that could not be fit convincingly via our cross-correlation procedure; these constituted fewer than 1 per cent of the profiles that we examined.

4.2.2 *Correction for outward displacement*

Various processes widen the zone in which magnetic field reversals are recorded in new oceanic crust (Atwater & Mudie 1973), including extrusion of new magma onto adjacent older crust, intrusion of dykes into adjacent older crust, accumulation of magnetized gabbros at the base of the crust (Sempere *et al.* 1987), and acquisition of a thermoviscous remanent magnetization in the lower crust and uppermost mantle (Dyment & Arkani-Hamed 1995). Because these processes preferentially affect older crust adjacent to the spreading axis, they shift the midpoint of a magnetic polarity transition zone outward from the spreading axis. The distance between two same-aged magnetic lineations is therefore greater than the total seafloor that accreted during that time. This outward displacement causes spreading rates that are estimated from reconstructions of the midpoints of magnetic polarity zones to exceed the true rates, thereby necessitating a correction.

From reconstructions of nearly 7000 crossings of young magnetic reversals at 29 locations along the mid-ocean ridges, DeMets & Wilson (2008) estimate the magnitude of the two-sided outward displacement to be 1–3 km at most locations and 3.5 and 5.0 km along the Carlsberg and Reykjanes ridges, respectively. The 2.2 ± 0.3 km (1σ) global average is the same within uncertainties as found by Sempere *et al.* (1987), who measured the widths of magnetic polarity reversal zones from magnetization distributions they

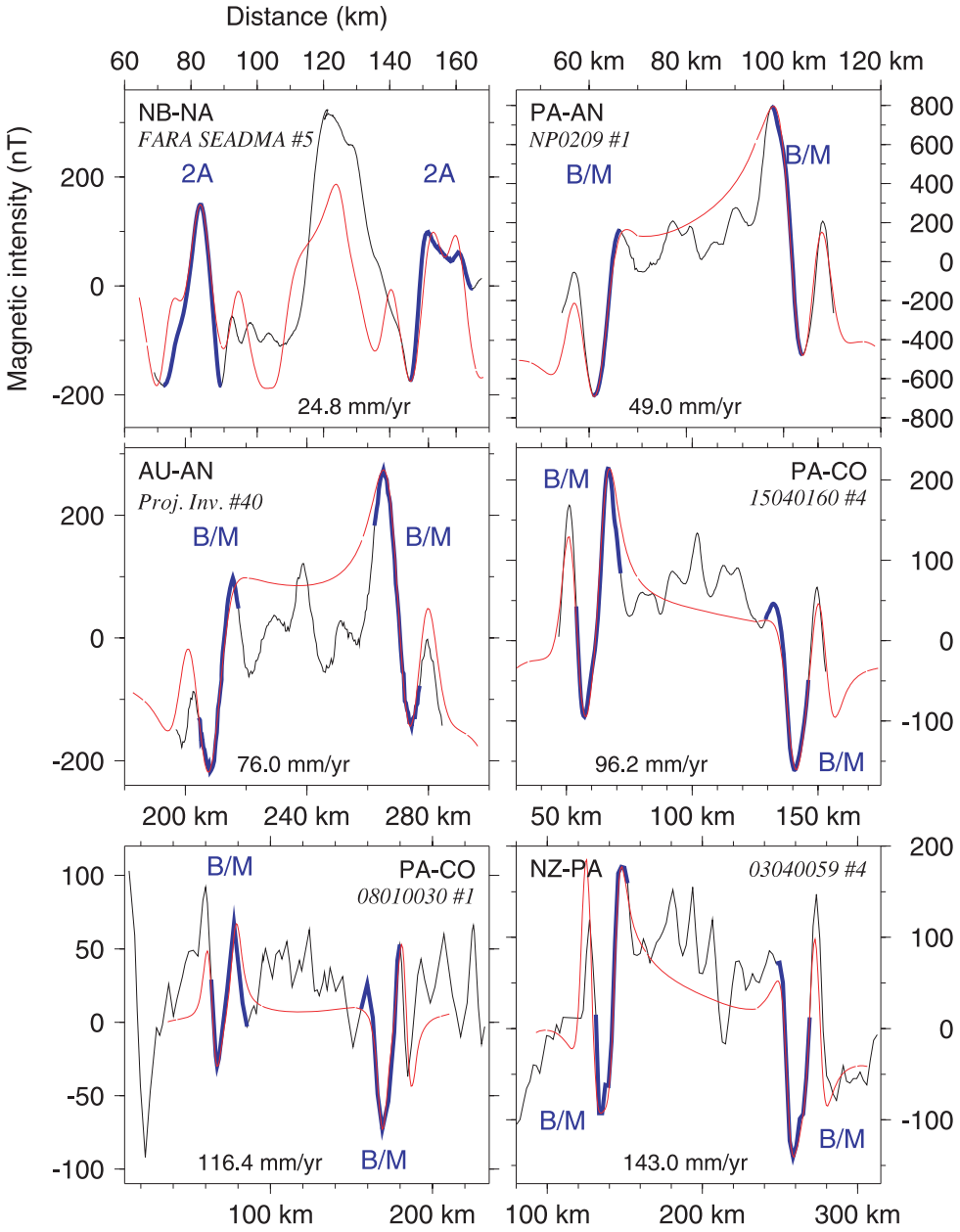

Figure 9. Cross-correlated fits for the Brunhes-Matuyama (B/M) reversal (0.78 Ma) or anomaly 2A for ridge-normal magnetic profiles with rates from 25 to 143 mm yr^{-1}. Black and blue curves show observed profile. Red curve shows synthetic magnetic profile. Parts of the observed profiles that are shown with blue are cross-correlated with the synthetic profile.

determined from deeply towed magnetic profiles for a wide range of spreading rates. The good agreement between these two estimates provides a firm basis for correcting the MORVEL spreading rates.

The MORVEL spreading rates are corrected assuming outward displacement of 2 km everywhere except the Carlsberg and Reykjanes ridges, where respective corrections for outward displacement of 3.5 and 5 km are instead applied. The effect of these corrections on spreading rates varies with the rate averaging interval (Table S1). The widely applied 2 km correction reduces spreading rates that average motion since anomaly 1n (0.78 Ma) by ≈2.56 mm yr^{-1}, whereas rates that average motion since anomaly 2A (2.58–3.60 Ma) are reduced by only ≈0.63 mm yr^{-1}. Along the Carlsberg and Reykjanes ridges, where rates are averaged since anomaly 2A, the respective corrections are ≈1.1 and ≈1.6 mm yr^{-1}.

4.2.3 Determination of uncertainties

Spreading rate uncertainties are assigned in two stages. First, a quality ranking of low, intermediate, or high is assigned to each magnetic profile depending on multiple factors that include a profile's obliquity relative to the ridge-normal direction, how well the anomaly sequence and anomaly amplitudes conform to those of its corresponding synthetic magnetic profile, the quality of the profile navigation, and the distance between magnetic intensity measurements, which is typically 50–100 m, but occasionally exceeds several km for profiles extracted from older cruises. Rates determined from profiles with high, intermediate, and low quality rankings are assigned initial uncertainties of ±1, ±1.5 or ±2 mm yr^{-1}, respectively. Rates for a single plate pair are then inverted and the initial assigned uncertainties are multiplied by a constant multiplicative

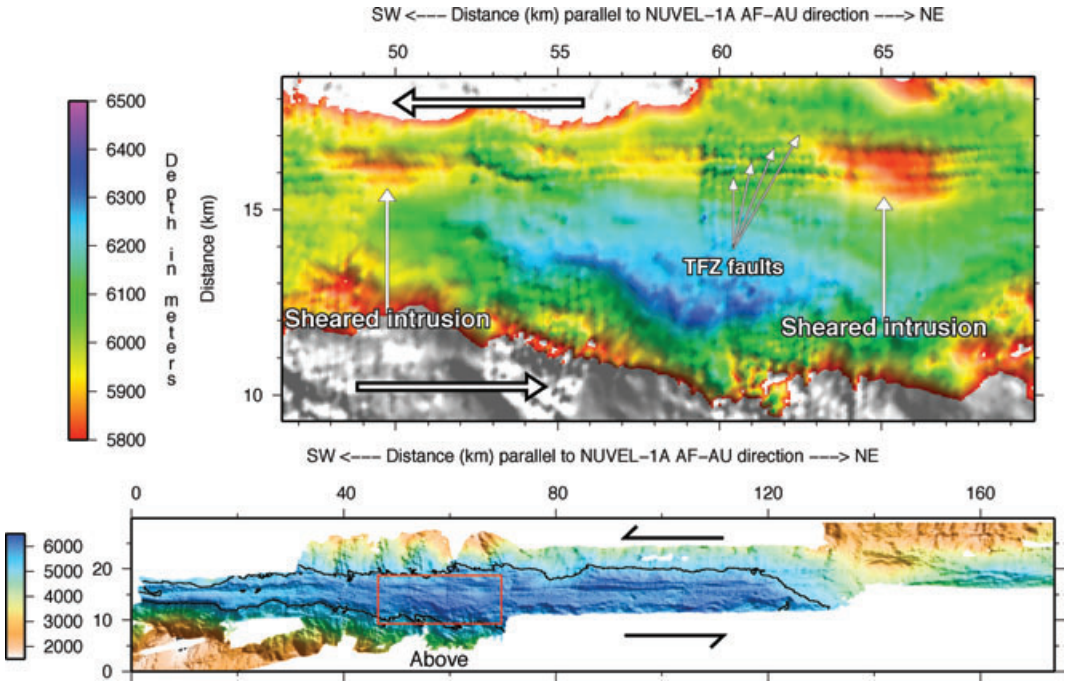

Figure 10. Lower panel: multibeam survey of the Vema transform valley, 9°–10°S, Central Indian ridge. Prominent lineations in the valley mark the zone of active faulting, constituting the transform fault zone (TFZ). The uncertainty in the fault azimuth is determined from the length and width of the TFZ, as described in the text. Upper panel: area identified in lower map. Slip in the TFZ is accommodated by multiple faults that offset apparent volcanic or serpentinite intrusions in a left-lateral sense. Projections are oblique Mercator about the NUVEL-1A Africa–Australia pole; horizontal features are thus small circles about that pole. Figure is adapted from Drolia & DeMets (2005).

factor to cause reduced chi-square to equal one. No further adjustment is made to the rate uncertainties.

4.3 Plate motion directions from transform fault azimuths

For all transform faults mapped with single-beam, multibeam or side-scan sonar, the azimuth of the narrowest imaged morphotectonic element that accommodates current strike-slip motion was estimated. This typically consists of the transform fault zone (TFZ), the zone in which all active strike-slip faulting occurs (Fox & Gallo 1984). For transform faults where the TFZ cannot be identified, the azimuth of the transform tectonized zone (TTZ), which is the zone within which both active and inactive strike-slip motion have been accommodated (Fox & Gallo 1984), is estimated.

For example, the TFZ within the Vema transform fault valley along the Central Indian Ridge (Fig. 10) is easily identified from individual strike-slip faults that can be traced continuously for 160 km (Drolia & DeMets 2005). Young intrusions within the Vema transform valley are offset by multiple fault strands within the 1- to 2-km-wide TFZ (upper panel of Fig. 10). These fault strands are the only features in the transform valley that appear to accommodate active strike-slip motion (Drolia & DeMets 2005), thereby permitting us to measure with high precision the local direction of motion between the Somalia and Capricorn plates.

The following expression from DeMets *et al.* (1994b) is used to estimate the uncertainty in a transform fault azimuth from the width (W) and surveyed length (L) of its narrowest, imaged tectonic element

$$\sigma = \frac{\tan^{-1}(W/L)}{\sqrt{3}}. \quad (1)$$

In many cases, the TFZ begins to curve inward towards the ridge axis at distances of ≈10 km from the ridge-transform intersection. Where this occurred, we measured the fault azimuth safely away from this region and reduced L accordingly. We found that the width (W) that we estimated for a given transform fault zone or transform tectonized zone often varied by several kilometres depending on which of us interpreted the data. We therefore used the rms misfits for transform fault azimuths that were determined by the different co-authors to scale the uncertainties in the transform fault azimuths such that the uncertainties were consistent throughout and faithfully reflect the dispersion of the data. In practice, the transform azimuth uncertainties were rendered consistent by multiplying all uncertainties that were originally determined by one of us by a single scaling factor of 0.6.

Fault azimuths were estimated from the highest resolution bathymetric grids available for a given fault (typically 200-m resolution grids) or the highest-quality map if a grid was not available. For eight transform faults that are imaged only by lower resolution satellite altimetric observations, the azimuths of their transform fault valleys was estimated with W assumed to equal 8 km or larger (Spitzak & DeMets 1996).

4.4 Site velocities from GPS data

4.4.1 Raw GPS data analysis

Most of the GPS station velocities used herein are determined from processing at UW-Madison of GPS code-phase measurements using GIPSY software from the Jet Propulsion Laboratory (JPL). Daily GPS station coordinates from the beginning of 1993–2008

September were estimated using a precise-point-positioning analysis strategy described by Zumberge *et al.* (1997) and employ precise satellite orbits and clocks from JPL. The daily fiducial-free coordinates are transformed both to ITRF2000 (Altamimi *et al.* 2002) and ITRF2005 (Altamimi *et al.* 2007) with daily seven-parameter Helmert transformations supplied by JPL. Daily and longer-period spatially correlated noise between sites is estimated and removed with a regional-scale noise stacking technique (Wdowinski *et al.* 1997; Marquez-Azua & DeMets 2003). After removing the common-mode noise from each GPS time-series, the daily site coordinate repeatabilities are reduced to 1–3, 2–4 and 6–10 mm in the north, east and down components, respectively, 10–40 per cent smaller than the daily coordinate repeatabilities for the uncorrected daily site coordinates. The common-mode corrections also effectively reduce longer-period noise in the GPS time-series, typically by 50–70 per cent in amplitude.

Some of the GPS data used to estimate the MORVEL GPS station velocities was processed by other authors (Shen *et al.* 2005; Jin *et al.* 2007; Simons *et al.* 2007; Smalley *et al.* 2007), who employed either GAMIT software (King & Bock 2000) or GIPSY software. At a handful of stations for which both software packages were used to process the original GPS data, we found that the velocities determined from the two were the same to within the likely uncertainties (± 0.5 mm yr^{-1} in most cases).

Following Argus (1996), Blewitt (2003) and Argus (2007), the Earth's centre-of-mass is adopted as the appropriate origin for geodetically described plate motions. Argus (2007) uses the horizontal components of geodetic velocities determined from four different geodetic techniques to estimate that Earth's centre-of-mass moves relative to the ITRF2005 geocentre at respective rates of 0.3, 0.0 and 1.2 mm yr^{-1} in the X, Y and Z directions. GPS velocities having a native geodetic reference frame of ITRF2005 are therefore corrected for these estimated translation rates prior to inverting the GPS velocities to estimate plate angular velocities. Similarly, GPS velocities with a native reference frame of ITRF2000 are corrected by respective rates of -0.1, 0.1 and -0.6 mm yr^{-1} in the X, Y and Z directions to bring those velocities into the same centre-of-mass reference frame as the corrected ITRF2005 GPS station velocities (D. Argus, personal communication, 2009).

4.4.2 Velocity transformation to plate-based reference frames

In order to minimize the influence of GPS station velocities on the angular velocity estimates for all plates with spreading rates and transform fault azimuths on one or more of their boundaries, we used a two-stage process to estimate the angular velocities for plates populated by GPS stations. In the first stage, we changed the original frames of reference for the GPS station velocities from ITRF2000 or ITRF2005 to plate-centric reference frames that are specified below. We then inverted the plate-centric GPS velocities and other MORVEL kinematic data to estimate the closure-enforced MORVEL angular velocities. Simple numerical experiments described in Section 5.2.4 confirm that the angular velocities for plates having motions that are determined from spreading rates and transform fault azimuths are influenced little or not at all by GPS station velocities. MORVEL thus describes plate motions over geological time spans for all the major plates and most of the minor plates.

For GPS stations on the Amur, Sundaland and Yangtze plates, we changed the frame of reference from ITRF2000 to the Australia plate (Fig. 2). We changed the frame of reference for GPS stations on the Caribbean and Philippine Sea plates from ITRF2005 to the North America and Pacific plates, respectively (Fig. 2). We selected the Australia, North America and Pacific plates as the geodetic reference plates based on the superior quality and coverage of GPS stations on each of these three plates and their geographic proximity to the five plates listed above. We use the angular velocity that best fits the station velocities for each reference plate (Table 4) to transform the station velocities on the Amur, Caribbean, Philippine, Sundaland and Yangtze plates to their designated, plate-centric reference frame. Additional uncertainty is propagated into each station velocity from the best-fitting angular velocity covariances. The transformed GPS station velocities and their modified uncertainties are listed in Table S4.

Additional information about all the GPS velocities described above is given in Section 5.

4.5 Estimation of angular velocities and their uncertainties

Our program for estimating angular velocities employs fitting functions for spreading rates and plate motion directions from DeMets *et al.* (1990) and fitting functions for GPS velocities from Ward (1990). Given N observations of the relative motions of P plates, the code determines the *P–1* angular velocities that simultaneously minimize the weighted least-squares misfit χ^2 and satisfy plate circuit closure. Reduced chi-square χ^2_ν [i.e. $\chi^2/(N-3P)$] is expected to equal $\approx$1 for large N if the assumed plate geometry is appropriate, if the plates do not deform, if the data are unbiased, and if the data uncertainties are correctly assigned and uncorrelated. The formal uncertainties in the angular velocities are specified by a 3(P–1) by 3(P–1) covariance matrix that is propagated linearly from the assigned data uncertainties.

The formal covariances do not incorporate any correlated errors that might affect the data and therefore constitute a minimum estimate of the parameter uncertainties. One such correlated error is a possible bias in the average correction for outward displacement, which has a global 1σ uncertainty of 0.3 km and exhibits variation of $\approx$1 km along individual plate boundaries (DeMets & Wilson 2008). If we conservatively assume a ± 1 km nominal 1σ uncertainty in outward displacement for all spreading centres, this implies a correlated error of ± 1.3 mm yr^{-1} in 0.78-Myr-average spreading rates and ± 0.32 mm yr^{-1} bias in 3.16-Myr-average spreading rates. These exceed the formal uncertainties of ± 0.1–0.3 mm yr^{-1} in the relative plate velocities that are calculated from the formal covariance matrix discussed above and thus should not be neglected.

We therefore incorporated this additional uncertainty into the best-fitting angular velocity covariance matrices (Table 1) and the MORVEL covariance matrix (Tables 2 and 3) as follows. In a numerical experiment, values of outward displacement are increased globally by 1 km from their preferred value, spreading rates are recalculated, and the data are inverted to obtain new angular velocities. The squared differences between the Cartesian components of the original angular velocities and the angular velocities for this experiment approximate the additional covariance that results from systematic error of outward displacement.

This procedure is repeated with all assumed outward displacements decreased, instead of increased, from their original values. Thus a second covariance matrix is generated. The average of these two covariance matrices is then added to the original, formally determined covariance matrix. This final matrix gives more realistic uncertainties for individual angular velocities.

Table 1. Best-fitting angular velocities and covariances.

Plate pair	N_{Data} R/T/S	Angular velocity			Variances (a, d, f) and covariances (b, c, e)					
		Lat. (°N)	Long. (°E)	ω (deg Myr^{-1})	a	b	c	d	e	f
AU-AN	167/19/0	11.3	41.8	0.633	2.60	1.85	0.97	2.18	0.18	1.04
CP-AN	35/1/0	17.2	32.8	0.580	55.09	30.12	−61.66	116.24	−52.93	81.69
LW-AN	16/6/0	−1.2	−33.6	0.133	3.06	2.29	−3.67	2.17	−3.11	4.86
NB-AN	59/4/0	−6.2	−34.3	0.158	2.25	0.48	−2.50	0.36	−0.72	3.22
NZ-AN	60/21/0	33.1	−96.3	0.477	0.11	0.34	−0.25	6.67	1.27	4.94
PA-AN	48/10/0	−65.1	99.8	0.870	0.81	1.00	0.13	3.62	−1.19	3.60
SM-AN	29/2/0	11.2	−56.7	0.140	1.89	3.41	−2.07	7.55	−4.54	3.33
EU-NA	453/5/0	61.8	139.6	0.210	0.18	−0.13	−0.07	0.14	0.07	0.13
NB-NA	161/4/0	79.2	40.2	0.233	0.95	−0.74	0.55	0.76	−0.43	0.66
AR-NB	45/0/0	30.9	23.6	0.403	33.74	30.02	17.99	29.24	17.99	11.66
CO-NZ	88/2/0	1.6	−143.5	0.636	4.59	0.60	0.04	15.41	−0.59	1.23
CO-PA	61/6/0	37.4	−109.4	2.005	9.52	16.31	−3.27	76.68	−15.69	7.92
JF-PA	27/1/0	−0.6	37.8	0.625	101.40	130.64	−156.42	174.03	−207.87	255.74
NZ-PA	42/15/0	52.7	−88.6	1.326	3.82	5.78	2.55	21.19	6.14	6.72
RI-PA	26/3/0	25.7	−104.8	4.966	235.85	773.86	−283.97	2566.19	−941.95	352.07
NB-SA	99/27/0	60.9	−39.0	0.295	0.17	−0.06	0.00	0.07	−0.04	0.32
SW-SC	18/4/0	−32.0	−32.2	1.316	1432.85	−798.88	−2569.96	548.04	1512.83	4693.34
AR-SM	51/5/0	22.7	26.5	0.429	4.24	4.49	0.96	5.40	1.01	0.50
CP-SM	56/10/0	16.9	45.8	0.570	4.30	5.54	0.73	11.90	−2.54	3.10
IN-SM	113/2/22	22.7	30.6	0.408	1.50	1.48	−0.43	3.32	0.24	0.91
AN-SR	9/2/0	85.7	−139.3	0.317	35.43	−4.86	−52.83	1.14	7.24	80.63
NB-SR	25/2/0	70.6	−60.9	0.346	43.94	−1.69	−59.58	1.66	3.53	83.23

Notes: Plate abbreviations are from Fig. 1. R, T and S are the numbers of spreading rates, transform fault azimuths and earthquake slip directions used to determine the best-fitting angular velocity, respectively. Angular velocities describe counter-clockwise rotation of the first plate relative to the second. Covariances are propagated from data uncertainties and also incorporate ±1 km systematic errors from uncertainty in outward displacement (see text). Covariances are Cartesian and have units of 10^{-8} rad^2 Myr^{-2}. Elements a, *d* and *f* are the variances of the (0°N, 0°E), (0°N, 90°E) and 90°N components of the rotation. The covariance matrices are reconstructed as follows:

$$\begin{pmatrix} a & b & c \\ b & d & e \\ c & e & f \end{pmatrix}.$$

4.6 Statistical comparisons of angular velocities

In the analysis below, we often compare two angular velocities for a given plate pair to determine the statistical significance of the combined difference in their pole locations and angular rotation rates. Given two angular velocities $\vec{\omega}$ and $\vec{\omega}^*$, we calculate their formal statistical difference as follows:

$$\chi^2 = (\vec{\omega} - \vec{\omega^*})(\mathrm{Cov} + \mathrm{Cov}^*)^{-1}(\vec{\omega} - \vec{\omega}^*)^T, \quad (2)$$

where Cov and Cov* are the 3 × 3 Cartesian covariance matrices for the two angular velocity estimates.

This χ^2 statistic provides a useful measure of the significance of the difference between two angular velocities. The probability level p for the calculated value of χ^2 is determined from standard tables for three degrees of freedom and represents the probability of obtaining a difference as large or larger than observed if the two angular velocities actually are identical.

5 DATA AND RESULTS: BEST-FITTING AND MORVEL PLATE MOTION ESTIMATES

We now describe in detail both the data and fits of the best-fitting angular velocities (Table 1) and MORVEL angular velocities (Tables 2 and 3) for the many plate boundaries and plates that we analyse. The description is organized as follows. We briefly describe the rms dispersions of the spreading rates, transform fault azimuths and GPS station velocities relative to the angular velocities that best fit them. These represent our best measures of the consistency of the data from individual plate boundaries and plates and hence their likely uncertainties. We then summarize general aspects of MORVEL, including descriptions of the average misfits to the different types of data and the relative contributions of the different data types to MORVEL.

Following the summary description, we describe the data and fits of the best-fitting, MORVEL and NUVEL-1A angular velocities for plate boundaries that are located within six geographic regions (Sections 5.3–5.8). This includes searches for the best locations of the Nubia–North America–South America triple junction along the Mid-Atlantic Ridge and the Capricorn–Australia–Antarctic triple junction along the Southeast Indian Ridge.

In Section 5.9, we describe the PVEL (Pacific VELocities) angular velocities, which specify the motions of the oceanic Cocos, Rivera and Juan de Fuca plates relative to the Caribbean and North America plates and are included here to satisfy the needs of investigators who are engaged in geodetic studies of deformation in western Central America and western North America. The modified PVEL plate circuit (Fig. 2) bypasses the extended MORVEL global plate circuit that links the motions of Pacific basin plates to the North America and Caribbean plates, where biases in the MORVEL estimates of their relative motions may accumulate.

Closures of the six three-plate circuits that constitute the backbone of the MORVEL global plate circuit are analysed and discussed in Section 6.

Table 2. MORVEL angular velocities and covariances relative to the Pacific plate.

Plate pair	Angular velocity			Variances and covariances					
	Lat. (°N)	Long. (°E)	ω (deg Myr^{-1})	a	b	c	d	e	f
AM	65.9	−82.7	0.929	2.09	−2.10	−0.73	4.00	2.51	6.28
AN	65.9	−78.5	0.887	0.82	1.39	0.09	4.28	0.09	1.06
AR	60.0	−33.2	1.159	2.54	2.41	1.12	10.42	0.84	2.11
AU	60.1	6.3	1.079	1.23	−0.75	0.95	1.41	−0.57	2.28
CA	55.8	−77.5	0.905	2.10	−1.11	−0.07	10.59	0.58	3.32
CO	42.2	−112.8	1.676	8.73	7.04	−6.48	14.83	−7.46	5.87
CP	62.3	−10.1	1.139	2.03	0.03	0.52	11.74	−6.01	5.10
EU	61.3	−78.9	0.856	1.86	0.81	−0.19	5.39	0.76	2.58
IN	61.4	−31.2	1.141	1.04	1.15	0.29	10.39	0.28	1.73
JF	−0.6	37.8	0.625	101.40	130.64	−156.42	174.03	−207.87	255.74
LW	60.0	−66.9	0.932	3.31	3.07	−3.52	7.60	−3.08	5.92
MQ	59.2	−8.0	1.686	147.89	−70.93	277.33	35.76	−133.60	527.58
NA	48.9	−71.7	0.750	1.65	−0.03	−0.36	7.05	1.51	2.75
NB	58.7	−66.6	0.935	1.07	0.49	−0.63	5.74	0.49	2.22
NZ	55.9	−87.8	1.311	1.11	2.89	−1.27	13.35	−4.84	3.06
PS	−4.6	−41.9	0.890	9.10	−9.91	−5.77	11.17	6.42	4.03
RI	25.7	−104.8	4.966	235.84	773.86	−283.97	2566.19	−941.94	352.09
SA	56.0	−77.0	0.653	1.24	0.64	−0.55	5.30	1.64	2.67
SC	57.8	−78.0	0.755	3.42	−2.63	−8.03	9.99	13.01	39.81
SM	59.3	−73.5	0.980	0.77	1.37	0.00	6.84	−0.01	1.55
SR	55.7	−75.8	0.636	16.33	−0.36	−22.09	5.14	4.00	34.42
SU	59.8	−78.0	0.973	2.03	−2.71	0.50	9.71	1.30	2.87
SW	−3.8	−42.4	1.444	1305.92	−658.62	−2281.21	367.97	1164.52	4029.32
YZ	65.5	−82.4	0.968	1.64	−1.55	0.46	3.07	0.45	2.95

Notes: All plates listed in this table rotate counter-clockwise relative to a fixed Pacific plate. Other conventions employed in this table are defined in note of Table 1. Plate abbreviations are from Fig. 1. The angular velocities are from an inversion of all the MORVEL data in Tables 1–4 in the electronic supplement. Covariances are propagated from data uncertainties and also incorporate systematic errors from uncertainty in outward displacement (see text).

5.1 Spreading rate, transform fault and GPS site velocity rms misfits

The 1696 MORVEL spreading rates range from 9.7 mm yr^{-1} in the northern Red Sea to 154.4 mm yr^{-1} along the East Pacific Rise and are assigned uncertainties that range from ±0.6 to ±5.1 mm yr^{-1} (Table S1). Spreading rates are averaged out to anomaly 2A for ten plate pairs, the same averaging interval as for NUVEL-1A. Inversions of only the spreading rates for these 10 plate pairs gives rms misfits that range from 0.37 to 1.03 mm yr^{-1} (Fig. 11b), comparable to the 0.25–1.2 mm yr^{-1} range of rms misfits for the NUVEL-1A rates from these same spreading centres.

The rms misfits to the 0.78-Myr-average rates from the 11 intermediate and fast spreading plate pairs range from 0.8 to 2.8 mm yr^{-1} (Fig. 11b). The greater dispersion for rates averaged over 0.78 Ma is expected from the four times longer averaging interval for 3.16-Myr averages versus 0.78-Myr averages.

The 163 transform fault azimuths have uncertainties of ±0.5° to ±6.0° (Table S2). Inversions of only the transform fault azimuths for the 13 plate pairs with three or more transform fault azimuths give rms misfits that range from 0.7° to 3.8°. Reduced chi-square for the 137 transform fault azimuths from these 13 plate boundaries is 0.95, close to that expected if their assigned uncertainties are appropriate. A simple geometric conversion of the rms directional misfit for each plate pair to its equivalent rms misfit in units of mm yr^{-1} gives values that range from 0.4 mm yr^{-1} for the Southwest Indian Ridge plate pairs to 3.7 mm yr^{-1} for the Pacific–Cocos plate pair. These are comparable to the range of rms misfits for the spreading rates (Fig. 11b) despite the fundamentally different nature of the two types of data.

The weighted rms misfits of the angular velocities that best fit the GPS station velocities from the Amur, Caribbean, Philippine, Sundaland and Yangtze plates average 0.8 and 1.0 mm yr^{-1} for the north and east velocity components, respectively. Most of these 141 velocities are from survey-mode sites and are thus determined from many fewer daily position estimates than is the case for a typical continuous GPS station.

All 498 GPS stations on the three geodetic reference plates (Australia, North America and Pacific) operate continuously and therefore should have better-determined velocities than survey-mode stations. This appears to be the case—the respective north and east component WRMS misfits for the 498 supplemental site velocities are 0.60 and 0.67 mm yr^{-1}, smaller than for the 137 survey mode sites.

5.2 MORVEL summary

5.2.1 Best-fitting and global angular velocity information

The angular velocity that best fits the data for each plate pair separated by a seafloor spreading centre is given in Table 1. Tables 2 and 3 give the MORVEL angular velocities, which are determined from a simultaneous inversion of all 2203 MORVEL data with closure enforced for all imposed plate circuits. Figs 12–14 show the best-fitting and MORVEL rotation poles and their confidence regions. Uncertainties quoted below and confidence regions for the poles of rotation are determined from the angular velocity covariances listed in the tables.

Table 3. MORVEL angular velocities and covariances for selected plate boundaries.

Plate pair	Angular velocity			Variances and covariances					
	Lat. (°N)	Long. (°E)	ω (deg Myr^{-1})	a	b	c	d	e	f
Antarctic plate fixed									
Australia	11.3	41.8	0.633	2.60	1.85	0.96	2.18	0.17	1.04
Capricorn	20.9	30.3	0.556	3.48	1.71	1.07	6.62	−3.43	3.58
Lwandle	−1.2	−33.6	0.133	3.06	2.29	−3.67	2.17	−3.11	4.86
Nubia	−4.3	−36.9	0.152	1.07	0.05	−1.03	0.21	−0.15	1.27
Nazca	35.7	−96.5	0.471	0.09	0.28	−0.21	3.97	−0.64	3.22
Pacific	−65.9	101.5	0.887	0.82	1.39	0.09	4.28	0.09	1.06
S. America	−87.9	−5.7	0.270	1.10	0.08	−1.29	0.21	−0.05	1.90
Scotia	−76.9	−73.4	0.176	3.34	−3.22	−8.75	4.28	11.43	39.03
Somalia	12.7	−60.9	0.147	0.42	0.41	−0.27	1.16	−0.40	0.56
Sur	−86.4	24.9	0.286	15.41	−1.95	−22.47	0.53	3.07	33.52
Sandwich	−37.8	−31.8	1.479	1308.26	−656.66	−2282.00	357.05	1163.79	4028.42
Arabia plate fixed									
India	−3.2	116.6	0.038	1.96	2.73	1.09	4.87	1.69	0.68
Australia plate fixed									
India	10.9	−101.1	0.355	1.49	2.64	0.58	7.51	0.80	1.64
Macquarie	54.5	−29.2	0.631	145.66	−69.88	275.48	35.19	−133.45	525.78
Pacific	−60.1	−173.7	1.079	1.23	−0.75	0.95	1.41	−0.57	2.28
Philippine Sea	−56.6	−79.1	1.206	10.33	−10.67	−4.83	12.58	5.85	6.30
Sundaland	−7.7	−128.8	0.697	0.80	−1.96	−0.45	8.30	1.88	0.59
Caribbean plate fixed									
Cocos[a]	23.3	−132.4	0.955	10.21	−1.32	−8.49	13.52	−2.27	11.63
Capricorn plate fixed									
Australia	−25.8	84.7	0.170	0.95	1.79	−0.94	9.32	−4.85	3.17
Eurasia plate fixed									
Amur	66.9	138.3	0.106	3.96	0.30	−0.77	5.61	3.69	7.27
Arabia	31.4	12.0	0.485	3.00	1.27	1.42	2.72	1.04	1.60
India	31.7	17.3	0.477	1.66	0.41	0.65	3.55	0.68	1.24
Nubia	21.6	−20.4	0.131	0.73	−0.32	0.39	0.18	−0.20	0.30
Sundaland	49.1	−73.2	0.120	3.89	−0.31	0.47	11.32	2.50	3.87
Yangtze	78.4	168.6	0.132	3.50	0.85	0.44	4.66	1.67	3.98
India plate fixed									
Australia	−10.9	78.9	0.355	1.49	2.64	0.58	7.51	0.80	1.64
Capricorn	2.0	74.4	0.198	2.31	3.75	0.30	9.90	−1.41	3.03
Sundaland	−21.2	−151.8	0.444	2.28	0.67	0.13	15.79	2.68	2.23
Yangtze	−15.8	−164.4	0.447	1.90	1.85	0.10	9.14	1.84	2.31
Lwandle plate fixed									
Nubia	−23.2	−59.2	0.022	3.65	2.64	−4.58	2.20	−3.34	6.14
Macquarie plate fixed									
Antarctic	−38.0	−163.3	1.037	150.24	−67.04	277.71	35.87	−131.42	526.09
Pacific	−59.2	172.0	1.686	147.89	−70.93	277.33	35.76	−133.60	527.58
N. America plate fixed									
Caribbean	73.9	−147.4	0.190	0.46	−1.09	0.29	3.56	−0.94	0.56
Cocos[a]	31.1	−133.2	1.085	9.73	−0.25	−8.76	9.96	−1.32	11.05
Eurasia	61.8	139.4	0.210	0.18	−0.13	−0.07	0.14	0.07	0.13
Juan de Fuca[a]	−32.0	68.3	1.081	103.05	135.05	−155.74	186.44	−203.56	259.51
Nubia	79.2	30.1	0.238	0.59	−0.31	0.24	0.25	−0.07	0.40
Rivera[a]	21.3	−108.6	4.369	237.49	776.21	−283.77	2577.04	−935.22	357.07
Nubia plate fixed									
Arabia	32.8	23.8	0.379	2.25	1.72	0.95	2.43	1.37	1.19
Sur	−62.2	136.8	0.309	16.40	−1.93	−22.89	0.64	2.82	33.65
Nazca plate fixed									
Cocos	3.5	−141.2	0.655	4.18	−1.98	−1.37	11.73	−0.39	1.38
Pacific plate fixed									
Cocos	42.2	−112.8	1.676	8.73	7.04	−6.48	14.83	−7.46	5.87
Juan de Fuca	−0.6	37.8	0.625	101.40	130.64	−156.42	174.03	−207.87	255.74
N. America	48.9	−71.7	0.750	1.65	−0.03	−0.36	7.05	1.51	2.75

Table 3. (*Continued.*)

Plate pair	Angular velocity			Variances and covariances					
	Lat. (°N)	Long. (°E)	ω (deg Myr^{-1})	a	b	c	d	e	f
Nazca	55.9	−87.8	1.311	1.11	2.89	−1.27	13.35	−4.84	3.06
Rivera	25.7	−104.8	4.966	235.84	773.86	−283.97	2566.19	−941.94	352.09
Philippine Sea plate fixed									
Amur	54.8	160.6	1.126	11.18	−12.01	−6.50	15.16	8.93	10.31
Eurasia	53.4	162.0	1.024	10.96	−9.10	−5.96	16.56	7.19	6.60
Pacific	4.6	138.1	0.890	9.10	−9.91	−5.77	11.17	6.42	4.03
Sundaland	58.0	168.5	1.076	11.13	−12.62	−5.27	20.87	7.73	6.90
Yangtze	56.2	162.3	1.145	10.73	−11.46	−5.31	14.23	6.87	6.99
S. America plate fixed									
Caribbean	55.2	−78.6	0.252	1.23	−1.50	0.54	3.92	−1.11	0.80
N. America	10.3	−57.1	0.136	0.78	−0.41	0.25	0.37	−0.17	0.24
Nubia	60.9	−39.0	0.295	0.16	−0.06	0.00	0.07	−0.04	0.32
Nazca	54.9	−98.0	0.666	1.36	1.06	−2.32	3.57	−1.64	7.42
Scotia	69.2	−87.7	0.105	1.76	−2.57	−7.02	4.63	10.59	36.76
Sur	−56.2	53.9	0.019	16.41	−1.90	−23.24	0.65	2.93	33.83
Sandwich	−28.8	−32.0	1.323	1305.06	−655.02	−2279.25	356.83	1162.08	4027.44
Scotia plate fixed									
Sandwich	−32.9	−30.5	1.356	1306.17	−656.82	−2283.64	359.12	1168.77	4028.41
Somalia plate fixed									
Arabia	23.0	25.4	0.412	2.70	2.77	0.72	3.44	0.73	0.42
Capricorn	17.0	45.7	0.567	2.59	2.51	1.07	6.95	−2.28	3.33
India	22.7	31.2	0.412	0.81	1.04	0.13	2.95	0.51	0.41
Lwandle	−27.8	52.0	0.075	3.21	2.94	−3.87	3.12	−3.56	5.43
Nubia	−35.3	33.8	0.076	0.59	0.16	−0.35	0.81	0.13	0.66
Sundaland plate fixed									
Yangtze	22.6	121.3	0.102	1.20	−2.75	−0.95	9.96	2.90	1.25
Sandwich plate fixed									
Sur	28.2	147.4	1.315	1334.17	−664.91	−2322.44	358.29	1175.44	4094.62
Yangtze plate fixed									
Amur	−54.2	102.5	0.039	1.26	−2.14	-2.17	4.25	4.10	4.67

Notes: See note of Table 1 for the conventions that are employed in this table. Angular velocities are from an inversion of all of the MORVEL data from Tables 1 to 4 in the electronic supplement. Covariances are propagated from data uncertainties and also incorporate systematic errors from uncertainty in outward displacement (see text). Plate names followed by an asterisk specify plate pairs for which the PVEL angular velocities are also estimated (Table 5.)

5.2.2 Overview of data misfits

The misfits of the MORVEL angular velocities to the spreading rates, transform fault azimuths, and earthquake slip directions are summarized in Fig. 15. For the 1696 spreading rates, 68.3 per cent have misfits smaller than 1.17 mm yr^{-1} and 95 per cent are smaller than 3.3 mm yr^{-1}. The distribution of residual rates normalized by their estimated uncertainties (right-hand column of Fig. 15) closely resembles a Gaussian distribution with mean of zero and standard error of 1. Misfits to the transform fault azimuths are as large as 10.2° and generally describe a Gaussian distribution. As expected, earthquake slip directions exhibit more dispersion than do the other types of data, with several misfits of 30° or more. All the largest misfits to the earthquake slip directions occur for earthquakes from the boundaries of the Scotia plate (Section 5.4).

Overall, the MORVEL angular velocities fit the 2203 MORVEL data with χ^2_ν of 1.06, indicating that the average data misfit is 3 per cent larger than its estimated uncertainty. For comparison, χ^2_ν for the NUVEL-1 data is 0.24, indicating that the average NUVEL-1A misfit was only half the estimated data uncertainty. This difference mostly reflects the rescaled uncertainties that we adopted for spreading rates based on their dispersions for each plate boundary (Section 4.2.3) and the procedure we used to estimate more objectively the uncertainty in transform fault azimuths (Section 4.3). Coupled with the additional uncertainty that we incorporated in the MORVEL angular velocity covariances to account for a possible bias in our estimate of outward displacement, it seems likely that the MORVEL angular velocity uncertainties more faithfully represent the uncertainties in present plate motions than do those for NUVEL-1 and NUVEL-1A.

5.2.3 Data importance

The 1696 spreading rates, 163 fault azimuths, 144 GPS station velocities (288 horizontal velocity components) and 56 earthquake slip directions that constitute the MORVEL data respectively contribute 47, 27, 23 and 3 per cent of the information that constrains the 72 MORVEL angular velocity components, as measured by summing the individual data importances. For comparison, the NUVEL-1 rates, transform fault azimuths, and earthquake slip directions contribute 46, 34 and 20 per cent of the information in NUVEL-1 and NUVEL-1A, respectively. The earthquake slip directions contribute much less information to MORVEL than to NUVEL-1, as expected.

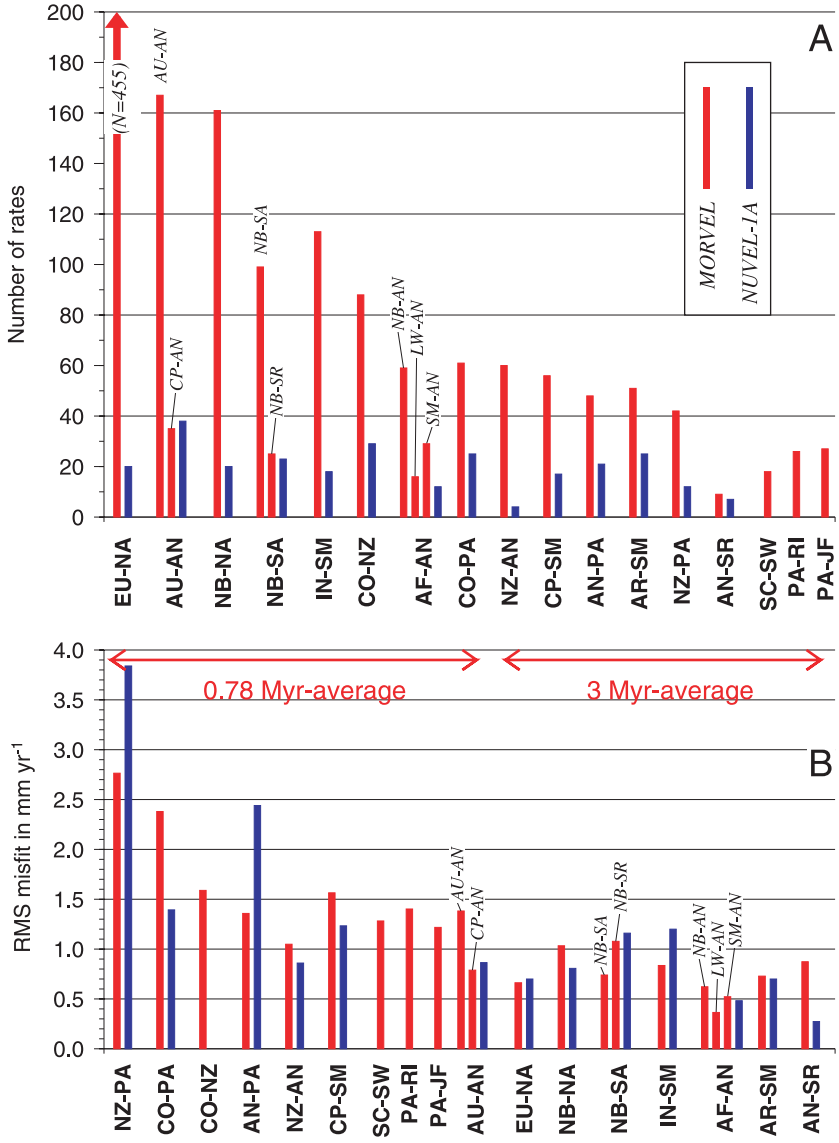

Figure 11. (a) Number of spreading rates per plate boundary that are used to determine the MORVEL (red) and NUVEL-1A (blue) best-fitting angular velocities. (b) Root-mean-square misfits (rms) in millimetres per year for the angular velocities that best fit only the spreading rates from individual plate boundaries. MORVEL rates are adjusted for outward displacement prior to their inversion, as described in text.

5.2.4 Influence of GPS velocities

Only three of the 144 MORVEL GPS station velocities, all from the Scotia plate (Figs 2 and 5), are located within a plate circuit that is also populated by spreading rates and transform fault azimuths. Thus, only those three GPS velocities are able to influence the angular velocities in MORVEL that average plate motion over geological intervals. The other 141 GPS station velocities, variously located on the Amur, Caribbean, Philippine Sea, Sundaland and Yangtze plates, constrain the best-fitting angular velocities for those five plates, but contribute no information to the global plate circuit.

To confirm this, we inverted the 141 GPS station velocities and remaining MORVEL data as separate data subsets and compared the two separately determined sets of angular velocities to the MORVEL angular velocities. As expected, both subsets of the angular velocities agree with the MORVEL angular velocities to the level of precision (four decimal places). The 141 GPS station velocities from the Amur, Caribbean, Philippine Sea, Sundaland and Yangtze plates thus contribute no information to the angular velocities for the other 20 plates and instead constrain only the angular velocities for these five plates. Of the 72 angular velocity components that comprise MORVEL, the 141 GPS station velocities completely determine fifteen (i.e. 5×3) angular velocity components, comprising $\approx$21 per cent of the cumulative data importance.

To determine whether the three Scotia plate GPS station velocities significantly influence angular velocity estimates for plates other than the Scotia and Sandwich plates, we compared the MORVEL angular velocities for all the plates except the Scotia and Sandwich plates to an alternative set of angular velocities we determined from an inversion of all 2203 MORVEL data except the three Scotia plate GPS velocities. Using eq. (2), the differences in these two sets of angular velocities are statistically insignificant ($p = 0.995$, where $p = 0.05$ represents a difference that is significant at the 95 per cent confidence level). Consequently, relatively little information propagates from the three Scotia plate GPS velocities outward into the wider global plate circuit.

Figure 12. Selected MORVEL poles (red) and 2-D, 95 per cent confidence ellipses (red), Atlantic and Arctic regions. Sense of motion is anticlockwise for the first listed plate relative to the second. The NB-SA and EU-NA pole confidence ellipses are too small to be seen at the scale of this map. Best-fitting poles for plate pairs with data in MORVEL are shown by open circles and dashed ellipses. Blue circles indicate locations of selected NUVEL-1A poles. The pole that specifies the motion of North America relative to South America is shown in Fig. 25. Plate abbreviations are defined in Fig. 1.

In summary, the 144 MORVEL GPS velocities do not significantly affect the angular velocity estimates for the nineteen plates with motions that are estimated over geological timescales. To a high degree, MORVEL therefore constitutes an independent geological standard against which to compare geodetic plate motion estimates for those plates.

5.3 Arctic and Atlantic Ocean basins

5.3.1 Data from the Arctic and northern Atlantic

Fig. 16 shows the tracks of magnetic profiles that we use to estimate spreading rates in the Arctic basin and along the Reykjanes Ridge and Mid-Atlantic Ridge north of the Azores triple junction. In the Arctic basin, Naval Research Laboratory aeromagnetic surveys from 1973 to 1975 of the Gakkel, Knipovich and Mohns ridges are our main source of spreading rates and are described by Feden *et al.* (1979), Vogt *et al.* (1979) and Kovacs *et al.* (1982). Despite the low fidelity of the magnetic anomalies along these ultra-slow spreading centres (see for example, the Gakkel Ridge profile in Fig. 8), anomaly 2A is expressed in most profiles and is used to estimate spreading rates since 3 Ma. Along the Kolbeinsey Ridge north of Iceland, we estimate many spreading rates from a low-altitude aeromagnetic survey in 1973 by the U.S. Naval Oceanographic Office (Vogt *et al.* 1980; Appelgate 1997).

Many cruises document the recent spreading histories of the Reykjanes and northern Mid-Atlantic ridges between Iceland and the Azores triple junction (left-hand panel of Fig. 16). These include a dense survey of the obliquely spreading Reykjanes Ridge from 59.5°N to 62.5°N (Searle *et al.* 1998), dense Russian surveys from 48°N to 59°N conducted in the 1970s and 1980s (Merkouriev & DeMets 2008), and the TRIATNORD multibeam ridge survey from 40.5°N to 45°N (Goslin & Triatnord Scientific Party 1999).

Marine magnetic coverage of the Nubia–North America portion of the Mid-Atlantic Ridge between the Azores triple junction and Fifteen-Twenty fracture zone (Fig. 17a) has also improved greatly since publication of NUVEL-1. The near-ridge seafloor morphology and magnetic anomalies from 29°N to 40°N are superbly imaged by the FARA-SIGMA (Detrick *et al.* 1995), SudAçores (Cannat *et al.* 1999) and R/V *Maurice Ewing* Leg EW9210 (Sempere *et al.* 1995) cruises and identify all spreading segments with correlatable anomaly sequences out to anomaly 2A. Densely spaced Russian data from the Canary-Bahamas transect define the magnetic anomaly sequence from 22.5°N to 30.5°N (Maschenkov & Pogrebitsky 1992), and are complemented by data from the FARA-SEADMA geophysical survey of the ridge crest from 20°N to 24°N (Gente *et al.* 1995). From 12°N to 20°N, where the boundary between the North and South America plates intersects the Mid-Atlantic Ridge (Roest & Collette 1986), we use a dense magnetic survey from 14°N to 16°N (Fujiwara *et al.* 2003) to estimate rates across the ridge segments immediately north and south of the Fifteen-Twenty transform fault and magnetic profiles from the Kroonvlag project (Collette *et al.* 1984) and other 1970s-vintage Dutch surveys (Roest & Collette 1986).

High resolution sonar surveys of the Charlie Gibbs and Molloy transform faults (Searle 1981; Crane & Solheim 1995) in the north

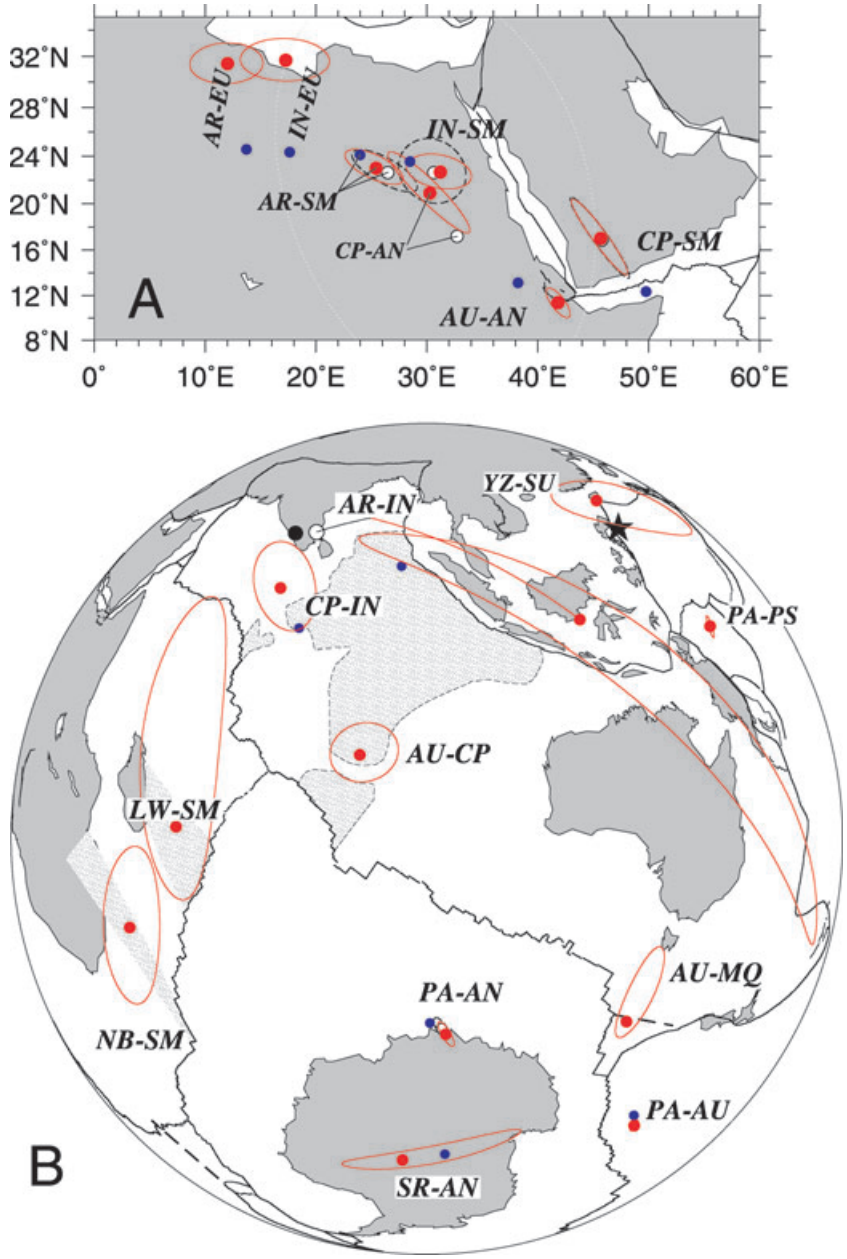

Figure 13. Selected MORVEL poles (red) and 2-D, 95 per cent confidence ellipses (red), Indian Ocean and Antarctic regions. Sense of motion is anticlockwise for the first listed plate relative to the second. The PA-AU pole confidence ellipse displayed in panel (b) is too small to be seen at the scale of this map. Best-fitting poles for plate pairs with data in MORVEL are shown by open circles and dashed ellipses. Blue circles indicate locations of selected NUVEL-1A poles. AR-IN pole designated with filled black circle is from Fournier *et al.* (2008). Black star shows YZ-SU pole from Simons *et al.* (2007). Plate abbreviations are defined in Fig. 1.

Atlantic and Arctic anchor our estimates of Eurasia–North America directions of motion and are supplemented by conventional bathymetric surveys of the Spitsbergen and Jan Mayen transform faults (Perry *et al.* 1978). The Oceanographer, Hayes, Atlantis and Kane transform faults south of the Azores triple junction have been mapped with one or both of side-scan and multibeam sonar systems (Roest *et al.* 1984; Pockalny *et al.* 1988; Thibaud *et al.* 1998) and strongly constrain the Nubia–North America plate motion direction. A GLORIA survey of the Gloria fault west of Gibraltar (Laughton *et al.* 1972), where strike-slip motion between Nubia and Eurasia occurs, is used to estimate the direction of Nubia–Eurasia motion.

5.3.2 *Data from the equatorial and southern Atlantic*

Many more magnetic data are now used to constrain spreading rates in the southern Atlantic basin than for NUVEL-1 (Figs 17b and c). Profiles from an aeromagnetic survey described by Brozena (1986) define the magnetic anomalies from 8°S to 18°S along the Nubia–South America plate boundary (Fig. 17b). Farther south, dense marine geophysical surveys define the anomaly sequence and near-ridge seafloor morphology from 25°S to 27.5°S and 31°S to 34.5°S (Carbotte *et al.* 1991; Weiland *et al.* 1995). South of 50°S, we use data from the Shona hotspot survey (Douglass *et al.* 1999) and an Italian–Russian survey of the spreading segments that intersect

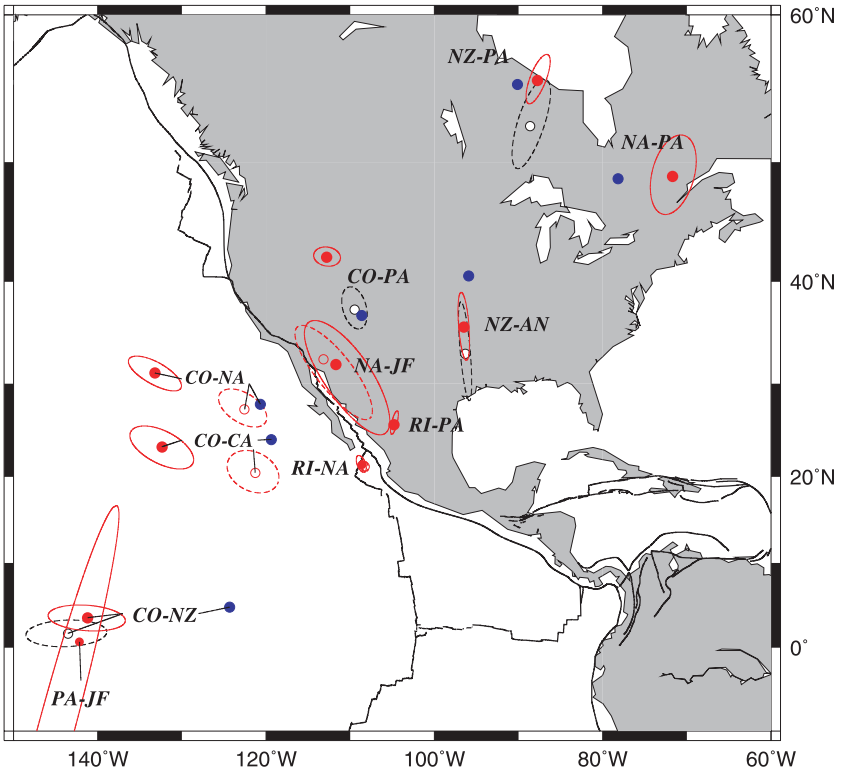

Figure 14. Selected MORVEL poles (solid red) and 2-D, 95 per cent confidence ellipses (red), Pacific region. Open red circles with dashed confidence ellipses are PVEL estimates, which use a shorter plate circuit to estimate subduction across the Middle America and Cascadia subduction zones in the eastern Pacific (Table 5). Best-fitting poles (Table 1) are shown by open circles and dashed ellipses. Blue circles show locations of selected NUVEL-1A poles. Sense of motion is anticlockwise for the first listed plate relative to the second. Plate abbreviations are defined in Fig. 1.

the Bouvet triple junction (Ligi *et al.* 1999) to define spreading rates.

The Mid-Atlantic Ridge between the Fifteen-Twenty fracture zone and Bouvet triple junction is offset by 75 axial discontinuities that exceed 10 km in length and have a cumulative length of 6040 km, equal to 40 per cent of the length of the Nubia–South America plate boundary. Forty-four of the 75 axial offsets are well-defined transform faults with potentially useful information about the directions of plate motion for this plate pair. We located partial or complete multibeam or side-scan sonar coverage for 15 of the 44 transform fault valleys and from these surveys estimated 22 azimuths for one or more fault strands within these transform fault valleys. Most (14) of the 22 azimuths were estimated from published data (Belderson *et al.* 1984; Roest *et al.* 1984; Macdonald *et al.* 1986; Searle 1986; Cherkis *et al.* 1989; Fox *et al.* 1991; Grindlay *et al.* 1991, 1992; Searle *et al.* 1994; Mazarovich *et al.* 2001; Smith *et al.* 2008). We estimated an additional eight azimuths from transit-track multibeam data and survey multibeam data that we obtained through the Marine Geoscience Data System (http://www.marine-geo.org), and the R/V *Conrad* 2806 partial Sea Beam survey of the St. Paul transform fault (J.-G. Schilling, personal communication, 2001). We used marine gravity measurements to estimate the azimuths of six transform faults with little or no bathymetric coverage.

New observations from the American–Antarctic ridge, which accommodates spreading between the Antarctic plate and newly named Sur plate, include a well-constrained azimuth for the Conrad transform fault from a multibeam survey of the Bouvet triple junction (Ligi *et al.* 1999), spreading rates from the same survey, and an azimuth from an unpublished side-scan survey of the westernmost 160 km of the 530-km-long Bullard transform fault (R. Livermore, personal communication, 2001). We do not use transform fault azimuths or spreading rates from the American–Antarctic ridge west of 59.5°S, 18°W, where a seismically active fracture zone between the ridge and South Sandwich subduction zone (Fig. 18a) defines the northern edge of an independently moving microplate (shown as the shaded region in Fig. 18c). Focal mechanisms for two earthquakes along this reactivated fracture zone (Fig. 18c) indicate that the sliver plate moves more rapidly towards the South Sandwich subduction zone than does the lithosphere immediately north of the fracture zone.

5.3.3 *Eurasia–North America plate motion*

Our best-fitting estimate of motion between the Eurasia and North America plates is determined from 453 spreading rates, which increase from 11 to 12 mm yr^{-1} along the Gakkel Ridge in the Arctic basin to 23 mm yr^{-1} just north of the Azores triple junction (Fig. 19), and five transform fault azimuths (Fig. 20). The rms misfit of the best-fitting angular velocity to the many rates is only 0.7 mm yr^{-1} (Fig. 11), similar to that for other slow and ultraslow spreading centres. Spreading rates that are estimated from the NUVEL-1A best-fitting angular velocity differ from our best-fitting estimates by an average of only 0.3 mm yr^{-1} (Fig. 21).

The best-fitting pole and angular rotation rate are well determined by the many data for this plate pair. For example, the formal uncertainty in the angular rotation rate is only ±0.5 per cent, which corresponds to an uncertainty of only ±0.1 mm yr^{-1} in the rates estimated along the plate boundary. The well-determined pole

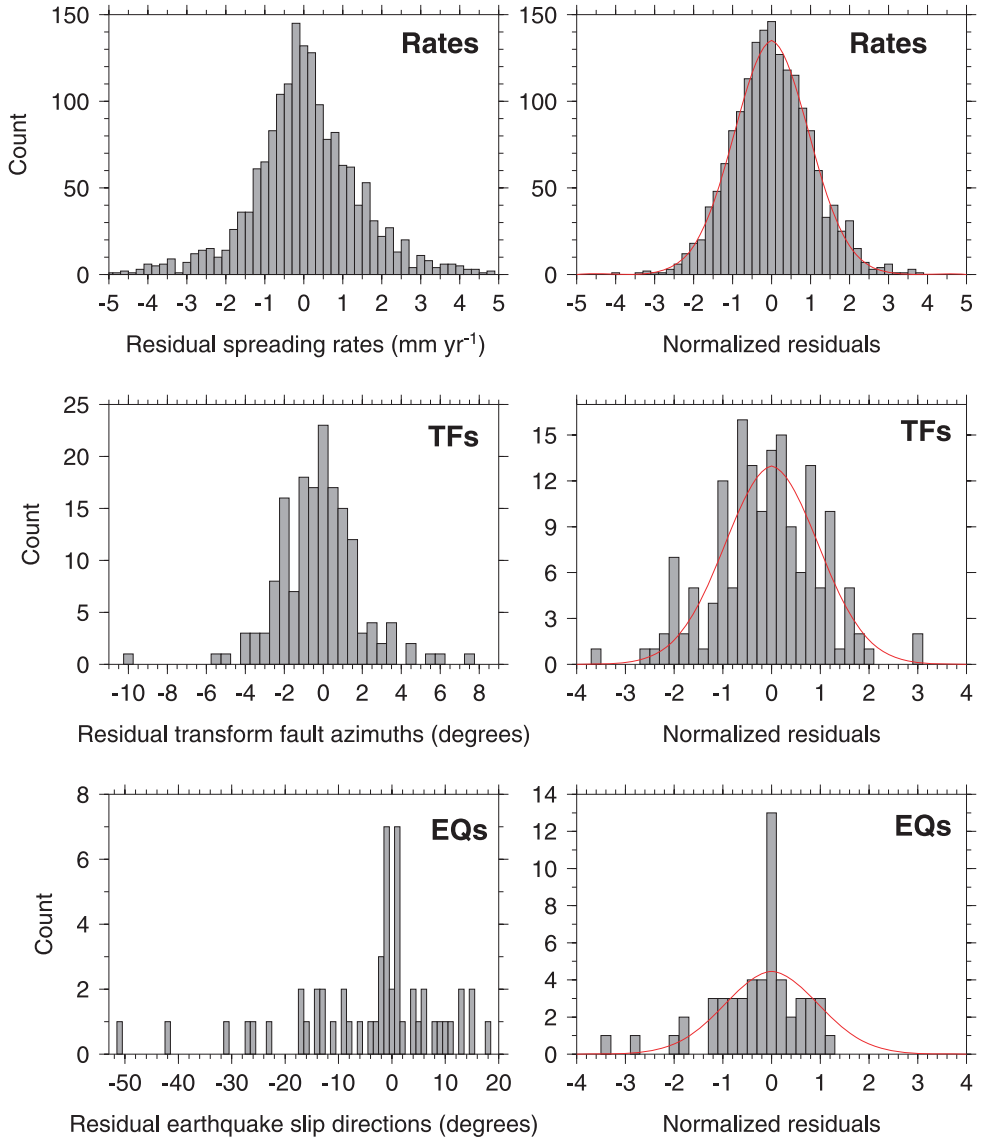

Figure 15. Left-hand column: residual seafloor spreading rates, transform fault azimuths (TF), and earthquake slip directions (EQ) determined by subtracting rates and azimuths determined with the MORVEL angular velocities from the observations. Twenty-two rates with absolute-valued misfits between 5 and 10.3 mm yr^{-1} are not shown. Right-hand column: data residuals divided by their estimated 1σ uncertainties. Gaussian distributions with mean values of zero and standard errors of 1 are shown by red curves.

location (Fig. 12) gives rise to a maximum uncertainty of only $\pm 0.5^\circ$ in the directions of motion estimated along the plate boundary.

The spreading rates and plate motion directions estimated from the MORVEL Eurasia–North America angular velocity differ by only 0.01 mm yr^{-1} and 0.2° from the best-fitting estimates (Figs 19 and 20). This good agreement results from the insignificant level of non-closure around the Nubia–Eurasia–North America plate circuit, as described in Section 6.

5.3.4 The Azores microplate

The Mid-Atlantic ridge spreading rates do not change abruptly at the Azores triple junction (Fig. 19), as should occur if the Eurasia, North America and Nubia plates meet at a discrete triple junction. They instead change gradually from 22.9 $\pm$ 0.1 mm yr^{-1} (1σ) at 40°N to 19.8 $\pm$ 0.2 mm yr^{-1} at 38°N (Fig. 22b). These transitional spreading rates coincide with the western boundary of the Azores microplate (Fig. 22a) and to our knowledge constitute the first kinematic evidence for its existence, which was previously inferred from seafloor morphology and seismicity (Searle 1980).

The many Mid-Atlantic Ridge spreading rates can be used to locate the northern and southern boundaries of the Azores microplate where it intersects the Mid-Atlantic Ridge (Fig. 22b). The northern boundary appears to intersect the ridge axis between 39.4°N and 40.0°N, consistent with the location proposed by Searle (1980) and Vogt & Jung (2004), who extrapolated the obliquely spreading Terceira rift to its intersection with the Mid-Atlantic Ridge. The southern microplate boundary appears to intersect the ridge between 38.2°N and 38.5°N (Fig. 22b), in accord with the location suggested by Luis *et al.* (1994) and Fernandes *et al.* (2006) from a zone of active seismicity that intersects the ridge at 38.5°N (Fig. 22a).

The 18 spreading rates located at the western edge of the Azores microplate (≈38.5°N to 39.5°N) can be used to estimate the motions of the microplate across its boundaries with the Eurasia and Nubia

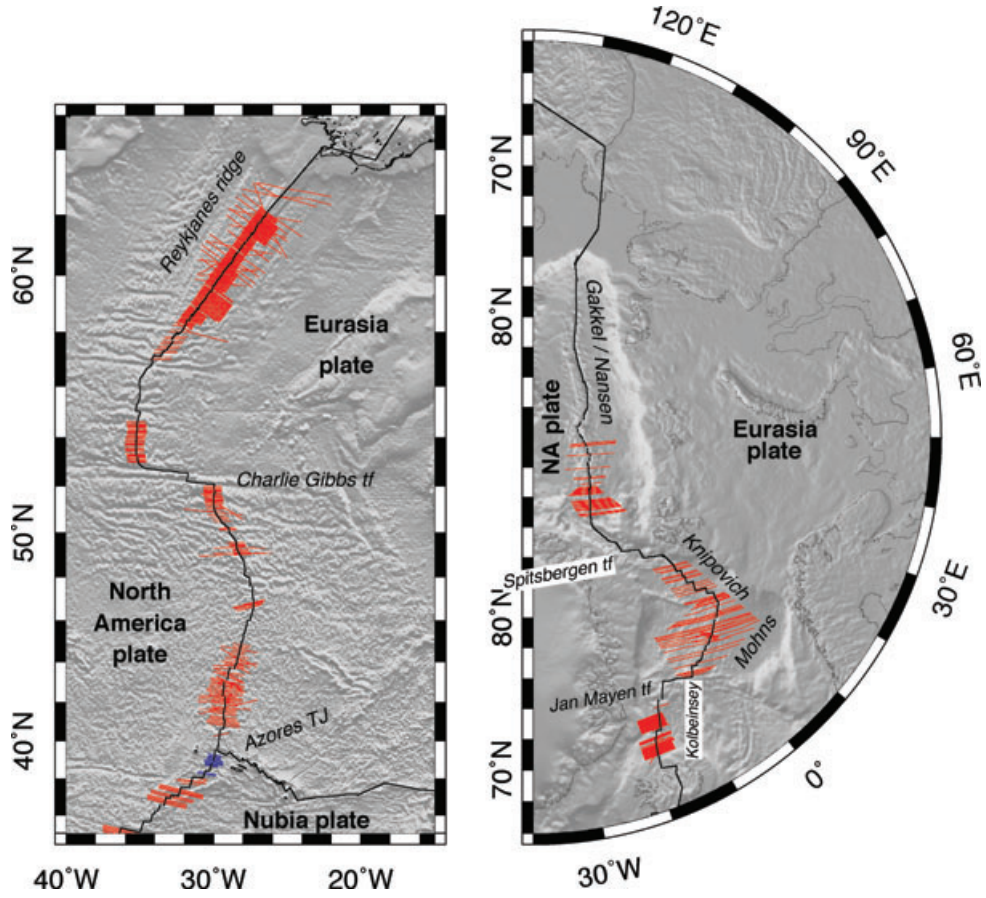

Figure 16. Ship and aeroplane tracks (red) of magnetic anomaly profiles used to determine MORVEL spreading rates in the north Atlantic (left-hand panel) and Arctic (right-hand panel) basins. Ship tracks coloured blue are used to determine Azores–North America spreading rates.

plates (Fig. 22c). At 39°N, midway along the boundary, the average spreading rate of 20.8 ± 1 mm yr^{-1} is ≈2 mm yr^{-1} lower than the opening rate estimated with the Eurasia–North America best-fitting angular velocity and ≈1.5 mm yr^{-1} higher than our best estimate of the Nubia–North America opening rate. If the Azores-North America direction of motion at this location is halfway between the well-determined Eurasia–North America and Nubia–North America directions, then 2 mm yr^{-1} of NE-to-SW oblique divergence is predicted across the Terceira rift between the Azores microplate and Eurasia plate (see the linear velocity diagram in Fig. 22c). The predicted motion is consistent with evidence for slow, NE-to-SW oblique spreading from GLORIA side-scan sonar mapping of the Terceira rift (Searle 1980) and earthquake focal mechanisms along the Azores–Eurasia plate boundary (Fig. 22a).

Our simplistic linear velocity analysis also predicts that the Azores microplate moves 2 mm yr^{-1} to the east–northeast along its boundary with the Nubia plate (Fig. 22c), consistent with the right-lateral, ENE–WSW directed motion that is indicated by earthquake focal mechanisms along the seismic zone that defines the southern boundary of the microplate (Fig. 22a).

Fernandes *et al.* (2006) report GPS measurements and velocities for sites in the Azores islands, including one site on San Jorge island that may lie within the boundaries of the Azores microplate (located by the red circle in Fig. 22a). The motion they report for this site, 3 ± 0.3 mm yr^{-1} (1σ) to the west relative to the Eurasia plate (red velocity arrow in Fig. 22c), is the same within uncertainties as our estimate of Azores microplate motion relative to the Eurasia plate.

Thus the kinematic, seismologic, marine geophysical and geodetic data support the existence of the Azores microplate with dimensions of ≈100 km by ≈100 km and suggest that its motion can be estimated successfully.

5.3.5 Nubia–Eurasia plate motion from the Azores to Gibraltar

Deformation along the Nubia–Eurasia plate boundary changes from ENE–WSW extension near the Azores triple junction to right-lateral strike-slip motion along the Gloria fault to oblique convergence at locations east of the Gloria fault (Fig. 23). The only direct constraints on the angular velocity for this plate pair are three azimuths we estimate for the Gloria fault (Table S2). These have a summed importance of only 0.87 in the MORVEL inversion and thus provide only 15 per cent (=0.87/6) of the information needed to specify the angular velocities in the Nubia–Eurasia–North America plate circuit. Encouragingly, the MORVEL Nubia–Eurasia angular velocity fits the three Gloria fault azimuths within their several degree uncertainties (Table S2) and the Nubia–Eurasia–North America plate circuit is consistent with closure (Section 6).

The motion estimated with the MORVEL Nubia–Eurasia pole can be tested against independent observations along the plate boundary. Small circles around the Nubia–Eurasia pole (Figs 23a and b) are consistent with both the sense and direction of plate motion inferred from marine geological and seismological observations. Along the Azores archipelago, detailed seafloor mapping (Searle 1980) and normal faulting earthquakes between 27°W and 24.5°W (Fig. 23)

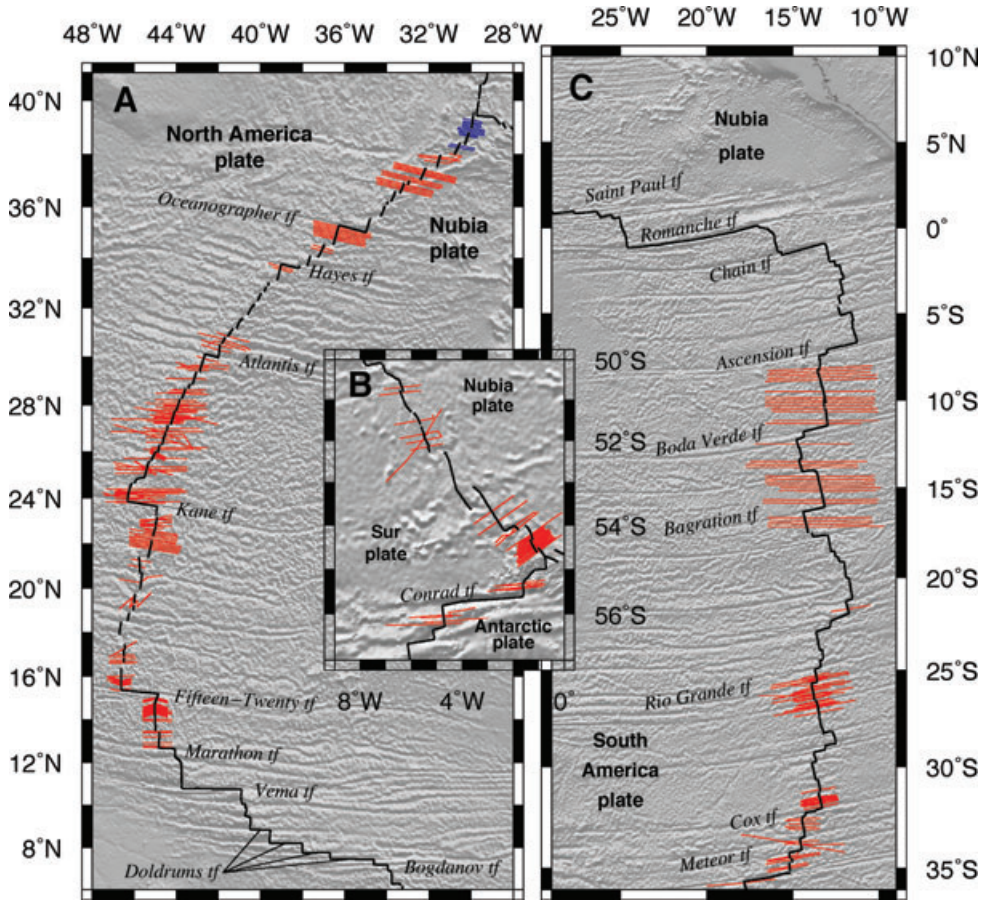

Figure 17. Ship and aeroplane tracks (red) of magnetic anomaly profiles used to determine Atlantic basin spreading rates. Ship tracks coloured blue are used to determine Azores–North America spreading rates.

both indicate that ENE–WSW oblique divergence occurs across the plate boundary, in accord with the sense and direction of motion given by the MORVEL pole. East of 14°W, the new pole indicates WNW–ESE to NW–SE obliquely convergent motion (Fig. 23b), consistent with marine seismic and side-scan sonar evidence for NW–SE to NNW–ESE oblique thrust faulting in the seafloor west of Gibraltar (e.g. Hayward *et al.* 1999).

The MORVEL and NUVEL-1A Nubia–Eurasia angular velocities differ by only 0.6 angular degrees in location (Fig. 12) and both predict rates of motion (4 ± 0.2 mm yr^{-1}) (1σ) that differ by only fractions of a millimetre per year everywhere along the plate boundary. For example, along the well-mapped Gloria fault, the velocities given by the two estimates differ by only 0.1 mm yr^{-1} and 1.0°, well within the uncertainties.

5.3.6 *Boundary between the North and South America plates*

The many MORVEL spreading rates and transform fault azimuths from the Mid-Atlantic Ridge (Fig. 24) permit a higher-resolution investigation of the location of the boundary between the North and South America plates and their relative motion than was possible before. Prior investigators described several lines of evidence that current motion between these two plates is focused between 12°N and 16°N near the ridge (Fig. 25), including morphologic evidence for extension across the Researcher Ridge, Researcher Trough and Royal Trough (Roest & Collette 1986), elevated seismicity and normal-faulting earthquakes west of the Mid-Atlantic ridge between 13°N and 16°N (Perry *et al.* 1981; Roest & Collette 1986), anomalous off-axis seismicity ≈70 km west of the Mid-Atlantic ridge between 12.65°N and 15.2°N (Ball & Harrison 1970; Gordon 1998; Escartin *et al.* 2003), and the pattern of the azimuths of the transform faults (DeMets *et al.* 1990; Gordon 1998). To first order, our new spreading rates and transform fault azimuths also suggest that the plate boundary intersects the ridge in this region (Fig. 24), although the poor fit to the Kane transform fault suggests that some deformation may extend as far north as 23.5°N.

The spreading rates we determined for the ridge segments immediately north and south of the Fifteen-Twenty transform fault indicate a previously unrecognized discontinuity in the spreading rate across the Fifteen-Twenty transform fault, with rates just south of the fault that are 2 mm yr^{-1} lower than rates north of the fault (Figs 24a and 26a). The sense and magnitude of the change are consistent with that expected if a transition from Nubia–North America to Nubia–South America seafloor spreading occurs across the Fifteen-Twenty transform fault. The change in rate implies that ≈2 mm yr^{-1} of left-lateral slip must occur along the Fifteen-Twenty fracture zone just west of the ridge axis. By implication, relative motion between the North and South America plates at this location does not consist purely of N–S extension, as was assumed by Roest & Collette (1986) for the purpose of locating the pole of rotation between these two plates.

We applied the Stein & Gordon (1984) test for an additional plate boundary to identify the North America–South America boundary

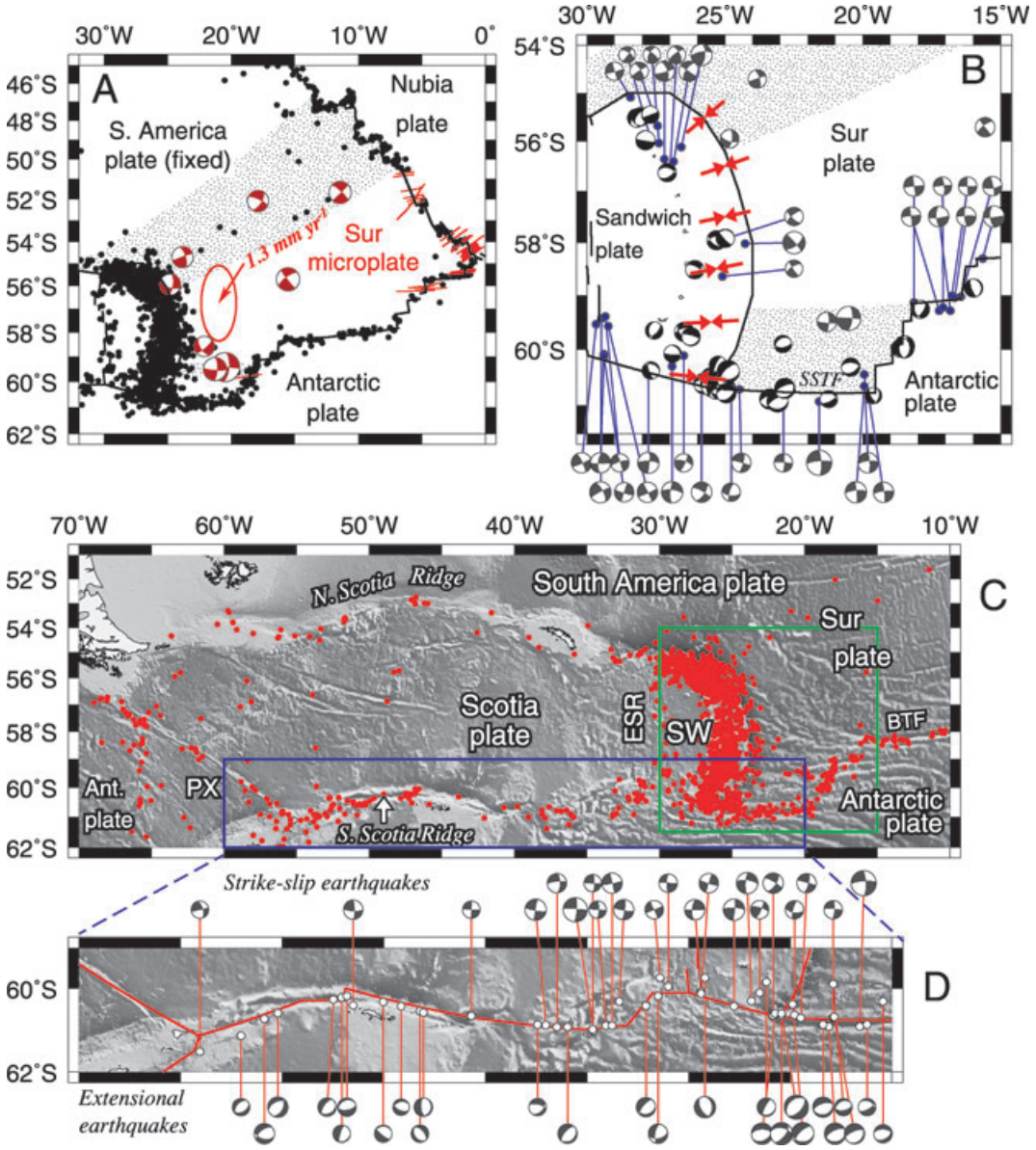

Figure 18. Seismotectonics of the southern Atlantic. (a) Sur plate seismicity and focal mechanisms for earthquakes east of the South Sandwich subduction zone. Motion of the Sur plate relative to South America predicted by MORVEL (1.3 ± 0.6 mm yr^{-1}) is indicated by red arrow and 2-D, 1σ ellipse. MORVEL magnetic profile tracks are shown in red. (b) Seismotectonic setting of the Sandwich plate. Red arrows show slip directions determined by Thomas *et al.* (2003) from summed moment tensors for shallow thrust earthquakes along the South Sandwich subduction zone. Focal mechanisms exclude the following: earthquakes deeper than 40 km, reverse-faulting earthquakes, outer arc rise earthquakes, and intra-slab normal faulting earthquakes. Stippled regions show the deforming zone discussed in the text. SSTF designates the South Sandwich transform fault. (c) Scotia plate tectonic setting with earthquake epicentres and 1-min predicted depth grid version 10.1 (Smith & Sandwell 1997). Green and blue rectangles depict areas of panels (b) and (d), respectively. Abbreviations: BTF, Bullard transform fault; ESR, East Scotia Ridge (backarc spreading centre); PX and SW, Phoenix and Sandwich plates. (d) Extensional and strike-slip focal mechanisms along the southern Scotia plate boundary for earthquakes shallower than 40 km. All earthquakes with epicentres shown in these figures were shallower than 40 km and occurred from 1963 to 2007.5. All earthquake focal mechanisms are extracted from the Global centroid moment tensor data base and cover the period 1976–2007.5.

location that gives the best least-squares fit to the many Mid-Atlantic ridge spreading rates and transform fault azimuths. Assuming that the plate boundary is narrow where it intersects the ridge, which it may not be, the many kinematic data are best fit if the boundary intersects the ridge at or just north of the Fifteen-Twenty transform fault (Fig. 26c). Boundary locations south of the Fifteen-Twenty transform fault or north of 15.7°N are rejected at the 95 per cent confidence level. We apply the narrow-boundary approximation and best-fitting boundary location for the remainder of the analysis given that all the data except the azimuth of the Kane transform fault are well fit for this geometry. In Section 7.5.3, we explore the consequences of extending the boundary north to the Kane transform fault.

5.3.7 Nubia–North America plate motion

Our best-fitting estimate of Nubia–North America motion is determined from the 161 spreading rates and four transform fault

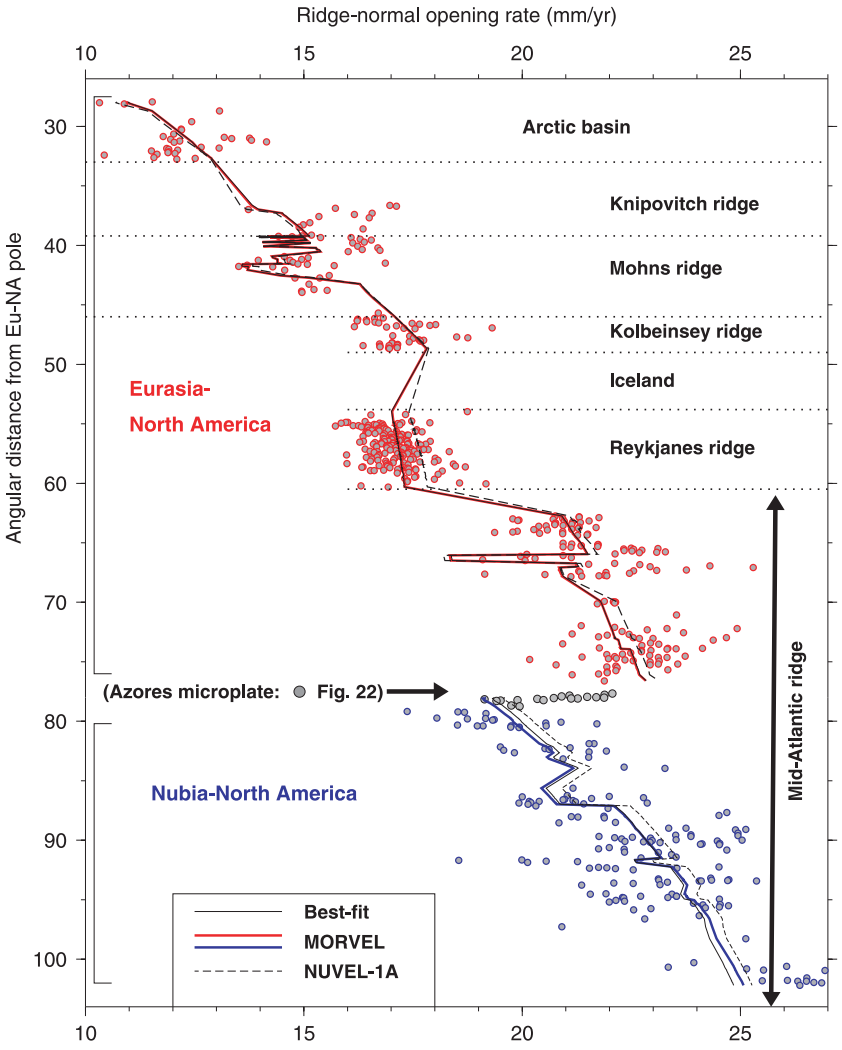

Figure 19. Arctic and north Atlantic basin spreading rates north of 14°N and rates calculated from best-fitting, MORVEL and NUVEL-1A angular velocities. All opening rates in this and later figures have been corrected for outward displacement. Spreading rate uncertainties are omitted for clarity. Fits to directions of motion for Nubia–Eurasia–North America plate circuit are shown in Fig. 20. Additional information about Azores microplate kinematics is given in Fig. 22.

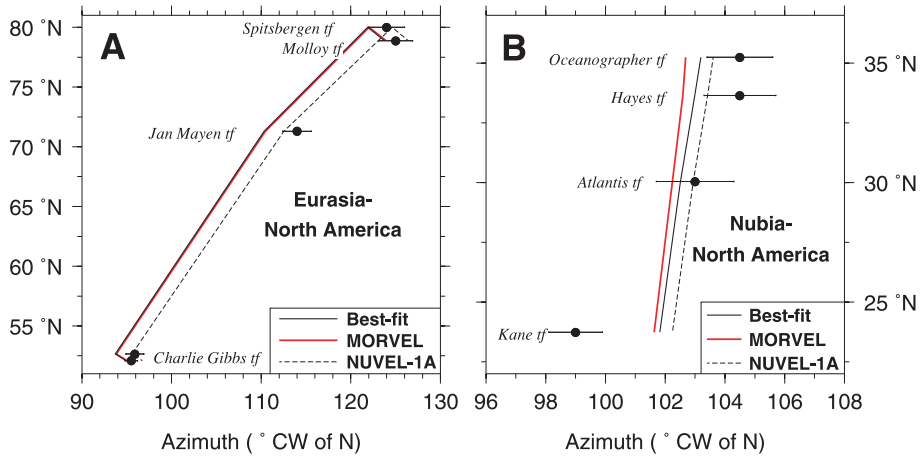

Figure 20. Transform fault azimuths and directions calculated from best-fitting, MORVEL, and NUVEL-1A angular velocities for (a) the Eurasia–North America plate pair and (b) the Nubia–North America or Africa–North America plate pair.

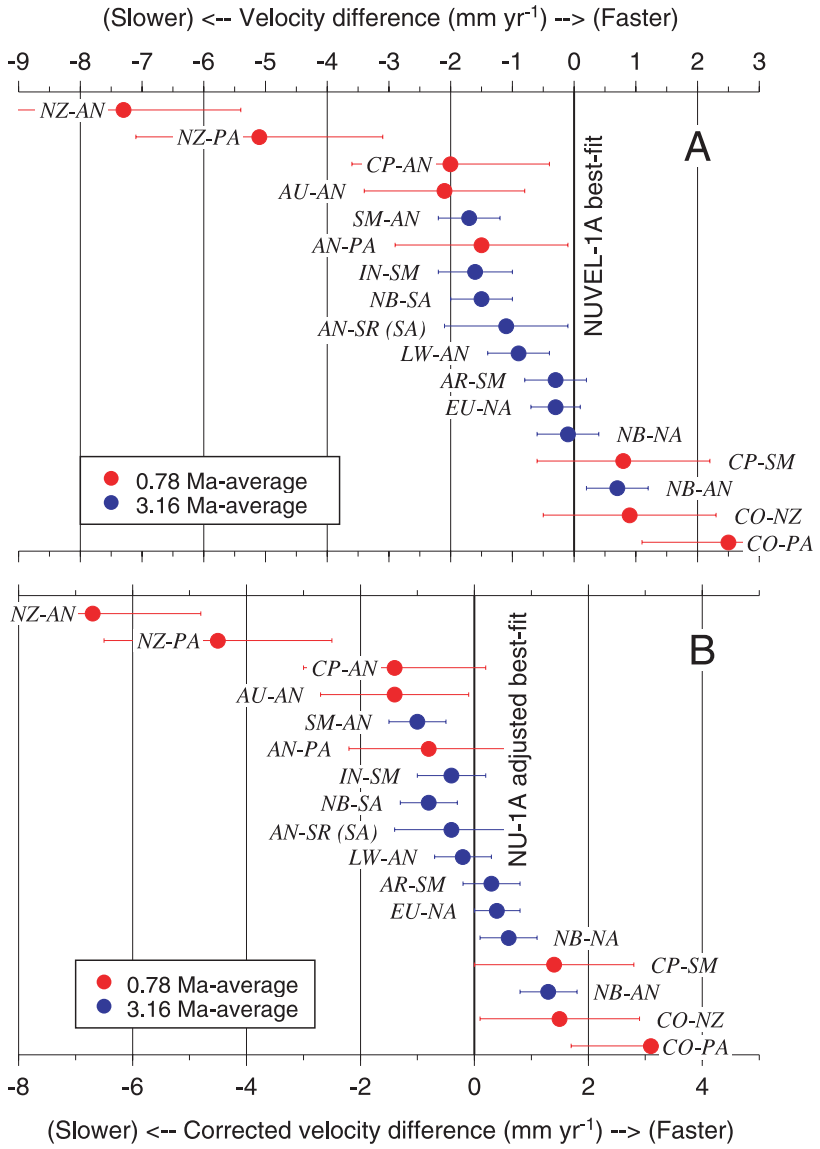

Figure 21. Differences between pure opening-rate components for the MORVEL and NUVEL-1A best-fitting angular velocities (BFAVs) per plate boundary. The pure opening-rate components are the projections of the BFAVs onto an axis that lies 90° from the centroid of the plate boundary along the great circle that includes the pole of rotation. They isolate the uniform component of the spreading rate along the plate boundary from the spreading-rate gradient (Wilson 1993). Differences in both panels are for the MORVEL data relative to the NUVEL-1A data and are expressed in mm yr^{-1} at the geographic centre of each plate boundary. Panel (a) shows differences per plate pair after applying corrections for outward displacement to the MORVEL but not the NUVEL-1A estimates. Panel (b) shows differences after corrections for outward displacement are applied to both the MORVEL and NUVEL-1A estimates. Standard errors are derived from linear propagation of the formal uncertainties in the MORVEL and NUVEL-1A opening-rate component angles and also incorporate an additional angular uncertainty for an assumed ±1 km uncertainty in the magnitude of outward displacement.

azimuths between the Fifteen-Twenty transform fault and Azores microplate (Figs 19 and 20). The spreading rates increase from 19.5 mm yr^{-1} near 38.5°N to 25 mm yr^{-1} at the spreading segment north of the Fifteen-Twenty transform fault, and have a rms misfit of 1.0 mm yr^{-1} (Fig. 11), typical for slow spreading centres.

The rates and directions of motion estimated from the new best-fitting and MORVEL angular velocities for this plate pair agree to within fractions of a millimetre per year (Fig. 19) and 0.5° (Fig. 20), respectively. Rates calculated from the NUVEL-1A angular velocity are systematically higher by 0.3–0.5 mm yr^{-1} than our newly estimated rates (Fig. 19), partly due to the correction that is applied here for outward displacement and partly due to differences between the MORVEL and NUVEL-1A plate circuit closures and seafloor spreading rates.

5.3.8 Nubia–South America plate motion

The 99 spreading rates that record Nubia–South America plate motion increase from 24 mm yr^{-1} at the Fifteen-Twenty transform fault (Figs 24 and 27a) to 33 mm yr^{-1} at 26°S. The rms misfit to the many spreading rates is 0.7 mm yr^{-1}, the same as for other slow spreading boundaries (Fig. 11b). The 27 transform fault azimuths for this plate pair (Fig. 27b) have an rms misfit of 1.4° and along with the many spreading rates give a well-determined pole with small uncertainties

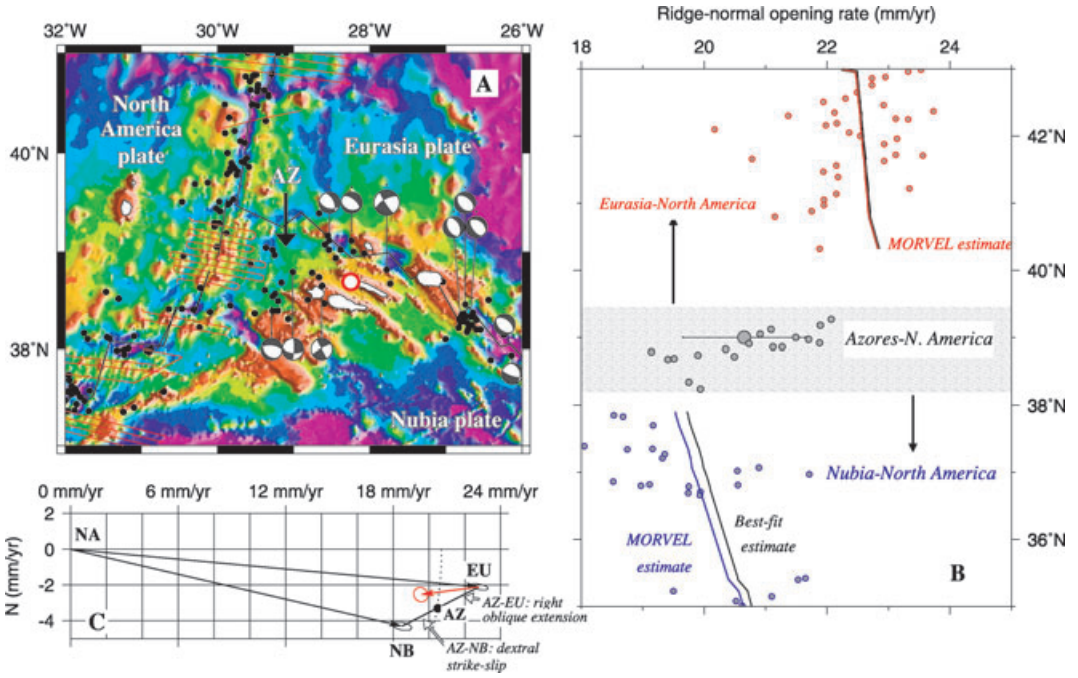

Figure 22. Tectonic setting and kinematic evidence for the Azores microplate. (a) Epicentres for earthquakes with $M_b > 3$ from 1967 to 2006 and Global centroid-moment tensors along the Azores microplate boundaries for the period 1976–2006 overlaid on the 1-min predicted depth grid, version 10.1 (Smith & Sandwell 1997). Red lines show tracks of shipboard magnetics used to estimate 3.16-Myr-average opening rates. Red circle shows location of GPS station SJRG on San Jorge island (Fernandes *et al.* 2006). (b) 3.16-Myr-average opening rates along Mid-Atlantic Ridge, 35°–43°N and rates determined with the MORVEL (red) and best-fitting (black) angular velocities. Large circle with error bar indicates the average opening rate for the Azores–North America plate seafloor spreading segments. (c) Linear velocity diagram for the North America–Eurasia–Nubia–Azores (NA-EU-NB-AZ) plate circuit at the Azores triple junction. Points on the dotted line specify the suite of velocities that are consistent with the average AZ-NA opening rate from (b). The AZ-NA direction is unknown, but is assumed to lie between the EU-NA and NB-NA directions. Red vector shows velocity of GPS site SJRG relative to the Eurasia plate from Fernandes *et al.* (2006).

(Fig. 12). Given the average spreading rate of 30 mm yr^{-1} along this plate boundary, the 1.4° rms angular misfit to the transform fault azimuths is geometrically equivalent to a ridge-parallel rms misfit of 0.7 mm yr^{-1}, similar to the rms misfit to the spreading rates from this plate boundary.

The best-fitting and MORVEL estimates of Nubia–South America motion are nearly identical (Figs 27a and b), with differences of only 0.01 mm yr^{-1} and 0.1° between the rates and directions estimated from the two angular velocities.

The NUVEL-1A Nubia–South America pole lies outside the 95 per cent confidence region of the MORVEL pole (Fig. 12) and indicates spreading rates 1.5–2 mm yr^{-1} higher than are given by MORVEL (Fig. 27a). Only part of this difference (≈40–50 per cent) can be attributed to the correction made here for outward displacement. The remainder reflects an improvement in the rate estimate due to the larger number of rates that are now available and possibly the automated cross-correlation procedure that we employ to estimate those rates.

5.3.9 Motion between the North and South America plates

The MORVEL pole of rotation for the North America relative to the South America plate is located near 10°N, 57°W (Fig. 25b). It predicts 3 ± 0.3 mm yr^{-1} of NNW- to NW-directed motion near the Mid-Atlantic ridge and 2–3 mm yr^{-1} of west-directed motion at locations farther west (Fig. 25b). The motion predicted near the Mid-Atlantic Ridge is consistent with evidence described by Roest & Collette (1986) for extension across the Royal Trough, Researcher Ridge, and Researcher Trough and with NNW–SSE tensional axes of moderate-magnitude earthquakes (Fig. 25b) and microearthquakes (Escartin *et al.* 2003) west of the Mid-Atlantic Ridge at 14°N. If the WNW-trending Barracuda Ridge accommodates some of the plate motion near the Lesser Antilles trench, as suggested by marine gravity (M̈ller & Smith 1993) and recent multibeam and seismic data (Benard *et al.* 2007), its oblique orientation relative to the predicted east–west direction of motion requires that it accommodate oblique convergence dominated by left-lateral slip.

All prior estimates for the North America–South America pole are located several hundred kilometre north of the MORVEL pole (Fig. 25b), including the NUVEL-1A 0–3 Ma pole, a pole found by differencing the NUVEL-1A best-fitting North America–Africa and South America–Africa best-fitting angular velocities (Gordon 1998), a long-term pole from Roest & Collette (1986), and a 0–10 Ma pole from Müller *et al.* (1999) based on a reconstruction of anomaly 5 from the Mid-Atlantic Ridge. All four poles predict that motion near the ridge is N–S. Two of the four poles (the NUVEL-1A and Müller *et al*. poles) also predict that motion decreases westward to negligible rates near the Lesser Antilles trench. Below, we explore possible reasons for the discrepancy between the locations of the MORVEL and prior poles.

We first consider whether inversions of any of several strategically selected subsets of the MORVEL data give a North America–South America pole that is located as far north as the prior poles (Fig. 25b). We first differenced the best-fitting angular velocities for the Nubia–North America and Nubia–South America plate pairs (Table 1), a procedure that eliminates the influence of all circuit closures, to determine whether the MORVEL circuit closures might be

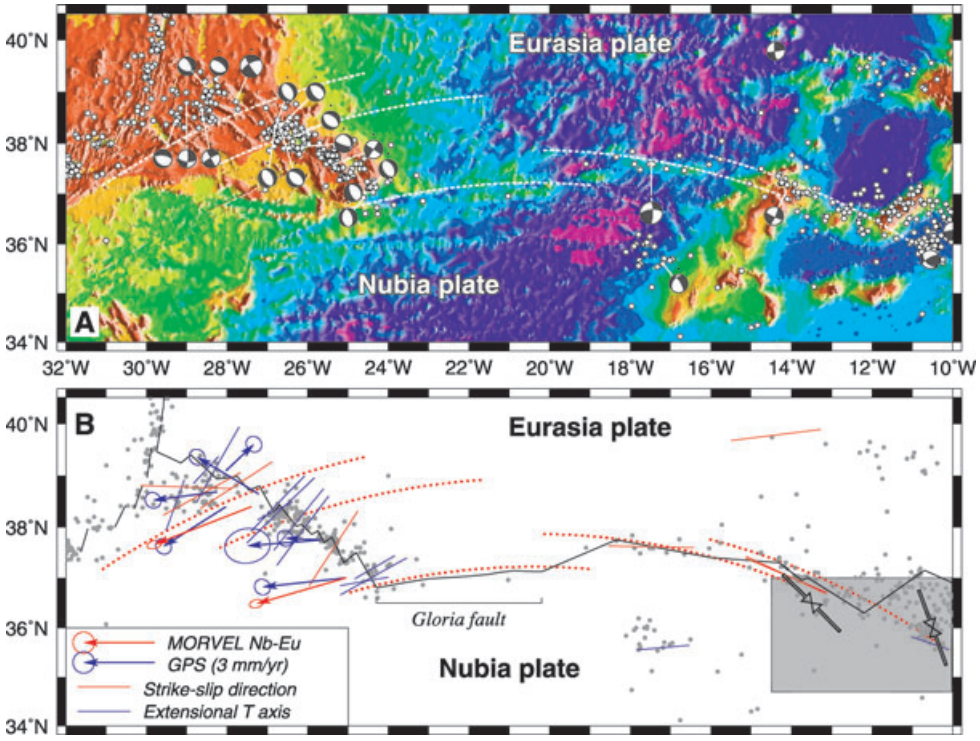

Figure 23. (a) Seafloor bathymetry, epicentres for 1963–2006 earthquakes, and 1976–2007 Global centroid moment tensor solutions along the Nubia–Eurasia plate boundary. White dashed curves show small circles around the MORVEL Nubia–Eurasia pole. (b) Seismicity, earthquake slip directions, and plate boundary structures east of the Azores triple junction. Red dotted curves are small circles around the MORVEL Nubia–Eurasia pole. Black line shows plate boundary interpretation from bathymetry, GLORIA (Laughton *et al.* 1972), and earthquake epicentres. Red and blue lines are horizontal slip directions for strike-slip earthquakes and tensional axes of normal faulting earthquakes, respectively, for focal mechanisms shown in panel (a). GPS velocities are relative to the Eurasia plate (Fernandes *et al.* 2006). Double-headed arrows indicate principal convergence directions inferred by Hayward *et al.* (1999) from a detailed seismic reflection and side-scan sonar survey of the Gorringe Bank (shaded region).

responsible for shifting the pole several degrees south of prior poles. The closure-free pole (Pole 1 in Fig. 25b), however, lies only one angular degree north of the closure-enforced MORVEL pole and is thus insufficient to explain the difference.

We next tested how the pole location is affected by our assumption that the North America–South America plate boundary is narrow where it intersects the Mid-Atlantic ridge. We omitted all rates and azimuths between the Marathon transform fault (12.65°N) and 18°N and re-inverted the remaining Nubia–North America and Nubia–South America data to estimate the North America–South America pole location. The resulting pole lies nearly as far north as the NUVEL-1A, Roest & Collette and Müller *et al*. poles (Pole 2 in Fig. 25b), suggesting that our narrow-boundary assumption influences the pole location. If we re-invert the data, however, while assuming that a hypothetically wide boundary intersects the ridge slightly farther to the north, between the Fifteen-Twenty and Kane (23.5°N) transform faults, the North America–South America pole (Pole 3 in Fig. 25b) shifts back southward to the latitude of the MORVEL pole. If we further enforce closure around the Nubia–Eurasia–North America plate circuit to better constrain the Nubia–North America angular velocity, Poles 2 and 3 shift even farther to the south, away from the NUVEL-1A, Roest & Collette and Müller *et al*. poles.

The difference between the MORVEL pole and prior poles is thus also robust with respect to permitting a wider North America–South America plate boundary.

With respect to the many new MORVEL data from the Mid-Atlantic Ridge, none of the prior poles successfully predict the newly discovered $\approx$2 mm yr^{-1} difference in spreading rates across the Fifteen-Twenty transform fault (Fig. 26a). Roest & Collette postulated that the pole must be located directly west of the Royal Trough, Researcher Ridge, and Research Trough based in part on their inference that motion across those features is dominated by north–south extension. That assumption and hence their pole location now appear to be only approximately correct. The NUVEL-1A angular velocity differs at high confidence level from the MORVEL angular velocity ($\chi^2 = 52.8$ and $p = 2 \times 10^{-11}$) when we compare the two angular velocity estimates with eq. (2). Given that the MORVEL estimate is determined from a factor-of-five more Mid-Atlantic Ridge spreading rates and transform fault azimuths than is the NUVEL-1A estimate, we interpret the difference between the two as evidence that the NUVEL-1A estimate is less accurate.

Finally, Müller *et al.* (1999) determined their 0–10 Ma pole from reconstructions of Mid-Atlantic ridge fracture zones and crossings of anomaly 5. We interpret the difference between the locations of the 0–3 Ma MORVEL pole and the 0–10 Ma pole as evidence that the pole has migrated southward since 10 Ma. Evidence that the pole, the location of the plate boundary, and the style of deformation across the plate boundary changed before 10 Ma (Müller & Smith 1993; Müller *et al.* 1999) is consistent with our interpretation. Accurate reconstructions of magnetic anomalies between anomaly 2A and anomaly 5 are needed to test our hypothesis.

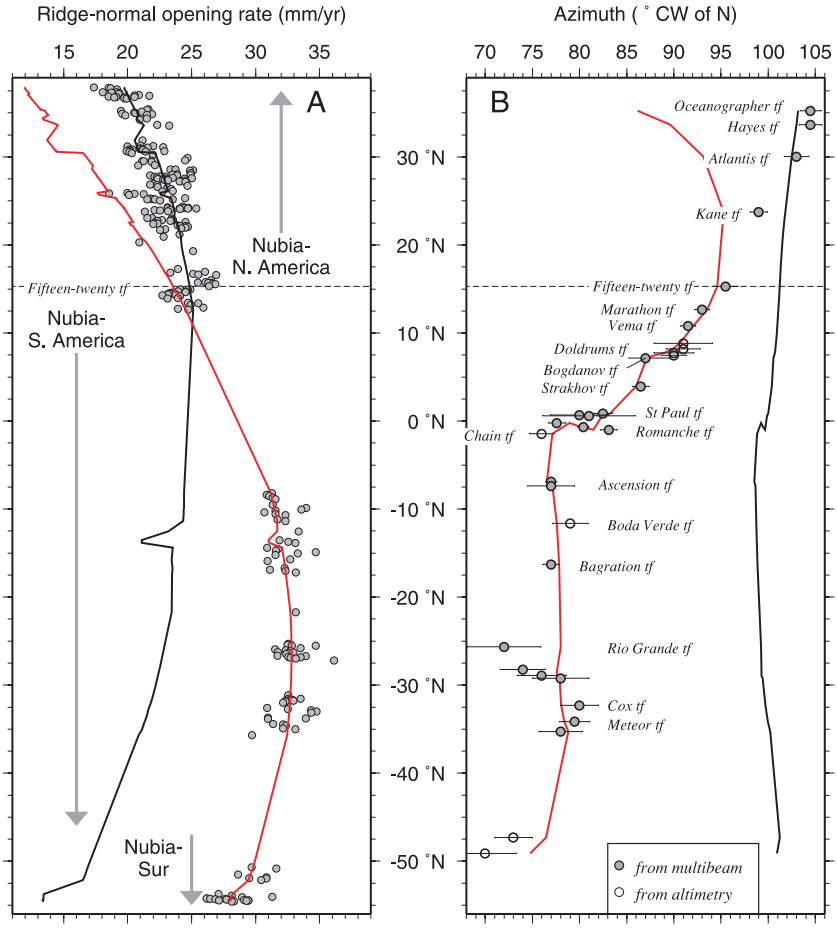

Figure 24. Mid-Atlantic Ridge spreading rates (a) and transform fault azimuths (b) from the Azores to the Bouvet triple junctions. Rates and directions are estimated with the best-fitting Nubia–North America (black) and Nubia–South America (red) angular velocities. Horizontal bars show 1σ uncertainties. 'tf' is transform fault.

5.3.10 Antarctic–Sur plate motion and evidence for a Sur microplate

A NE–SW-striking zone of earthquakes connects the Mid-Atlantic ridge near ≈48°S to the northeast corner of the South Sandwich subduction zone (Fig. 18a), which suggests that the lithosphere south of this diffuse seismic zone may move as an independent plate (DeMets *et al.* 1990; Gordon & Stein 1992). We employed the Stein & Gordon (1984) test for an additional plate to determine whether the MORVEL data from this region are fit significantly better by assuming the existence of a microplate, as follows: Assuming that no such plate exists, we first inverted the seafloor spreading rates and transform fault azimuths from the Nubia–South America–Antarctic plate circuit to estimate a set of closure-enforced angular velocities, giving χ^2 of 281.8. We then re-inverted the same data after including an additional small plate bounded by the American–Antarctic Ridge, the Mid-Atlantic Ridge from 47°S to the Bouvet triple junction, and the South Sandwich trench. The resulting lower value for χ^2, 271.5, is significant ($p = 0.044$).

The angular velocity that describes the relative motion of this small plate relative to South America predicts slow southwest-directed motion along their diffuse boundary (Fig. 18a), in agreement with the directions of plate motion that are suggested independently by focal mechanisms of small earthquakes within the diffuse seismic zone. The predicted relative motion is qualitatively consistent with a model in which westward subduction along the South Sandwich trench causes the seafloor east of the trench to move slightly faster to the west than the non-subducting seafloor farther north, as also appears to have occurred for an even smaller lithospheric sliver that has detached from the South America plate immediately north of the South Sandwich fracture zone (described below and shown in Figs 18a and c).

We refer to this plate as the Sur microplate (translated from Spanish as the 'Southern' microplate) and incorporate this plate into MORVEL. Few data can be used to estimate its motion, consisting of 27 rates and azimuths from the Mid-Atlantic ridge between 47°S and the Bouvet triple junction and ten rates and azimuths from the American–Antarctic ridge. These data only loosely constrain the location of the MORVEL Sur–South America pole, which has a 95 per cent confidence ellipse (not shown) that includes much of one hemisphere.

The angular velocity that best fits the sparse data from the American–Antarctic ridge indicates 18 ± 1 mm yr^{-1} of nearly east–west motion along the plate boundary (Figs 27c and d). As a test, we inverted the slip directions of 24 strike-slip earthquakes from the 530-km-long Bullard transform fault and found a best average slip direction of N84°E at the western end of the Bullard transform fault. This differs negligibly from and corroborates the N83°E ± 1.0° azimuth that we estimate from the partial side-scan sonar survey of the western end of this

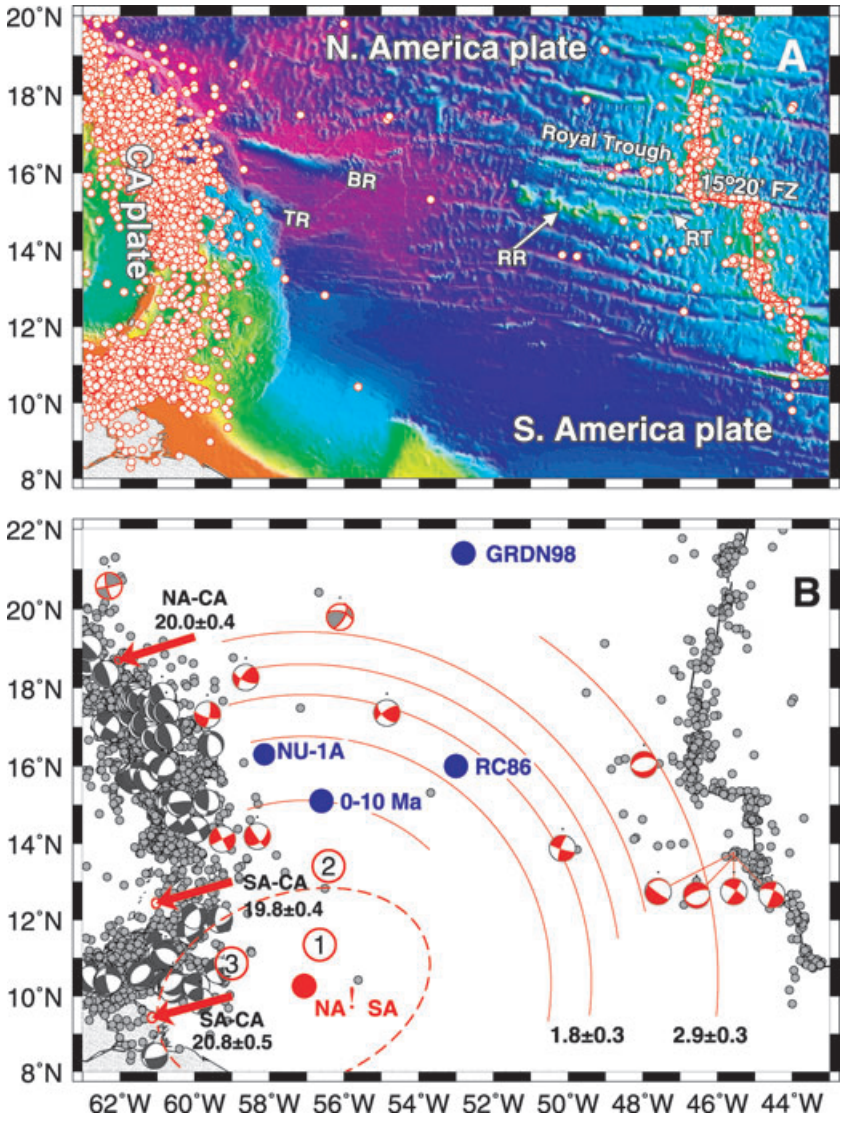

Figure 25. Seismotectonics of the North America–South America plate boundary. (A) Epicentres for 1920–1962 relocated earthquake (Wysession *et al.* 1995) and 1963–2007 USGS earthquake epicentres on one-minute predicted depth grid, version 10.1 (Smith & Sandwell 1997). Abbreviations: BR, Barracuda Ridge; CA, Caribbean plate; RR, Researcher Ridge; RT, Researcher Trough; TR, Tiburon Rise. (B) Plate velocities, seismicity, pole locations, focal mechanisms for the 10.23.64 $m_b = 6.2$ and 9.3.68 $m_b = 5.6$ earthquakes (grey) from Bergman (1986), and 1976–2007 Global centroid-moment tensor solutions (red). Red circle and dashed red ellipse show the MORVEL pole and 95 per cent uncertainty ellipse for North America plate relative to South America. Red arcs show small circles around the MORVEL pole. Red velocities show MORVEL estimates of the motions of North America (NA) and South America (SA) plates relative to the Caribbean (CA) plate. All numerals give predicted rates and 1σ uncertainties in mm yr^{-1}. Blue circles labelled 'NU-1A', 'RC86', 'GRDN98' and '0–10 Ma' show poles from NUVEL-1A, Roest & Collette (1986), Gordon (1998) and Müller *et al.* (1999). Circled numbers specify poles for alternative estimates that are described in the text. Earthquakes with red focal mechanisms may record deformation between the North and South America plates.

transform fault (Table S2 and R. Livermore, personal communication, 2001).

At the western end of the American–Antarctic ridge, the azimuth of the 320-km-long South Sandwich transform fault (SSTF in Fig. 18b) and slip directions for the two largest strike-slip earthquakes along this fault are all rotated 6°–7° clockwise from the direction estimated with the best-fitting Antarctic–Sur angular velocity (Fig. 27d). The misfit is consistent with a small component of extension across or north of the South Sandwich transform fault, in accord with normal-faulting earthquakes along and north of the South Sandwich transform fault that have extensional axes orthogonal to the transform fault (Fig. 18c). The available evidence strongly suggests that a lithospheric sliver north of and adjacent to the South Sandwich transform fault has detached from the Sur plate and subducts independently along the southern 25 per cent of the South Sandwich subduction zone.

The best-fitting Antarctic–Sur plate angular velocity gives spreading rates along the American–Antarctic Ridge that are 2 mm yr^{-1} higher than, and 1°–2° anticlockwise from, the rates and directions given by the closure-enforced MORVEL angular velocity (Figs 27c and d). The differences between the best-fitting and closure-enforced angular velocities are caused by non-closure of the Nubia–Antarctic–Sur plate circuit, which is discussed in Section 6.

The NUVEL-1A Antarctic–South America and MORVEL Antarctic–Sur angular velocities also differ significantly. The NUVEL-1A pole lies far outside the 95 per cent confidence region

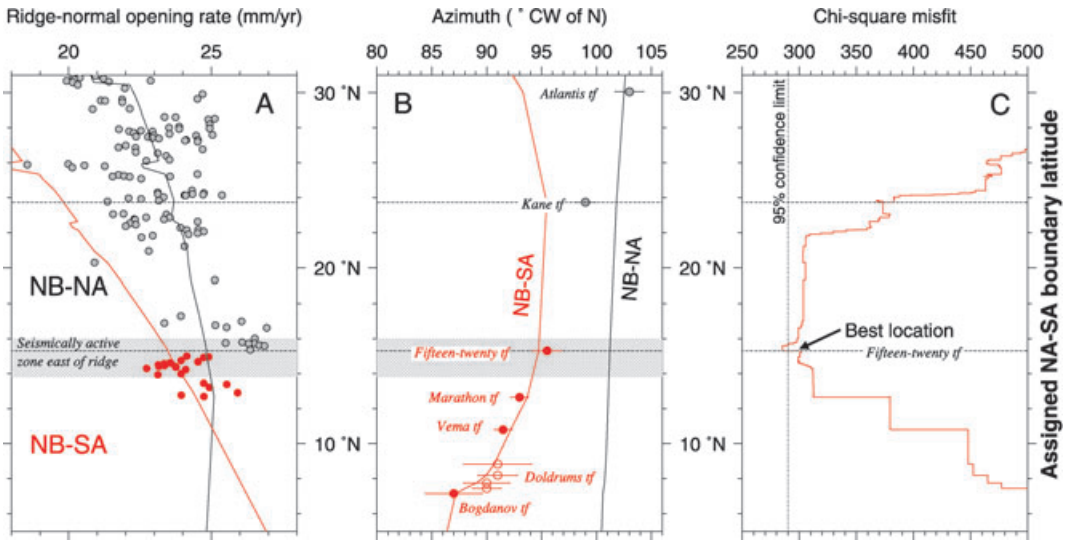

Figure 26. Test for location of Nubia–North America–South America plate triple junction. (a) Mid-Atlantic Ridge seafloor spreading rates, 5°N to 31°N, and rates determined with the best-fitting Nubia–North America (black) and Nubia–South America (red) angular velocities. (b) Transform fault azimuths and calculated plate motion directions in the same region. 'tf' is transform fault. (c) Variation in least-squares misfit to Mid-Atlantic Ridge rates and directions from the Bouvet to Azores triple junctions for different assumed triple junction locations, 5°N to 31°N. The best fit occurs if the northern limit of the Nubia–South America plate boundary is assumed to coincide with, or lie just north of, the Fifteen-Twenty transform fault. Ninety-five per cent limits for the assumed-discrete triple junction extend from 15.3°N to 15.7°N.

for the MORVEL pole (Fig. 13b) and gives directions of motion that poorly fit the well-determined azimuths of the Bullard and Conrad transform faults (Fig. 27d). Neither closure-enforced angular velocity fits the available data well.

5.4 The Scotia Sea

5.4.1 Data description

The Scotia and Sandwich plates extend eastward into the Atlantic Ocean basin from Cape Horn at the southern tip of South America (Figs 1 and 18). Transcurrent plate motion dominates along the North Scotia Ridge and South Scotia Ridge, which mark the northern and southern boundaries of the Scotia plate (Pelayo & Wiens 1989). The East Scotia Ridge, which marks the eastern boundary of the Scotia plate, accommodates backarc spreading between the Scotia plate and the Sandwich microplate, which lies west of the South Sandwich subduction zone. The western edge of the Scotia plate is defined by the Phoenix microplate, with boundaries that are delineated by earthquake epicentres in the Drake Passage south of Tierra del Fuego (Fig. 18) (Livermore *et al.* 2004). No attempt is made here to estimate Phoenix plate motion.

Here we combine observations from Thomas *et al.* (2003) and Smalley *et al.* (2007) with new earthquake focal mechanisms to estimate Scotia and Sandwich plate motions. Most of our data are adopted from Thomas *et al.* (2003), who determine spreading rates and seafloor fabric orientations from a dense geophysical survey of the East Scotia backarc spreading centre and also estimate slip directions for 68 earthquakes along the Scotia and Sandwich plate boundaries (Fig. 28). We adjusted all 18 anomaly 1n rates from Thomas *et al*., who used an age of 0.778 Ma for anomaly 1n, to account for the 0.781 Ma age we use herein. In the absence of East Scotia ridge transform faults, we adopt Thomas *et al*.'s strategy of using the direction of the well-mapped seafloor fabric along the East Scotia Ridge to estimate directions of relative motion along the plate boundary (Table S2).

Along the South Sandwich trench, Thomas *et al.* (2003) estimate mean convergence directions by summing the centroid-moment-tensors of shallow-thrust subduction earthquakes within 1° latitudinal bins from 61°S to 55°S (Table S3 and red arrows in Fig. 18b). We chose not to use their mean direction for 56°S–55°S, where a sharp westward bend in the trench, an anticlockwise rotation of the subduction direction, and the presence of strike-slip earthquakes in the upper plate (not seen elsewhere along the trench; Fig. 18b) all indicate that slip partitioning and northwest-directed transport of the edge of the Sandwich plate occur in response to the increasingly oblique plate convergence. We also do not use their mean subduction directions south of 59°S, where, as described above, a sliver of oceanic lithosphere appears to subduct independently beneath the edge of the Sandwich microplate (Figs 18a and b).

Along the sparsely mapped North and South Scotia Ridges, we use earthquake slip directions from Thomas *et al.* (2003) to constrain our estimates of Scotia–South America and Scotia–Antarctic plate motions (Figs 18(a), (b) and Table S3). Although we assume that motion along both of these plate boundaries is mainly strike-slip, as did Thomas *et al*. and Pelayo & Wiens (1989), many normal-faulting earthquakes occur between 60°W and 40°W along the South Scotia Ridge (Fig. 18b). Motion between the Scotia and Antarctic plates may therefore also include a component of boundary-normal extension. Selecting an unbiased set of earthquake slip directions for these two dominantly transcurrent plate boundaries is further complicated by localized restraining and releasing fault bends along this plate boundary.

A network of GPS stations that straddles the Scotia–South America plate boundary in Tierra del Fuego (Smalley *et al.* 2003, 2007) provides the least ambiguous measurements of Scotia plate motion. We selected the velocities of three Scotia plate stations from these studies (Table S4) to constrain our estimate of Scotia plate motion. One site (ORNO) lies far enough south of the major plate boundary fault(s) to escape most or all their elastic effects (Fig. 28). Two other sites (AUTF and PWMS) are located several tens of kilometres south of the main plate boundary fault in this region and could

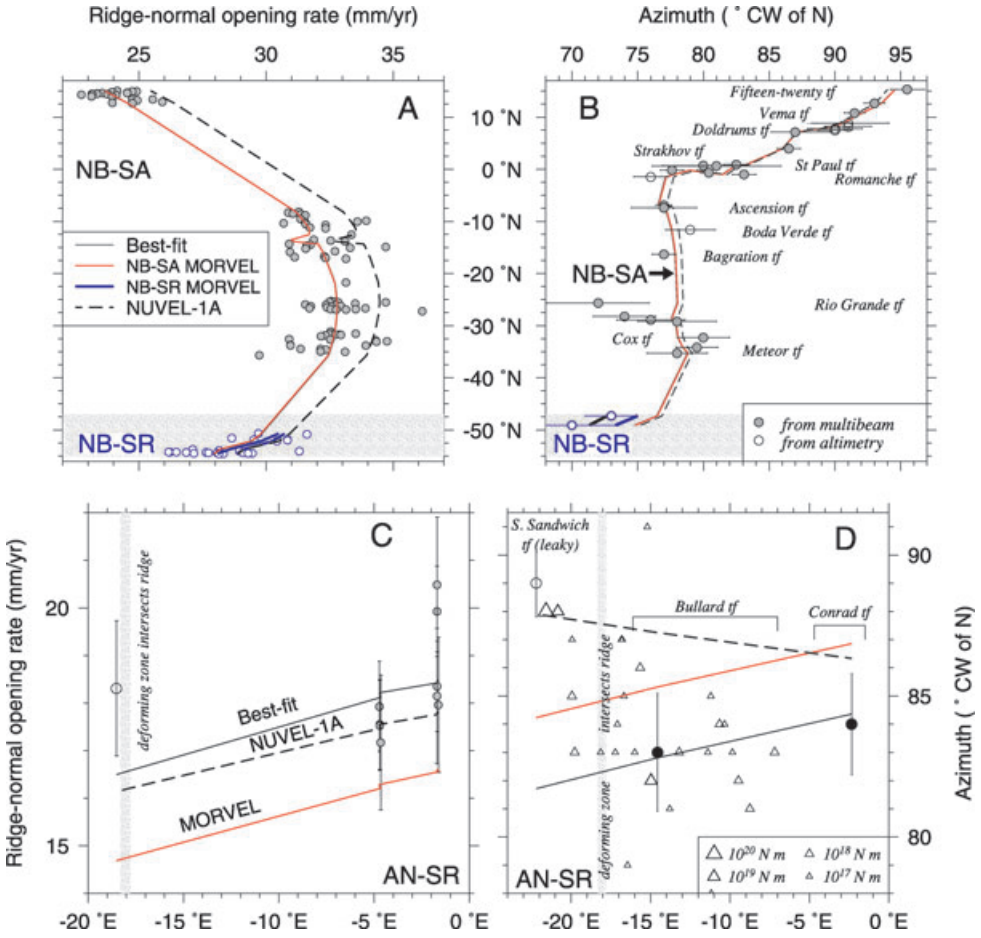

Figure 27. (a) Spreading rates from the Mid-Atlantic Ridge between the Bouvet triple junction and Fifteen-twenty transform fault and rates calculated from best-fitting, MORVEL and NUVEL-1A angular velocities (refer to legend in panel A). Rate uncertainties are omitted for clarity. (b) Observed and calculated transform fault azimuths from the Mid-Atlantic Ridge south of the Fifteen-twenty transform fault. (c) Spreading rates from the American–Antarctic Ridge and rates calculated from the best-fitting (black) and MORVEL (red) Antarctic–Sur angular velocities and the NUVEL-1A (dashed) Antarctic-South America angular velocity. In (c) and (d), only the data shown with solid or shaded symbols were used to derive the best fit and MORVEL angular velocities. (d) Antarctic–Sur transform fault azimuths. Triangles indicate horizontal slip directions of 1976–2006 strike-slip earthquakes from Global centroid moment tensor solutions, with symbol size scaled to moment release (see legend). All uncertainties are 1σ. Fig. 18(c) shows the location of the deforming zone referred to in (c) and (d).

experience elastic slip deficits of as much as $1\,\mathrm{mm\,yr^{-1}}$ relative to the full plate rate at those sites (Smalley *et al.* 2003). We conservatively allowed for potential elastic slip deficits at all three sites by increasing the uncertainty in each site rate to $\pm 3\,\mathrm{mm\,yr^{-1}}$, larger than the formal uncertainties estimated by Smalley *et al.* (2007). We did not, however, increase the uncertainty in any of the site directions since the directions should be relatively unaffected by elastic deformation along the linear strike-slip fault(s) that characterize the plate boundary in this region.

Smalley *et al.* (2007) specify the velocities of their Scotia plate sites relative to the South America plate, the motion of which they determine from the velocities of nine continuous GPS stations in the South America plate interior (locations indicated in Fig. 5). To assess the reproducibility of their results, we processed the continuous data from 1999 to 2008 for one of their three GPS stations (AUTF) and transformed the resulting station velocity into our own GPS-based realization of the South America plate reference frame. Encouragingly, our velocity for AUTF differs by only $0.1\,\mathrm{mm\,yr^{-1}}$ in rate and 1° in azimuth from that determined by Smalley *et al.* (2007), much smaller than the formal 1σ uncertainties in the rate and direction for this site. We therefore employ all three GPS site velocities given by Smalley *et al.* (2007) without any modification.

5.4.2 *Scotia and Sandwich plate motions*

Fig. 28 compares the fits of the MORVEL and Smalley *et al.* (2007) angular velocities with the kinematic data from the boundaries of the Scotia and Sandwich plates. The linear plate velocities estimated from MORVEL and the Smalley *et al*. studies are similar. Along the Scotia–Antarctic plate boundary, MORVEL indicates left-lateral slip with a minor component of extension (Fig. 28), in agreement with the left-lateral strike-slip and normal-faulting earthquakes that occur along the plate boundary (Figs 18b and d). The MORVEL and Smalley *et al*. angular velocities for this plate pair both indicate that motion is only 6–7 $\mathrm{mm\,yr^{-1}}$ along the boundary (shown by the blue and red arrows along the Scotia–Antarctic plate boundary in Fig. 28).

Along the boundaries of the Sandwich plate, the plate velocities estimated from the MORVEL and Smalley *et al*. angular velocities agree well with our best-fitting estimates (Fig. 28). The average earthquake slip directions from the South Sandwich subduction

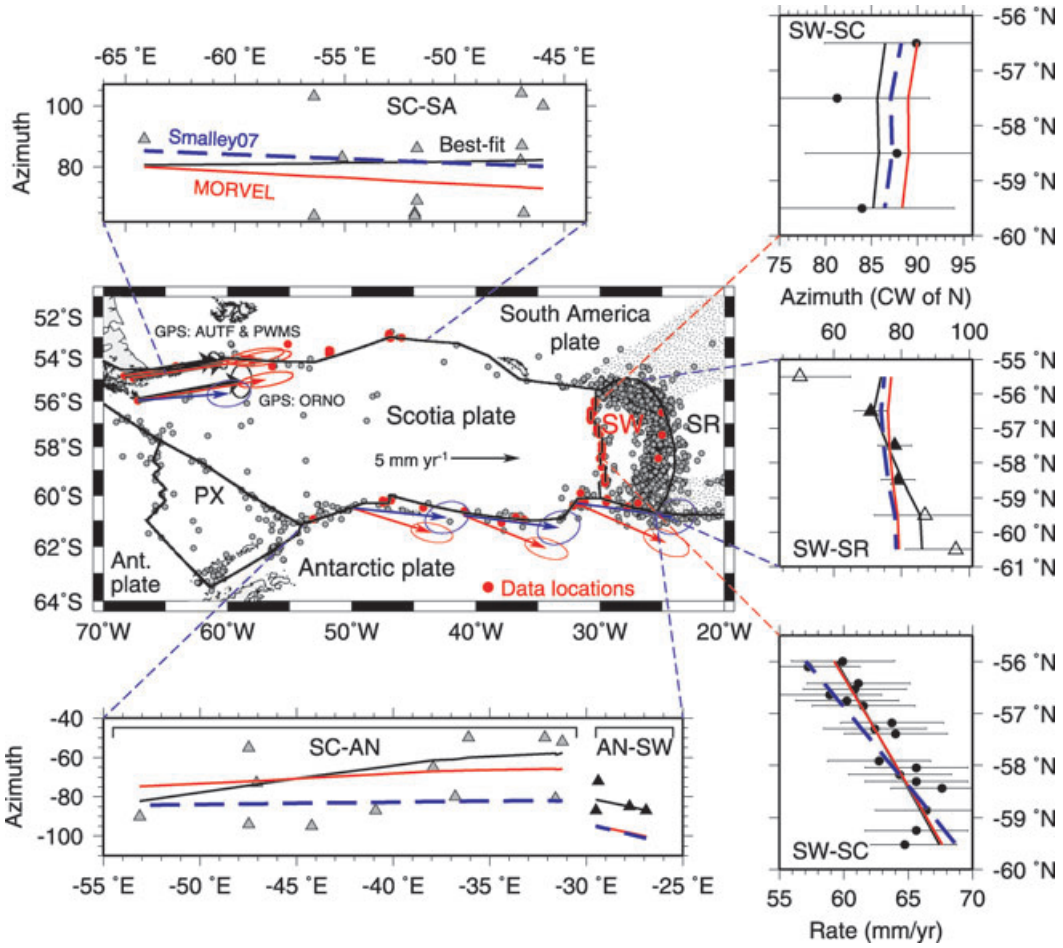

Figure 28. Centre map shows plate geometry, 1964–2006 shallow earthquake epicentres, and GPS velocity information for the Scotia plate region. Dashed blue lines and arrows show plate velocities determined with the Smalley *et al.* (2007) angular velocities. Red lines and arrows show velocities determined with the MORVEL angular velocities. Black arrows indicate measured GPS site motions relative to the South America plate from Smalley *et al.* (2007). Uncertainty ellipses are 2-D, 1σ. Black curves show best fits to kinematic data from the Scotia and Sandwich (SW) plate boundaries. 'PX' is Phoenix plate. Panel labelled SC-SA shows observed earthquake slip directions (triangles) and directions calculated from the Scotia–South America angular velocity. Panel labelled with SC-AN and SW-AN shows strike-slip earthquake slip directions from the Scotia–Antarctic and Sandwich–Antarctic plate boundaries and directions determined with their respective angular velocities. Panel labelled SW-SR shows slip directions for summed moment tensors for shallow thrust earthquakes from the South Sandwich subduction zone. Solid symbols show directions used to estimate MORVEL and the best-fitting angular velocities. Open symbols show directions that are excluded for reasons given in the text. Panels labelled SW-SC show full opening rates and opening directions across the East Scotia Ridge. In all the panels with kinematic data, the first labelled plate moves relative to the second and uncertainties are 1σ.

zone (labelled SS-SR in Fig. 28) are well fit by both the MORVEL Sur–Sandwich and Smalley *et al*. South America–Sandwich angular velocities. The same two angular velocities predict convergence rates at 57.5°S, 25.0°W, along the subduction zone, of 72.6 ± 2.2 mm yr^{-1} (1σ) and 71 mm yr^{-1}, respectively. These are encouragingly similar despite the different data and circuit closure conditions that are used to determine these two angular velocities.

The MORVEL and Smalley *et al*. Scotia–South America plate velocity estimates differ more than for the other plate pairs within the Scotia–Sandwich plate circuit. MORVEL gives plate rates that decrease gradually from 9.6 ± 1.4 mm yr^{-1} (1σ) at the western end of the North Scotia Ridge (65°W) to 8.9 ± 1.2 mm yr^{-1} at its eastern end (35°W). These are 3–4 mm yr^{-1} higher than the rates measured at all three GPS sites on the Scotia plate (compare red and wide black arrows on the map in Fig. 28) and are also higher than the 6.6 to 6.8 ± 1 mm yr^{-1} rates that are estimated by Smalley *et al*. The several millimetres year difference in the estimates is caused mainly by the different closure constraints that must be satisfied by the two estimates, prominent among these being the differing constraints that are imposed for Antarctic–South America plate motion. Better constrained estimates for plate motions in this remote region await more data.

5.5 Indian Ocean basin

5.5.1 Data from the Southwest Indian ridge

Along the 7750 km long, ultraslow spreading Southwest Indian Ridge, no multibeam coverage was available for NUVEL-1. An international effort during the 1990s to map this spreading centre resulted in multibeam coverage of nearly 6000 km of the plate boundary. The morphology and tectonics of the plate boundary are described in many papers, including the following: 0.7°W to 5°E (Ligi *et al.* 1999; Mitchell *et al.* 2000), 9°15′E to 16°E (Dick *et al.* 2003), 15°15′E to 35°E (Grindlay *et al.* 1998; Sclater *et al.* 2005), 49°15′E to 57°E (Sauter *et al.* 2001), 57°E to 70°E (Mendel *et al.*

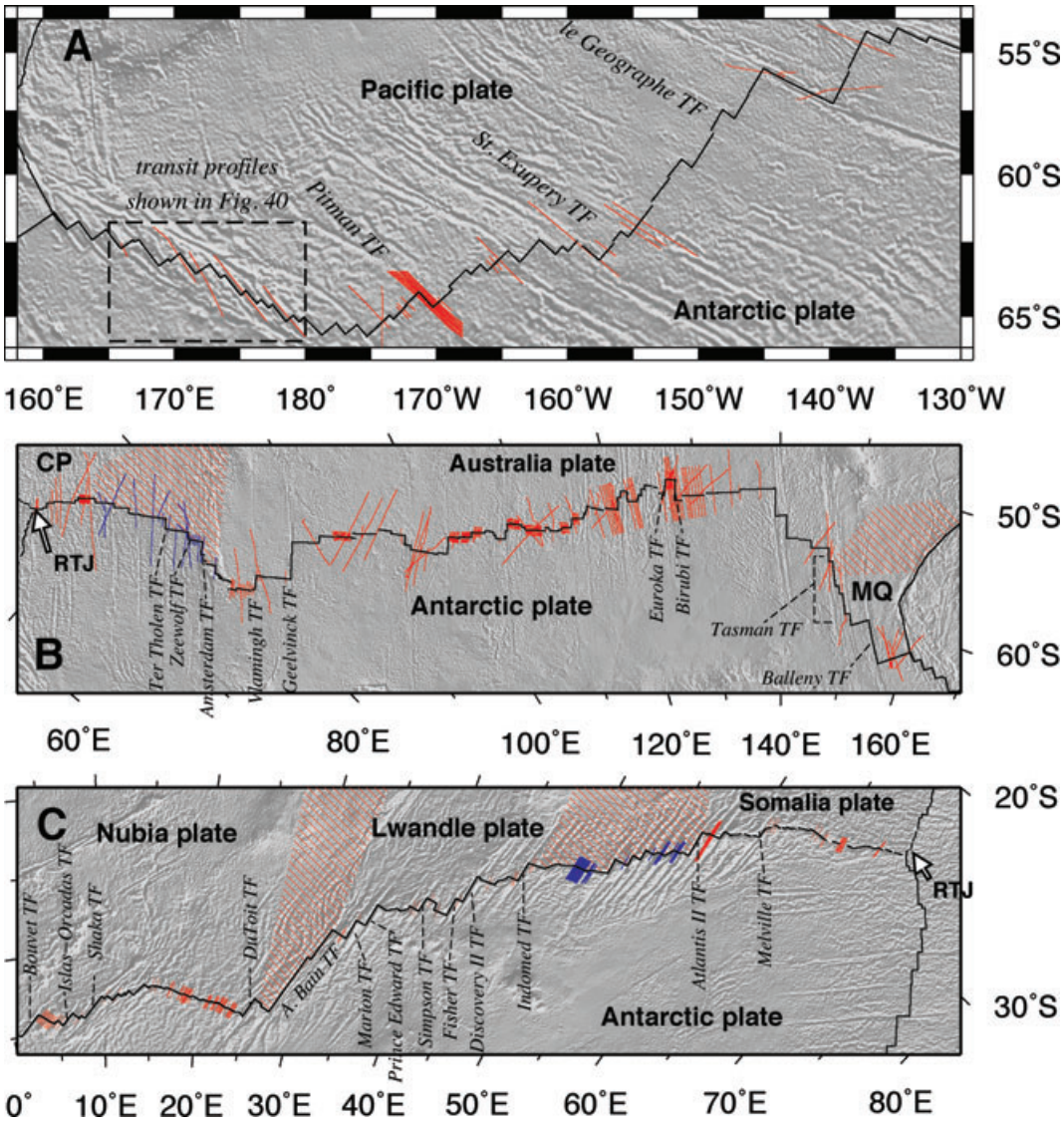

Figure 29. Ship and aeroplane tracks (red) of magnetic anomaly profiles used to determine MORVEL spreading rates. (a) Pacific–Antarctic rise west of 130°W. Tracks from the northeastern section of this plate boundary are shown in Fig. 39. Mercator projection. (b) Tracks for the Southeast Indian Ridge. 'CP' is Capricorn plate; 'MQ' is Macquarie plate; 'RTJ' is Rodrigues triple junction. Oblique Mercator projection. (c) Tracks for the Southwest Indian Ridge. Blue lines show tracks for rates that are located in deforming zones between the Lwandle and Somalia plates (b) and Australia and Capricorn plates (c). Oblique Mercator projection.

1997; Patriat *et al.* 1997), and a detailed survey of the Atlantis II transform fault at 57.1°E (Dick *et al.* 1991).

From the multibeam data described in these publications and bathymetric charts from Sclater *et al.* (1997), we estimated azimuths for the well-surveyed transform faults along the Southwest Indian Ridge (Fig. 29c and Table S2). Where possible, we estimated the azimuths from large-scale maps with the original depth grids. The long-offset Andrew Bain transform fault has a complex morphologic expression and is not used used for our analysis (Sclater *et al.* 2005). Several other well-mapped transform faults are located within zones of distributed deformation between the Nubia, Lwandle and Somalia plates north of the spreading centre (Horner-Johnson *et al.* 2007) and are not used to constrain MORVEL. Active normal faulting occurs adjacent to the well-mapped Bouvet transform fault (at the western end of the Southwest Indian Ridge). Mitchell *et al.* (2000) propose that transtensional motion across the Bouvet transform fault and adjacent lithosphere is partitioned into this normal faulting plus pure strike-slip along the Bouvet principal transform displacement zone (PTDZ). If true, the azimuth of the Bouvet PTDZ is biased several degrees clockwise from the plate motion direction. We therefore doubled the uncertainty of the Bouvet transform fault azimuth relative to those assigned to the other Nubia–Antarctic transform fault azimuths.

Magnetic survey coverage of the Southwest Indian Ridge (Fig. 29c) has also improved greatly relative to the dozen analogue magnetic profiles that were used to estimate Africa–Antarctic spreading rates for NUVEL-1. We use the many spreading rates from Horner-Johnson *et al.* (2005) and estimated additional new rates from densely spaced magnetic profiles from the R/V *Knorr* cruise 145 between 15°E and 25°E (Grindlay *et al.* 1998), older magnetic profiles from the AG44101 survey in the same region, and closely spaced profiles from 57°E to 58.5°E near the Atlantis II transform fault (Hosford *et al.* 2003). From 15°E to 25°E, where the rates estimated by Horner-Johnson *et al.* (2005) and our newly estimated

rates overlap substantially, the mean values for these two sets of opening rates differ by only 0.15 mm yr^{-1} and are thus consistent.

5.5.2 Southwest Indian ridge plate motions

The ≈160 spreading rates from the Southwest Indian Ridge (Fig. 29a) do not vary sinusoidally along the plate boundary, as would be the case if this spreading centre accommodated motion between only two plates. The rates instead exhibit distinctly different patterns along the eastern, middle, and western thirds of the spreading centre, consistent with a geometry in which the formerly assumed Africa plate north of the ridge is instead divided into distinct Nubia, Lwandle and Somalia plates (Horner-Johnson *et al.* 2007). The confidence regions for all three of the poles that best fit these rates are elongated towards the Southwest Indian Ridge (Fig. 12), reflecting the poorly determined spreading rate gradients along each of these three short plate boundaries.

Unlike the spreading rates, the azimuths of the 18 well-mapped long-offset transform faults from the Southwest Indian Ridge change consistently along the plate boundary (Fig. 29b). An inversion of all 18 azimuths to estimate a single best-fitting pole of rotation gives a weighted average misfit of only 1.0° to the azimuths, smaller than their estimated average uncertainty. The evidence that the Southwest Indian Ridge comprises three distinct plate boundaries is thus inferred from the spreading rate pattern, as well as the improved fits that result to all the data when circuit closure is enforced around the triple junctions at either end of the ridge, as well as in the Somalia–Arabia–Nubia–Antarctic circuit (Horner-Johnson *et al.* 2007).

Along the Nubia–Antarctic plate boundary, the best-fitting and MORVEL angular velocities both give spreading rates that are 1.5–2 mm yr^{-1} higher than are estimated from NUVEL-1A (Fig. 29a). The lower rates indicated by NUVEL-1A poorly match the many new spreading rates and can be rejected with high confidence based on their poor fits to individual magnetic profiles from this plate boundary. For example, the least-squares misfits of synthetic magnetic anomaly profiles to two ridge-normal magnetic profiles from the well-surveyed part of the ridge between 15°E and 25°E (Fig. 30) increase rapidly for synthetic spreading rates that are lower than 16 mm yr^{-1} (Fig. 30). Rates as low as the 13.7 mm yr^{-1} spreading rate given by NUVEL-1A at these profile locations can be excluded.

The NUVEL-1A Africa–Antarctic pole lies northeast of the MORVEL Nubia–Antarctic pole, outside its 95 per cent confidence region (Fig. 12). The difference in pole location reflects the much smaller length of the Southwest Indian Ridge from which the MORVEL data are used to estimate motion for this plate pair (0°E to 25°E) than for NUVEL (0°E to 61°E). The improved estimate of Nubia-Antarctic motion eliminates an important source of error in the NUVEL-1A Africa–Antarctic angular velocity that propagated into the NUVEL-1A angular velocity estimates for other plate pairs in the global circuit.

Along the Somalia–Antarctic plate boundary, the best-fitting and MORVEL angular velocities indicate nearly identical motions (Fig. 29), reflecting the negligible non-closure of the Capricorn–Antarctic–Somalia plate circuit (Section 6). The NUVEL-1A Africa–Antarctic pole lies outside the 95 per cent confidence limits of the MORVEL Somalia–Antarctic pole (Figs 12) and indicates a different spreading-rate gradient and different

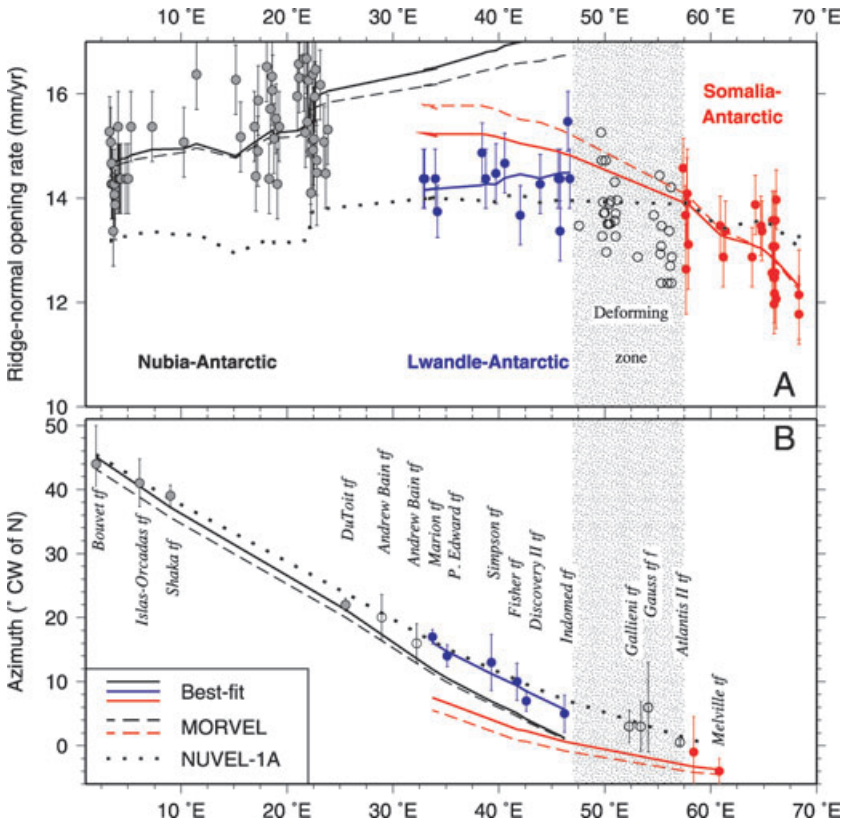

Figure 30. Southwest Indian Ridge spreading rates (a) and transform fault azimuths (b) and rates and directions determined with angular velocities that describe Nubia–Antarctic, Lwandle–Antarctic and Somalia–Antarctic plate motions. Dotted line shows motion determined with the NUVEL-1A Africa–Antarctic angular velocity. All data uncertainties are 1σ.

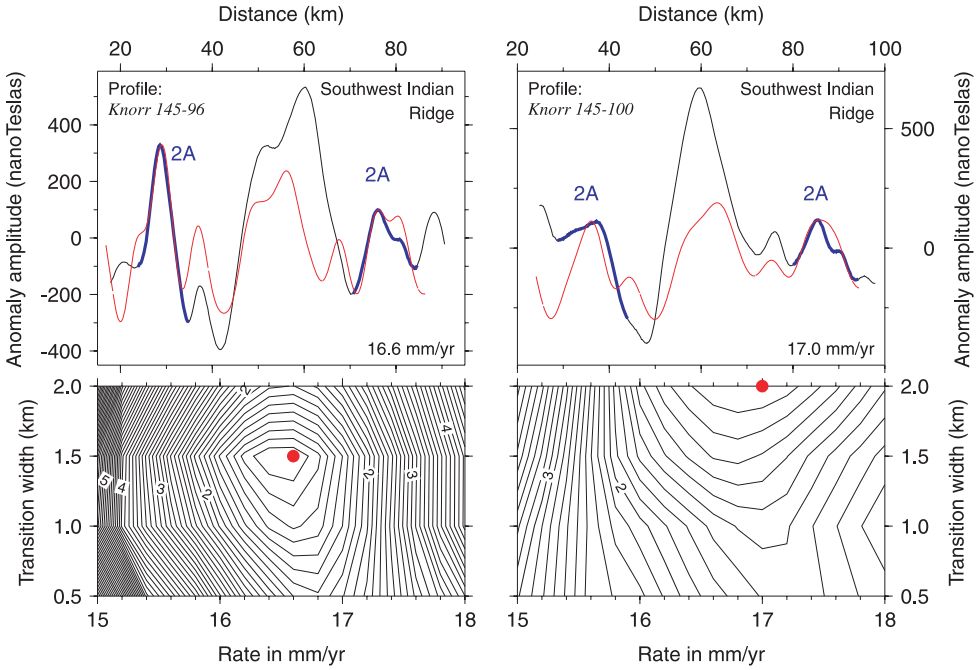

Figure 31. Examples of cross-correlated fits of the anomaly 2A sequence for two ridge-normal magnetic profiles across the Southwest Indian Ridge. Black and blue lines show observed profile and red curve shows synthetic magnetic profile. Blue curve indicates the part of the observed profile that is anomaly 2A and is cross-correlated with the synthetic profile. Lower diagrams show contours of least-squares misfit normalized by the misfit of the best-fitting least-squares model (red circle) for the suite of spreading rates and anomaly transition widths that were explored during the cross-correlation procedure.

directions than do the new best-fitting and MORVEL angular velocities (Fig. 29b).

5.5.3 Lwandle plate motions

The Lwandle plate extends northwards from the Southwest Indian Ridge between 30°E and 50°E and shares boundaries with the Nubia, Somalia and Antarctic plates (Fig. 1). Sixteen spreading rates and six transform fault azimuths from the Lwandle–Antarctic segment of the Southwest Indian Ridge determine the best-fitting and MORVEL Lwandle-Antarctic angular velocities (Fig. 2).

The angular velocity that specifies Lwandle–Somalia plate motion lies between the Southwest Indian Ridge and Madagascar (Fig. 13b), within one angular degree of the pole estimated by Horner-Johnson *et al.* (2007) from many of the same data. The angular velocity successfully predicts the south-to-north transition from ENE–WSW thrust faulting near the Southwest Indian Ridge to E–W normal faulting in Madagascar (Horner-Johnson *et al.* 2007). The slow relative motions predicted near the ridge (1.3 ± 0.5 mm yr^{-1} at 37°S, 50°E) and in Madagascar (1.4 ± 0.7 mm yr^{-1} at 20°S, 46°E) are consistent with the sparse seismicity along this diffuse boundary.

The angular velocity that specifies Nubia–Lwandle plate motion lies in South America, far from the hypothesized Nubia–Lwandle plate boundary (Fig. 12), but consistent with the results of (Horner-Johnson *et al.* 2007) from many of the same data. If the boundary lies near or along the Andrew Bain fracture zone, the indicated motion is $\approx$2 mm yr^{-1} of right-lateral shearing with some extension. We are aware of no morphologic evidence for active deformation along this boundary. The evidence for seismicity along this hypothesized boundary is sparse (Hartnady 2002). The main evidence for motion along this boundary comes from the misfit to anomaly 5 west of the Andrew Bain fracture zone when reconstructed by the rotation that best fits the data east of the Andrew Bain fracture zone (Lemaux *et al.* 2002; Royer *et al.* 2006). Patriat *et al.* (2008) recently presented a plausible alternative interpretation of the location of anomaly 5 that differs from that of Lemaux *et al.* (2002) in the region that is both south of the Southwest Indian Ridge and west of the Andrew Bain fracture zone. In the interpretation of Patriat *et al.* (2008), there has been no measurable motion between Nubia and Lwandle since 11 Ma.

The motion estimated by Horner-Johnson *et al.* (2007) and herein is small enough that we cannot categorically exclude the possibility that it could be an artefact of a systematic error such as variations in the magnitude of outward displacement along the Southwest Indian Ridge similar to those described by DeMets & Wilson (2008) for the Southeast Indian Ridge. If so, then what we take to be the Lwandle plate is either part of the Nubia plate, or part of the Nubia–Somalia diffuse plate boundary, or some of each. We refer readers to Horner-Johnson *et al.* (2007) for further discussion of Lwandle–Nubia–Somalia plate motions and their uncertainties.

In any event, no kinematic information from the Lwandle plate boundaries propagates via circuit closures into MORVEL; the angular velocities for other plates would remain the same if the Lwandle plate were excluded.

5.5.4 Data from the Southeast Indian ridge

Multibeam coverage of the 11 800-km-long Southeast Indian Ridge was non-existent in the mid-1980s and bathymetric measurements were limited to only 13 sparsely surveyed transform faults. In contrast, more than 70 per cent of the plate boundary (8300 km) had been mapped with multibeam as of mid-2005, including partial or full coverage of 25 transform faults. In particular, the Boomerang 6 multibeam survey of the ridge from 78°E to 88°E (Conder *et al.* 2000; Scheirer *et al.* 2000), the R/V *Melville* Westward 9 and 10 cruises from 88°E to 118°E (Ma & Cochran 1997; Sempere *et al.* 1997; Shah & Sempere 1998), and SeaMARC II and side-scan sonar

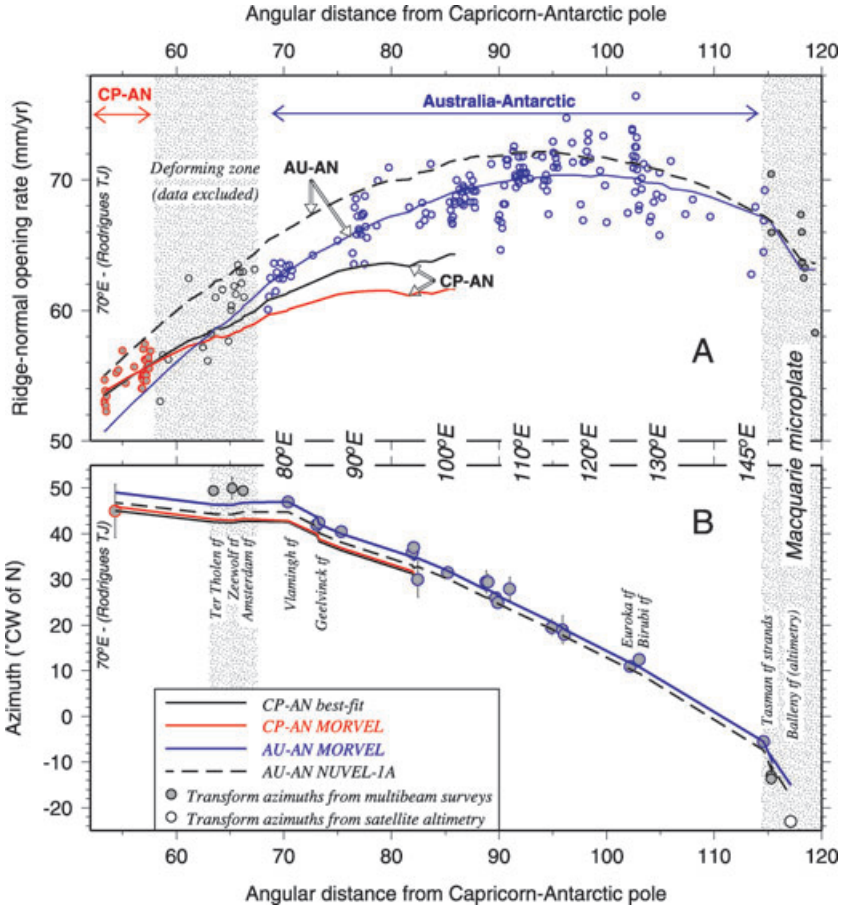

Figure 32. Spreading rates (a) and transform fault azimuths (b) for the Southeast Indian Ridge, 70°E–161°E, and rates and directions calculated from angular velocities that describe Australia–Antarctic and Capricorn–Antarctic plate motions. Vertical bars on transform fault azimuths show the 1σ uncertainties. Spreading rate uncertainties are omitted for clarity. Plate name abbreviations are from Fig. 1. Data located at angular distances of 114.5°–120° from the pole constrain the relative motion of the Macquarie and Antarctic plates.

surveys of the Australia–Antarctic Discordance (123°E–128°E) (Sempere *et al.* 1991; Palmer *et al.* 1993) provide excellent multibeam and magnetic coverage in their respective survey areas. Along the 580-km-long Tasman transform fault near the eastern end of the Southeast Indian Ridge, we use transit track multibeam sonar along two strands of this transform fault to establish the direction of motion of the Macquarie microplate relative to the Antarctic plate.

Magnetic profile coverage of the Southeast Indian Ridge has also improved dramatically since the publication of NUVEL-1. Many well navigated magnetic profiles from a variety of sources (Fig. 29 and Table S1) give well-determined 0.78-Myr-average spreading rates nearly everywhere along the plate boundary, in contrast to the isolated and more poorly navigated profiles that constituted the majority of the shipboard data that were available prior to 1990. Sources of these data include various French cruises that document spreading rates between the Rodrigues triple junction and 78°E, the Boomerang 6 and Westward cruises from 78°E to 118°E, and the Project Investigator aeromagnetic survey of the Australia-Antarctic Discordance between 117°E and 132°E (Vogt *et al.* 1983).

We next use the many spreading rates (230) and transform fault azimuths (26) from the Southeast Indian Ridge (Fig. 32) to determine the best locations for the Capricorn–Australia and Australia–Macquarie plate boundaries north of the spreading centre and estimate relative motions of the Antarctic, Australia, Capricorn and Macquarie plates across their respective boundaries.

5.5.5 *Capricorn–Australia plate boundary location*

The distributed deformation that accommodates Capricorn–Australia plate motion may span a zone as wide as 2000 km along the Southeast Indian ridge (Royer & Gordon 1997; Conder & Forsyth 2001). We searched for the western limit of the deforming zone using 242 spreading rates and transform fault azimuths between the Rodrigues triple junction (70°E) and the Tasman transform fault (146°E). Fig. 33(a) shows variations in the least-squares misfits of the angular velocities that best fit the data for different assumed locations of the Capricorn–Australia plate boundary. The best overall fit occurs for hypothetical boundary locations from 100°E to 105°E (Fig. 33a); however, the improvements in fit at these hypothetical boundary locations are artefacts of previously described variations in outward displacement that bias seafloor spreading rates at these locations (DeMets & Wilson 2008). Since these are unrelated to intraplate deformation on either side of the ridge, we ignore them below.

Elsewhere along the Southeast Indian Ridge, the fit becomes increasingly worse if we assume that the Capricorn–Australia plate boundary intersects the ridge at, or northwest of, the Amsterdam transform fault at the northwestern edge of the Amsterdam hotspot plateau (Fig. 33a). The pattern of misfits suggests that the western limit of the Australia plate extends no farther west than the Ter Tholen transform fault and more likely coincides with or lies east

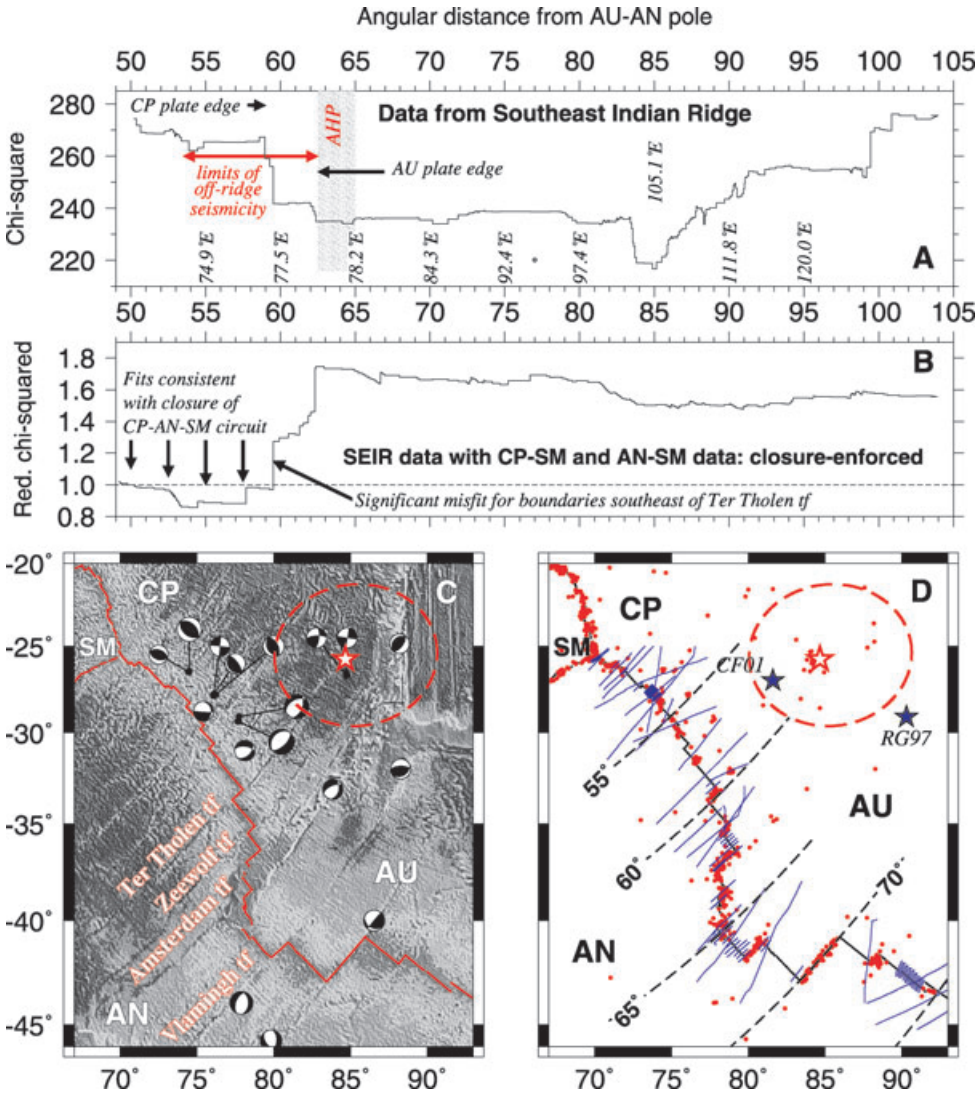

Figure 33. Search for Capricorn–Australia plate boundary. (a) Least-squares fits versus angular distance for different assumed boundary locations along the Southeast Indian Ridge (SEIR), 70°E–135°E. Misfit is calculated from inversions of all SEIR rates and transforms, with data located west and east of the assumed boundary location assigned to the Capricorn-Antarctic (CP-AN) or Australia–Antarctic (AU-AN) plate pairs, respectively. The data are poorly fit for all boundary locations west of the Amsterdam hotspot plateau (AHP). (b) Reduced chi-square from inversions of Capricorn–Antarctic–Somalia (CP-AN-SM) kinematic data for hypothetical boundary locations progressively farther to the east along the SEIR. Significant non-closure of the CP-AN-SM plate circuit is found for all boundaries that intersect the SEIR southeast of the Ter Tholen transform fault. (c) MORVEL pole for Australia relative to Capricorn plate (red star) and 2-D, 95 per cent confidence ellipse with 1976–2007 Global centroid moment tensor earthquake focal mechanisms and transform fault names and locations. (d) Epicentres for earthquakes of all magnitudes for the period 1963–2007, ship tracks for seafloor spreading rates used in the analysis (blue), and Australia-Capricorn pole and 2-D, 95 per cent confidence ellipse. Dashed curves relate angular distances from A and B to geographic locations. Blue stars labelled 'RG97' and 'CF01' specify Royer & Gordon (1997) and Conder & Forsyth (2001) pole locations, respectively.

of the Amsterdam transform fault and its fracture zone north of the ridge.

The fit if the eastern limit of the Capricorn–Australia deforming zone intersects the ridge at the Amsterdam transform fault is significantly better ($p = 3 \times 10^{-7}$) than if no plate boundary is assumed to intersect the ridge. This location is consistent with the tendency for earthquakes that occur north of the Southeast Indian Ridge to concentrate along the Amsterdam fracture zone and locations farther northwest (Fig. 33d), rather than along the fracture zones that are located southeast of the Amsterdam transform fault.

We similarly searched for the western limit of the diffuse Capricorn–Australia plate boundary (i.e. the eastern edge of undeformed Capricorn plate) by using the 242 Southeast Indian Ridge data described above and 97 additional spreading rates and transform azimuths from the Somalia–Antarctic and Capricorn–Somalia plate boundaries. The latter data impose additional constraints on Capricorn–Antarctic motion via closure of the Antarctic–Capricorn–Somalia plate circuit. Repeated inversions of these data for different assumed Capricorn–Australia boundary locations (Fig. 33b) give values of χ^2_ν that are close to 1.0 for all assumed boundary locations between the Rodrigues triple junction and the Ter Tholen transform fault. The data are thus well fit and consistent with closure of the Capricorn–Antarctic–Somalia plate circuit if the Capricorn plate interior is assumed to extend to the Ter Tholen transform fault. The misfit becomes rapidly worse for hypothetical boundaries that intersect the Southeast Indian Ridge southeast of the Ter Tholen transform fault (Fig. 33b).

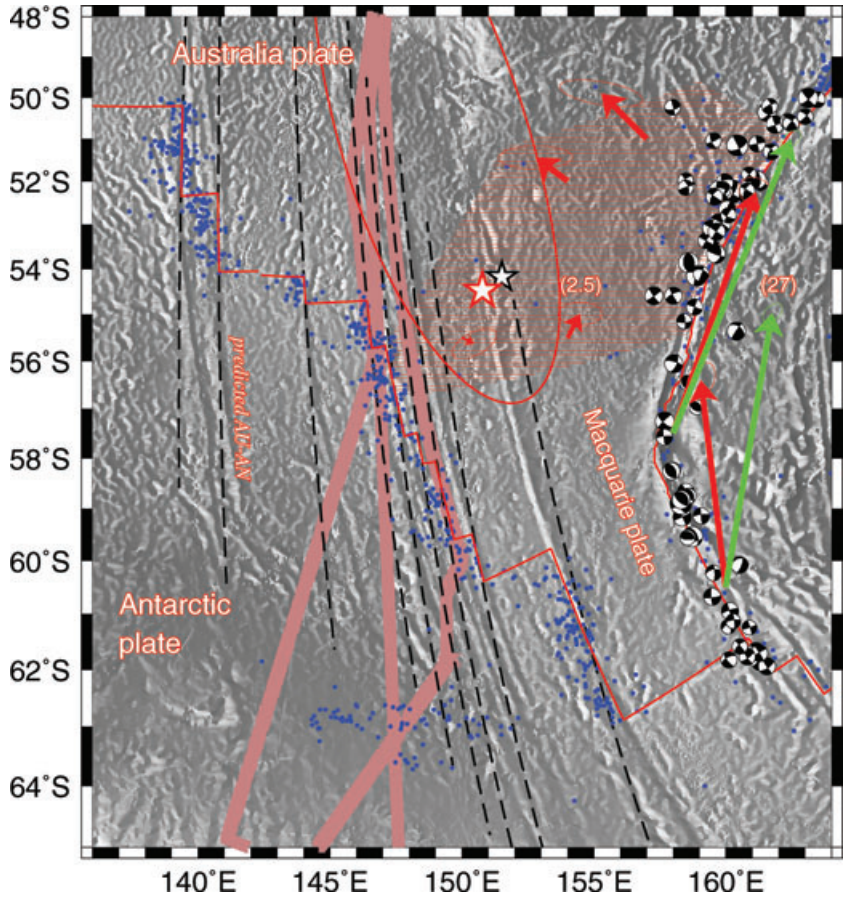

Figure 34. Macquarie plate tectonics. Pink shaded lines show transit multibeam tracks from which azimuths were derived at three locations along the Tasman transform fault. Dashed curves show small circles around the best-fitting Australia–Antarctic MORVEL pole. Blue dots show shallow seismicity from 1963 to 2006. Black star indicates the pole of rotation for the Australia plate relative to the Macquarie plate since anomaly 2Ay (2.59 Ma) from Cande & Stock (2004). Red star and ellipse show the MORVEL Australia–Macquarie rotation pole and 2-D, 95 per cent confidence ellipse for 0.78 Ma. Red arrows and ellipses in the diffuse boundary show Australia plate velocities and their 1σ, 2-D uncertainties relative to the Macquarie plate for points within the hypothesized diffuse plate boundary, as predicted by MORVEL. The red and green arrows along the Macquarie Ridge Complex show linear velocities predicted by MORVEL for the motions of the Macquarie (red) and Australia (green) plates relative to the Pacific plate. Parenthetical numerals adjacent to some velocity arrows indicate the predicted rate in millimetres per year and are given for scale.

Although the data suggest that the Capricorn plate does not deform northwest of the Ter Tholen fracture zone, the seafloor north of the ridge is seismically active for hundreds of kilometres northwest of the Ter Tholen fracture zone (Fig. 33d). Our kinematic data in this region consist almost entirely of seafloor spreading rates and are thus poorly suited for detecting any stretching or shortening of the seafloor parallel to the ridge. Several normal-faulting earthquakes north of the ridge in this region however have *T* axes parallel to the ridge (Fig. 33c), indicating ridge-parallel extension.

Guided by earthquake epicentres, we thus assigned a more western location for the western intersection of the deforming zone with the ridge, corresponding to a location ≈600 kilometres northwest of the Ter Tholen transform fault (29°S, 75°E). Consequently, we excluded all five magnetic profiles that cross this ≈600-km-long stretch of the ridge from our determination of the Capricorn–Antarctic angular velocity (Fig. 32a).

5.5.6 Macquarie–Australia plate boundary location

From their analysis of fracture zone flow lines from the eastern end of the Southeast Indian Ridge, Cande & Stock (2004) conclude that the Tasman fracture zone north of the ridge axis marks the boundary between the Macquarie plate and the Australia plate. We tested this with our new data set. Transit-track multibeam sonar data (shown by the shaded areas in Fig. 34) illuminate three segments of the transform tectonized zone at different locations along the Tasman transform fault. The N05.4°W ± 0.7° azimuth of the 115-km-long northern segment (Table S2) agrees to within 0.2° with the Australia–Antarctic direction of motion determined from transform faults farther west along the plate boundary. In contrast, the azimuths of well defined, 70-km-long and 90-km-long transform fault segments located 300–400 km south of the northernmost mapped segment are both 4° anticlockwise from the direction predicted for Australia–Antarctic motion, several times larger than their respective uncertainties of ±0.8° and ±1.1°. These azimuths suggest that the northern diffuse boundary of the Macquarie plate intersects the Tasman transform fault somewhere along its length, consistent with conclusions of Cande & Stock (2004). We thus assign the northernmost azimuth to the Australia–Antarctic plate pair and use the other two azimuths to estimate Macquarie–Antarctic plate motion.

5.5.7 Capricorn–Antarctic plate motion

Our best-fitting Capricorn–Antarctic angular velocity (Table 1) is determined from 35 spreading rates and one transform fault azimuth

from the western 500 km of the Southeast Indian Ridge (Fig. 32a). Along this part of the ridge, the 0.78-Myr-average spreading rates increase from 53 ± 1 mm yr^{-1} at the triple junction to 56 ± 2 mm yr^{-1} near 28°S, 74°E (Fig. 32a) and are lower than the NUVEL-1A rates by 3 mm yr^{-1} (Fig. 21a). The rates and directions estimated from the best-fitting and closure-enforced MORVEL angular velocities differ by no more than 0.3 mm yr^{-1} and 0.7°, reflecting the consistency with closure of the Capricorn–Antarctic–Somalia plate circuit (Section 6).

5.5.8 Australia–Antarctic plate motion

The 167 Australia–Antarctic spreading rates increase from 60 mm yr^{-1} at the Amsterdam transform fault to a maximum of 70 mm yr^{-1} within the Australia–Antarctic Discordance (≈115–125°E) and vary sinusoidally with angular distance along the plate boundary (Fig. 32), as expected. The many high quality data, which also include 19 transform fault azimuths, strongly constrain the best-fitting and MORVEL angular velocities (Fig. 13a and Tables 1 and 3). The MORVEL angular velocity for this plate pair is identical to the best-fitting angular velocity since plate circuit closures do not influence the former.

The NUVEL-1A angular velocity indicates spreading rates that are 1–3 mm yr^{-1} higher than observed everywhere along the boundary (Fig. 32). Some of this difference, which averages 2.1 mm yr^{-1} (Fig. 21a), is attributable to the ≈2.6 mm yr^{-1} downward adjustment to the MORVEL rates for outward displacement; however, a systematic difference of 1.4 mm yr^{-1} remains if we also downward adjust the 3.16-Myr-average NUVEL-1A rates for the same amount of outward displacement (2 km) and repeat the comparison (Fig. 21b). The NUVEL-1A estimate also misfits the spreading rate gradient (Fig. 32a), consistent with its pole location several angular degrees farther from the plate boundary than the MORVEL pole (Fig. 13a). The MORVEL and NUVEL-1A angular velocities differ significantly ($p < 10^{-15}$).

5.5.9 Macquarie–Antarctic plate motion

The motion between the Macquarie and Antarctic plates is determined from the azimuths of the two southern strands of the Tasman transform fault, the azimuth of the 370-km-long Balleny transform fault, and eight spreading rates (Figs 32 and 34). The measured spreading rates decrease from 68 ± 2 mm yr^{-1} at the Tasman transform fault to 64 ± 2 mm yr^{-1} just west of the Macquarie triple junction (Fig. 32a), consistent with the gradient extrapolated from rates farthest west along the Southeast Indian Ridge. The rapidly changing transform fault directions are fit poorly by the Australia–Antarctic angular velocity (Fig. 32b), constituting the main kinematic evidence for the existence of the Macquarie plate. The motion of the Macquarie plate relative to both the Australia and Pacific plates is further described in Section 5.5.11.

5.5.10 Australia–Capricorn plate motion

The Capricorn plate rotates relative to the Australia plate about a pole located north of the Southeast Indian ridge, in the zone of diffuse deformation between these two plates (Figs 13b, 33c and d). When compared with a null rotation, the slow relative angular velocity between these two plates is significant ($\Delta\chi^2 = 88.6$; $p < 10^{-15}$) and appears to be well resolved by the data. At 30°S, 80°E, in a region of active seismicity within the diffuse Australia–Capricorn plate boundary, the new angular velocity predicts Capricorn plate motion of 1.9 ± 0.5 mm yr^{-1} (1σ) towards N45°W ± 15° relative to the Australia plate. The predicted motion is consistent with ridge-parallel stretching indicated by normal-faulting earthquake mechanisms at this location (Fig. 33c). At 15°S, 95°E, the new angular velocity predicts Capricorn plate motion of 4.7 ± 0.9 mm yr^{-1} towards S50°E ± 6°. The motion is consistent with contractional deformation indicated by the NW–SE *P*-axes of earthquakes in this region (Royer & Gordon 1997) and is also perpendicular to the strikes of hypothesized lithospheric folds in the region (Stein *et al.* 1989; Petroy & Wiens 1989).

The Capricorn–Australia poles estimated by Royer & Gordon (1997) and Conder & Forsyth (2001) (shown by red stars in Fig. 33d) lie within the 95 per cent uncertainty region of the MORVEL estimate and predict linear velocities that differ by no more than 1–3 mm yr^{-1} from those predicted by MORVEL at 30°S, 80°E and 15°S, 95°E. Our analysis therefore reinforces conclusions reached by Royer & Gordon and Conder & Forsyth regarding slow deformation between the Capricorn and Australia plates and the transition from extensional deformation at the southern terminus of their boundary to convergent motion north of ≈25°S.

5.5.11 Australia–Macquarie–Pacific plate motion

The angular velocity that describes Macquarie–Australia plate motion (Table 3) is inferred from closure of the Macquarie–Australia–Antarctic plate circuit and lies within the zone of diffuse deformation between these two plates (Fig. 34). The new angular velocity predicts motion of only 1–2 mm yr^{-1} along this poorly understood boundary, the same within the uncertainties as that estimated by Cande & Stock (2004). Despite the slow motion, a comparison of the angular velocity to a null rotation with eq. (2) gives $\Delta\chi^2$ of 133, which is significant ($p < 10^{-15}$). We refer readers to Cande & Stock (2004) for a more in-depth discussion of Macquarie plate tectonics.

Along the Macquarie Ridge Complex north of the Pacific–Antarctic–Macquarie triple junction (Fig. 34), the Pacific–Macquarie plate angular velocity predicts motion that is ≈6 mm yr^{-1} slower than predicted by the Pacific–Australia angular velocity (Fig. 34). The predicted motion is also less oblique to the plate boundary south of 57°S (Fig. 34) and more consistent with the directions of motion indicated by the many strike-slip earthquake focal mechanisms along the plate boundary. The seismological evidence and our new estimate for motion along the Macquarie–Pacific plate boundary indicate that motion everywhere south of ≈58°S is dominated by right-lateral shear.

5.5.12 Data from the central and northern Indian basin, Gulf of Aden and Red Sea

Geophysical data coverage of the southern Central Indian Ridge (Fig. 35) has improved greatly since NUVEL-1. Magnetic data from British, French and Indian cruises and an aeromagnetic survey of the spreading segments located north of 19°S (DeMets *et al.* 1994b) provide spreading rates everywhere along the plate boundary. The magnetic data are complemented by multibeam and side-scan sonar data that constrain the plate motion directions, including partial or complete GLORIA side-scan sonar surveys of the transforms between 12°S and the Rodrigues triple junction (Parson *et al.* 1993), a SeaBeam survey of the multiple-strand Egeria transform fault at 20°S (Briais 1995) and Hydrosweep coverage of the

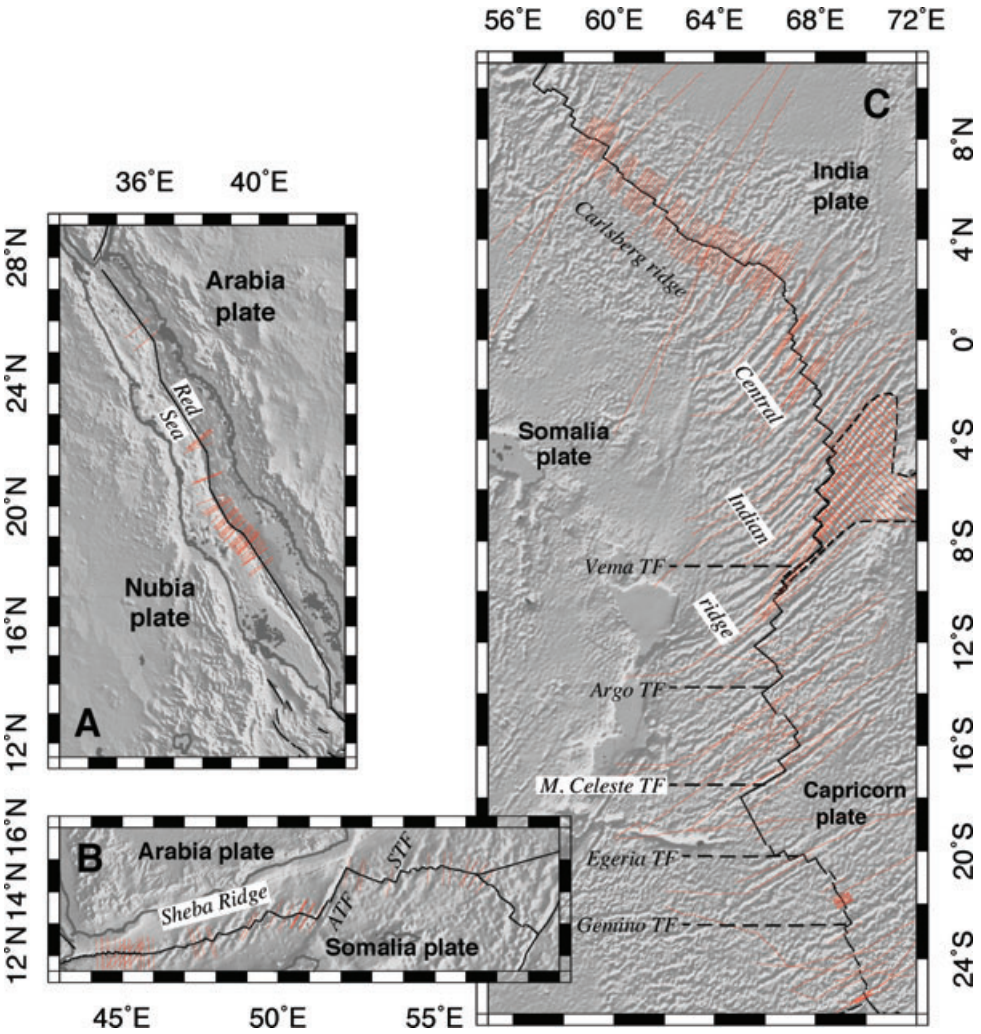

Figure 35. Ship and aeroplane tracks (red) of magnetic anomaly profiles used to determine MORVEL spreading rates in the Red Sea (a), in the Gulf of Aden and along the Sheba ridge (b) and along the Carlsberg and Central Indian ridges (c). ATF and STF in panel (b) represent the Alula-Fartak and Socotra transform faults, respectively.

240-km-long Vema transform fault and Fracture Zone O at 10°S (Drolia & DeMets 2005).

Magnetic surveys of the northern Central Indian and Carlsberg ridges are among the most extensive of any plate boundary (Merkouriev & DeMets 2006). Systematic Russian surveys in the 1980s crossed the ridge hundreds of times within a 1100-km-long portion of the plate boundary (Glebovsky *et al.* 1995; Merkouriev & Sotchevanova 2003)). From these crossings, we selected 94 magnetic profiles that sample spreading rates along 90 per cent of the plate boundary (Fig. 35c). Additional rates are estimated from 19 aeromagnetic and ship-board profiles (Table S1). Deformation associated with the diffuse India-Capricorn-Somalia triple junction extends from the Vema transform fault at 10°S to Fracture Zone H at 3°S (DeMets *et al.* 2005; Drolia & DeMets 2005) and thus precludes the use of any data from these latitudes.

The directions of India–Somalia motion along the plate boundary are known less well. We estimate one azimuth for the 330-km-long Owen transform fault at the northwest end of the Carlsberg Ridge from partial multibeam coverage of the northernmost 45 km of the transform fault (Fournier *et al.* 2008). We also estimate a second azimuth from conventional bathymetry for the remainder of the fault (Table S2). Published multibeam or side-scan sonar surveys are unavailable for the transform faults elsewhere along the plate boundary. We therefore use the slip directions of 22 transform fault earthquakes to constrain opening directions (Table S3), the only spreading centre for which we do so.

Motion between Arabia and Somalia across the Sheba Ridge in the Gulf of Aden is constrained by 51 spreading rates and the azimuths of several well-mapped transform faults (Fig. 35b). The 210-km-offset Alula-Fartak transform fault, which has the longest offset of any transform fault along this plate boundary, has been mapped with both GLORIA side-scan sonar (Tamsett & Searle 1990) and multibeam bathymetry (Leroy *et al.* 2004; d'Acremont *et al.* 2006). The nearby Socotra transform fault at 55°E has also been mapped with multibeam bathymetry (Leroy *et al.* 2004). Seafloor spreading rates are estimated from original data that we obtained for many older cruises described by Laughton *et al.* (1970) and Girdler *et al.* (1980) and for the more recent TADJOURADEN cruise (Dauteil *et al.* 2001), which mapped the plate boundary in detail from its termination at the Afar triple junction (42.6°E) to 46°E. Azimuths of three smaller offset transform faults between 48°E and 50°E are estimated from GLORIA side-scan sonar (Tamsett & Searle 1988).

The 1700-km-long Arabia–India plate boundary comprises a series of structures that accommodate slow, right-lateral slip motion

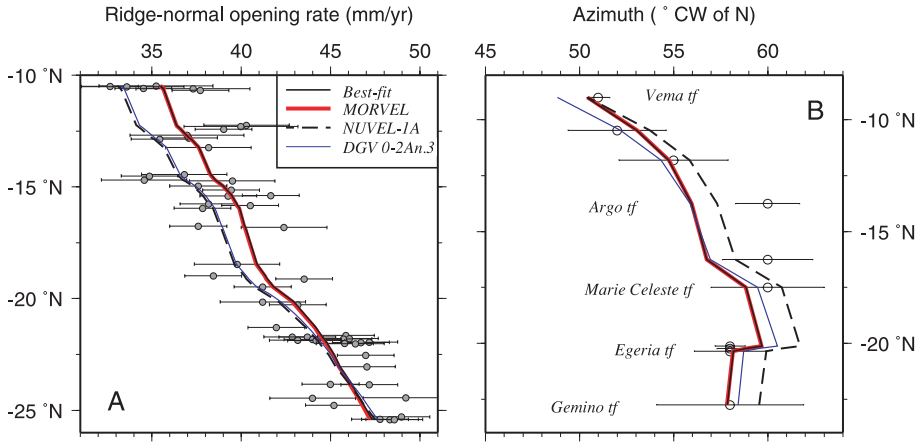

Figure 36. Capricorn–Somalia spreading rates (a) and transform fault azimuths (b) from the Central Indian Ridge and Capricorn-Somalia rate and azimuth estimates for the best fitting and MORVEL angular velocities, the DeMets *et al.* (2005) reconstruction of anomaly 2An.3 (DGV 0-2An.3), and the NUVEL-1A Australia–Africa angular velocity. Horizontal bars show 1σ uncertainties.

between these two plates. The best known of these structures is the Owen Fracture Zone, which extends 1100 km north–northeast from the Owen transform fault at the eastern end of the Sheba Ridge. Fournier *et al.* (2001, 2008) show that the seismically inactive, southernmost 300 km of the Owen Fracture Zone is bypassed by a zone of diffuse deformation that extends to the west from a deep extensional basin adjacent to the Owen Fracture Zone at 15.2°N to a diffuse triple junction with the Sheba Ridge at ≈57°E. Seafloor spreading along the Sheba Ridge between ≈57°E and the Owen transform fault thus does not record Arabia-Somalia motion (Fig. 35b). We therefore exclude magnetic profiles from this part of the Sheba Ridge.

The active portion of the Owen Fracture Zone north of 15.2°N accommodates right-lateral strike-slip motion to 22.5°N. Farther north, motion is accommodated by a series of connected, oceanic pull-apart basins that White (1984) refers to collectively as the Dalrymple Trough. We constrain the Arabia–India direction of motion with the azimuth of a well-imaged strike-slip fault that defines the southern limit of the actively slipping portion of the Owen Fracture Zone (Fournier *et al.* 2008), and three azimuths at locations farther north that we estimate from 1-min marine altimetry.

The 45 Red Sea magnetic profiles that are used to estimate Nubia–Arabia motion since anomaly 2A (Fig. 35a) are described in detail by Chu & Gordon (1998), who estimate seafloor spreading rates from profiles that were digitized from analogue records obtained from Roeser (1975), Girdler & Southren (1987), Izzeldin (1987) and digital profiles from the National Geophysical Data Center.

5.5.13 Capricorn–Somalia plate motion

The 56 spreading rates from the Capricorn–Somalia plate boundary increase from 35.5 ± 0.5 mm yr^{-1} near 10°S to 47 ± 0.5 mm yr^{-1} at the Rodrigues triple junction (Fig. 36a). Their dispersion is similar to that for other plate pairs for which rates are averaged since 0.78 Ma (Fig. 11b). The best-fitting and MORVEL angular velocities differ insignificantly.

The NUVEL-1A Africa–Australia pole is located six angular degrees closer to the plate boundary than are the new best-fitting and MORVEL poles (Fig. 13a), well outside the 95 per cent confidence region of the MORVEL pole. The difference between the MORVEL and NUVEL-1A angular velocities is significant ($p = 2 \times 10^{-8}$) and is manifested as misfits of NUVEL-1A to both the rates and directions of motion (Fig. 36). For example, NUVEL-1A gives directions south of 17°S that are systematically 2–3° anticlockwise from the best-fitting directions, including the strongly constrained azimuths of the multistrand Egeria transform fault. The NUVEL-1A angular velocity also misfits the gradient in the observed spreading rates (Fig. 36a), mainly north of 20°S where it underestimates the new rates by 1–2.5 mm yr^{-1}.

To test whether the difference from NUVEL-1A is caused by a difference between 3.16-Ma average rates and 0.78-Ma average rates, we estimated 3.16-Myr-average spreading rates from many of the same Central Indian Ridge magnetic profiles that we use in MORVEL and inverted those rates to estimate a 3.16-Myr-average angular velocity. The 0.78-Myr-average and new 3.16-Myr-average angular velocities give spreading rates that differ by no more than 0.5 mm yr^{-1} from each other when both are corrected for outward displacement. Thus any change since 3.16 Ma in opening rates across this plate boundary has been small, consistent with the prior results of DeMets *et al.* (2005) from reconstructions of young seafloor spreading magnetic anomalies along the Central Indian Ridge.

5.5.14 India–Somalia plate motion

The 113 India–Somalia seafloor spreading rates increase from 23 ± 0.5 mm yr^{-1} at the western end of the Carlsberg Ridge to 32 ± 0.5 mm yr^{-1} along the northern Central Indian Ridge (Fig. 37a). Their 0.8 mm yr^{-1} rms misfit (Fig. 11) is consistent with dispersions of 3.16-Myr-average rates from other slow spreading boundaries. The many new spreading rates and plate motion directions (Fig. 37b) impose strong constraints on the best-fitting angular velocity. Encouragingly, the best fitting pole (Fig. 13a) is located less than one angular degree from the 9.1-Ma-to-present pole (21.9°N, 30.7°E) estimated by Merkouriev & DeMets (2006) from reconstructions of ≈4000 crossings of magnetic anomalies and fracture zones younger than 9.1 Ma. The rates given by our new best-fitting estimates differ by only 0.5 mm yr^{-1} from those estimated by Merkouriev & DeMets (2006), within their 95 per cent confidence limits.

Although the India-Somalia transform fault azimuths and earthquake slip directions are well fit by the new best-fitting angular velocity (Fig. 37b), we are less confident about the accuracy of those directions given that only one of the transform azimuths that

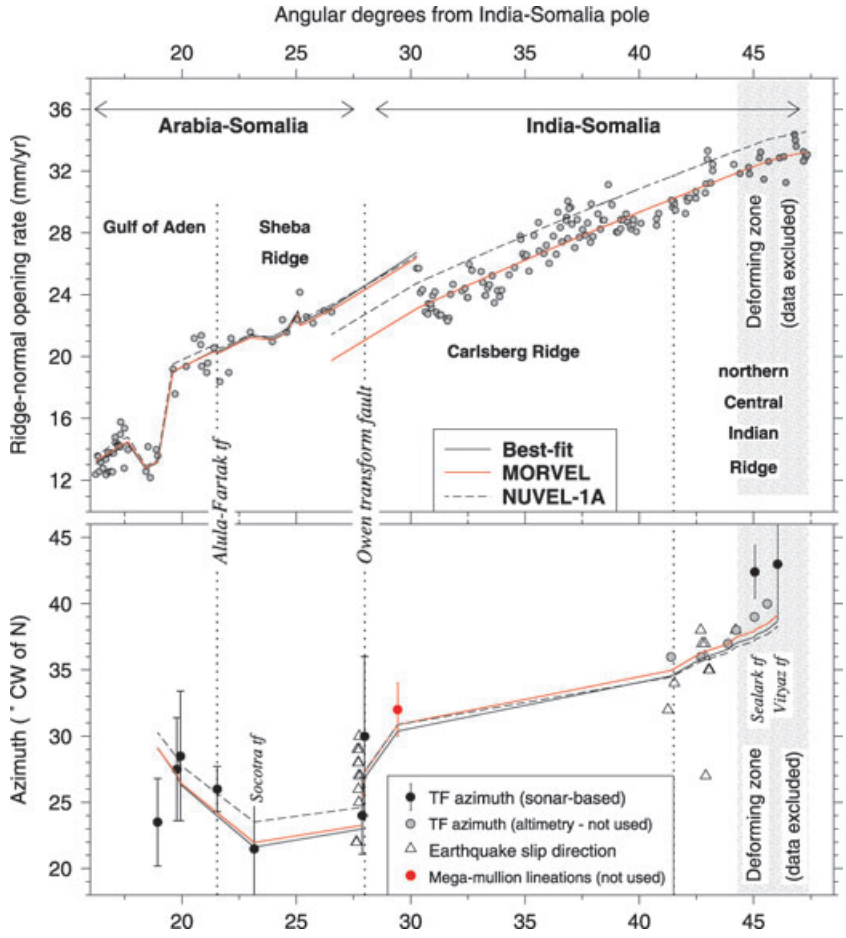

Figure 37. Upper panel: spreading rates from the Gulf of Aden, Sheba Ridge, Carlsberg Ridge and northern Central Indian Ridge, and rates calculated from Arabia–Somalia and India–Somalia angular velocities. Dashed lines show rates calculated from the NUVEL-1A Arabia–Africa and India–Africa angular velocities. Spreading rate uncertainties are omitted for clarity. Lower panel: transform fault azimuths and other slip direction indicators relative to directions determined with the same angular velocities. Azimuths determined from 1-minute satellite altimetry (Smith & Sandwell 1997) and lineations on a prominent megamullion at 9.1°N, 58.3°E (Murton and Le Blas, personal communication, 2007) are used as independent checks on MORVEL's accuracy, but are not used to derive MORVEL. Vertical bars for transform fault azimuths show their 1σ uncertainties. 'tf' is transform fault.

constrain the angular velocity is determined from multibeam or side-scan sonar data. We therefore also evaluated the directions calculated from the new best-fitting angular velocity using two independent estimates of the direction of plate motion, megamullion lineation azimuths and transform fault azimuths estimated from satellite altimetry (Fig. 37b). A reconnaissance multibeam survey of the Carlsberg Ridge (Murton & Le Blas, personal communication, 2007) mapped a prominent megamullion at 9.1°N, 58.3°E with a surface that has several well-defined lineations that record near-ridge tectonic displacement and may therefore approximate the plate extension direction. Encouragingly, our new best-fitting pole misfits by only 1.5° the N32°E ± 2° mean azimuth that we measured for these lineations. The azimuths of six transform faults that we estimated from satellite altimetry for the northern Central Indian Ridge (shaded circles in Fig. 37b) are also well fit, with an average difference of only 1° between the measured azimuths and estimated directions. These good fits give us some confidence in the directions we estimate from the earthquake slip directions. Multibeam surveys of the transform faults from the equatorial regions of the Carlsberg and northern Central Indian ridges are needed for a stronger test of our new estimates.

The spreading rates and directions estimated from the MORVEL India–Somalia angular velocity agree with those given by the best-fitting angular velocity to within 0.2 mm yr^{-1} and 1.5° (Fig. 37) everywhere along the plate boundary and are consistent with closure of the Arabia–India–Somalia plate circuit (Section 6.2). The megamullion lineation azimuth and six altimetrically determined transform fault azimuths are fit even better by the MORVEL angular velocity than by the best-fitting angular velocity (Fig. 37).

India–Somalia spreading rates estimated with NUVEL-1A are 1.8 mm yr^{-1} higher than the MORVEL rates (Figs 21a and 37a). Most of this difference is attributable to the 1.1 mm yr^{-1} downward adjustment that we make to the India–Somalia spreading rates to compensate for 3.5 km of outward displacement. Adjusting the NUVEL-1A estimate downward by a similar amount to compensate for outward displacement eliminates nearly all of the small difference (Fig. 21b).

5.5.15 *Arabia–India plate motion*

The MORVEL Arabia–India angular velocity predicts slip rates that average 3 ± 0.4 mm yr^{-1} (1σ) along the Owen Fracture Zone, the same as a recent GPS estimate of 3 mm yr^{-1} (Fournier *et al.* 2008) and consistent with the 2 ± 2 mm yr^{-1} rate predicted from the NUVEL-1 and NUVEL-1A data (Gordon & DeMets 1989;

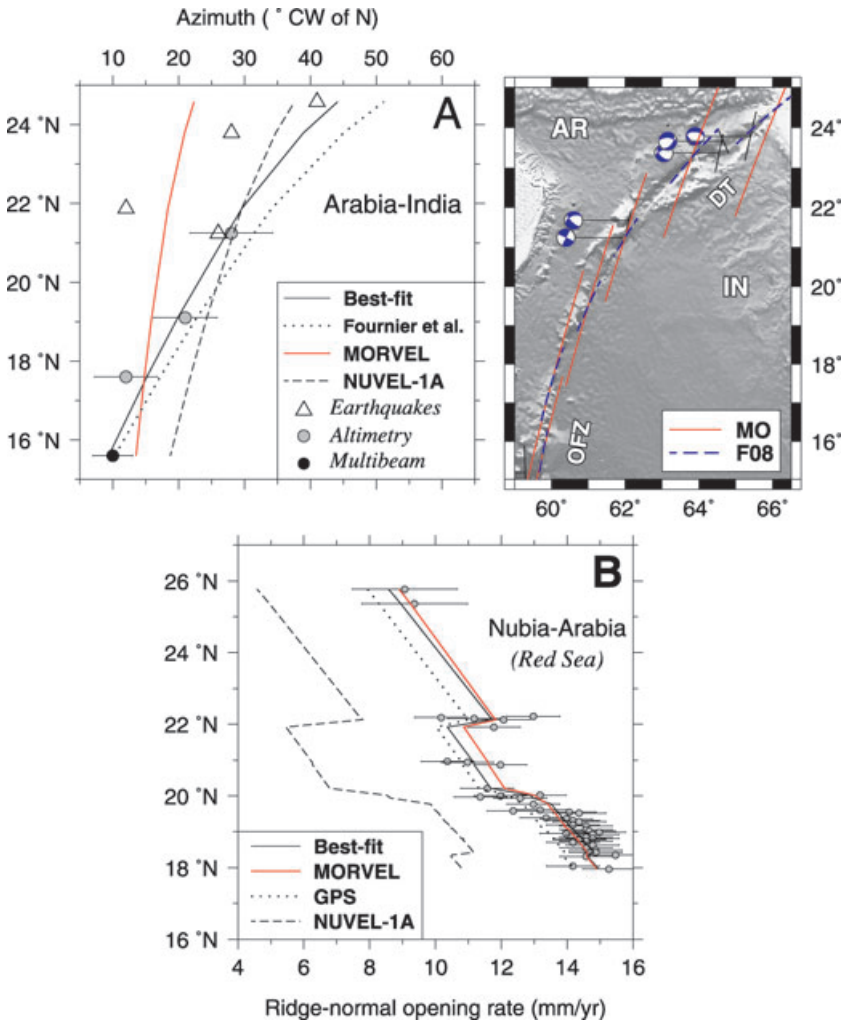

Figure 38. (a) Fault azimuths from the Owen Fracture Zone and directions determined with the best-fit, MORVEL, NUVEL-1A and Fournier *et al*. (2008) India–Arabia angular velocities. The earthquake slip directions are not used to derive MORVEL and thus constitute a useful independent check on its accuracy. Horizontal bars show the 1σ uncertainties. Map—Seafloor depths, 1976–2007 Global centroid moment tensor solutions along the Owen Fracture Zone (OFZ) and Dalrymple Trough (DT), and small circles around the MORVEL (MH) and Fournier *et al.* (2008) (F08) Arabia–India poles. Black lines show *T*-axis orientations for normal faulting earthquakes. (b) Spreading rates in the Red Sea and motion calculated from the best-fit, MORVEL and GPS-based Reilinger *et al.* (2006) Nubia–Arabia angular velocities and the NUVEL-1A Africa–Arabia angular velocity.

DeMets *et al.* 1990, 1994a). The rate of motion is thus well described.

The pole location and hence directions of motion along the boundary are less well known, as shown by the large uncertainties in the pole location (Fig. 13b). The closure-enforced MORVEL angular velocity indicates that motion consists of right-lateral slip parallel to the fracture zone at locations between 15.2°N and 18°N (map and panel A in Fig. 38), but becomes increasingly transtensional north of ≈18°N. Fournier *et al.* (2008) instead locate the Arabia–India pole more than 40 angular degrees closer to the plate boundary (Fig. 13b), in a location where it indicates that strike-slip predominates nearly everywhere along the boundary (Fig. 38). South of ≈19°N, the two poles give nearly identical motions (compare red and blue dashed small circles in Fig. 38). The directions estimated from the two poles however diverge increasingly along the boundary north of ≈19°N (Fig. 38a) and differ by nearly 30° at the northern end of the Dalrymple Trough.

Despite the large difference between the MORVEL and Fournier *et al.* (2008) Arabia–India pole locations, the elongate confidence ellipse for the MORVEL pole nearly encompasses the Fournier *et al*. estimate (Fig. 13b). The MORVEL kinematic data are thus permissive of Arabia–India motion dominated by strike-slip motion nearly everywhere along the Owen Fracture Zone and Dalrymple Trough.

5.5.16 Arabia–Somalia plate motion in the Gulf of Aden

Spreading rates from the Sheba Ridge and Gulf of Aden increase rapidly from 12.8 ± 0.4 mm yr^{-1} in the western Gulf of Aden to 23 ± 0.4 mm yr^{-1} near the eastern end of the plate boundary (Fig. 37). The 51 rates and five transform fault azimuths give a well-determined best-fitting pole that includes the NUVEL-1A Africa–Arabia pole within its 95 per cent confidence limits (Fig. 13a). The rms misfit to the 51 spreading rates is 0.7 mm yr^{-1}, similar to other slow-spreading plate pairs (Fig. 11b).

The plate velocities estimated from the best-fitting and MORVEL Arabia–Somalia angular velocities differ by no more than 1 mm yr^{-1}

and 1.5° anywhere along the plate boundary (Fig. 37). Opening rates estimated with the MORVEL angular velocity and NUVEL-1A Arabia–Africa angular velocity (Fig. 37a) differ on average by only 0.3 mm yr^{-1} (Fig. 21).

5.5.17 Nubia–Arabia plate motion in the Red Sea

Spreading rates in the Red Sea decrease rapidly northward from 15 ± 0.5 mm yr^{-1} in the central Red Sea to only 9 ± 1 mm yr^{-1} in the northern Red Sea (Fig. 38b). The many spreading rates and their steep gradient strongly constrain the rate of angular opening and distance to the pole, constituting two of the three components of the best-fitting angular velocity, but only weakly constrain the azimuth to the pole from the Red Sea due to the absence of morphologic or seismic information about the current direction of plate motion (Fig. 12).

The MORVEL and best fitting estimates of Nubia–Arabia spreading rates (Fig. 38b) differ by less than 1 mm yr^{-1} everywhere along the plate boundary and also agree closely with spreading rates predicted from an angular velocity determined by Reilinger *et al.* (2006) from 33 Arabia plate GPS station velocities and 39 Nubia plate station velocities (Fig. 38b). For example, at 20.0°N, 38.5°E, along the axis of the Red Sea, the MORVEL Nubia–Arabia angular velocity gives motion of 13.2 ± 0.4 mm yr^{-1} towards N47°E ± 2.6°, only 0.7 mm yr^{-1} higher than and in the same direction as the 12.5 mm yr^{-1}, N47°E velocity predicted by Reilinger *et al.*'s GPS estimate. The consistency between the geological and GPS estimates indicates that Nubia–Arabia motion has remained constant for the past few Myr within the ≈±1 mm yr^{-1} data uncertainties.

5.6 Pacific Ocean basin

5.6.1 Data description

The magnetic and multibeam coverage of the Pacific basin spreading centres has improved greatly since NUVEL-1 (Figs 31 and 39). Along the 4000-km-long Chile Ridge (Fig. 39), where no multibeam and only sparse magnetic data were available for NUVEL-1, nearly continuous multibeam and magnetic coverage is now available for the plate boundary east of the Chile fracture zone (Fig. 39). The new Chile Ridge data include an extensive U.S.-Chilean aeromagnetic survey (Tebbens *et al.* 1997), a multibeam and magnetic survey

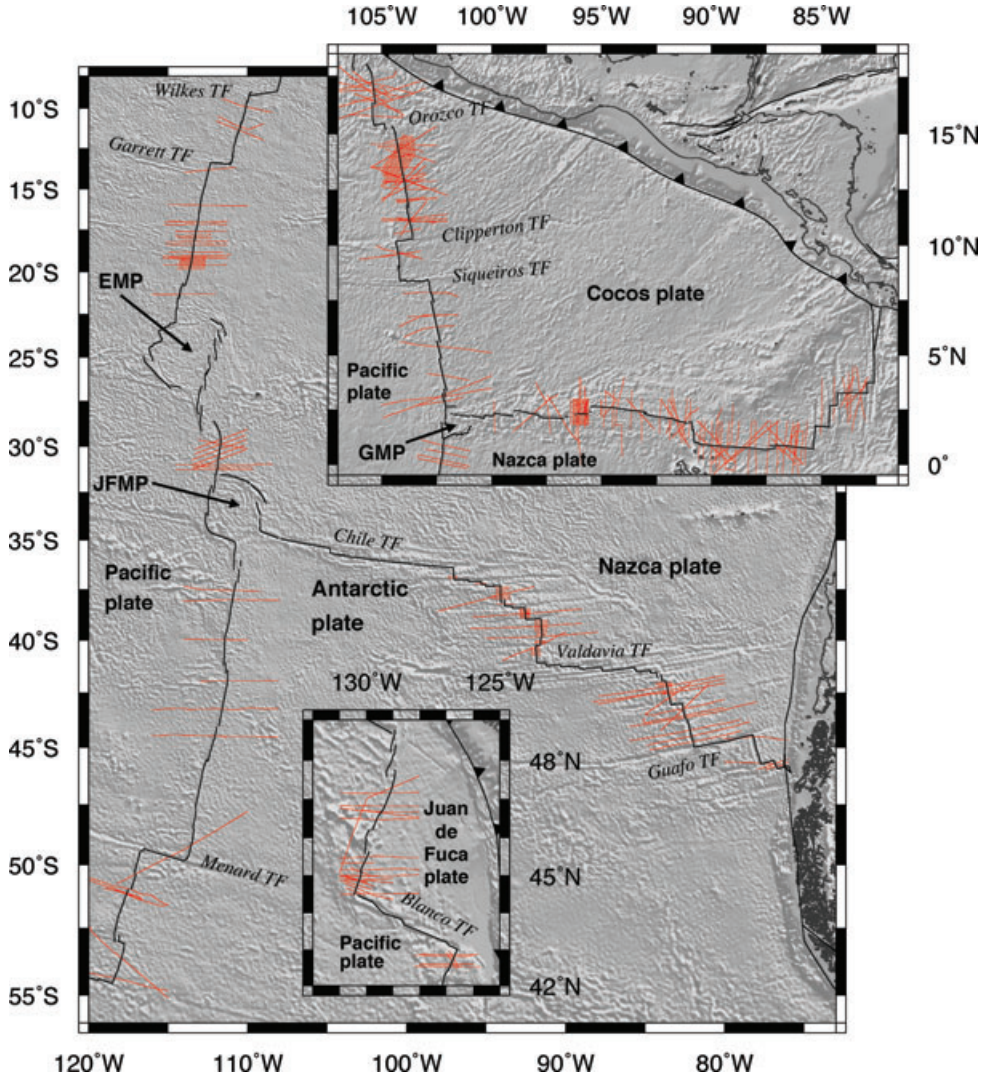

Figure 39. Ship and aeroplane tracks (red) of magnetic anomaly profiles used to determine MORVEL spreading rates along the boundaries of the Nazca, Cocos, Antarctic and Juan de Fuca plates in the eastern Pacific basin. 'EMP', 'GMP' and 'JFMP' designate the Easter, Galapagos and Juan Fernandez microplates.

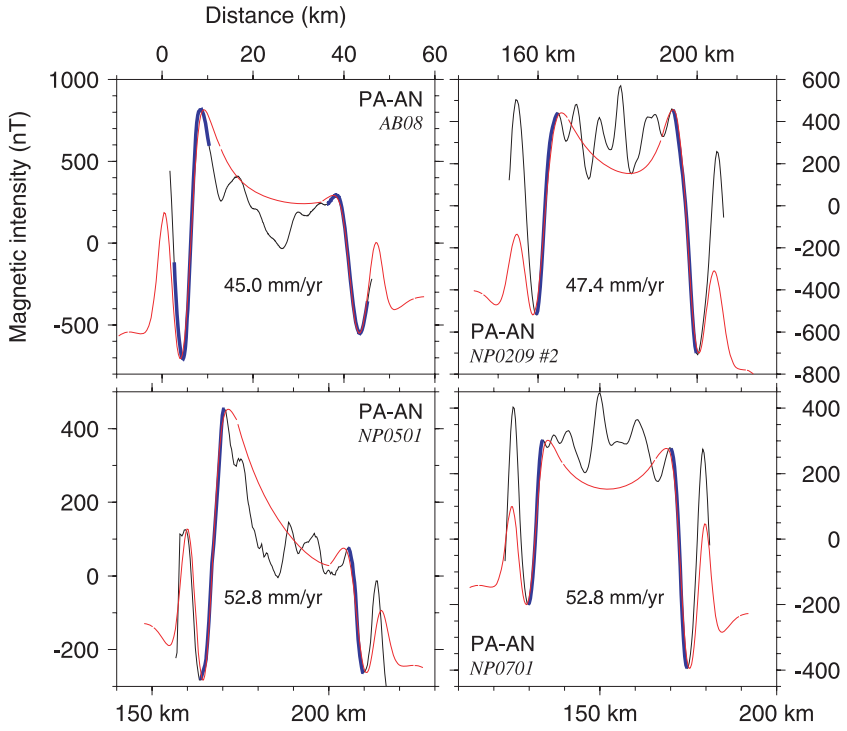

Figure 40. Cross-correlated fits of the Brunhes-Matuyama reversal for ridge-normal magnetic profiles from the sparsely surveyed Pacific–Antarctic rise west of 180°E. Also see profile NP0209 #1 from Fig. 9. Black and blue lines show the observed profiles and red curves show the best-fitting synthetic magnetic profiles. The part of each observed profile that is cross-correlated with the synthetic profile is coloured blue. Profiles designated with the 'NP' identifier are unpublished transit tracks from the RV *Nathaniel Palmer* (S. Cande, personal communication, 2007).

of the ridge between 97°W and 83.5°W (Karsten *et al.* 1999), a partial multibeam survey of the western end of the Chile transform fault (Kleinrock & Bird 1994), and a Sea Beam and GLORIA side-scan sonar survey of the plate boundary between 82°W and the Peru–Chile trench (Tebbens *et al.* 1990; Lothian 1995). From these data, we estimated 60 spreading rates and 21 multibeam-constrained transform fault azimuths (Tables S1 and S2), many more than the four isolated magnetic profiles and eight sparsely surveyed transform faults in NUVEL-1. Of the NUVEL-1 data from this plate boundary, only four azimuths are retained, all determined from single-beam sonar measurements of the Chile transform fault (Anderson-Fontana *et al.* 1987).

Important new data are also available for the 8950-km-long Pacific–Antarctic rise, which consists of 5830 km of spreading segments and 3120 km of transform faults or other higher-order axial discontinuities. Along the geographically remote southwestern half of the plate boundary (Fig. 31a), a dense multibeam and magnetic survey of the Pitman fracture zone (Cande *et al.* 1995) and multibeam and magnetic data from an extensive survey of the plate boundary between 175°W and 142°W (Ondreas *et al.* 2001) greatly increase the number and quality of the available data where it was sparse before. We also determined five spreading rates from isolated magnetic profiles of the sparsely surveyed ridge axis between the Macquarie triple junction and 180°E, four from transit tracks of the R/V *Nathaniel B. Palmer* (shown in Figs 9 and 40) and one from an isolated magnetic profile (AB08 in Fig. 40) collected during an Italian cruise (Lodolo & Coren 1997).

Nearly continuous multibeam coverage of the Pacific-Antarctic Rise north of the Udintsev transform fault (55°S) strongly constrains the azimuths of the Tharp, Heezen, Raitt and Menard transform faults (Lonsdale 1994). For these transform faults, we compared azimuths that we determined from multibeam grids from the Marine Geoscience Data System (http://www.marine-geo.org) with azimuths estimated by Lonsdale (1994). Encouragingly, the two agree within their uncertainties. Azimuths from the long-offset Udintsev transform fault are excluded from our analysis in light of evidence described by Lonsdale (1994) for a tectonic bias in the directions determined for that fault.

The Pacific–Nazca plate boundary extends more than 4000 km from the Galapagos triple junction to the Juan Fernandez triple junction (Fig. 39). All 3825 km of spreading segments and 640 km of transform fault offsets that constitute the plate boundary have been surveyed with one or both of GLORIA side-scan sonar (Searle 1983) and Sea Beam (Lonsdale 1989; Goff *et al.* 1993). Based on Sea Beam surveys of the transform faults between 20°S and the Galapagos triple junction at ≈1°N, Lonsdale (1989) suggests that the last measurable change (>≈5°) in the relative plate motion direction occurred between ≈6 and ≈3 Ma. Searle (1983) similarly concludes that the direction of plate motion has not changed by more than two degrees since 1 Ma.

Magnetic anomalies along the Pacific–Nazca plate boundary are well mapped everywhere except between ≈9.5°S and the equator (Fig. 39), where the anomaly amplitudes are low and the anomaly sequence is difficult to correlate due to the ≈N–S ridge orientation and its proximity to the magnetic equator. Four spreading rates we determined from shipboard profiles north of the equator (Lonsdale 1988) improve the constraints on the spreading-rate gradient and thus reduce the pole location uncertainties. Near the southern end of the plate boundary (26°S–32°S), Korenaga & Hey (1996) describe a dense multibeam, side-scan sonar and magnetic survey of the rise crest between the Easter and Juan Fernandez microplates, from which we determine well-constrained spreading rates.

The well-surveyed Pacific–Cocos plate boundary extends 2000 km from the Galapagos triple junction to the Manzanillo spreading

segment (Fig. 39). Multibeam and magnetic surveys of the 1925 km of rise segments and 280 km of transform offsets that constitute the plate boundary are nearly complete. A synthesis of the spreading centre morphology from 8°N to 18°N based on a compilation of Sea Beam and SeaMARC II data (Macdonald *et al.* 1992) and detailed descriptions of multibeam data from this part of the ridge (Gallo *et al.* 1986; Madsen *et al.* 1986; Fornari *et al.* 1989; Pockalny 1997) give well-determined azimuths for the Orozco, Clipperton and Siquieros transform faults (Table S2). Additional studies of the abundant magnetic data describe their implications for the recent evolution of seafloor spreading along this plate boundary (Perram & Macdonald 1990; Carbotte & Macdonald 1992; Macdonald *et al.* 1992; Madsen *et al.* 1992). Together, the magnetic and multibeam data indicate that a 3–6° anticlockwise rotation of the Pacific–Cocos plate spreading direction has occurred since 0.4–0.5 Ma, possibly continuing to the present. Well-mapped intratransform spreading segments that are found along the left-stepping Siquieros and Orozco transform faults and prominent median ridges along the right-stepping Clipperton transform fault (Pockalny 1997) are consistent with this rotation.

The Cocos–Nazca plate boundary, which connects the Galapagos triple junction to the Middle America trench (Fig. 39), consists of 2080 km of spreading segments and 880 km of transform faults. West of 85°W, where the plate boundary consists almost entirely of spreading segments, multibeam sonar coverage is complete (Searle 1989; Canales *et al.* 1997; Sinton *et al.* 2003). In contrast, multibeam coverage is sparse east of 85°W, where the long-offset Inca, Ecuador and Panama transform faults dominate the plate boundary. We estimate the azimuth of the 120-km-long Inca transform fault from partial multibeam coverage (from the Marine Geoscience Data System) and conventional bathymetric measurements of the northern half of the transform fault. We estimate the azimuth of the 160-km-long southern segment of the Panama transform fault from conventional bathymetry that we compiled from National Geophysical Data Center cruises (Table S2).

Good magnetic coverage of the Cocos–Nazca plate boundary exists at all locations east of 97°W (Fig. 39). In the sparsely surveyed region from 101.5°W to 97°W, Hey *et al.* (1977) and Searle (1989) show magnetic profiles from the Bartlett and De Steiguer cruises; however, the digital data for these two cruises were lost during a relocation of the U.S. Naval Oceanographic Office data archives in 1976 and hence are not used here. Between 101.5°W and 102.1°W, the Galapagos rise spreading rates record motion between the Cocos plate and Galapagos microplate (Lonsdale 1988; Klein *et al.* 2005) and are thus not used here.

The well surveyed, 500-km-long Pacific-Rivera rise forms the western boundary of the Rivera plate (Fig. 3), which subducts to the northeast beneath western Mexico at rates up to 35 mm yr^{-1}. Magnetic and multibeam data from the Pacific–Rivera rise record an acceleration and clockwise rotation of seafloor spreading since 3 Ma (DeMets & Stein 1990; Bandy 1992; DeMets & Traylen 2000), possibly continuing to the present (Bandy *et al.* 1998). The kinematic changes coincided with a reconfiguration from 3 to 2 Ma of the southern boundary of the Rivera plate (DeMets & Traylen 2000) and the detachment of the northern ∼25 per cent of the Rivera plate from the remainder of the plate interior (Lonsdale 1995). Evidence for the latter event includes multibeam and marine seismic observations of active fault zones east of the rise axis at 22°N and 22.5°N, where motion between the detached region and the Rivera plate interior appears to be accommodated. In addition, recent seafloor spreading rates from the Pacific–Rivera rise axis north of 22°N are too fast to record Pacific–Rivera plate motion and instead appear to record motion equal or nearly equal to that expected between the Pacific and North America plates (Lonsdale 1995; DeMets & Wilson 1997).

We estimate Pacific–Rivera plate motion from 24 magnetic profiles that cross the rise axis south of 22°N (Fig. 3) and two magnetic profiles from the Manzanillo spreading segment at the eastern end of the Rivera transform fault. Although DeMets & Wilson (1997) find that recent seafloor spreading across the Manzanillo segment is consistent with Pacific–Rivera plate motion, we assign both rates from this spreading segment larger uncertainties due to its proximity to the diffuse Rivera–Cocos plate boundary near the intersection of the eastern Rivera fracture zone and Middle America trench (Suarez *et al.* 1999). Directions of Rivera plate motion are determined from multibeam coverage of portions of the Rivera transform fault (Michaud *et al.* 1997) and are taken from Wilson & DeMets (1998).

The superb magnetic survey coverage of the Juan de Fuca and Gorda ridges is described and used by Wilson (1993) to show that changes in Juan de Fuca plate motion have occurred over the past few million years. Our estimate of Pacific–Juan de Fuca motion since 0.78 Ma is determined from 27 magnetic profiles that cross the Juan de Fuca ridge and northern end of the Gorda ridge (Fig. 39) and a single azimuth from the well-mapped Blanco transform fault (Embley & Wilson 1992). Along the Gorda ridge, we did not use any magnetic profiles from spreading segments located south of the northernmost spreading segment due to distributed deformation within the Gorda plate interior (Chaytor *et al.* 2004). We also exclude data from the Endeavour segment of the Juan de Fuca Ridge, where deformation occurs within the seafloor flanking this segment (Wilson 1993).

5.6.2 *Pacific–Antarctic plate motion*

Motion along the Pacific-Antarctic rise is estimated from 48 spreading rates and 10 transform fault azimuths well distributed along the plate boundary (Fig. 41). Spreading rates increase by more than a factor of two from 42 ± 1 mm yr^{-1} near the Macquarie triple junction to 94 ± 1 mm yr^{-1} near the Juan Fernandez triple junction. The 1.4 mm yr^{-1} rms misfit for the 48 spreading rates is lower than the 2.4 mm yr^{-1} rms misfit for the 21 NUVEL-1 Pacific–Antarctic rates despite the factor-of-four shorter averaging interval for the MORVEL rates (Fig. 11b). The new rates are thus more internally consistent than those used for NUVEL-1A.

The rms dispersion of the ten transform fault azimuths is only 0.8°, much smaller than the 5.9° rms misfit of the eight NUVEL-1 Pacific–Antarctic transform fault azimuths. The new and improved spreading rates and directions of plate motion strongly constrain our new estimates for the best-fitting pole (Fig. 13b) and rate of angular opening.

The spreading rates and directions estimated with the best-fitting and MORVEL angular velocities differ by only fractions of a degree and fractions of a millimetre per year everywhere along the plate boundary (Fig. 41). These small differences reflect the consistency with closure of the Pacific–Nazca–Antarctic plate circuit (Section 6.2).

The NUVEL-1A Pacific–Antarctic angular velocity differs significantly ($p = 5 \times 10^{-15}$) from the 0.78-Myr-average MORVEL angular velocity. NUVEL-1A gives rates that are, on average, 1.5 mm yr^{-1} higher than MORVEL (Fig. 21a), a difference that is reduced to 0.8 mm yr^{-1} if we also adjust downward the NUVEL-1A rates for outward displacement (Fig. 21b). The along-axis change in

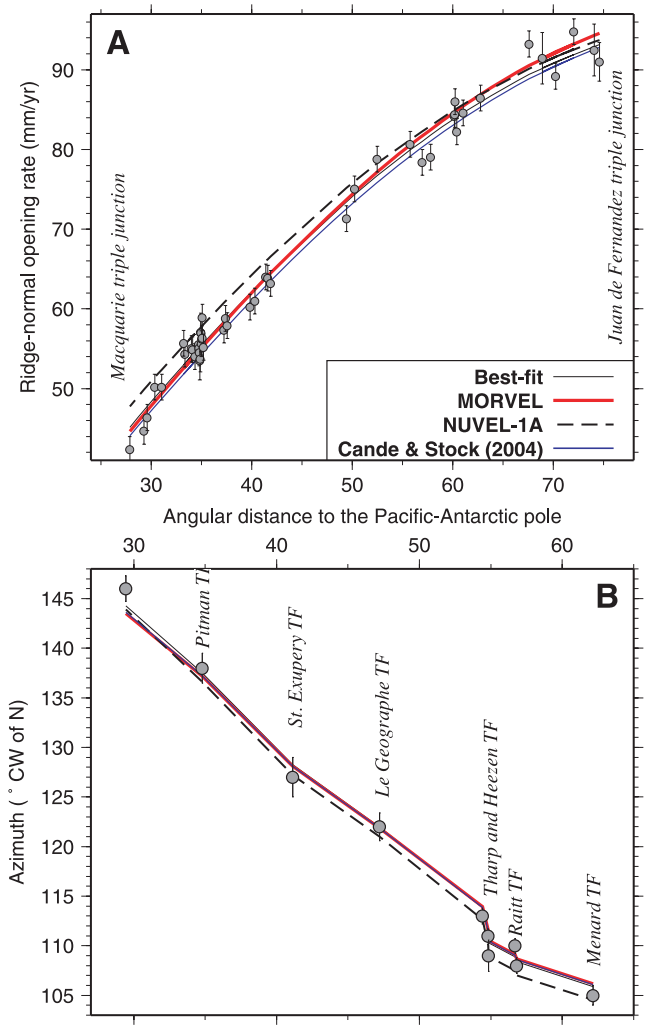

Figure 41. Pacific–Antarctic rise spreading rates (a) and transform fault azimuths (b) and rates and directions determined with angular velocities specified in the figure legend. Vertical bars show 1σ uncertainties. The best-fitting and MORVEL rate estimates are nearly identical and are thus difficult to distinguish in the figure. Directions and rates from Cande & Stock (2004) are determined with a 2.58-Myr-average angular velocity of 65.77°N, 78.91°W, 0.870° Myr^{-1}, which we derived by summing Cande & Stock Cande's Chron 2Ay finite rotation of 65.53°N, 79.48°W, 2.259° with a counter-rotation of 29.0°N, 110.1°W, −0.02° that compensates for 2 km of outward displacement everywhere along the plate boundary.

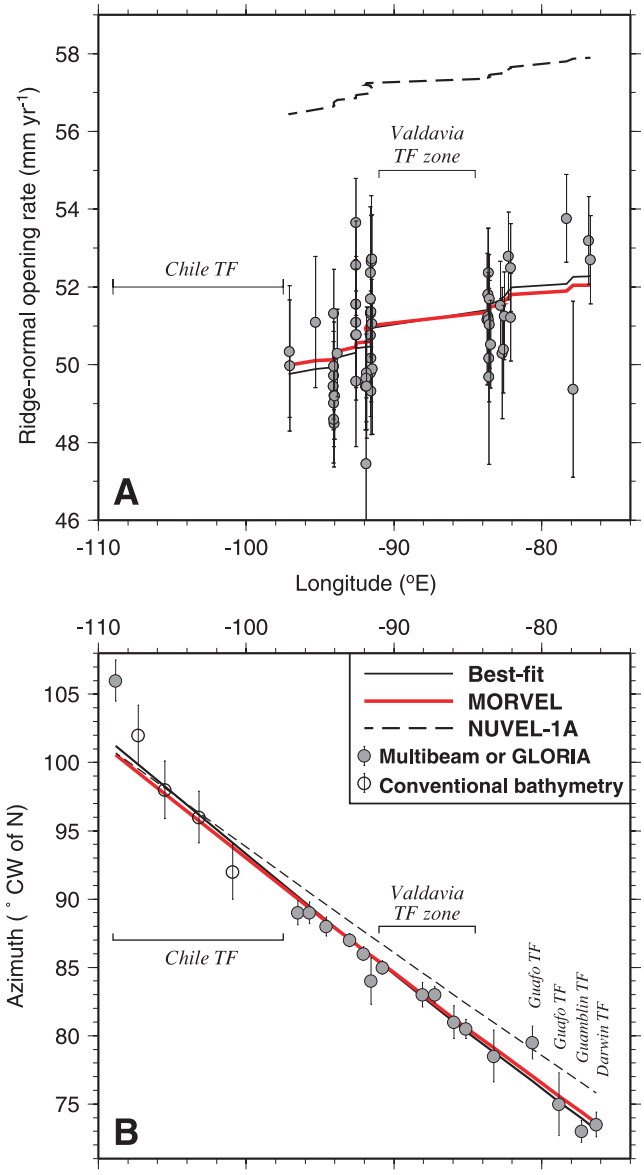

Figure 42. Nazca–Antarctic spreading rates (a) and transform fault azimuths (b) and rates and directions calculated from best-fitting, MORVEL, and NUVEL-1A Nazca–Antarctic angular velocities. Vertical bars show 1σ uncertainties. 'TF' is transform fault.

spreading rates estimated from MORVEL is also modestly steeper than for the NUVEL-1A pole, which lies several angular degrees farther from the plate boundary than do the MORVEL and best-fitting poles (Fig. 13). We attribute these differences to the fewer and lower quality data that were used to determine NUVEL-1A and the absence of any correction for outward displacement in NUVEL-1A.

5.6.3 Nazca–Antarctic plate motion

Along the transform-dominated Chile Ridge, transform fault azimuths change from S74°E ± 1° at the western end of the plate boundary to N73°E ± 0.5° at its eastern end (Fig. 39 and 42b). The 21 smoothly varying transform fault azimuths have a rms misfit of only 1.0°. East of the Chile transform fault, the azimuths calculated from NUVEL-1A (Fig. 42b) are systematically 1° to 3° clockwise of the many new azimuths, indicating that the NUVEL-1A estimate of Nazca–Antarctic plate motion is inaccurate. Unlike most spreading centres, where spreading rates contribute more information to the angular velocity determination than do transform faults, the 21 Chile Ridge transform fault azimuths contribute more information (56 per cent) to the best-fitting angular velocity than do the spreading rates (44 per cent), which exhibit only a weak gradient (Fig. 42a).

The Chile Ridge spreading rates, which average motion since 0.78 Ma, increase from 50 ± 1 mm yr^{-1} along the spreading segments west of the Valdavia transform fault to 52 ± 1 mm yr^{-1} along spreading segments east of the Valdavia transform fault (Fig. 42a). The new spreading rates are lower than the 57–58 mm yr^{-1} rates calculated from NUVEL-1A, which average motion since 3.16 Ma (Fig. 42a). This difference is larger than for any other plate pair (Figs 21a and b) and corroborates a well-documented slowdown

in spreading rates along this plate boundary (Morgan *et al.* 1969; Tebbens *et al.* 1997).

The rates and directions estimated from the best-fitting and MORVEL Nazca–Antarctic angular velocities differ negligibly everywhere along the plate boundary (Fig. 42), reflecting the consistency with closure of the Pacific–Nazca–Antarctic plate circuit (Section 6).

5.6.4 *Pacific–Nazca plate motion*

The fastest spreading on the planet occurs across the Pacific–Nazca plate boundary, across which motion is estimated from 42 spreading rates and the azimuths of 15 well-mapped fault segments from the six transform faults that offset this plate boundary (Fig. 43). The estimated spreading rates increase from $120 \pm 3\,\mathrm{mm\,yr^{-1}}$ near the Galapagos triple junction to $145 \pm 4\,\mathrm{mm\,yr^{-1}}$ near the Chile triple junction and have the highest rms misfit ($3.2\,\mathrm{mm\,yr^{-1}}$) of any plate pair (Fig. 11b). Although some of the dispersion is caused by difficulties in estimating reliable rates from the poorly defined, low-amplitude magnetic anomalies between the equator and ≈15°S, the dispersion is also high for spreading rates from magnetic profiles south of ≈15°S, where anomaly 1n is well defined and easily fit by our cross-correlation procedure (see for example, magnetic profile 03040059 in Fig. 9). The higher misfit may therefore be characteristic of fast spreading centres, as we also observe for rates from the fast spreading Pacific–Cocos plate boundary.

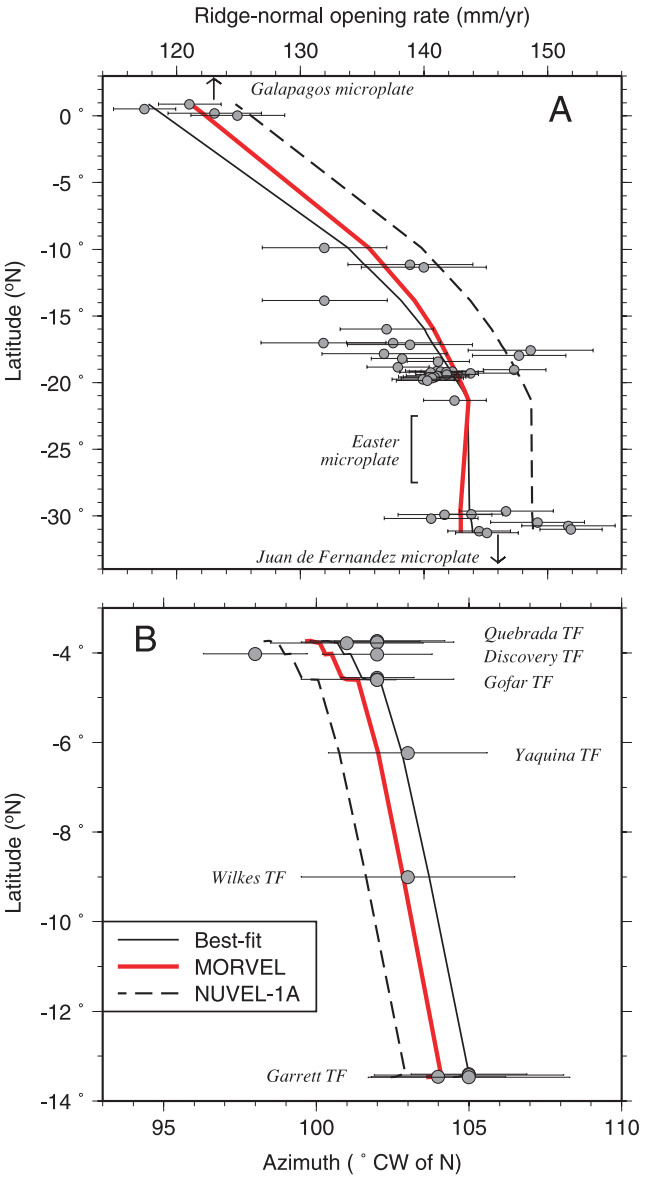

Figure 43. Nazca–Pacific spreading rates (a) and transform fault azimuths (b) and rates and directions calculated from best-fitting, MORVEL and NUVEL-1A angular velocities. Horizontal bars show 1σ uncertainties. 'TF' is transform fault.

The higher dispersion and hence larger uncertainties in the Pacific–Nazca spreading rates make the spreading rate gradient less certain along the plate boundary and therefore increase the uncertainties in the best-fitting pole location (Fig. 14). In contrast, the formal uncertainties in the closure-enforced MORVEL estimate are much smaller due to the additional information from closures of the Pacific–Nazca–Antarctic and Pacific–Cocos–Nazca plate circuits (Fig. 14).

The 0.78-Myr-average spreading rates and directions estimated from the MORVEL and best-fitting estimates for Pacific–Nazca motion agree well with each other (Fig. 43a), but are $5\,\mathrm{mm\,yr^{-1}}$ lower than the 3.16-Myr-average spreading rates calculated from NUVEL-1A (Fig. 43a). This difference is consistent with a slowdown in Pacific–Nazca motion since 3.16 Ma and is similar to the $\approx 6\,\mathrm{mm\,yr^{-1}}$ slowdown in Nazca–Antarctic spreading rates described above. Coupled with the evidence for constant Pacific–Antarctic motion since 3.16 Ma at the northern end of the plate boundary [Fig. 41(a) and Croon *et al.* (2008)], the available observations indicate that the eastward component of the absolute motion of the Nazca plate has slowed significantly since 3.16 Ma.

To better characterize the uncertainty in our estimate of Pacific–Nazca motion, we separately inverted the data from the Nazca–Antarctic–Pacific and Nazca–Cocos–Pacific plate circuits to determine independent estimates of Pacific–Nazca plate motion. The closure-enforced estimates of the Pacific–Nazca spreading rates from these two inversions (Fig. 44) are both $1–4\,\mathrm{mm\,yr^{-1}}$ higher than the best-fitting estimate at the northern end of the plate boundary (Fig. 44b) and are both $1–2\,\mathrm{mm\,yr^{-1}}$ lower than the best-fitting estimate at the southern end of the plate boundary. Similarly, the Pacific–Nazca directions of motion (not shown) estimated from these two three-plate circuits differ by only 0.5° and 0.2° at the two ends of the plate boundary. The independent information supplied by closures about these two three-plate circuits is thus consistent and suggests that the closure-enforced MORVEL estimate is more accurate than the best-fitting estimate. Some caution is however warranted as the Nazca–Pacific–Cocos circuit fails closure (Section 6.2.3).

5.6.5 *Cocos–Nazca plate motion*

The 88 Galapagos rise spreading rates decrease from $62\,\mathrm{mm\,yr^{-1}}$ at the eastern end of the plate boundary (Fig. 45a) to $48\,\mathrm{mm\,yr^{-1}}$ at 101.0°W–100.5°W, where the Cocos–Nazca–Galapagos triple junction terminates the Cocos–Nazca plate boundary (Lonsdale 1988, 1989). West of this triple junction, the rate of seafloor spreading between the Cocos plate and Galapagos microplate decreases from $44 \pm 2\,\mathrm{mm\,yr^{-1}}$ near 100.5°W to only $26 \pm 2\,\mathrm{mm\,yr^{-1}}$ at 101.6°W, typical of the rapid variations in plate velocities often observed along the boundaries of oceanic microplates.

The 0.78 Ma best-fitting Cocos–Nazca pole is located 19.4 angular degrees (2160 km) farther from the Galapagos spreading centre

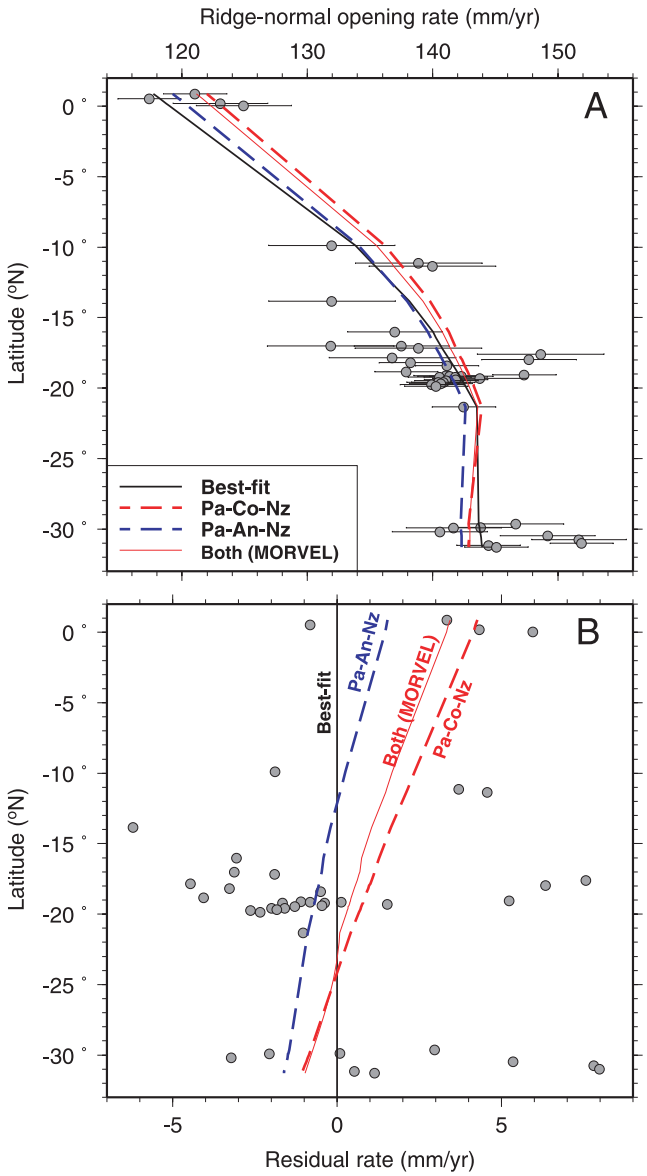

Figure 44. (a) Effect of circuit closures on fits to Nazca–Pacific spreading rates. Solid line shows rates calculated from the best-fitting Nazca–Pacific angular velocity. Dashed red and dashed blue lines show rates calculated from Nazca–Pacific angular velocities that were determined from inversions of all data from the Nazca–Pacific-Cocos and Nazca–Pacific–Antarctic three-plate circuits, respectively. Horizontal bars show 1σ uncertainties. (b) Observed rates and rates determined with the angular velocities from (a) with respect to rates determined with the best-fitting angular velocity.

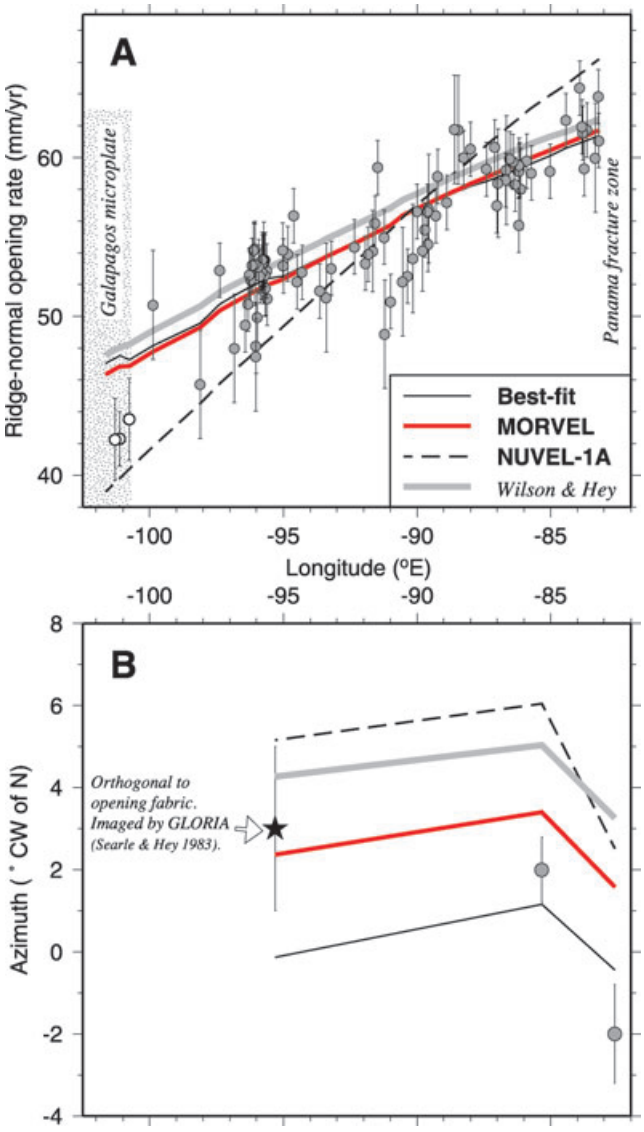

Figure 45. Cocos–Nazca spreading rates (a) and transform fault azimuths (b) and rates and directions calculated from the Cocos–Nazca angular velocities specified in the figure legend. Vertical bars show 1σ uncertainties. Rates shown by open circles are biased by Galapagos microplate motion and are not used to estimate Cocos–Nazca motion. Wilson & Hey angular velocity is from Wilson & Hey (1995).

than is the 3.16-Myr-average NUVEL-1A pole (Fig. 14), reflecting a change in the along-axis spreading-rate gradient since 3.16 Ma (Fig. 45a). The data thus require rapid westward migration of the pole from 3.16 to 0.78 Ma. Despite the large change in pole location, the average spreading rate along the plate boundary accelerated by only 1.5 $\pm$ 1.5 mm yr^{-1} during the same period (Fig. 21b).

Wilson & Hey (1995) also describe evidence for rapid westward migration of the pole of rotation after anomaly 3 (4 Ma) based on opening poles and angles reconstructed for seven magnetic reversals younger than anomaly 3. As is shown by Fig. 45(a), their best-fitting reconstruction of anomaly 1n (0.78 Ma) gives spreading rates that are only 1.1 mm yr^{-1} higher than estimated from our best-fitting angular velocity. Adjusting the Wilson & Hey spreading rates downward to correct for an assumed 2 km of outward displacement gives rates that are 1.5 mm yr^{-1} lower on average than the MORVEL estimate. The two independent estimates thus agree to the nearest 1–1.5 mm yr^{-1}.

The best-fitting and MORVEL poles are consistent within their combined 95 per cent confidence regions (Fig. 14), and the spreading rates estimated from the two angular velocities differ by no more than 0.4 mm yr^{-1} anywhere along the plate boundary (Fig. 45a). The directions estimated from the two angular velocities however differ systematically by 2° (Fig. 45b), a difference attributable to significant non-closure of the Cocos–Nazca–Pacific plate circuit (Section 6). The best-fitting and MORVEL estimates both fit the few available Cocos–Nazca directions better than does NUVEL-1A.

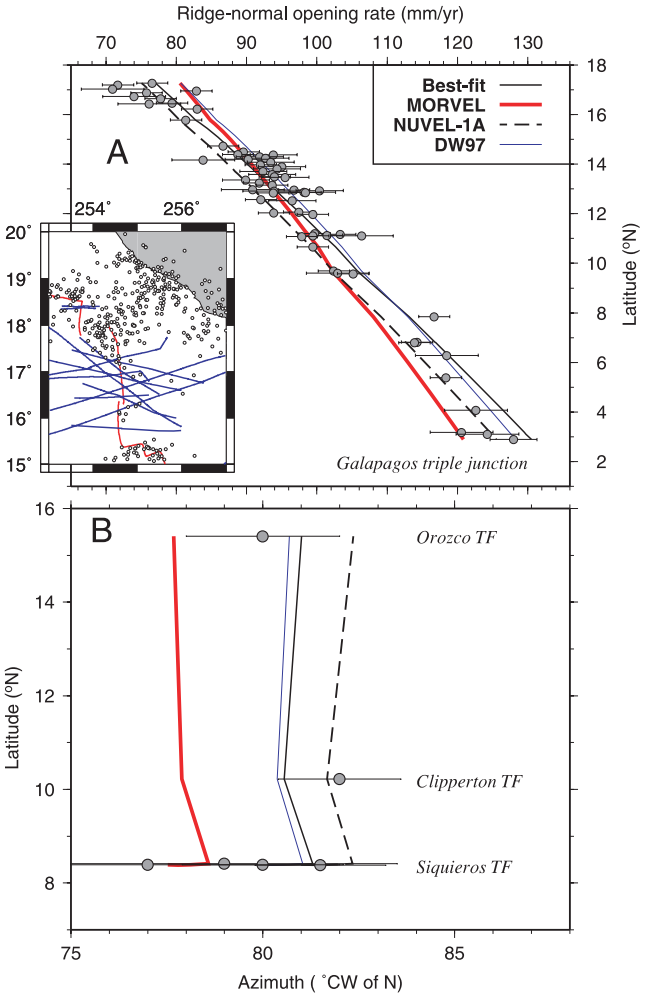

Figure 46. Pacific–Cocos spreading rates (a) and transform fault azimuths (b) and rates and directions calculated from Pacific–Cocos angular velocities listed in the figure legend. Horizontal bars show 1σ uncertainties. 'DW97' is DeMets & Wilson (1997). Map inset depicts tracks of magnetic profiles (blue), present plate boundary (red) and epicentres of shallow earthquakes from 1967 to 2006. 'TF' is transform fault.

5.6.6 Pacific–Cocos plate motion

The 68 spreading rates from the Pacific–Cocos plate boundary increase rapidly from 72 mm yr^{-1} at the northern end of the plate boundary to 128 mm yr^{-1} near the Galapagos triple junction, at the southern end of the plate boundary (Fig. 46). The Pacific–Cocos pole location is well determined due to the abundance of rates and their steep gradient (Fig. 14). Similar to the large rms misfit for the fast spreading Pacific–Nazca plate boundary, the 2.8 mm yr^{-1} rms misfit of the best-fitting Pacific–Cocos angular velocity is large relative to slower-spreading plate boundaries (Fig. 11b).

The rates estimated with our best-fitting angular velocity are 1–2 mm yr^{-1} lower at most locations (Fig. 46a) than are 0.78-Myr-average rates estimated by DeMets & Wilson (1997) from a reconstruction of crossings of anomaly 1n along this plate boundary. A downward adjustment of 2.6 mm yr^{-1} to the latter rates for an assumed 2 km of outward displacement improves the agreement between the two estimates to better than 1 mm yr^{-1} at most locations along the plate boundary.

Along the plate boundary north of ≈16.5°N, the spreading rates calculated from the best-fitting angular velocity are higher than the observed rates (Fig. 46a) and reach a maximum difference of 7 mm yr^{-1} for the two northernmost magnetic profiles, which cross the rise axis near 17.2°N (shown on the inset map in Fig. 46a). Similar misfits to the data north of ≈16.5°N are reported by DeMets *et al.* (1990) and DeMets & Wilson (1997). Fitting the spreading rates north and south of ≈16.5°N with separate angular velocities gives a least-squares misfit that is significantly smaller ($p = 0.006$) than that for the Cocos–Pacific best-fitting angular velocity. The rates north of ≈16.5°N are thus significantly lower than expected if they record Pacific–Cocos plate motion.

Some of the above misfit may be attributable to active deformation of the lithosphere on one or possibly both sides of the rise axis. West of the rise axis, many earthquakes occur between the overlapping rise segments at 18°N (inset to Fig. 46), presumably reflecting deformation that transfers motion between the overlapping rifts. These earthquakes extend southward to 17.1°N, thus indicating that not all the plate motion north of ≈17°N is concentrated along the rise axis. Deformation may also occur within the young oceanic lithosphere between the Middle America subduction zone and the rise axis. A diffuse band of earthquakes that extends southwest from the Middle America trench may intersect the East Pacific Rise as far south as 16°N (inset to Fig. 46). The seafloor north of ≈16°N therefore may move slowly relative to the Cocos plate interior, similar to the northern, detached region of the Rivera plate (Lonsdale 1995). The subduction of young, buoyant seafloor from the nearby East Pacific Rise along the trench north of ≈16.5°N may slow the rate of subduction there and thus cause deformation in the lithosphere.

The plate velocities estimated from the best-fitting and closure-enforced MORVEL angular velocities differ by 7 mm yr^{-1} at the southern end of the Pacific–Cocos rise (Fig. 46a) and by 2–3° along the entire plate boundary (Fig. 46b), the largest such discrepancies for any plate pair. Some possible causes for these differences are discussed in Section 6.2.

5.6.7 Pacific–Rivera plate motion and evidence for Rivera plate break up

The 26 Pacific–Rivera spreading rates increase rapidly from 51 ± 1 mm yr^{-1} at the northern end of the plate boundary to 73 ± 3 mm yr^{-1} along the Manzanillo spreading segment (Figs 47b and 3). The steep gradient in these rates constrains the best-fitting pole to lie just northeast of the plate boundary (Fig. 14). No plate circuit closures influence our estimate of the Pacific–Rivera plate angular velocity, hence the best-fitting and MORVEL estimates are identical.

Our new Pacific–Rivera angular velocity is similar to that estimated by DeMets & Wilson (1997) from crossings of anomaly 1n and selected crossings of the Rivera fracture zone. The two pole locations differ by only 0.3 angular degrees and hence indicate nearly identical spreading rate gradients and directions of motion. Although the spreading rates given by our new angular velocity are 2.1 mm yr^{-1} lower than are given by the DeMets & Wilson estimates (Fig. 47b), the difference is reduced to only 0.5 mm yr^{-1} if we correct the DeMets & Wilson rates for the effect of outward displacement.

Magnetic profiles that cross the rise axis north of 22.0°N are best fit by spreading rates that range from 47 to 49 mm yr^{-1} (Fig. 47b), 1–8 mm yr^{-1} higher than given by the Pacific–Rivera best-fitting angular velocity, but nearly the same as spreading rates from the Gulf Rise in the southern Gulf of California (Fig. 3), where spreading occurs between the Baja California peninsula and North America

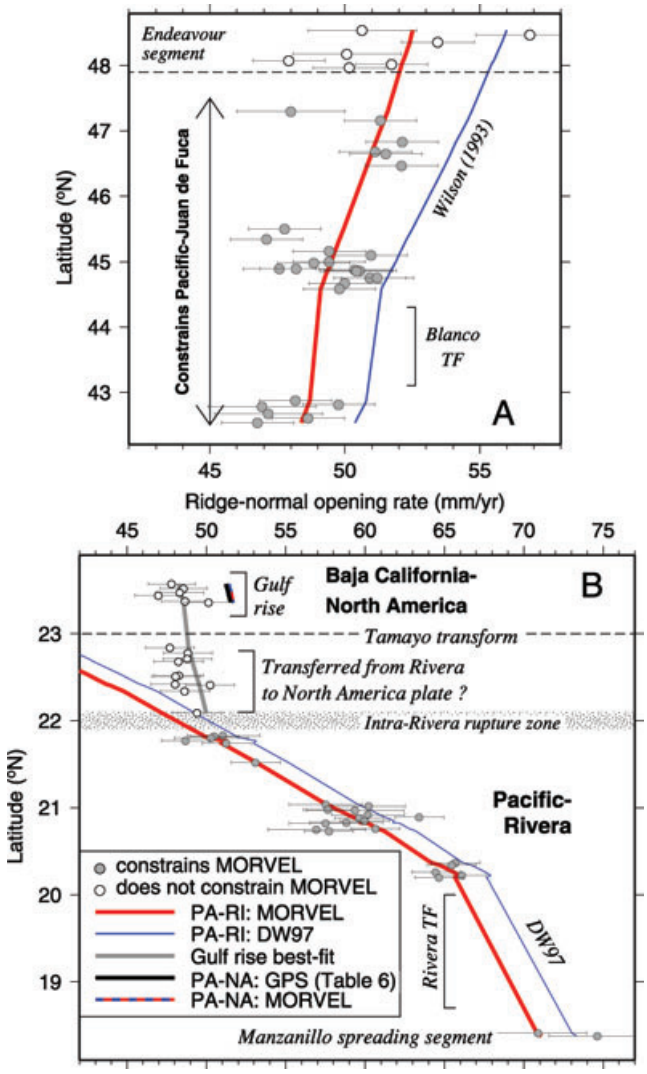

Figure 47. (a) Juan de Fuca and northern Gorda rise spreading rates and rates calculated from the Juan de Fuca–Pacific MORVEL (red) and Wilson (1993) (blue) 0.78-Myr-average angular velocities. Endeavour segment rates are not used to constrain MORVEL. Horizontal bars show 1σ uncertainties. 'TF' is transform fault. (b) Pacific–Rivera and Gulf of California 0.78-Myr-average spreading rates and rate estimates from Pacific–Rivera and Pacific–North America angular velocities specified in the figure legend. 'DW97' indicates rates determined with the DeMets & Wilson (1997) 0.78-Myr-average Pacific–Rivera plate angular velocity. The best-fitting and MORVEL angular velocities are identical for the Juan de Fuca–Pacific and Rivera–Pacific plate pairs due to the absence of circuit closure constraints for both plate pairs.

plate. The change in the spreading rate gradient at 22.0°N supports evidence described by Lonsdale (1995) and DeMets & Wilson (1997) that the northern area of the Rivera plate has detached from the plate interior and now moves with the North America plate or slowly relative to it.

5.6.8 Pacific–Juan de Fuca plate motion

The 27 spreading rates from the Pacific–Juan de Fuca plate boundary increase from 48 ± 1 mm yr^{-1} along the northern Gorda ridge to 51.5 ± 1 mm yr^{-1} along the northern Juan de Fuca ridge (Fig. 47a). The large uncertainties in the pole location (Fig. 14) reflect the short angular distance spanned by the data and the imprecisely defined spreading rate gradient. No circuit closures influence our estimate of the angular velocity for this plate pair, thus the best-fitting and MORVEL estimates are the same.

Spreading rates estimated from our new angular velocity (Fig. 47a) are lower by 2–3 mm yr^{-1} than rates estimated from the anomaly 1n rotation of Wilson (1993), consistent with the 2.6 mm yr^{-1} downward correction that we apply to our 0.78-Myr-average spreading rates to compensate for outward displacement. Applying the same correction to the rates calculated from Wilson's (1993) angular velocity reduces the difference to less than 0.5 mm yr^{-1}.

5.7 The western Pacific basin and eastern Asia

Through the use of GPS data, the Amur, Sundaland and Yangtze continental plates of eastern Asia, and the Philippine Sea plate, which shares convergent boundaries with these and other plates in the region, were incorporated into MORVEL. Our description of the tectonic implications of these angular velocities is limited in scope and focuses mainly on areas where subduction occurs or the plate boundaries are narrow enough to compare earthquake slip directions from the plate boundary faults with the predicted directions of plate motion.

5.7.1 The Sundaland plate and convergence along the Java-Sumatra trench

The India and Australia plates, as well as their intervening diffuse oceanic plate boundary, subduct beneath southeastern Asia along the Java–Sumatra trench (Fig. 48), where oblique subduction of these two plates is accompanied by varying degrees of trench-parallel forearc translation (McCaffrey 1991). Using velocities measured between 1994 and 2004 at more than 100 GPS sites in southeastern Asia, Simons *et al.* (2007) show that regions located far inland from the Java-Sumatra trench move as part of a coherent Sundaland plate. From the velocities of 28 GPS stations within the Sundaland plate interior and additional GPS sites on adjacent plates, they estimate angular velocities for Sundaland relative to its neighboring plates. Their work sets the stage for incorporating this plate into MORVEL.

Fig. 49 shows the motions of all 28 GPS stations that were used by Simons *et al.* (2007) to estimate Sundaland plate motion. Relative to the interior of the Sundaland plate, all nine stations that are located within several hundred km of the Sumatra trench move northeastward away from the trench at rates of 1.5–3 mm yr^{-1} (blue arrows in Fig. 49). Their motions are consistent with elastic shortening that should occur inland from a strongly locked subduction interface. We therefore do not use any of these nine velocities to estimate Sundaland plate motion. We also excluded a tenth station on the island of Java, which is located close enough to the trench to be affected by interseismic and post-seismic effects of plate boundary earthquakes.

Fig. 49 shows the tangential and radial velocity components for the 18 remaining Sundaland sites, all located far from the Java-Sumatra subduction zone. The weighted rms misfits for the north and east velocity components of these 18 stations are 0.7 and 1.4 mm yr^{-1}, respectively, typical for networks dominated by survey-mode GPS measurements. The motions of these 18 stations relative to the plate interior (shown by the red arrows in Fig. 49) exhibit no obvious pattern, consistent with the hypothesis that they

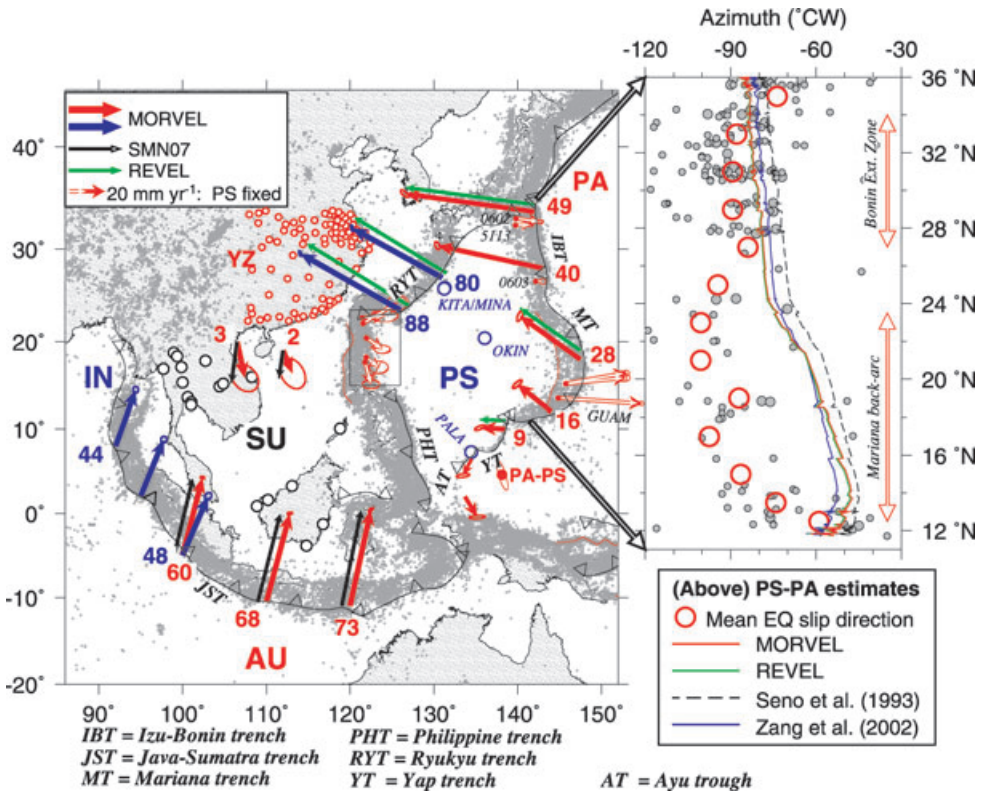

Figure 48. Left-hand panel: motion estimates across boundaries of the Sundaland (SU) and Philippine Sea (PS) plates. Estimates for Australia and India plate motion relative to Sundaland along the Java-Sumatra trench (JST) are shown by red (AU) and blue (IN) arrows for MORVEL and black arrows (AU only) for Simons *et al.* (2007) (SMN07). Red and black arrows along the northern boundary of Sundaland show MORVEL and SMN07 estimates for Yangtze plate motion relative to Sundaland. Red and green arrows along the Izu-Bonin (IBT), Mariana (MT) and Yap (YT) trenches and the Ayu Trough (AT) show MORVEL and REVEL (Sella *et al.* 2002) estimates, respectively, of Pacific plate motion relative to the Philippine Sea plate. Blue and green arrows along the Ryukyu trench (RYT) show MORVEL and REVEL estimates for Philippine plate motion relative to the Yangtze plate. Velocity arrows are scaled differently by plate boundary for clarity. Estimated rates in mm yr^{-1} accompany each velocity arrow. Uncertainty ellipses are 2-D, 95 per cent. All open red arrows show motions of GPS stations near the Philippine Sea plate boundaries relative to the Philippine Sea plate and are scaled as shown in the legend at the upper left. Open arrows in the rectangle at the centre of the map include three sites near the intersection of the Ryukyu and Philippine trenches that were used by Zang *et al.* (2002) to estimate Philippine Sea plate motion. Open circles show locations of the Philippine Sea, Yangtze and Sundaland GPS stations used to estimate the motions of these plates in MORVEL. 'PA-PS' indicates location of the MORVEL Pacific-Philippine Sea pole and 2-D 95 per cent confidence ellipse. Right-hand panel: individual and moment-weighted, mean horizontal slip directions for shallow thrust earthquakes from the Izu-Bonin and Mariana trenches and directions calculated from Pacific–Philippine Sea plate angular velocities specified in the legend beneath the figure. Sixteen of the individual earthquake directions are from table 1 of Seno *et al.* (1993) and the other 224 from 1976 to 2008 Global centroid moment-tensor solutions. Mean directions are for 2° latitudinal bins. Earthquake directions are rotated systematically anticlockwise from the predicted directions due to slow to rapid backarc extension along the Bonin extension zone and Mariana backarc spreading centre.

are located in undeforming areas of the plate interior. We therefore use these 18 station velocities to define Sundaland plate motion.

We transformed the 18 station velocities from ITRF2000 to an Australia plate reference frame with the angular velocity that best fits the velocities of 19 Australia plate GPS stations relative to ITRF2000 (Table S5 and Figs 6c and d). The 19 Australia plate station velocities have respective north and east velocity component rms misfits of 0.54 and 0.60 mm yr^{-1} and impose strong constraints on the plate angular velocity. Our best-fitting Australia plate angular velocity (Table 4) gives motions at Australian sites that differ by less than 0.5 mm yr^{-1} from those estimated by Simons *et al.* (2007) from their independent analysis of Australia plate GPS station velocities.

The 18 transformed Sundaland plate station velocities (Table S4) were inverted with the other MORVEL data to estimate the best-fitting Australia-Sundaland angular velocity and via circuit closures the angular velocities for the Sundaland plate relative to all the other plates. The Australia–Sundaland angular velocity predicts convergence velocities that decrease from 73 ± 0.8 mm yr^{-1} (1σ) along the Java trench to 60 ± 0.4 mm yr^{-1} along the southern Sumatra trench (red arrows in Fig. 48). The predicted velocities differ by less than 1 mm yr^{-1} and 1° from the motions predicted at the same locations (black arrows in Fig. 48) by the Australia–Sundaland angular velocity of Simons *et al.* (2007).

Unlike the Australia–Sundaland angular velocity, which is estimated entirely from GPS observations, the motions of the India and Sundaland plates are linked to each other via an extended plate circuit through several seafloor spreading centres in the Indian Ocean (Fig. 2). The India–Sundaland angular velocity predicts north–northeast-directed convergence at rates that decrease slowly from 48 ± 1.2 mm yr^{-1} along the southern Sumatra trench to 44 ± 1.0 mm yr^{-1} near the northern end of the Sumatra trench (Fig. 48). The 12 mm yr^{-1} difference in the Australia–Sundaland and India-Sundaland convergence rates at the southern end of the Sumatra subduction zone reflects relative motion between the India and Australia plates across their broad, oceanic plate boundary west

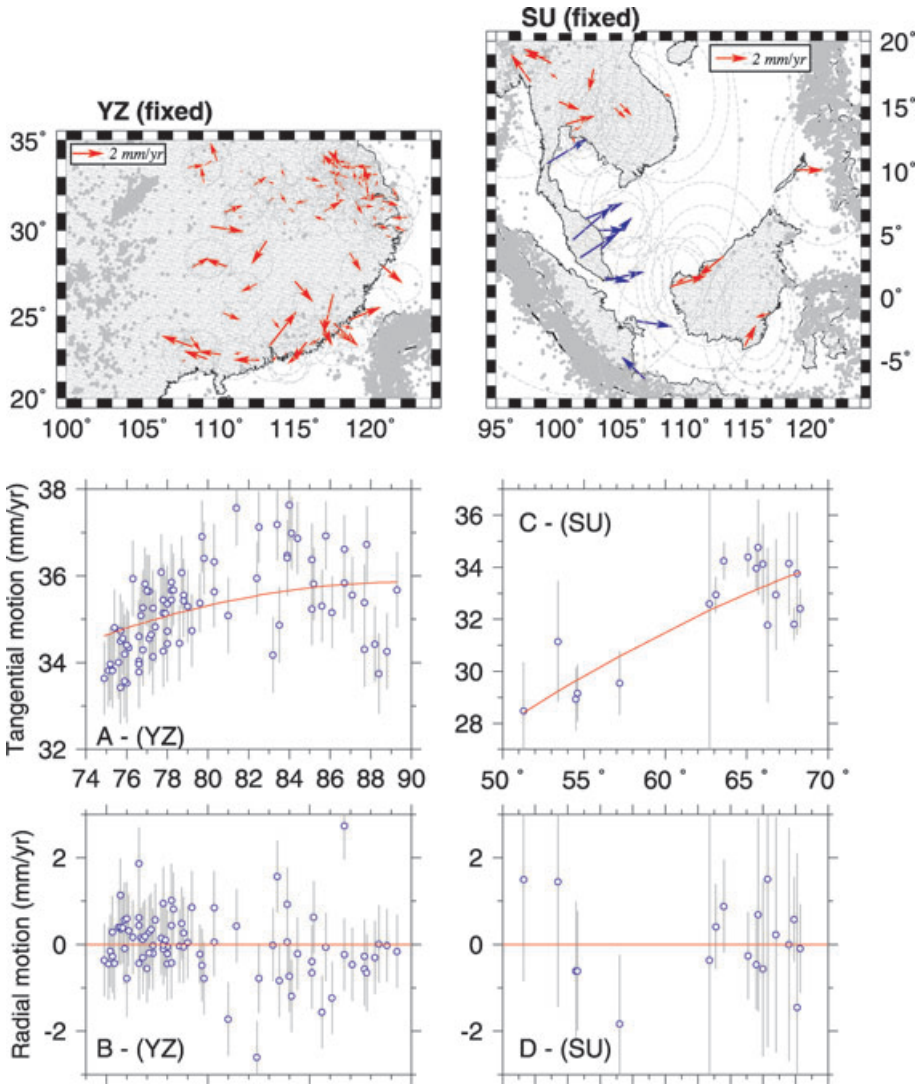

Figure 49. (a–d) Yangtze (YZ) and Sundaland (SU) plate GPS station velocity components (blue circles) and motions calculated from best-fitting angular velocities (red curves) as a function of angular distance from their best-fitting poles (horizontal axes). Station locations are shown in maps and Fig. 5. All velocities are relative to ITRF2000. Panels (a) and (c) show the component of the station motion parallel to small circles around the best-fitting poles. Panels (b) and (d) show the radial component of the station motion, which is orthogonal to small circles around the pole. Vertical bars show 1σ uncertainties. The maps labelled 'YZ (fixed)' and 'SU (fixed)' show residual motions of the Yangtze and Sundaland plate GPS stations relative to the motions calculated from their best-fitting angular velocities (Table 4). Red arrows show station velocities that are used to estimate the best-fitting angular velocities. Blue arrows indicate stations that Simons *et al.* (2007) use to estimate Sundaland plate motion, but that we elected not to use (Section 5.7.1). Uncertainty ellipses are 2-D, 95 per cent. Grey circles show epicentres of 1963–2008 shallow earthquakes.

of the Java-Sumatra trench (Royer & Gordon 1997; Gordon *et al.* 2008).

5.7.2 Yangtze–Sundaland plate motion

Shen *et al.* (2005) use a several-hundred-station GPS velocity field from eastern Asia (Fig. 48) to estimate the motion of the Yangtze plate, which is bordered to the east by the Ryukyu trench and to the west by a broad region of distributed deformation associated with the Tibetan plateau. From a joint inversion of 81 Yangtze plate station velocities from Shen *et al.* and 28 Sundaland plate station velocities, Simons *et al.* (2007) find that the Yangtze plate rotates slowly anticlockwise relative to Sundaland around a pole located near the northern end of the Philippine trench (Fig. 13b). The pole predicts that motion along most of the poorly defined boundary between the two plates consists of 3 mm yr^{-1} or less of ≈N–S convergence (see black arrows in Fig. 48).

We transformed the velocities of 83 Yangtze plate stations from Shen *et al.* (2005) (locations shown in Figs 5, 48 and 49) to the same Australia plate frame of reference that we employ for the Sundaland plate (Table S4). The 83 station velocities are well fit by a single angular velocity (Figs 49a and b), with a weighted rms misfit of only 0.76 and 0.87 mm yr^{-1} in the north and east velocity components, respectively. Relative to the plate interior, the station residual motions are apparently random (see map in Fig. 49), consistent with that expected for an undeforming plate.

The MORVEL angular velocity for the Yangtze plate relative to Sundaland is located at the southern end of the Ryukyu trench, several hundred kilometres north of the Simons *et al.* pole (Fig. 13b), but with an uncertainty region large enough to include the Simons *et al*. pole. The new pole predicts rates similar to those found by

Table 4. Best-fitting GPS angular velocities and covariances relative to ITRF2000 and ITRF2005.

Plate	Num. stations	Angular velocity			Variances and covariances					
		Lat. (°N)	Long. (°E)	ω (deg Myr^{-1})	a	b	c	d	e	f
AM-ITRF2000	20	61.9	−120.5	0.283	0.82	−1.29	−1.60	2.95	3.83	3.83
AU-ITRF2000[a]	20	32.6	37.5	0.626	0.12	−0.09	0.08	−0.07	0.11	0.11
CA-ITRF2005	16	−36.9	81.1	0.261	0.71	−1.56	0.48	−1.31	0.72	0.72
NA-ITRF2005[a]	457	6.8	95.2	0.189	0.00	−0.00	0.00	−0.02	0.02	0.02
PA-ITRF2005[a]	21	63.4	−68.2	0.677	0.17	0.03	−0.01	−0.00	0.06	0.06
PS-ITRF2005	4	47.1	150.4	0.925	8.60	−9.49	−5.54	6.20	3.89	3.89
SU-ITRF2000	18	48.5	−93.9	0.326	0.75	−1.81	−0.43	1.80	0.57	0.57
YZ-ITRF2000	83	61.9	−114.7	0.320	0.38	−0.75	−0.47	0.97	0.63	0.63

[a]Geodetic reference plate for MORVEL. Plate abbreviations are defined in Fig. 1. Angular velocities describe counter-clockwise rotation of the given plate relative to either ITRF2000 or ITRF2005. All site velocities were adjusted for geocentral translation prior to the estimation of the best-fitting angular velocities, as described in the text. Cartesian covariances are propagated from the GPS velocity uncertainties and have units of 10^{-8} rad^{2}Myr^{-2}. Additional information about the covariances is given in the note of Table 1.

Simons *et al*. for locations along the poorly defined boundary between these two plates, but predicts that the direction of motion is ≈20° anticlockwise from that predicted by Simons *et al.* (Fig. 48). The S10°E ± 8° direction predicted by our new angular velocity along the slow-slipping Red River strike-slip fault of southern China and Vietnam (not shown) is better aligned with the S45°E fault trend than is the S10°W direction predicted by the Simons *et al.* angular velocity and predicts slightly faster strike-slip motion along the fault (2.3 mm yr^{-1}) than does the Simons *et al*. estimate (1.7 mm yr^{-1}). Both of the predicted rates agree, however, with geologically estimated slip rates lower than 5 mm yr^{-1} along this fault (Simons *et al.* 2007).

5.7.3 Amur plate motion: northeast Asia

The Amur plate, which is located north of a wide deforming region that separates it from the Yangtze plate (inset to Fig. 50), moves eastward at rates of only 3–4 mm yr^{-1} relative to the Eurasia plate (inset to Fig. 50), much slower than the 12 mm yr^{-1} eastward motions of the Sundaland and Yangtze plates relative to Eurasia (Calais *et al.* 2003; Jin *et al.* 2007).

Petit & Fournier (2005) describe in detail prior estimates of Amur plate motion in the context of GPS and seismic evidence for deformation along the boundaries that the Amur plate shares with the Eurasia, Okhotsk, Philippine Sea and Yangtze plates. They conclude that only the northern and eastern boundaries of the Amur plate with Eurasia and the Philippine Sea plate accommodate localized deformation and thus resemble classic 'narrow' plate boundaries (Fig. 50). Along the Amur–Eurasia plate boundary, they conclude that prior poles that are located north of the plate boundary and between longitudes of 125°E and 135°E correctly predict the observed transition from NW–SE opening across Lake Baikal (indicated by the tensional axes shown in Fig. 50) to nearly E-W, left-lateral strike-slip faulting east of ≈120°E. They also find that recent poles based on GPS station velocities (Sella *et al.* 2002; Kreemer *et al.* 2003) predict dominantly extensional deformation everywhere along the plate boundary, in poor agreement with the geological and seismic data. A recent GPS-based pole for Amur–Eurasia motion from Jin *et al.* (2007) also predicts motion that is dominated by N–S extension everywhere along the plate boundary (black arrows in Fig. 50), inconsistent with the available data.

We estimate motion of the Amur plate with the velocities of fourteen survey-mode and six continuous GPS stations (map and panels A and B in Fig. 50), of which 19 are from Jin *et al.* (2007) and one (KHAJ) from our own analysis of continuous GPS data in Asia (Table S4). The station velocities are well fit, with north and east weighted rms values of 1.0 and 1.2 mm yr^{-1}, respectively. Four of the residual velocities (Fig. 50) for stations on the east edge of the plate point towards the plate interior, suggesting that all four sites may record 1–2 mm yr^{-1} of interseismic elastic shortening related to the Japan and southern Kuril trenches east of those stations. No other patterns in the residual velocities are apparent.

We link the Amur plate to the global plate circuit using the Australia plate, the same as we used for the Yangtze and Sundaland plates (Fig. 2). Doing so ensures that any errors in the Australia plate angular velocity will cancel during the estimation procedure for the angular velocity that specifies the slow motion across the wide deforming zone between the Amur and Yangtze plates. The new Yangtze–Amur angular velocity (Table 3) predicts Yangtze plate motion of 4.4 ± 0.4 mm yr^{-1} towards the east relative to the Amur plate across their wide, seismically active boundary in northern China (Fig. 50), in good accord with deformation in this region indicated by earthquake focal mechanisms.

Estimation of the Amur–Eurasia plate angular velocity requires a lengthy plate circuit (AM-AU-AN-NB-NA-EU in Fig. 2), which increases the opportunities for plate circuit and data errors to accumulate and propagate into the Amur–Eurasia angular velocity estimate. Encouragingly, the MORVEL Amur–Eurasia angular velocity successfully predicts the changing style of deformation along the slowly deforming Amur–Eurasia plate boundary (Fig. 50). The new pole is located north of the plate boundary at 66.5°N, 138.5°E (Table 3) and predicts extensional displacements of 4.2 ± 1.2 mm yr^{-1} (1σ) across Lake Baikal, consistent with the 3–4 mm yr^{-1} (1σ) opening rate determined by Calais *et al.* (2003) from detailed GPS measurements in this region. Small circles about the new pole (red-white dashed lines in Fig. 50) are parallel to the tension axes for normal-faulting earthquakes along Lake Baikal and farther east and thus successfully describe the directions of motion. The direction and sense of the predicted motion east of 120°E also agree well with evidence presented by Petit & Fournier (2005) for E-W right-lateral strike-slip faulting along that part of the plate boundary and further agree with both the rate and direction of motion predicted by another recent GPS solution (Apel *et al.* 2006).

We conclude that the MORVEL Amur–Eurasia angular velocity is consistent with independent observations of deformation along their plate boundary, despite the extended plate circuit that links the two plates. The consistency between the predicted and observed rates and directions of motion at various locations along the plate

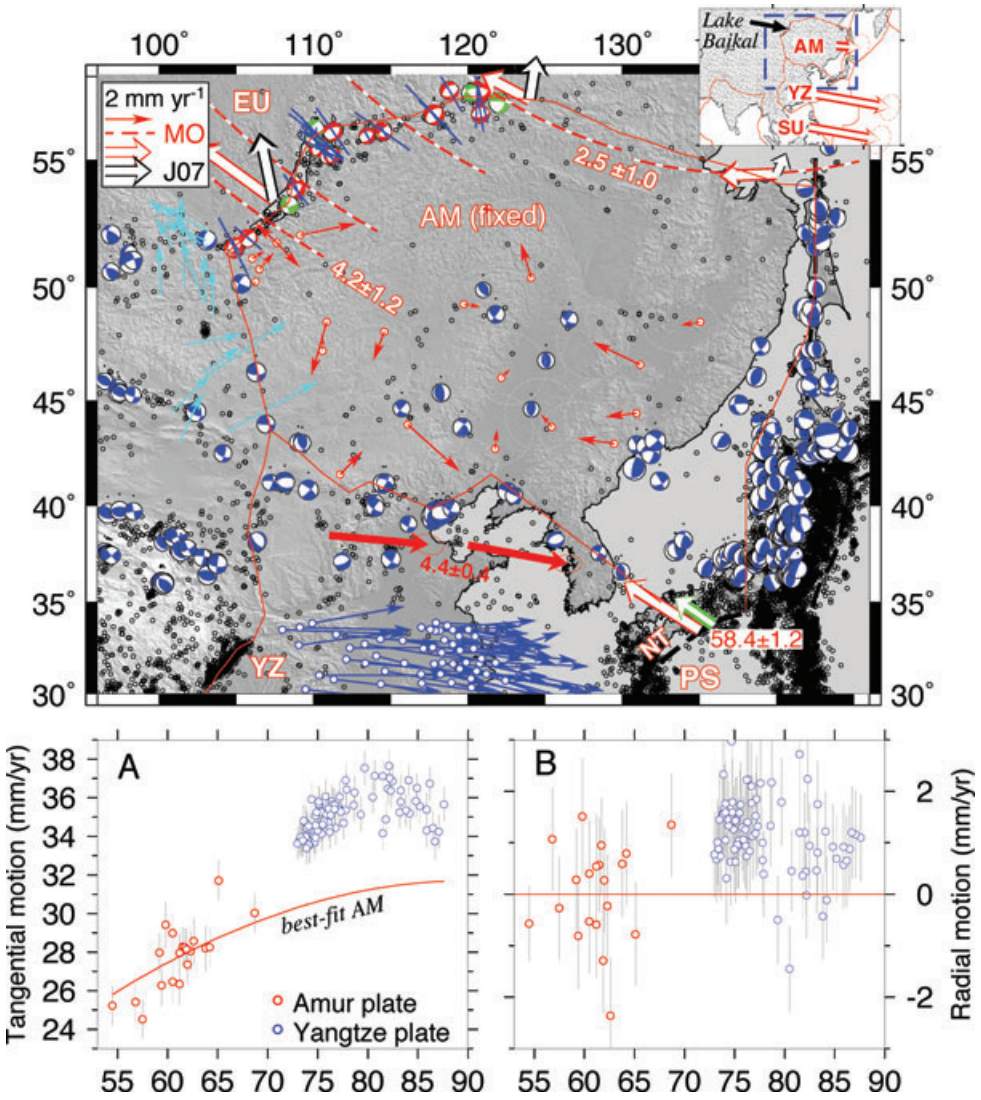

Figure 50. Location map, tectonic setting, and GPS station velocities for Amur plate. Inset shows MORVEL estimates for Amur, Yangtze and Sundaland plate motions relative to Eurasia at respective rates of 3.8 ± 1, 12.1 ± 1 and 11.6 ± 1 mm yr^{-1}. Map shows Global centroid moment tensor solutions for the period 1976–2008 with centroid depths less than 40 km for locations inland from the Japan and northern Izu-Bonin trenches. Earthquakes are from 1963 to 2008 and have magnitudes greater than 3.5. All velocities on the large map are relative to a fixed Amur plate (see legend). Thin red arrows and dashed ellipses show residual motions and 2-D, 1σ uncertainties for the 20 GPS site velocities used to estimate the Amur plate best-fitting angular velocity (Table 4). Open black arrows (J07) show motions predicted by the Amur–Eurasia angular velocity of Jin *et al.* (2007). Dark and light blue vectors indicate motions of GPS stations from the Yangtze plate (Shen *et al.* 2005) and other sites near the Amur plate boundaries (Jin *et al.* 2007), respectively. Bold red arrows show MORVEL velocities and 2-D, 1σ uncertainties for the Yangtze plate at the southern edge of the Amur plate. Red-white dashed curves and numerals show small circles and rates in mm yr^{-1} predicted by the MORVEL Amur–Eurasia angular velocity. Open red and green arrows show respective MORVEL and Sella *et al.* (2002) predictions for Philippine Sea–Amur plate convergence (not drawn to scale). Red and green focal mechanisms are for normal-faulting and strike-slip earthquakes along the Amur–Eurasia plate boundary and blue lines indicate tension axis orientations for selected normal-faulting earthquakes. Panels (A) and (B) show tangential and radial components of the 20 Amur plate station velocities in ITRF2000 relative to motion calculated from their best-fitting angular velocity (red curve) and for comparison, the motions of stations from the Yangtze plate (blue circles). 'NT' labels the Nankai Trough.

boundary implies that the accumulated errors within the circuit that links these two plates are small.

5.7.4 The Philippine Sea plate and subduction in the western Pacific

More than 90 per cent of the Philippine Sea plate is bordered by active subduction zones (Fig. 48), with active backarc spreading or slow extension occurring behind the Mariana, Izu-Bonin and Ryukyu trenches. Because much of the plate interior lies beneath water and is thus impractical for geodetic monitoring, estimating its motion has proved challenging. Prior to the advent of modern GPS measurements, Seno *et al.* (1993) used a combination of earthquake slip directions from the circum-Philippine subduction zones and plate circuit closure constraints from NUVEL-1A and the Caroline plate to estimate the angular velocities that describe Philippine Sea plate motion. More recent estimates also use velocities for the handful of GPS stations from the plate interior and near its boundaries (Sella *et al.* 2002; Zang *et al.* 2002).

We estimate Philippine Sea plate motion solely from the velocities of four GPS stations (Figs 5 and 48). Station Okino Torishima (site 1140 in Table S4 and OKIN in Fig. 48) is located close to the

geographic centre of the plate and should unambiguously record its motion. Two other sites, KITA and MINA, are located only 180 km east of the Ryukyu trench (Fig. 48). Although the velocities at these two sites could conceivably be affected by elastic strain associated with subduction along the Ryukyu trench, GPS measurements on islands in the Ryukyu arc indicate that little or no elastic strain accumulates within the arc (Nishimura *et al.* 2004). Subduction is instead accommodated by frequent slow slip events that quickly relieve any accumulating elastic strain (Heki & Kataoka 2008). The velocities for sites KITA and MINA are therefore likely to record Philippine Sea plate motion. Station PALA lies directly west of the southern end of the Yap trench (Fig. 48), where the rate of subduction is only 0–3 mm yr^{-1} (Seno *et al.* 1993; Sella *et al.* 2002; Zang *et al.* 2002). Even if the nearby subduction interface is fully locked, any elastic shortening at PALA should be only fractions of a millimetres per year, small enough to neglect.

Our selection of Philippine Sea plate GPS stations differs substantially from that of Zang *et al.* (2002), who estimate the plate motion using published velocities for the GPS station at Okino Torishima and campaign GPS stations BTS3, S063, and S102, from a seismically active region east of the Manila trench between Taiwan and the Philippines (Fig. 48). Given our concerns about their locations within an active seismic zone, we obtained and processed the original GPS data for these three and two additional campaign sites in the northern Philippines (locations and motions indicated by the open red arrows within the rectangle in Fig. 48). All five sites move relative to the plate interior at rates of 11.5 ± 2.6 to 23 ± 3.6 mm yr^{-1}, several times larger than their estimated uncertainties. Given their locations within an active seismic zone and significant motions relative to the plate interior, we elected not to use these stations to estimate Philippine Sea plate motion.

We also considered whether other GPS sites near the boundaries of the Philippine Sea plate might be located on undeforming areas of the plate. Along the eastern boundary of the Philippine plate, continuous sites CNMI, CNMR and GUAM in the Mariana trough (Fig. 48) move rapidly eastward away from the plate interior at rates of 34.4 ± 1.2 mm yr^{-1} (CNMI) to 47.6 ± 0.8 mm yr^{-1} (GUAM). Their motions are consistent with velocities measured at other GPS sites in the Mariana trough (Kato *et al.* 2003) and with rapid extension across the Mariana backarc. In the Izu-Bonin backarc north of the Mariana trench, continuous stations 0602, 0603 and 5113 also move eastward at rates of 4.1 ± 1.2 to 14.1 ± 1.1 mm yr^{-1} (Fig. 48). Their motions are consistent with marine geophysical evidence for slow extension behind the Izu-Bonin trench (Taylor *et al*. 1991). None of the GPS sites along the eastern border of the Philippine Sea are therefore suitable for estimating Philippine Sea plate motion.

Based on the geological evidence and our extended analysis of GPS station motions in the Philippine Sea region, we find that the only group of stations on the Philippine Sea plate with velocities that can be fit satisfactorily by a single angular velocity are OKIN, PALA, MINA and KITA. All other plausible station groupings give rise to significant misfits to one or more of the station velocities that are assumed to record the motion of the plate interior.

The Philippine Sea plate angular velocity that best fits the velocities for stations KITA, MINA, OKIN and PALA (Table 4) has respective weighted rms misfits of 0.62 and 0.75 mm yr^{-1} to the north and east velocity components for these four stations, consistent with the rms misfits for the other plates with GPS data. The four Philippine Sea plate station velocities are linked to the MORVEL plate circuit via the Pacific plate (Fig. 2), the motion of which is defined from the velocities of 21 continuous stations in the central and western Pacific (Figs 5, 6e and f). The 21 Pacific plate station velocities have respective rms misfits for the north and east velocity components of 0.72 and 0.77 mm yr^{-1}, comparable to the residual velocities reported by Beavan *et al.* (2002) and Plattner *et al.* (2007) for Pacific plate GPS stations. The Pacific plate angular velocity (Table 4) is strongly constrained due to the large geographic area spanned by these 21 stations (Fig. 5).

Relative to the Philippine Sea plate, the Pacific plate rotates anticlockwise around a pole near the southern end of their plate boundary (Figs 13a and 48). The best-fitting angular velocity predicts that convergence rates decrease rapidly southward, from 49 ± 0.7 mm yr^{-1} (1σ) at the northern end of the Izu-Bonin trench to 9 ± 0.8 mm yr^{-1} of orthogonal subduction along the southern Yap trench (Fig. 48). Several hundred kilometres south of the Yap trench, the plate angular velocity predicts 9 ± 0.6 mm yr^{-1} of oblique extension across the Ayu Trough ('AT' in Fig. 48). The predicted motion agrees with evidence for slow NW-directed extension across this feature (Fujiwara *et al.* 1995; Lee & Kim 2004), but is more than twice as fast as the 4 mm yr^{-1} maximum opening rate estimated by Fujiwara *et al.* (1995) for this possibly inactive spreading centre. The Ayu Trough instead likely accommodates slow relative motion between the Philippine Sea and Caroline plates (Weissel & Anderson 1978).

The newly estimated Philippine Sea–Pacific plate velocities agree to within 1 mm yr^{-1} and 2° everywhere along the plate boundary with those estimated by Sella *et al.* (2002) (Fig. 48), reflecting the overlap in the GPS stations that are used in both studies to estimate the motions of these two plates. In contrast, the Pacific-Philippine Sea angular velocity of Zang *et al.* (2002) predicts convergence rates that are 10–12 mm yr^{-1} higher along the entire plate boundary than are calculated from MORVEL. These large differences reflect the different data and approaches that are used in our two studies.

The Philippine Sea plate subducts beneath the eastern boundary of the Yangtze plate along the Ryukyu trench, where slow backarc spreading decouples the forearc from the interior of the Yangtze plate (Nishimura *et al.* 2004). The MORVEL angular velocity for the Philippine Sea–Yangtze plate pair predicts that convergence across the Ryukyu trench (Fig. 48) is in the same direction, but is 3 mm yr^{-1} slower than predicted by Sella *et al.* (2002). The many additional station velocities that we use to estimate Yangtze plate motion therefore only modestly alter the Philippine Sea–Yangtze angular velocity estimate relative to that of Sella *et al*., who used only three station velocities to estimate Yangtze plate motion.

Along the Nankai Trough, where the Philippine Sea plate subducts beneath the eastern boundary of the Amur plate (Fig. 50), MORVEL predicts WNW-directed convergence of 58.4 ± 1.2 mm yr^{-1} (1σ). The angular velocity estimated by Sella *et al.* (2002) for this plate pair gives a rate of 31 mm yr^{-1} (green arrow in Fig. 50), nearly a factor-of-two lower than MORVEL. In contrast, the Amur–Philippine Sea plate angular velocity estimated by Kreemer *et al.* (2003) gives a rate of 67 mm yr^{-1}, significantly higher than MORVEL. Both prior estimates are based on fewer station velocities from the Amur plate and are thus likely to be less accurate than MORVEL. Jin *et al.* (2007) describe an extensive GPS velocity field for much of eastern Asia that suggests possible slow motion between the Amur plate and the lithosphere situated inland from the Nankai Trough. Our understanding of the tectonic setting of the Nankai Trough thus may evolve as further information about the tectonics of eastern Asia is extracted from future GPS velocity fields for this complexly deforming region.

5.8 The Caribbean Sea

5.8.1 Data description

The NUVEL-1 Caribbean plate angular velocities were estimated from a poorly known spreading rate from the mid-Cayman spreading centre, azimuths of the Swan Island and Oriente strike-slip faults, and earthquake slip directions from the Middle America and Lesser Antilles subduction zones. Subsequent work has shown, however, that almost none of these data unambiguously record Caribbean plate motion. For example, partitioning of oblique convergence along the Middle America trench biases the earthquake slip directions that were used in NUVEL-1 to constrain the Cocos-Caribbean direction of motion (White & Harlow 1993; Deng & Sykes 1995; DeMets 2001). Similarly, GPS measurements on the islands of Hispaniola (Mann *et al.* 2002) and Jamaica (DeMets & Wiggins-Grandison 2007) indicate that the mid-Cayman spreading centre does not accommodate Caribbean–North America plate motion, as was assumed for NUVEL-1 and NUVEL-1A, but instead accommodates motion of an elongate, Gonave microplate relative to North America (Mann *et al.* 1995).

Following DeMets *et al.* (2007), we estimate Caribbean plate motion mainly from 16 GPS station velocities (Fig. 5), twelve of which are survey-mode sites and four of which are continuous. In addition, we retain two of the NUVEL-1A data, both from the strike-slip Swan Islands fault, which separates the Caribbean and North America plates between the mid-Cayman rise and Central America. The well-defined, narrow trace of this fault has been mapped with SeaMARC side-scan sonar (Rosencrantz & Mann 1991) and appears to accommodate all the plate motion from 84°W to 82°W, where we estimate both azimuths. The well-determined azimuths of this fault are consistent with a purely geodetic estimate of Caribbean–North America plate motion (DeMets *et al.* 2000), lending confidence that the fault accommodates all of the plate motion at these longitudes.

The respective weighted rms misfits for the 16 Caribbean plate GPS station velocities (Table S4) are 1.0 and 1.6 mm yr^{-1} in the north and east components relative to the velocities estimated from their best-fitting angular velocity (Table 4). The misfits are modestly larger than for the other plates with motions determined from GPS velocities, but are unsurprising given that six of the 16 stations are located within 100 km of an active plate boundary fault and 12 stations are survey-mode sites.

As measured by their summed data importances, the 16 station velocities and two Swan Islands fault azimuths respectively provide 87 and 13 per cent of the information about Caribbean plate motion. The MORVEL determination of Caribbean plate motion is thus based predominantly on GPS observations. We refer readers to DeMets *et al.* (2007) for a more in-depth analysis of the robustness of the Caribbean plate angular velocity.

The Caribbean plate is linked to the MORVEL plate circuit via the North America plate (Fig. 2), the motion of which is determined from the velocities of 457 continuous GPS stations from the North America plate interior (Figs 5 and 6). Stations from areas of North America that are affected by postglacial rebound are excluded (Calais *et al.* 2006b) and stations located in actively deforming areas of western North America (Bennett *et al.* 1999) are not used to define its motion. The 457 North America plate GPS site rates vary by nearly a factor of two (Fig. 6) and increase sinusoidally with angular distance from their best-fitting pole, as expected. The respective weighted rms misfits for the north and east velocity components are 0.60 mm yr^{-1} and 0.64 mm yr^{-1} relative to motion estimated from the North America plate best-fitting angular velocity (Fig. 6), consistent with previously reported misfits for North America plate stations (e.g. Calais *et al.* 2006b; Sella *et al.* 2007).

5.8.2 Caribbean plate motion

The new Caribbean–North America plate angular velocity gives rates that range from 19 to 21 mm yr^{-1} at most locations along the Caribbean–North America plate boundary. These are consistent with other recent estimates, which are determined from many of the same data (DeMets *et al.* 2000, 2007). The new estimates confirm that NUVEL-1 and NUVEL-1A underestimate the rate of Caribbean–North America plate motion by nearly 50 per cent, as was first reported by Dixon *et al.* (1998). For example, at a location along the Lesser Antilles trench (Fig. 25), the new Caribbean–North America angular velocity gives motion of 20 ± 0.4 mm yr^{-1} towards S74°W $\pm$ 1°, in nearly the same direction but at almost twice the rate given by NUVEL-1A (11.4 ± 3.2 mm yr^{-1} towards S81°W $\pm$ 6°).

Along the Central Range fault of Trinidad (10.4°N, 61.2°W), within the shear-dominated Caribbean–South America plate boundary in northeastern South America, Perez *et al.* (2001) and Weber *et al.* (2001) estimate respective motions of 20.2 mm yr^{-1} towards S81.5°W and 20 ± 3 mm yr^{-1} towards S86°W $\pm$ 2° for the Caribbean plate relative to South America. At the same location, the MORVEL Caribbean–South America plate angular velocity predicts motion of 20.0 ± 0.5 mm yr^{-1} (1σ) towards S78.2°W $\pm$ 1.3°, consistent with that estimated by Perez *et al*. and Weber *et al*., but more than 50 per cent higher than the NUVEL-1A prediction of 13 ± 3 mm yr^{-1} of east–west motion along this plate boundary. The highly oblique convergence predicted by MORVEL resolves into fault-parallel and fault-normal components of 19.6 ± 0.5 mm yr^{-1} and 3.5 ± 0.5 mm yr^{-1} along the N68°E-striking Central Range fault, consistent with structural observations of strike-slip motion along the fault and thrust faulting and folding in adjacent areas of the Central Range (Weber *et al.* 2001).

5.9 PVEL estimates of Cocos, Juan de Fuca and Rivera plate motions

Studies of earthquake cycle deformation along the Cascadia subduction zone and Middle America trench, which accommodate subduction of the Juan de Fuca, Rivera and Cocos plates beneath the North America and Caribbean plates, require well-determined angular velocities for the relative motions between these plates. In MORVEL, these plate motions are estimated from lengthy plate circuits that cross the northern Mid-Atlantic Ridge (NA-NB), the Southwest Indian Ridge (NB-AN), the Pacific-Antarctic rise (AN-PA) and the spreading centres that the Juan de Fuca, Rivera and Cocos plates share with the Pacific plate (Fig. 2). Possible systematic errors or slow deformation of any of these plates may therefore bias the MORVEL angular velocities that describe Cocos, Juan de Fuca and Rivera plate motions.

We therefore estimate an alternative set of angular velocities for these three plates from a shorter, geodetically based plate circuit (Fig. 2). This set of angular velocities, which we refer to as PVEL (Pacific VELocity estimates), is designed mainly for investigators who are engaged in geodetic studies of western North America and Central America. The PVEL angular velocities (Table 5) are

Table 5. PVEL angular velocities and angular velocity covariances.

Plate pair	Angular velocity			Variances and covariances					
	Lat. (°N)	Long. (°E)	ω (deg Myr $^{-1}$)	a	b	c	d	e	f
CO-CA	21.0	−121.4	1.270	9.96	15.71	−3.09	78.67	−16.24	8.27
CO-NA	27.3	−122.6	1.380	9.69	16.34	−3.27	76.75	−15.72	7.98
JF-NA	−32.5	66.8	1.099	101.57	130.66	−156.43	174.09	−207.89	255.82
RI-NA	21.1	−108.3	4.355	236.01	773.89	−283.98	2566.25	−941.97	352.14

Notes: See note of Table 1 for the conventions that are employed in this table and Fig. 1 for plate abbreviations. Angular velocities for the Cocos, Juan de Fuca and Rivera plates are derived from data along their boundaries with the Pacific plate and are linked to North American or Caribbean plate motion through the velocities of GPS stations on the Caribbean, Pacific and North American plate (Fig. 2 and supplementary Table 4). Covariances are propagated from data uncertainties and also incorporate systematic errors from uncertainties in the magnitude of outward displacement (see text).

determined from a simultaneous inversion of the MORVEL data from the Pacific-Cocos, Pacific-Juan de Fuca and Pacific–Rivera plate boundaries (Tables S1 and S2) and the GPS station velocities from the Caribbean, North America and Pacific plates (Tables S4 and S5). The PVEL angular velocities supersede estimates given by DeMets (2001) for some of these same plate pairs.

We assessed the differences between the PVEL and MORVEL angular velocities for the Juan de Fuca–North America, Rivera–North America, Cocos–North America and Cocos–Caribbean plate pairs from eq. (2) and through a comparison of the linear velocities predicted by both estimates at several locations along the boundary of each plate pair. For the Juan de Fuca–North America plate pair, the PVEL and MORVEL angular velocities do not differ significantly ($p = 0.22$). At 46°N, 125°W, near the midpoint of the Cascadia subduction zone, PVEL predicts motion of 34.2 ± 1.2 mm yr^{-1} towards N52°E ± 3°, the same within uncertainties as is predicted by MORVEL (35.9 ± 2.4 mm yr^{-1} towards N49°E ± 2.7°). The good agreement suggests that motion for this plate pair since 0.78 Ma is well determined.

The MORVEL and PVEL angular velocities for the Rivera–North America plate pair also do not differ significantly ($p = 0.15$). At 18.7°N, 105°W, offshore from the Colima-Jalisco region of western Mexico, PVEL predicts convergence of 33.0 ± 1.6 mm yr^{-1} towards N39°E ± 2.5°, 10 per cent slower than, but parallel to the motion predicted by MORVEL (36.1 ± 2.2 mm yr^{-1} towards N38°E ± 3.2°).

For the Cocos–North America plate pair, the MORVEL and PVEL angular velocity estimates differ significantly ($p < 10^{-15}$). The PVEL pole lies closer to the northwest end of the Middle America trench than does the MORVEL pole (Fig. 14) and thus predicts more rapid changes in convergence rates along the plate boundary than does MORVEL. The PVEL and MORVEL estimates predict similar convergence directions, with differences of less than 1° everywhere along the plate boundary. PVEL however predicts lower convergence rates than does MORVEL, with differences that range from 2.5 ± 3 mm yr^{-1} at the southeastern end of the plate boundary (near 15.0°N, 96°W) to 8 ± 3 mm yr^{-1} at the northwestern end of the plate boundary (18.0°N, 104°W).

The PVEL and MORVEL Cocos-Caribbean angular velocities also differ significantly ($p < 10^{-15}$). Both estimates predict that convergence directions are N20°E ± 2° everywhere along the Central America subduction zone. Both also predict 68 ± 4 mm yr^{-1} convergence rates beneath Guatemala, near the western limit of their boundary. Due to their differing pole locations (Fig. 14), PVEL however predicts that the convergence rates increase more rapidly to the east and reach 82.3 ± 2.2 mm yr^{-1} offshore from the Nicoya Peninsula of Costa Rica (9.5°N, 86°W), where MORVEL predicts a rate of only 76.8 ± 2.6 mm yr^{-1}.

The PVEL and MORVEL angular velocities therefore differ significantly only for the two plate pairs that include the Cocos plate. These differences are largely caused by the Pacific–Cocos–Nazca circuit closure requirement that is enforced for the MORVEL, but not the PVEL angular velocities. More work is needed to determine which of the two more accurately describes the present motions of these plate pairs. Smaller differences between the PVEL and MORVEL estimates for the Juan de Fuca and Rivera plates relative to North America arise from errors that presumably accumulate around the lengthy global circuit that is used in MORVEL to link the motions of the Pacific and North America plates. Further discussion of this topic is given in Section 7.

6 PLATE CIRCUIT CLOSURES AND OUTWARD DISPLACEMENT

The failure of a plate circuit to satisfy closure may be caused by unrecognized plate boundaries, plate deformation, or by a variety of systematic errors. Here we test whether significant non-closures occur in the MORVEL data and also test the sensitivity of the results to the assumed value of outward displacement used to adjust the MORVEL spreading rates.

Our analysis of the MORVEL circuit closures focuses on six three-plate circuits from which kinematic data are available for all three of the intersecting boundaries (Fig. 2). Four of these consist of three spreading centres that intersect at a triple junction. These offer strong tests for circuit closure because the motions along all three intersecting plate boundaries are well determined. The other two three-plate circuits, those for Nubia–Eurasia–North America and Arabia–India–Somalia, have spreading rates and fault azimuths along two of the three boundaries that meet at their triple junctions, but have only fault azimuths along the third boundary. Absent any constraint on the rate of motion for one of the three plate boundaries in these circuits, they offer weaker tests of circuit closure. Our circuit closure analysis excludes all plate circuits that include the Scotia and Sandwich plates, for which the available data are too incomplete or too unreliable to merit a meaningful test of circuit closure. One four-plate circuit, Nubia–Arabia–Somalia–Antarctic is discussed elsewhere (Horner-Johnson *et al.* 2005, 2007).

6.1 Methods for determining circuit non-closure

We determine the magnitude of circuit non-closure using two complementary methods. The first, described by Gordon *et al.* (1987), employs an F-ratio or χ^2 test to compare the summed least-squares misfits of the best-fitting angular velocities for a given plate circuit with the least-squares misfit for the angular velocities that satisfy

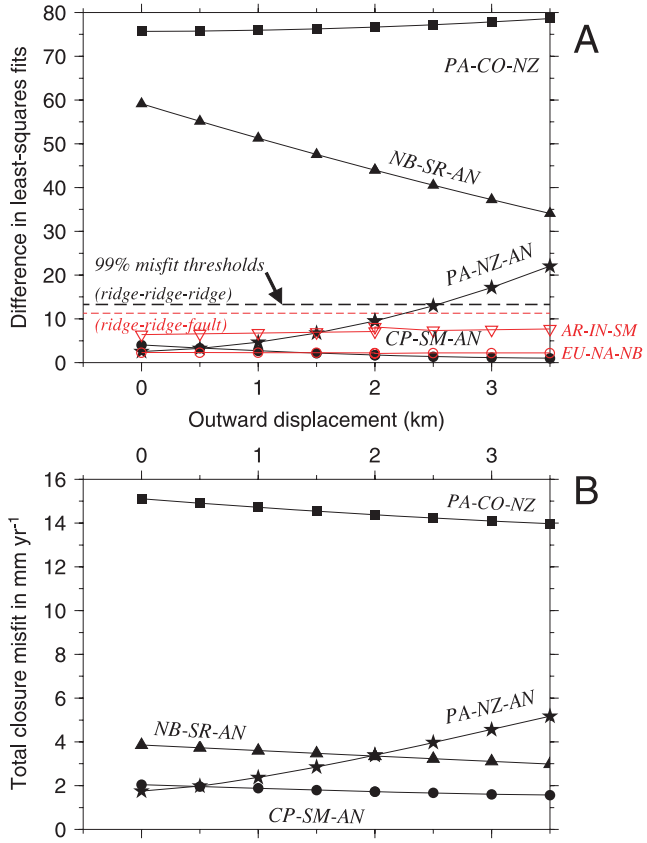

Figure 51. (a) Difference in least-squares fits of best-fitting and closure-enforced angular velocities for three-plate circuits and different assumed values for outward displacement. Black dashed line indicates the value (13.3) above which the difference between the best-fitting and closure-enforced least-squares misfits becomes significant at the 99 per cent confidence level for circuits that meet in ridge–ridge–ridge triple junctions (see text). Red dashed line similarly indicates the 99 per cent confidence threshold (11.3) for ridge–ridge–fault plate circuits (see text). (b) Linear velocities of circuit non-closure at the location of the circuit triple junction, represented by the difference between the linear velocities that are calculated with the best-fitting angular velocity for any one of the three intersecting plate boundaries and the angular velocity that is summed from the best-fitting angular velocities for the other two plate pairs in the circuit (see text). Values are shown only for ridge–ridge–ridge plate circuits since unique velocities of non-closure cannot be determined for ridge–ridge–fault plate circuits.

closure of that circuit. We examine the effect of outward displacement on circuit non-closure by determining the variation in the misfit and thus the magnitude of non-closure as we change the assumed value for outward displacement (Fig. 51a).

For the four ridge–ridge–ridge circuits that we analyse, we evaluate the statistical significance of the differences in the fits of the best-fitting and closure-enforced angular velocities using a χ^2 test for four degrees of freedom. Three of these additional degrees of freedom represent the additional parameters that are used to estimate three instead of two angular velocities in the best-fitting versus the closure-enforced estimates. The fourth degree of freedom represents the value for outward displacement that is adjusted to explore its effect on the misfit.

For the two ridge–ridge–fault plate circuits, no rate data are available from one of the three plate boundaries and hence only a best-fitting pole can be estimated from the data for that boundary. Thus the statistical significance of the differences in the fits of the best-fitting and closure-enforced estimates is evaluated with a χ^2 test for one fewer degree of freedom (3) than was the case for the ridge–ridge–ridge plate circuits.

We also determine a linear rate of non-closure for each of the ridge–ridge–ridge plate circuits to complement the statistical measure of circuit non-closure. We define this as the difference between the motion that is given at the circuit triple junction by any one of the three best-fitting angular velocities and the motion that is predicted from the sum of the remaining two best-fitting angular velocities. The former gives the plate motion independent of the condition of plate circuit closure whereas the latter predicts motion purely from closure of the plate circuit, thereby providing completely independent estimates of motion. The difference between the two constitutes a useful practical measure of the consistency of the two estimates.

6.2 Three-plate circuit non-closures

6.2.1 Nubia–Antarctic–Sur plate circuit

Repeated inversions of the 101 rates and azimuths from the Nubia–Antarctic–Sur plate circuit for assumed values of outward displacement between 0 and 3.5 km result in differences in the least-squares fits of the best-fitting and closure-enforced angular velocities that decrease rapidly for larger values of outward displacement (Fig. 51a). The non-closure is significant for all values of outward displacement that we explored ($p \leq 2 \times 10^{-7}$). The corresponding linear velocity of circuit non-closure at the Bouvet triple junction varies between 2.5 and 4 mm yr^{-1} (Fig. 51b) and is thus relatively small in magnitude although significant. Non-closure of this plate circuit is manifested mainly as a 2 mm yr^{-1} systematic misfit to the spreading rates from the American–Antarctic ridge (Fig. 27c).

The few millimetres per year non-closure might be caused by biases in one or more subsets of the kinematic data from this plate circuit. For example, Sempere *et al.* (1987) and DeMets & Wilson (2008) find a large range of observed values for outward displacement (0–8 km) for slow spreading rates, suggesting that the average value for outward displacement in this slow-spreading plate circuit might be even larger than the range of values we explored (0–3.5 km). We explored the effect of using values of outward displacement as large as 5 km, but find that even for such large values, significant circuit non-closure remains. Differences between the average magnitudes of outward displacement for the three spreading centres in this plate circuit might also contribute to the circuit non-closure, but we did not explore this because of the poorly posed nature of the problem. Better constraints on outward displacement, particularly for ultraslow spreading centres such as the Southwest Indian Ridge, are needed.

Distinguishing between the above hypotheses will require additional high-quality observations, mainly from sparsely surveyed areas of the Mid-Atlantic Ridge south of 50°S and the American–Antarctic ridge. The effect of non-closure around the Bouvet triple junction on the MORVEL angular velocities is small given that the non-closure is absorbed within this three-plate circuit, mainly as a misfit to data along the American–Antarctic ridge (Fig. 27c).

6.2.2 Pacific–Antarctic–Nazca plate circuit

The difference between the best-fitting and closure-enforced angular velocities for motion around the Pacific–Antarctic–Nazca plate circuit is statistically insignificant for values of outward displacement equal to or less than 2.5 km (Fig. 51a). For assumed values

of outward displacement that are larger than 2.5 km, the difference in fits between the best-fitting and closure-enforced angular velocities becomes significant at the 99 per cent confidence level. The data thus suggest that outward displacement is unlikely to be larger than 2 km along these three spreading centres. The linear velocities of non-closure range from 2 to 4 mm yr^{-1} (Fig. 51b) for values of outward displacement smaller than 2.5 km. We conclude that the cumulative effect of any data biases or deformation within these three plates is unlikely to exceed ≈4 mm yr^{-1}.

6.2.3 Pacific–Cocos–Nazca plate circuit

The large misfits and significant non-closure of this three-plate circuit pose a challenge to the rigid plate approximation. The fits of the best-fitting and closure-enforced angular velocities for motions within the Pacific–Cocos–Nazca plate circuit differ at high confidence level ($p = 1 \times 10^{-16}$) (Fig. 51a) and have a huge 14 ± 5 mm yr^{-1} linear velocity of non-closure at the Galapagos triple junction (Fig. 51b). The non-closure is manifested mainly as systematic misfits of the closure-enforced angular velocities to the Pacific–Nazca and Pacific–Cocos spreading rates (Figs 44 and 46a). These misfits reach a maximum of 7 mm yr^{-1} at the southern end of the Pacific–Cocos rise and are similar to the misfit reported by DeMets *et al.* (1990) for the NUVEL-1 data from this plate circuit.

The non-closure of this plate circuit is insensitive to the assumed value of outward displacement (Fig. 51), thereby excluding an error in the value of outward displacement as a possible explanation for the circuit non-closure. Below, we address two hypotheses for the cause of the non-closure, namely, a possible diffuse plate boundary within one or possibly both of the Nazca and Cocos plates, or an inconsistency between the spreading rate and transform fault data, possibly due to a change in plate motion within this plate circuit since 0.78 Ma.

We evaluated whether a diffuse plate boundary in any of the three plates in this circuit might be responsible for the circuit non-closure via a systematic search for a zone of deformation that might intersect any of the three plate boundaries within this plate circuit (Stein & Gordon 1984). We find no evidence that any deforming zone intersects the Pacific–Nazca plate boundary, in accord with the small degree of non-closure for the Nazca–Antarctic–Pacific plate circuit (see previous section). We also find no evidence that a deforming zone intersects the Cocos–Nazca plate boundary. Along the Pacific–Cocos plate boundary, deformation within the Pacific or Cocos plates may occur north of the Orozco transform fault on one or both sides of the rise axis, as described in Section 5.6.6 Although omitting all Pacific–Cocos rates north of 16.5°N reduces by 30 per cent the magnitude of the circuit non-closure, the remaining non-closure is still significant ($p = 2 \times 10^{-10}$). The circuit non-closure thus also does not appear to be caused solely by deformation of the portion of the Cocos plate north of the Orozco fracture zone.

Some of the circuit non-closure may be caused by a hypothesized change in motion within this plate circuit since 0.78 Ma. Multibeam surveys of the Pacific–Cocos seafloor fabric and transform faults indicate that the directions of Pacific–Cocos plate motion have rotated 3°–6° anticlockwise since 0.4–0.5 Ma (Carbotte & Macdonald 1992; Macdonald *et al.* 1992; Pockalny 1997), possibly introducing an inconsistency between the Pacific–Cocos transform fault azimuths and 0.78-Myr-average spreading rates. The rapid westward migration of the Cocos–Nazca pole from 4 Ma to at least 0.78 Ma (Wilson & Hey 1995) may also have continued to the present, possibly causing an inconsistency between the Cocos–Nazca spreading rates and transform fault azimuths.

To test whether a change in motion for one or more of the plate pairs might be responsible for the apparent circuit non-closure, we inverted only the spreading rates, which average motion consistently over the past 0.78 Myr. All Pacific-Cocos spreading rates north of 16.5°N were excluded to ensure that they did not corrupt the result. For this rates-only inversion, the fits of the closure-enforced and best-fitting angular velocities differ at only the 1 per cent confidence level. Although the data are therefore more consistent than for the inversion that includes both the rates and directions, the Pacific–Cocos and Pacific–Nazca angular velocities predict respective directions of motion for these two plate pairs that are 20° and 10° anticlockwise from the well-determined transform fault azimuths along their respective plate boundaries. These differences in direction are several times larger than any proposed change for the directions of plate motion for these two plate boundaries since 0.78 Ma. The circuit non-closure is thus not resolved by a rates only inversion, but is instead shifted by an unacceptably large amount to the directional components of motion.

We experimented with other subsets of the rates and transform azimuths from these three plate boundaries, but found none that reduce the circuit non-closure to insignificant levels without systematically misfitting either the rates or directions along one or more of the three plate boundaries. A satisfactory explanation of the cause of this circuit non-closure is left for future studies, including those that investigate how much of the misfit could be caused by horizontal thermal contraction of oceanic lithosphere (Kumar & Gordon 2009).

6.2.4 Capricorn–Somalia–Antarctic plate circuit

The best-fitting and closure-enforced angular velocities for the Capricorn–Somalia–Antarctic plate circuit do not differ significantly (Fig. 51a) and are insensitive to the value of outward displacement that is used to correct the spreading rates. The linear velocity of non-closure at the Rodrigues triple junction is only 1.5 mm yr^{-1} (Fig. 51b), indicating that the data from these three plate boundaries are consistent. The low level of circuit non-closure is partly an outcome of our systematic search for a Capricorn plate geometry that minimizes non-closure of this plate circuit (Section 5.5.5 and Fig. 33b) and the shortness of the three boundaries, each of which is truncated by a diffuse oceanic plate boundary.

6.2.5 Nubia–Eurasia–North America and Arabia–India–Somalia plate circuits

Both of the three-plate circuits that include one plate boundary without rates are consistent with closure (Fig. 51a). Along the Nubia–Eurasia plate boundary, the three Gloria fault azimuths are fit well when inverted with the many (623) spreading rates and azimuths from the Eurasia–North America and Nubia–North America plate boundaries (Fig. 23). The data from this plate circuit are therefore consistent with strike-slip motion along the well-mapped Gloria fault. Similarly, the data from the Arabia–Somalia and India–Somalia plate boundaries are consistent with the Owen Fracture Zone azimuths that are used to estimate Arabia–India motion. In particular, the data are consistent with the well-determined azimuth of the strike-slip fault imaged by multibeam sonar at the southern, active end of the Owen Fracture Zone (Fournier *et al.* 2008).

Changing the assumed value for outward displacement has little effect on the closure of these two plate circuits (Fig. 51a), mainly

because the estimated motion across the boundary without rates in each circuit is insensitive to a systematic change in the spreading rates across the two boundaries with rates.

7 DISCUSSION

The explosive growth of geodetic measurements over the past 15 yr has stimulated many comparative studies of geological and geodetic estimates of plate motion for a variety of tectonic and geodynamic applications. We therefore devote most of the discussion to an evaluation of the precision and accuracy of the MORVEL angular velocities, both of which must be known to determine how plate motions have changed over the past few million years. We begin the discussion with a brief evaluation of the impact of the new plate geometry on the fit to the data relative to the simpler geometry employed for NUVEL-1 and NUVEL-1A. We then compare the 3.16-Myr-average spreading rates in the MORVEL and NUVEL-1A data sets, which were determined from largely non-overlapping data with different techniques for finding the best-fitting rates. Following this, we quantify which of the MORVEL and NUVEL-1A angular velocities differ significantly, and repeat the comparison with a modified set of NUVEL-1A angular velocities that incorporate the same correction for outward displacement as was used to determine MORVEL.

Angular velocities determined from geodetic measurements constitute the only independent standard against which to compare geologically current angular velocities. As a test of the relative accuracies of the MORVEL, NUVEL-1A, NUVEL-1, RM2 (Minster & Jordan 1978), and P071 (Chase 1978) angular velocities, we compare each of these geologically determined sets of angular velocities to GPS-derived estimates. For this comparison, we assume that the most accurate estimate of plate motions over the past few million years is the one that requires the least amount of change in recent plate motions. We thus assess the accuracy of the geologically derived angular velocities based on their similarity to the GPS-derived angular velocities. Our evaluation also includes a test of whether the correction we make to spreading rates for the effect of outward displacement improves the agreement between the geological and GPS angular velocity estimates. A useful byproduct of this comparison is a catalogue of plate pairs with measurable changes in plate motion since 0.78 or 3.16 Ma.

Our comparison continues with a more in-depth analysis of long-term and geodetic estimates of Pacific–North America plate motion in western North America in order to evaluate the influence of global plate circuit closures on estimates of Pacific–North America motion and describe the factors that limit the accuracy with which Pacific–North America motion can be described over geological timescales absent any unambiguous kinematic data from their mutual plate boundary.

Finally, we briefly describe additional evidence from this work for a relationship between the kinematics and rheology of deformation across diffuse oceanic plate boundaries.

7.1 Fit to MORVEL data with the NUVEL-1 global plate geometry

7.1.1 Effect of single Africa, Australia and South America plates

The MORVEL plate geometry subdivides the Africa, Australia, and South America plates that were assumed for NUVEL-1 and NUVEL-1A into eight plates separated by five diffuse oceanic plate boundaries, with Africa subdivided into the Lwandle, Nubia and Somalia plates, Australia into the Australia, Capricorn and Macquarie plates, and South America into the South America and Sur plates. The simpler NUVEL-1 and NUVEL-1A plate geometries therefore have five fewer plates and 15 fewer estimated parameters than MORVEL. We use the χ^2 statistical test to determine whether the more complex configuration of plate boundaries used for MORVEL significantly improves the fit to the MORVEL data relative to the fit for the simpler NUVEL-1 and NUVEL-1A plate geometries. An inversion of the 2203 MORVEL data while using the latter, simpler geometry gives a least-squares misfit χ^2 of 2835.3. An inversion of the same data with the MORVEL plate geometry gives $\chi^2 = 2255.5$. The $\approx$20 per cent improvement in fit for the MORVEL geometry is significant at a confidence level of one part in 10^{100} ($p < 1 \times 10^{-100}$). The simpler NUVEL-1 plate geometry is thus rejected at high confidence level.

7.1.2 Baja sliver plate and data from the Gulf of California

As a consequence of the assumption in NUVEL-1 that the Baja California peninsula moves as part of the Pacific plate, seafloor spreading rates and transform fault directions from the Gulf of California were used in NUVEL-1 and NUVEL-1A to estimate Pacific–North America plate motion. For reasons described in Section 2.2, we abandoned this assumption for MORVEL. Below, we examine whether significant misfits occur to the MORVEL kinematic data if we restore this assumption and use six 0.78-Myr-average seafloor spreading rates and four well-determined transform fault azimuths from the Gulf of California (give in Tables S1 and S2) to enforce closure of the MORVEL plate circuit.

A simultaneous inversion of the ten additional data from the Gulf of California and the 2203 MORVEL data for a global plate geometry that requires the Baja California peninsula to move with the Pacific plate gives $\chi^2 = 2293.8$. An inversion of the same data while using a plate geometry that includes an independently moving Baja California sliver plate (and hence three additional degrees of freedom) gives $\chi^2 = 2260.7$. The improvement in fit for the plate geometry with an independent Baja sliver plate is significant ($p = 3 \times 10^{-7}$). The MORVEL data are therefore inconsistent with the assumption that spreading rates and directions in the Gulf of California record Pacific–North America plate motion.

There are several possible causes for this apparent inconsistency. One is that differential motion may occur between the Baja California peninsula and Pacific plate, possibly by slip along the Tosco-Abreojos fault along the western edge of the peninsula (Michaud *et al.* 2004) or by slip along normal faults along the eastern edge of the peninsula (e.g. Munguia *et al.* 2006). Alternatively, data errors and possible slow intraplate deformation may accumulate within the global circuit between the Pacific and North America plates, thus complicating efforts to close the global plate circuit across the Gulf of California. We discuss the first hypothesis below and in Section 7.5 test whether the inconsistency may arise from data errors or circuit non-closures within the wider global circuit.

The above inversion of the 2203 MORVEL data and data from the Gulf of California gives a Baja peninsula–North America plate angular velocity of 48.0°N, 81.9°W, −0.814° Myr^{-1}. This angular velocity indicates that the peninsula has moved 48.6 ± 1.2 mm yr^{-1} towards N55.9°W ± 1.9° in the southern Gulf of California for the past 780 000 yr (see also Fig. 47b), representing the best least-squares fit to the spreading rates and fault azimuths from the Gulf of California. The Baja peninsula–Pacific plate angular velocity from

the same inversion, 20.6°S, 42.2°E, 0.113° Myr^{-1}, predicts peninsular motion of 4.8 ± 1.3 mm yr^{-1} towards S11°E ± 16° (shown by the green arrow in Fig. 3) along the Tosco-Abreojos fault at the western edge of the peninsula. A marine seismic and multibeam survey of this fault indicates that it accommodates active, right-lateral transtensional slip (Michaud *et al.* 2004). The right-lateral sense of slip predicted by the angular velocity agrees with the observed sense of slip; however, the angular velocity predicts 2 mm yr^{-1} of contraction across the fault, in disagreement with the marine seismic evidence for a divergent component of motion across the fault.

In the southern Baja peninsula, the Baja–Pacific plate angular velocity predicts peninsular motion of 5.3 ± 0.9 mm yr^{-1} towards S02°E ± 12° (Fig. 3). Within the 95 per cent uncertainties, the velocity agrees with the 3.5 ± 0.8 mm yr^{-1} average rate of motion measured by Plattner *et al.* (2007) for GPS stations in this region. The predicted motion however is directed 43° clockwise of the average S45°E ± 22° direction of motion measured at the same GPS stations.

That the Baja peninsula–Pacific plate angular velocity successfully predicts both the sense of slip along the Tosco-Abreojos fault and rates of motion of GPS sites from the southern Baja peninsula suggests that some of the aforementioned inconsistency between the Gulf of California kinematic data and the MORVEL data and circuit closure conditions can be attributed to slow motion of the Baja peninsula relative to the Pacific plate. The poor agreement between the predicted and observed directions of peninsular motion however suggests that intraplate deformation or data errors elsewhere in the global plate circuit may also contribute to the inconsistency. In Section 7.5, we describe a small, but persistent difference between MORVEL and GPS estimates of the Pacific–North America angular velocity that may be evidence for one or both of these effects.

7.2 NUVEL-1A and MORVEL spreading rate comparison

Given the different techniques and largely non-overlapping sets of magnetic profiles that were used to estimate the 270 NUVEL-1A spreading rates and 1696 MORVEL rates, a comparison of the 3.16-Myr-average NUVEL-1A rates to the subset of the MORVEL rates that also measure motion over the past 3.16 Ma can be used to assess the reproducibility of both sets of plate rates. To first order, we expect the 3.16-Myr-average rates estimated from the best-fitting angular velocities determined from the MORVEL rates (Table 1) to be 0.6–0.7 mm yr^{-1} lower than those estimated from the NUVEL-1A best-fitting angular velocities given that the MORVEL rates are corrected systematically downward by 0.6–0.7 mm yr^{-1} or more to compensate for 2 km or more of outward displacement.

Fig. 21(a) compares spreading rates for all nine plate boundaries along which rates are averaged over 3.16 Ma in both MORVEL and NUVEL-1A. The MORVEL best-fitting rates are lower than their corresponding NUVEL-1A best-fitting rates by an average of 0.63 mm yr^{-1}, in excellent agreement with our expectations. If we adjust the NUVEL-1A spreading rates downward for outward displacement with the same procedures as were used to correct the MORVEL rates, the weighted average difference between the MORVEL and modified NUVEL-1A rates for these nine plate pairs is reduced to only 0.06 mm yr^{-1} (Fig. 21b). The two sets of spreading rates thus agree to within one tenth of a millimetre per year when both are adjusted for outward displacement. This suggests that the 3.16-Myr-average rates given by the MORVEL best-fitting angular velocities are precise to within a few tenths of a millimetre per year.

As a test, we also compared 0.78-Myr-average MORVEL rates for eight plate pairs to the 3.16-Myr-average NUVEL-1A rates for those same plate pairs after correcting both sets of rates for outward displacement (Fig. 21b). The weighted average difference between the two sets of rates is only 0.5 mm yr^{-1} even though they average motion over different intervals. On average, the spreading rates along these eight plate boundaries have therefore changed relatively little since 3.16 Ma. We note however that the 0.78-Myr-average spreading rates along the Nazca–Antarctic and Nazca–Pacific plate boundaries are 7 and 4.5 mm yr^{-1} lower than the 3.16-Myr-average rates, respectively. Both differences are too large to attribute to random errors or other systematic effects, suggesting that opening rates across both of these plate boundaries have slowed down since 3.16 Ma. Further discussion of apparent changes for these and other plate pairs is found in Section 7.4.

7.3 NUVEL-1A and MORVEL angular velocity comparisons

Comparisons of the NUVEL-1A and MORVEL angular velocities with eq. (2) are shown in Fig. 52 for all 29 plate pairs that are common to both studies. Twenty-six of the 29 NUVEL-1A angular velocities lie outside the 3-D 99.99 per cent confidence regions of the MORVEL angular velocities. An inversion of the NUVEL-1A data after correcting all 270 NUVEL-1A spreading rates for outward displacement results in little overall change between the MORVEL and modified NUVEL-1A angular velocities (shown by the red bars in Fig. 52), with differences reduced along 15 of the 29 plate boundaries, increased for 13 plate boundaries, and unchanged for one. Twenty-four of the 29 modified angular velocities still lie outside of the 3-D 99.99 per cent confidence regions of their corresponding MORVEL angular velocities.

The NUVEL-1A estimates of present plate motions thus differ significantly from the MORVEL estimates with or without a correction to the NUVEL-1A spreading rates for outward displacement. The different rate-averaging intervals and plate geometries, and additional data used in the present study therefore lead to significantly different estimates of geologically current plate motions than are given by NUVEL-1A.

7.4 Comparison of MORVEL and NUVEL-1A to plate velocities from GPS

Our comparison of MORVEL and prior estimates of geologically current plate motion to geodetic estimates of current plate motions occurs in two stages. In the first stage, we use eq. (2) to determine the cumulative least-squares difference between angular velocities determined from GPS (Table 6) and the angular velocities that constitute the MORVEL, NUVEL-1A, NUVEL-1, RM2 and P071 estimates of geologically current plate motions (Fig. 53). Included in the analysis is an assessment of the effect of the correction for outward displacement on the level of agreement between angular velocities estimated from GPS station velocities and from the MORVEL and NUVEL-1A data.

In the second stage of the analysis, we compare linear plate velocities that are given by MORVEL, NUVEL-1A and GPS at geographically central locations along selected major plate boundaries (Fig. 54b). This comparison projects the 3-D differences between the angular velocities onto a 2-D linear site velocity difference and is therefore less rigorous than the comparison that employs eq. (2). The results of the comparison are however easier to interpret in the

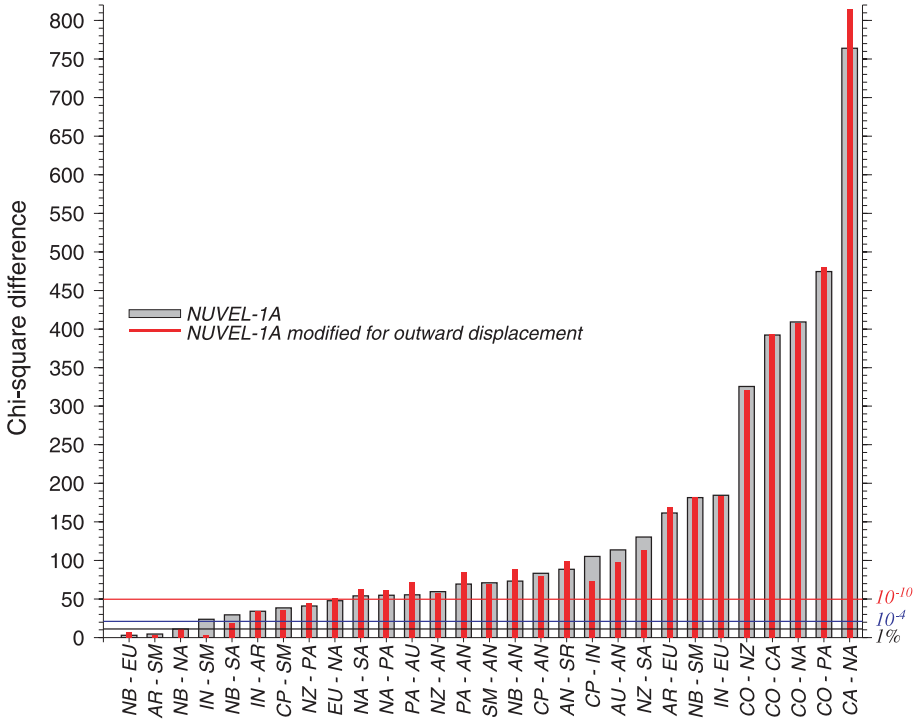

Figure 52. Statistical test for consistency between MORVEL, NUVEL-1A and modified NUVEL-1A angular velocities for shared plate pairs. Grey bars show chi-square difference from eq. (2) for NUVEL-1A relative to its corresponding MORVEL angular velocity and covariances (Table 3). Red bars show chi-square difference from MORVEL using eq. (2) for angular velocities derived from the NUVEL-1A data after corrections are made to all NUVEL-1A spreading rates for outward displacement. Black, blue and red lines show values of chi-square for which differences between the two estimates are significant at respective levels of 99, 99.99 per cent, and 1 part in 10^{10}. Plate abbreviations are defined in Fig. 1.

Table 6. Angular velocities and covariances from GPS station velocities.

Plate pair	Angular velocity			Variances and covariances					
	Lat. (°N)	Long. (°E)	ω (deg Myr $^{-1}$)	a	b	c	d	e	f
AU-AN	13.9	39.4	0.650	0.26	−0.12	0.07	0.23	−0.21	0.77
NB-AN	5.9	−41.6	0.120	0.62	0.01	−0.01	0.19	−0.12	0.82
NZ-AN	37.0	−92.3	0.442	0.45	0.73	0.15	5.02	1.04	1.48
SM-AN	26.5	−72.6	0.133	1.36	0.98	−0.55	1.04	−0.54	1.07
NB-EU	−9.1	−24.9	0.054	0.59	0.00	0.09	0.11	0.00	0.26
EU-NA	74.2	134.1	0.237	0.04	0.01	0.05	0.04	−0.01	0.09
NB-NA	83.7	82.1	0.221	0.55	−0.01	0.05	0.13	−0.03	0.21
AN-PA	65.1	−83.2	0.872	0.24	0.04	−0.07	0.13	−0.11	0.69
AU-PA	60.6	3.9	1.087	0.36	−0.10	0.12	0.17	−0.10	0.19
NA-PA	50.2	−74.5	0.759	0.17	0.03	−0.01	0.07	−0.02	0.08
NZ-PA	55.8	−87.6	1.278	0.54	0.74	0.19	4.96	1.14	0.90
AN-SA	89.2	−169.3	0.224	0.39	−0.23	−0.19	0.46	0.05	0.86
NA-SA	6.8	−51.4	0.134	0.32	−0.24	−0.14	0.39	0.14	0.25
NB-SA	63.5	−42.8	0.263	0.87	−0.25	−0.09	0.46	0.15	0.43
NZ-SA	54.1	−92.8	0.604	0.70	0.47	0.07	5.29	1.31	1.08
IN-SM	21.3	23.1	0.386	5.18	16.76	3.41	68.93	16.43	5.06
AR-EU[1]	28.4	18.4	0.428	–	–	–	–	–	–
AR-SM[1]	20.3	27.4	0.455	–	–	–	–	–	–
IN-EU[2]	23.4	5.4	0.352	–	–	–	–	–	–

Notes: Covariances are Cartesian and have units of 10^{-8} rad^{2}Myr^{-2}. See note of Table 1 for other conventions used in this table and Fig. 1 for plate abbreviations. Angular velocities for all plate pairs are derived solely from GPS station velocities from the interiors of the specified plates. GPS station locations are shown in Fig. 54(a). ITRF2005 is the geodetic reference frame implicitly used for all of the station velocities used to derive these angular velocities except for the AR-EU, AR-SM and IN-EU estimates. [1] From Reilinger *et al.* (2006). [2] From T. Apel (personal communication, 2007). Numbers of GPS stations per plate are as follows: AN (9), AU (19), EU (73), IN (4), NA (457), NB (10), NZ (4), PA (21), SA (9) and SM (6).

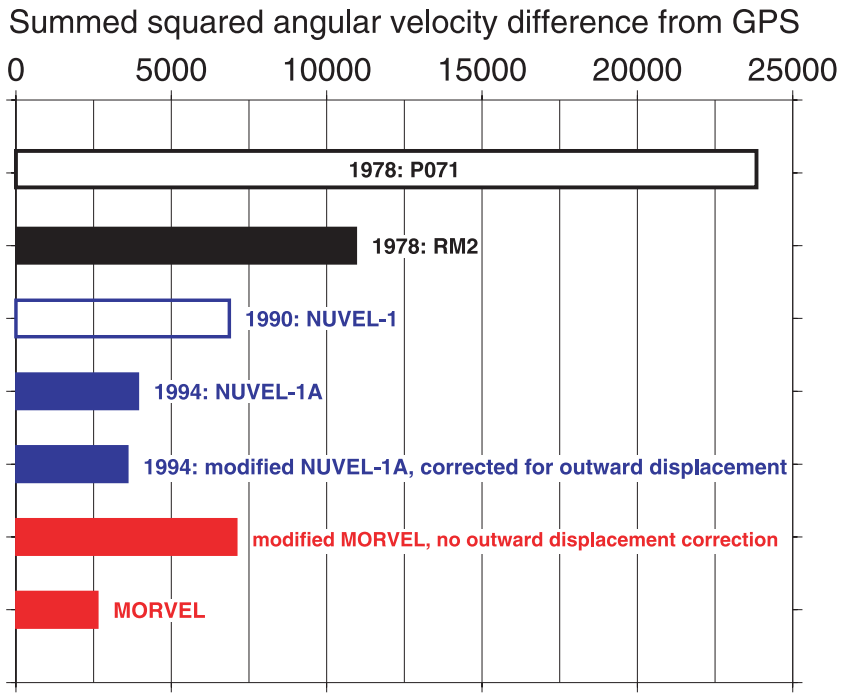

Figure 53. Sums of squared differences from eq. (2) between GPS-derived angular velocities from Table 6 and the closure-enforced angular velocities for seven geological estimates of global plate motions, as follows: P071 (Chase 1978), RM2 (Minster & Jordan 1978), NUVEL-1 (DeMets *et al.* 1990), NUVEL-1A (DeMets *et al.* 1994a), MORVEL and alternative estimates based on the NUVEL-1A and MORVEL data. Due to differences in how the original angular velocity uncertainties were computed for the different geological estimates, only the covariances for the GPS-derived angular velocities are used in eq. (2) to determine the weighted, summed-square difference. Angular velocity comparisons are limited to the plates for which both geological and GPS estimates are available, consisting of the Antarctic, Australia, Eurasia, India, Nubia (AF), Nazca, North America, Pacific, South America and Somalia (AF) plates. Locations of GPS stations used to estimate the plate angular velocities are shown in Fig. 54. Further details about the comparison are given in the text.

context of the correction that we make for outward displacement and the magnitude of recent changes in plate motions along some plate boundaries.

Our GPS-based estimates of plate rates are determined from two sources. Station velocities determined solely from GPS measurements are used to estimate 19 angular velocities (Table 6) that best describe the relative motions of ten plates with enough GPS stations to reliably estimate their motions (Fig. 54a). These 19 plate pairs include most or all the plate boundaries across which motion can be estimated reliably with GPS, MORVEL, and NUVEL-1A. Sixteen of the 19 angular velocities are estimated from the velocities of 612 GPS stations (Fig. 54a) for which daily data are processed at the University of Wisconsin. These are supplemented with angular velocities for the Arabia-Eurasia, Arabia–Somalia and India–Eurasia plate pairs from Reilinger *et al.* (2006) and T. Apel (personal communication, 2007) (Table 6). Geocentre translation rate corrections are applied to the geodetic velocities, as described in Section 4.4, to minimize the effect of a likely error in the geocentre translation rates that are applied in ITRF2000 and ITRF2005 (Argus 2007). Other effects may also increase the errors in GPS-based estimates of plate motions, including the protracted viscoelastic response of the mantle to large earthquakes (Pollitz *et al.* 1998), isostatic glacial rebound (Argus *et al.* 1999; Calais *et al.* 2006b; Sella *et al.* 2007), and errors in satellite antenna phase centre offsets (Cardellach *et al.* 2007). No effort is made here to correct for these.

7.4.1 Angular velocity comparisons

Fig. 53 shows a comparison of MORVEL and other geological angular velocity estimates to GPS-based angular velocities for all ten plates with enough GPS stations to estimate well-constrained angular velocities (the ten plates are listed in the caption to Fig. 53). The North America plate is fixed for the comparison and the angular velocities of the other nine plates are specified relative to North America. Eq. (2) is applied to find the cumulative, weighted least-squares difference between the Cartesian components of the geodetically and geologically determined angular velocities for the nine moving plates. Only the covariances in the GPS-based angular velocities are used for the calculation, thereby enabling a meaningful comparison of the weighted least-squares differences between each set of geologically estimated angular velocities and the GPS-based angular velocities.

The MORVEL angular velocities agree better with the angular velocities estimated from GPS than any of the other geological models, with a least-squares difference (χ^2) of 2634 (Fig. 53). If we omit the correction to the MORVEL spreading rates for outward displacement, re-invert the modified MORVEL data and compare the modified angular velocities to the GPS-based angular velocities, χ^2 increases to 7104, 270 per cent higher than for MORVEL. The improvement in fit for the single additional fitting parameter (outward displacement) is significant ($p < 1 \times 10^{-100}$). The correction for outward displacement is thus strongly validated by the improved agreement between the geologically estimated plate motions and the independent geodetic estimates.

The least-squares difference between the NUVEL-1A and GPS-based angular velocities is 50 per cent higher than for MORVEL (Fig. 53). Angular velocities determined from the NUVEL-1A data after applying corrections for outward displacement to the NUVEL-1A spreading rates agree better with the GPS estimates, but are still 37 per cent higher than for MORVEL. The correction for outward

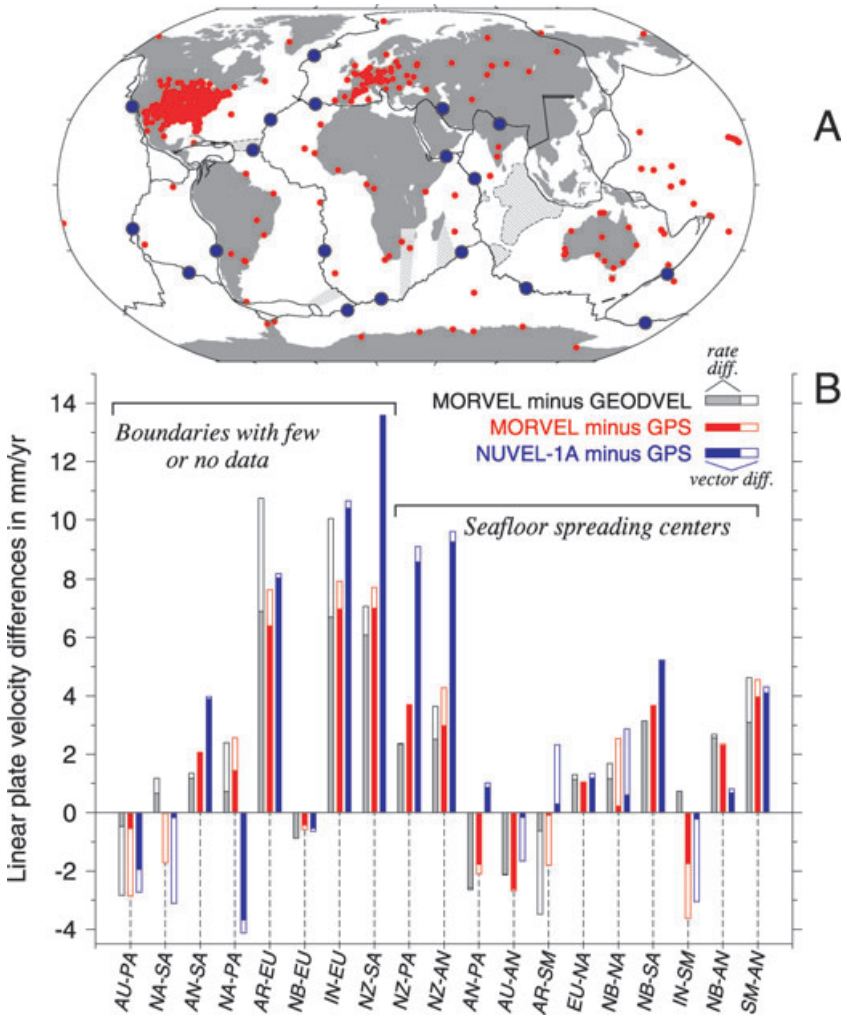

Figure 54. (a) Locations of continuous GPS stations (red) that are used to estimate motions of designated plate pairs at locations shown by the blue circles. (b) Red bars show differences between relative plate velocities determined with MORVEL and GPS (Table 6). Blue bars show differences between relative plate velocities determined with NUVEL-1A and GPS (Table 6). Grey bars show differences between plate velocities determined using MORVEL and GEODVEL, which is a set of plate angular velocities determined from GPS, very-long-baseline interferometry, satellite laser ranging and radio beacon (DORIS) data (Argus *et al*. 2010). The shaded area of each bar shows the difference in the estimated velocity magnitudes. The shaded and unshaded areas together indicate the magnitude of the velocity vector difference and thus also include any difference in the calculated directions. Velocities are determined at the following locations: AU-PA (40.7°S, 176.9°E); NA-SA (16.0°N, 50.0°W); NA-PA (36.0°N, 120.6°W); AR-EU (35.0°N, 50.0°E); NB-EU (37.1°N, 20.0°W); IN-EU (28.0°N, 80.0°E); NZ-SA (30.0°S, 72.0°W); NZ-PA (20.0°S, 113.7°W); NZ-AN (40.0°S, 91.6°W); AN-PA (64.1°S, 168.8°W); AU-AN (47.2°S, 100.3°E); AR-SM (13.2°N, 51.0°E); EU-NA (60.0°N, 29.3°W); NB-NA (30.0°N, 42.8°W); NB-SA (30.0°S, 13.8°W); AN-SA (57.8°S, 6.9°W); IN-SM (3.0°N, 65.5°E); NB-AN (52.2°S, 15.0°E) and SM-AN (30.5°S, 60.0°E).

displacement has a smaller impact on the level of agreement between NUVEL-1A and GPS than it does for MORVEL because the correction is about a factor of four smaller ($\approx$0.7 mm yr^{-1}) for the 3.16-Myr-average NUVEL-1A spreading rates than for the 0.78-Myr-average MORVEL spreading rates ($\approx$2.6 mm yr^{-1}). This emphasizes the importance of correcting for outward displacement when testing for changes in plate motion since 1 Ma.

Finally, the least-squares differences between GPS-determined angular velocities and the angular velocities that constitute NUVEL-1, RM2 and P071 are respectively 260, 420 and 900 per cent higher than for MORVEL. Successive generations of global plate motion estimates have thus more closely approached geodetically measured plate motions.

7.4.2 Linear velocity comparisons for spreading centres and other plate boundaries

Fig. 54(b) shows in more detail the relative motions of 19 major plate pairs estimated with MORVEL, NUVEL-1A and GPS. Eleven of the 19 plate pairs shown in Fig. 54(b) are separated by seafloor spreading centres and thus have well constrained angular velocities determined from spreading rates and transform fault azimuths. At central locations along these 11 plate boundaries (indicated by blue circles in Fig. 54a), the magnitude of the mean differential velocity between the 11 MORVEL and GPS estimates is only 1.1 mm yr^{-1}, 60 per cent smaller than the 2.9 mm yr^{-1} mean differential velocity between the NUVEL-1A and GPS estimates. On average, the plate motions determined with MORVEL thus agree better with

the GPS estimates than do the NUVEL-1A estimates. The rms difference between the MORVEL and GPS plate motion estimates is 2.9 mm yr^{-1}, 20 per cent smaller than the 3.8 mm yr^{-1} rms difference between NUVEL-1A and GPS. The MORVEL estimates thus also exhibit less dispersion about the GPS estimates than do plate motions determined with NUVEL-1A.

We attribute this improved agreement to four factors: (1) the MORVEL spreading rates are adjusted downward to compensate for outward displacement, (2) many MORVEL spreading rates average motion since 0.78 Ma and thus better approximate current plate motions than do the 3.16-Myr-average NUVEL-1A rates, (3) accuracy is improved in MORVEL due to the many more kinematic data that are used and (4) the MORVEL plate geometry is improved relative to that used for NUVEL-1A.

Fig. 54(b) also shows a comparison of plate motion estimates for eight plate pairs with convergent or complexly deforming plate boundaries. Because the MORVEL and NUVEL-1A data include few or no kinematic data from any of these eight plate boundaries, the MORVEL and NUVEL-1A angular velocities for these eight plate pairs are determined mostly or entirely from plate circuit closures. A comparison of the MORVEL, NUVEL-1A and GPS motion estimates for these eight plate boundaries thus constitutes a strong test of the predictive capabilities of the two geological models.

Encouragingly, the velocities predicted by MORVEL agree better with the GPS estimates for seven of the eight plate pairs than do the NUVEL-1A estimates (Fig. 54b). Differences between the MORVEL and GPS velocity predictions are smaller than 3 mm yr^{-1} for five of the eight plate pairs, a level of agreement that is achieved for only two plate pairs for NUVEL-1A. The rms dispersion of the eight MORVEL estimates relative to GPS is 4.1 mm yr^{-1}, 30 per cent smaller than that for the NUVEL-1A estimates (5.9 mm yr^{-1}).

NUVEL-1A predicts motions for the Arabia–Eurasia, India–Eurasia and Nazca–South America plate pairs that differ from their GPS estimates by respective values of 8.2, 10.7 and 13.6 mm yr^{-1} (Fig. 54b). Although MORVEL reduces these surprisingly large differences to values of 6.4–7.7 mm yr^{-1}, the remaining velocity differences nonetheless still exceed by a factor of two or more the combined uncertainties in the MORVEL and GPS estimates ($\approx \pm 2$–3 mm yr^{-1}) . In the following section, we discuss whether these differences may be evidence for recent changes in motion for these three plate pairs.

Fig. 54(b) also shows a comparison of the MORVEL plate velocity estimates for the same 19 plate pairs to velocities estimated with GEODVEL, which is a set of angular velocities determined from DORIS, GPS, satellite laser ranging and very long baseline interferometry data (Argus *et al.* 2010). For 17 of the 19 plate pairs, the velocities estimated with GEODVEL and the GPS-derived angular velocities in Table 6 agree to 1 mm yr^{-1} or better. The two plate pairs for which the GEODVEL and GPS velocities differ by more than 1 mm yr^{-1} involve the India or Nazca plates, which have the fewest geodetic sites of the major plates and are thus likely to have less robust velocity estimates. None of the conclusions that we reach above change if we use GEODVEL instead of GPS as the basis for the comparison to MORVEL and NUVEL-1A.

7.4.3 Evidence for changes since 1–3 Ma in Arabia, India and Nazca plate motions

The largest differences between the MORVEL and GPS angular velocities for the 19 plate pairs considered above occur along the boundaries of the Nazca, India and Arabia plates. These three plates have the fewest continuous GPS stations of the major plates that are included in this analysis. Their geodetic estimates may thus be less robust and could be systematically in error by as much as several millimetres per year. Alternatively, the differences might be evidence for non-rigidity in the global plate circuit or that the motions of one or more of these plates have changed in the past few million years, which we discuss below.

The implied slowdowns in the motions of the Nazca plate relative to the Pacific, Antarctic and South America plates (Fig. 54b) are consistent with kinematic evidence reported by Tebbens *et al.* (1997), Angermann *et al.* (1999) and Norabuena *et al.* (1999) for a slowdown in Nazca plate motion over the past several million years. As is shown by Fig. 54(b), the 3.16-Myr-average seafloor spreading rates estimated with NUVEL-1A along both the Nazca–Antarctic and Nazca–Pacific plate boundaries are 9–10 mm yr^{-1} higher than their corresponding GPS estimates, whereas the 0.78-Myr-average MORVEL spreading rates are only 3–4 mm yr^{-1} higher. The time sequence of spreading rates along both plate boundaries thus defines progressive, similar slowdowns in spreading rates for both. Convergence between the Nazca and South America plates across the Peru–Chile trench has also slowed rapidly since 3.16 Ma; the 3.16-Myr-average NUVEL-1A and 0.78-Myr-average MORVEL convergence rates are 14 ± 2 and 7 ± 2 mm yr^{-1} higher than the GPS estimate for this plate pair, respectively.

The progressive deceleration of spreading rates along the western and southern divergent boundaries of the Nazca plate and slowdown in convergence across the Peru–Chile trench at the eastern edge of the Nazca plate are consistent with a slowdown in the eastward component of the Nazca plate's absolute motion since at least 3.16 Ma. Iaffaldano *et al.* (2006) hypothesize that the growing load of the Andean mountain belt above the Peru–Chile trench has gradually increased the frictional forces that resist the eastward subduction of the Nazca plate beneath South America, thereby slowing down their relative motion. We note that the same proposed increase in coupling might also be expected to increase the Nazca plate's eastward push on South America and hence cause a slowdown in seafloor spreading rates in the southern Atlantic. In support of this, our GPS estimate for Nubia–South America motion along the southern Mid-Atlantic ridge is 3.7 mm yr^{-1} lower than the 3.16-Myr-average MORVEL estimate for this plate pair (Fig. 54b).

Along the India–Eurasia plate boundary, the NUVEL-1A and MORVEL motion estimates are 10.7 and 7.9 mm yr^{-1} higher than the GPS estimate (Fig. 54b), respectively. Despite the improved consistency between the MORVEL and GPS estimates, the 7.9 mm yr^{-1} difference between the two estimates exceeds their combined uncertainties of ± 1–2 mm yr^{-1}. Convergence across this plate boundary may thus have slowed since 3.16 Ma. A similarly large 7.6 mm yr^{-1} difference between the MORVEL and GPS estimates for Arabia-Eurasia motion may also indicate a recent slowdown in convergence between these two plates (Fig. 54b).

7.5 Test for global circuit closure: Pacific–North America plate motion

Unlike prior estimates of global plate motion, no data from the Pacific–North America plate boundary are used to determine the MORVEL angular velocities (Fig. 2). Pacific–North America motion predicted by MORVEL can therefore be compared with independent estimates without any circularity. We next compare GPS and MORVEL estimates of Pacific–North America plate motion and document a small, but apparently robust difference between the geodetic and MORVEL estimates. To better understand the cause(s)

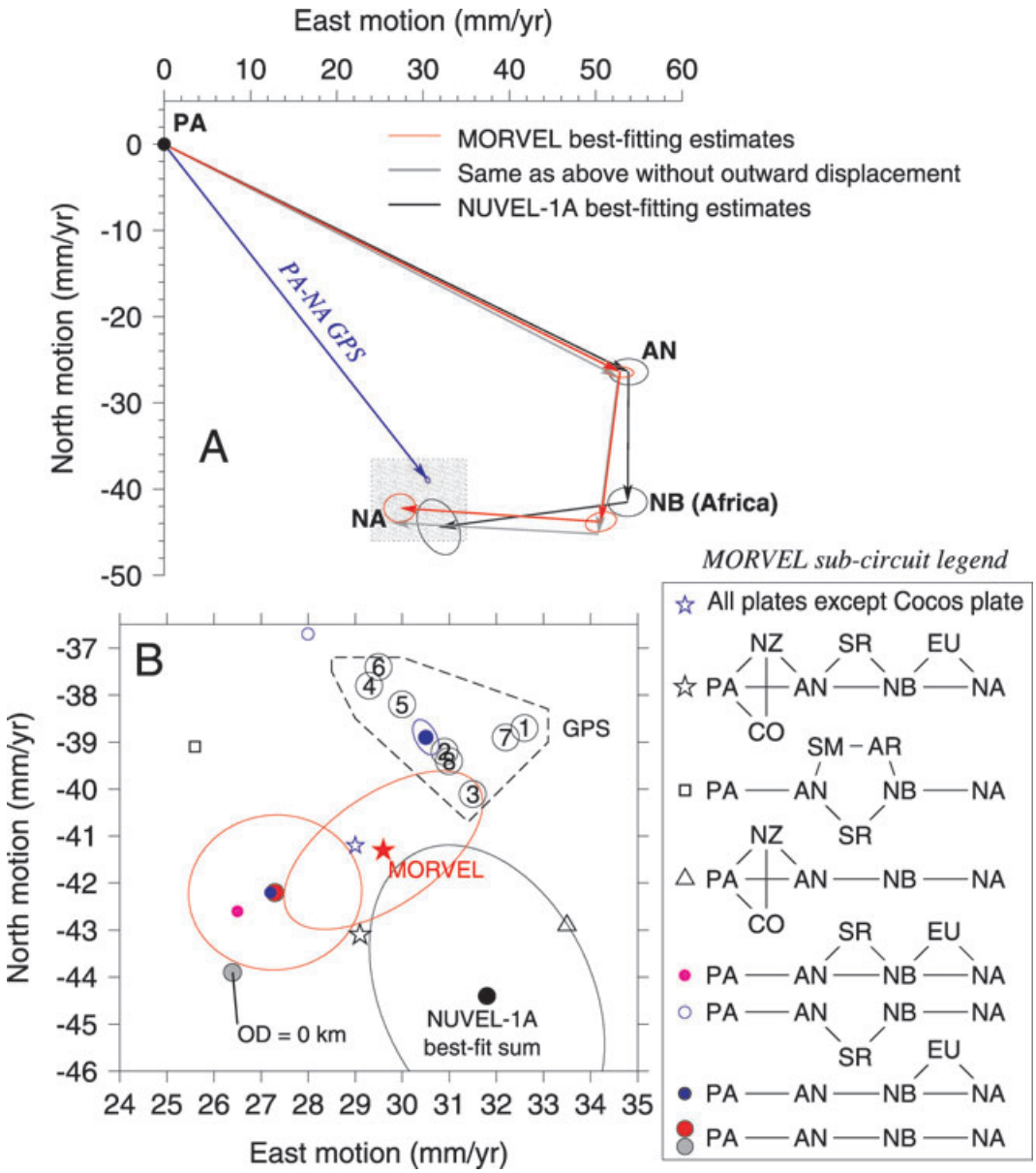

Figure 55. Pacific–North America plate circuit analysis. (a) Linear velocities at 36.0°N, 120.6°W along the San Andreas fault predicted by best-fitting angular velocities determined from the MORVEL data with and without corrections for outward displacement (red and grey, respectively), best-fitting angular velocities determined from the NUVEL-1A data (black), and from GPS (Table 6). No circuit closures are enforced for this plate circuit. Shaded area is enlarged in (b). Plate abbreviations are specified in caption to Fig. 1. (b) North America–Pacific plate motion estimates at 36°N, 120.6°W from different subsets of the MORVEL plate circuits and data (specified in the legend). GPS-based estimates are as follows: 1, DeMets & Dixon (1999); 2, Beavan *et al.* (2002); 3, Sella *et al.* (2002); 4, Gonzales-Garcia *et al.* (2003); 5, Marquez-Azua *et al.* (2004); 6, Plattner *et al.* (2007); 7, Kogan & Steblov (2008) and 8, Argus *et al.* (2010). Blue circle with ellipse is the GPS estimate from this study (Table 6). All ellipses are 2-D, 1σ.

of this difference, we explore the factors that may influence the MORVEL estimate of Pacific–North America motion (Fig. 55), including small systematic errors that may remain in the geological data or plate-circuit closures, and hypothesized horizontal thermal contraction of the Pacific plate (Kumar & Gordon 2009) or possibly other plates.

7.5.1 Effects of local plate circuit closures and outward displacement

Fig. 55 summarizes estimates of Pacific–North America motion from different GPS velocity solutions and different combinations of the MORVEL data circuits. The shortest plate circuit that links the Pacific and North America plates, corresponding to the circuit widely used in estimating late Cenozoic motion between the Pacific and North America plates (e.g. Atwater & Stock 1998; Wilson *et al.* 2005; Royer *et al.* 2006), is the Pacific–Antarctic–Nubia–North America circuit. A sum of the three best-fitting angular velocities for the plate pairs in this circuit (PA-AN, AN-NB and NB-NA) results in a Pacific–North America angular velocity that predicts motion of 50.2 ± 1.1 mm yr^{-1} towards N32.8°W $\pm$ 1.4° (1σ) along the San Andreas fault in central California. For comparison, our GPS-determined Pacific–North America angular velocity (Table 6) gives motion of 49.4 ± 0.3 mm yr^{-1} towards N38.1°W $\pm$ 0.2° (1σ),

slower than, and significantly anticlockwise (5.3° ± 1.4°) of, the geological estimate. The differential velocity between these two estimates has a magnitude of 4.6 ± 2.6 mm yr^{-1} (95 per cent). Absent any correction for outward displacement, the magnitude of the differential velocity between the best-fitting MORVEL estimate and the GPS estimate increases by 40 per cent to 6.4 ± 2.6 mm yr^{-1} (95 per cent) (Fig. 55b).

Repeating the same calculation with the NUVEL-1A best-fitting angular velocities for the same plate pairs results in a predicted velocity of 54.6 ± 2.3 mm yr^{-1} towards N35.7°W ± 1.6° (1σ) at the same location. The differential velocity magnitude is 5.6 ± 4.9 mm yr^{-1} (95 per cent) (Fig. 55b), 20 per cent larger than for the MORVEL best-fitting angular velocity.

The full MORVEL plate circuit predicts motion in central California that differs by 2.6 ± 1.7 mm yr^{-1} (95 per cent uncertainty) from the GPS estimate (Fig. 55b). Although this is more than 40 per cent smaller than the differential velocity for the best-fitting plate circuit, a comparison of the MORVEL and GPS Pacific–North America angular velocities with eq. (2) gives $p = 0.003$, indicating that the difference between the two estimates is significant at the 99.7 per cent confidence level.

We examined whether the difference between the GPS and MORVEL estimates may be a consequence of the previously described non-closures of the Nazca–Cocos–Pacific or Antarctic–Sur–Nubia plate circuits (Section 6.2). Beginning with the former circuit, we relaxed the requirement for closure around this plate circuit and re-inverted the MORVEL data. The resulting differential velocity between the GPS and modified MORVEL estimates for the Pacific–North America plate pair changes negligibly, to 2.7 mm yr^{-1} from its previous value of 2.6 mm yr^{-1} (shown by the open blue and red stars in Fig. 55b). Relaxing the closure requirement for the latter plate circuit also changes the differential velocity negligibly, to 2.4 mm yr^{-1}. The difference between the GPS and MORVEL estimates of Pacific–North America motion is thus not an artefact of non-closures of either of these two plate circuits.

We also tested numerous other combinations of the MORVEL plate circuits (shown in the legend at the right-hand side of Fig. 55b), but none predict motion closer to the GPS estimate than does the full MORVEL solution. This may be evidence that each plate circuit closure in MORVEL incrementally improves the accuracy of the estimated Pacific–North America angular velocity, such that the most accurate solution is the one with the most circuits that satisfy closure (MORVEL).

7.5.2 Comparison to geodetic estimates

We also investigated whether other geodetic estimates of Pacific–North America motion agree more closely with the MORVEL estimate than does our own (Fig. 55b). Of the seven additional geodetic estimates we examined, the Sella *et al.* (2002) REVEL GPS estimate has the smallest vector magnitude difference from MORVEL (2.2 mm yr^{-1}) and differs the least from the MORVEL angular velocity ($p = 0.33$ with eq. 2). All four recent GPS estimates for Pacific–North America motion (including our own) differ from MORVEL at the 99.7 per cent or greater confidence level (Plattner *et al.* 2007; Kogan & Steblov 2008; Argus *et al.* 2010). All eight of the geodetic solutions give motion that is 2–4° anticlockwise from the geological estimate.

We evaluated whether the corrections we make to our GPS station velocities for the motion of ITRF2005 relative to the geocentre (Argus 2007) significantly affect the magnitude of the velocity difference between the GPS and geological estimates, but found that eliminating these corrections only increases the estimated velocity differential by 0.1 mm yr^{-1}.

The persistent differences between the GPS and MORVEL estimates of Pacific–North America motion thus seem unlikely to be an artefact of either a particular geodetic reference frame or a particular geodetic solution.

7.5.3 Influence of the Kane transform fault

The Kane transform fault, which lies along the Nubia–North America plate boundary several hundred kilometres north of the poorly defined North America–South America plate boundary, is the worst fit, high importance datum that influences the MORVEL Pacific–North America angular velocity (Figs 20b and 24b). Excluding this datum and re-inverting the remaining MORVEL data reduces the difference between the GPS-determined Pacific–North America velocity and the modified MORVEL estimate in central California to 1.93 ± 1.8 mm yr^{-1} (95 per cent), one-fourth smaller than for MORVEL (2.6 ± 1.7 mm yr^{-1}). A comparison of these two angular velocity estimates with eq. (2) gives $p = 0.051$. The two estimates thus differ insignificantly.

It seems unlikely that the 2.6° misfit of MORVEL to the azimuth of the Kane transform fault can be attributed to an error in our estimate of the azimuth of this fault. A Sea Beam survey of the 150-km-long transform valley (Pockalny *et al.* 1988) reveals a narrow (3-to 6-km-wide), uninterrupted linear zone of strike-slip tectonism that connects the eastern and western ridge-transform intersections. Pockalny *et al*. estimate an azimuth of 98° for the transform tectonized zone, only 1° different from our own estimate (99° ± 0.9°). They further interpret the linearity and continuity of the transform fault zone as evidence that the direction and locus of strike-slip plate motion have remained steady since at least 10 Ma.

If the poor fit to the Kane transform fault is evidence that distributed deformation between the North and South America plates extends north to, and includes, the Kane transform fault, then the many spreading rates from south of the Kane transform fault that are used to estimate the Nubia–North America angular velocity may also bias the MORVEL Pacific–North America angular velocity. When we eliminate both the Kane transform fault and these spreading rates and invert the remaining MORVEL data, the resulting differential velocity between the GPS and modified MORVEL estimate is 1.87 ± 1.79 mm yr^{-1}, negligibly lower than if we eliminate only the Kane transform fault (1.93 ± 1.8 mm yr^{-1}). The spreading rates thus neither support nor exclude the hypothesis that distributed deformation between the North and South America plates extends north to the Kane transform fault.

We thus find that the mismatch between the MORVEL and GPS estimates of Pacific–North America plate motion can be reduced by eliminating the poorly fit Kane transform fault, but at the cost of distributing the deformation that accommodates motion between the North America and South America plates over a much wider boundary east of the Lesser Antilles trench. Absent any independent additional evidence that the zone of deformation between the North and South America plates extends as far north as the Kane transform fault, this remains a topic for further research.

7.5.4 Plate motion changes or thermal contraction as cause of non-closure

We cannot exclude the possibility that the difference between the GPS and MORVEL estimates of Pacific–North America plate motion is caused by a possible ≈2° anticlockwise change in the

direction of Pacific–North America motion in the past 3.16 Myr. Detecting a change this small would be difficult or impossible given the uncertainties and limited temporal resolution of published reconstructions of Neogene Pacific–North America plate motions (Atwater & Stock 1998; Argus & Gordon 2001; Wilson *et al.* 2005). A geologically recent, 2° anticlockwise rotation of Pacific–North America motion would have decreased by 2 mm yr^{-1} the convergent component of plate motion orthogonal to the strike-slip plate boundary in the Gulf of California and San Andreas fault. The post-3.16 Ma deformation histories of the Pacific–North America plate boundary faults might thus also be used to test for a change in motion.

Thermal contraction of the Pacific plate (Kumar & Gordon 2009) and other plates, or near-ridge thermal contraction that could affect transform faults may also contribute to the difference between the geodetic and geological estimates. The size and direction of the contributions of thermal effects is however not well quantified. Horizontal thermal contraction within the Pacific plate as the lithosphere ages, cools, and subsides would cause young Pacific plate lithosphere to move slowly relative to the old part of the Pacific plate. Simple forward calculations of the horizontal thermal contraction of the Pacific plate integrated from the Pacific–Antarctic rise to the southern Baja California peninsula suggest that contraction-induced displacements as fast as ≈10 mm yr^{-1} could occur between different points on the Pacific plate (Kumar & Gordon 2009). Recent geodetic work shows that the island of Guadalupe, which lies west of Baja California on the youngest seafloor of any Pacific plate site, moves at 2.0 ± 1.2 (95 per cent) mm yr^{-1} towards 149° relative to the older part of the Pacific plate [see fig. 3 of Plattner *et al.* (2007)]. This velocity may be consistent with the pattern of strain due to hypothesized thermal contraction. Baja California also moves relative to the Pacific plate at ≈3–4 mm yr^{-1} to the south–southeast. Plattner *et al.* (2007) convincingly argue for a separate Baja microplate, but part (i.e. ≈2 mm yr^{-1}) of the difference between the motion of Baja California and the older part of the Pacific plate may also be due to thermal contraction of young Pacific Oceanic lithosphere.

7.6 Poles of rotation in diffuse oceanic plate boundaries

The poles that describe the relative motions of plates separated by a diffuse oceanic plate boundary tend to lie in the diffuse plate boundary (Gordon 1998). The MORVEL results confirm this pattern (e.g. Figs 12 and 13), with the following poles lying in or near their mutual diffuse oceanic plate boundary: Australia–Capricorn, Australia–Macquarie, Capricorn–India, Lwandle–Somalia, North America–South America and Nubia–Somalia. The pole of rotation for the diffuse continental Eurasia–North America boundary also appears to follow this pattern (Fig. 12). An analysis of the torques across such boundaries suggests that plates are tightly coupled across them, more so than plates separated by a traditional narrow plate boundary, which tend to have poles of rotation far from the boundaries (Zatman *et al.* 2001, 2005). That the poles of rotation for some plate pairs lie near but not in their mutual boundaries, such as Nubia–Eurasia, Cocos–Nazca, Cocos–Caribbean and Rivera–North America, may also indicate relatively strong coupling across those plate boundaries.

8 CONCLUSIONS

MORVEL describes the motions of 25 tectonic plates, including all major plates, most smaller oceanic plates, and several continental plates in eastern Asia not included in prior geological models. The global plate geometry differs substantially from that used for prior geological models, most notably for the former Africa and Australia plates. The data used to estimate the MORVEL angular velocities were compiled from archives and investigators in ten countries and greatly improve the geographic coverage and quality of mid-ocean ridge spreading rates and transform fault azimuths relative to prior efforts. GPS station velocities are used to estimate angular velocities for several smaller plates with motions that would otherwise be poorly constrained or unconstrained by conventional data, but in a manner that avoids influencing relative motion estimates for the other plates. Fewer than 1 per cent of the data from NUVEL-1 and NUVEL-1A were used to estimate MORVEL. Some of the main results and differences from prior studies are enumerated below.

(1) All MORVEL spreading rates are adjusted downward 0.6–2.6 mm yr^{-1} to compensate for 2 km of outward displacement along most spreading centres. This correction decreases by 30 per cent the degree of MORVEL global circuit non-closure relative to that for NUVEL-1A and significantly improves the agreement between the MORVEL and independent GPS estimates of plate motions. Estimated uncertainties in the correction for outward displacement are propagated systematically into the MORVEL angular velocity covariances to provide more realistic uncertainties in estimates of present plate motions.

(2) The 1696 spreading rates, 163 transform fault azimuths, and 56 earthquake slip directions in MORVEL are well fit by the closure-enforced MORVEL angular velocities, as evidenced by the absence of systematic misfits at most locations. Although this indicates that the rigid plate approximation is useful, five diffuse plate boundaries in the Indian Ocean, comprising large areas of oceanic lithosphere, are required to achieve acceptable fits in this region. Data around the Galapagos and Bouvet triple junctions fail tests for circuit closure and thus differ significantly from consistency with the rigid plate hypothesis. The causes of both circuit non-closures are unclear, but may include deformation of one or more of the plates in these circuits, at least in part by thermal contraction. We conclude that the rigid plate approximation continues to be tremendously useful, but—absent any unrecognized systematic errors—the plates deform measurably, possibly by thermal contraction and wide plate boundaries with deformation rates near or beneath the level of noise in plate kinematic data.

(3) Global best-fitting and closure-enforced angular velocities for the Pacific–North America plate pair both differ at high confidence level from GPS estimates of Pacific–North America motion, though less so than for NUVEL-1A. Possible reasons for the persistent difference between geodetic and geological estimates of Pacific–North America plate motion include a potentially wider zone of deformation between the North and South America plates than is assumed for MORVEL, a small anticlockwise change in Pacific–North America plate motion over the past 1–3 Myr, or deformation of one or more of the plates in the global circuit, possibly by thermal contraction.

(4) Various measures of the precision and likely accuracy of MORVEL indicate that it improves on, and differs from, all prior estimates of geologically current plate motions. In particular, 26 of the 29 MORVEL angular velocities for plate pairs with well determined motions differ at the 99.9 per cent confidence level from their NUVEL-1A counterparts, and the MORVEL angular velocities differ less from GPS estimates and hence imply steadier plate motions since 3.16 Ma than all prior geological estimates. The plate boundaries where the largest differences between the

MORVEL and GPS estimates remain, namely the Nazca–South America, Nazca–Antarctic, Nazca–Pacific, India–Eurasia and Arabia–Eurasia plate boundaries, are candidates for likely changes in motion during the past 3.16 Myr.

(5) The relative rotation poles of plates separated by a diffuse oceanic plate boundary tend to lie in the diffuse plate boundary. Examples include the India–Capricorn, Capricorn–Australia, Australia–Macquarie, Lwandle–Somalia, Nubia–Somalia, North America–South America and Eurasia–North America plate pairs and boundaries. This pattern indicates that plates are more strongly coupled across diffuse oceanic plate boundaries than they are across narrow plate boundaries (Zatman *et al.* 2001, 2005).

ACKNOWLEDGMENTS

The following individuals, whom we thank, kindly contributed published and unpublished original data that were critical for this project: Daniel Aslanian, Anne Briais, John Brozena, Steve Cande, Mathilde Cannat, Jim Cochran, Rajendra Drolia, Javier Escartin, Marc Fournier, Toshiya Fujiwara, Pascal Gente, Jean Goslin, Nancy Grindlay, Allegra Hosford, Philippe Huchon, Jill Karsten, Teruyuki Kato, Skip Kovacs, Tim Le Bas, Marco Ligi, Roy Livermore, Emanuele Lodolo, Ron Macnab, Fernando Martinez, the late Sergei Maschenkov, Serguei Merkouriev, Bramley Murton, Rob Pockalny, Walter Roest, Jean-Yves Royer, Takeshi Sagiya, Dan Scheirer, Jean-Guys Schilling, Roger Searle, Shuanngen Jin, Wim Simons, Chris Small, Bob Smalley, Joann Stock, Graham Westbrook and Shui-Beih Yu. We also thank Ben Horner-Johnson for supplying software to facilitate plotting pole uncertainty ellipses and Indrajit Das for assembling from multibeam data a new digital file of the mid-ocean ridges for the paper figures. We also thank Thorsten Becker and two anonymous reviewers for constructive comments. Figures were produced with Generic Mapping Tool software (Wessel & Smith 1991). This work was funded by NSF grants OCE-0453113 (CD) and OCE-0453219 (RG). Part of this material is based on data provided by the UNAVCO Facility with support from the National Science Foundation and NASA under NSF Cooperative Agreement No. EAR-0735156.

REFERENCES

Altamimi, Z., Sillard, P. & Boucher, C., 2002. ITRF2000: a new release of the International Terrestrial Reference Frame for earth science applications, *J. geophys. Res.,* **107,** 2214, doi:10.1029/2001JB000561.

Altamimi, Z., Collilieux, X., Legrand, J., Garayt, B. & Boucher, C., 2007. ITRF2005: a new release of the International Terrestrial Reference Frame based on time series of station positions and Earth orientation parameters, *J. geophys. Res.,* **112,** B09401, doi:10.10292007JB004949.

Anderson-Fontana, S., Engeln, J.F., Lundgren, P., Larson, R.L. & Stein, S., 1987. Tectonics of the Nazca-Antarctica plate boundary, *Earth planet. Sci. Lett.,* **86,** 46–56.

Angermann, D., Klotz, J. & Reigber, C., 1999. Space-geodetic estimation of the Nazca-South America Euler vector, *Earth planet. Sci. Lett.,* **171,** 329–334.

Apel, E.V., Burgmann, R., Steblov, G., Vasilenko, N., King, R. & Prytkov, A., 2006. Independent active microplate tectonics of northeast Asia from GPS velocities and block modeling, *Geophys. Res. Lett.,* **33,** L11303, doi:10.10292006GL026077.

Appelgate, B., 1997. Modes of axial reorganization on a slow-spreading ridge: the structural evolution of the Kolbeinsey Ridge since 10 Ma, *Geology,* **25,** 431–434.

Argus, D.F., 1996. Postglacial uplift and subsidence of earth's surface using VLBI geodesy: on establishing vertical reference, *Geophys. Res. Lett.,* **23,** 973–976.

Argus, D.F., 2007. Defining the translational velocity of the reference frame of Earth, *Geophys. J. Int.,* **169,** 830–838, doi:10.1111j.1365-246X.2007.03344.x.

Argus, D.F. & Gordon, R.G., 1990. Pacific-North American plate motion from very long baseline interferometry, *J. geophys. Res.,* **95,** 17 315–17 324.

Argus, D.F. & Gordon, R.G., 2001. Present tectonic motion across the Coast Ranges and San Andreas fault system in central California, *Geol. Soc. Am. Bull.,* **113,** 1580–1592.

Argus, D.F. & Heflin, M.B., 1995. Plate motion and crustal deformation estimated with geodetic data from the Global Positioning System, *Geophys. Res. Lett.,* **22,** 1973–1976.

Argus, D.F., Gordon, R.G., DeMets, C. & Stein, S., 1989. Closure of the Africa-Eurasia-North America plate motion circuit and tectonics of the Gloria fault, *J. geophys. Res.,* **94,** 5585–5602.

Argus, D.F., Peltier, W.R. & Watkins, M.M., 1999. Glacial isostatic adjustment observed using very long baseline interferometry and satellite laser ranging geodesy, *J. geophys. Res.,* **104,** 29 077–29 093.

Argus, D., Gordon, R., Heflin, M., Ma, C., Eanes, R., Willis, P., Peltier, W.R. & Owen, S., 2010. The angular velocities of the plates and the velocity of Earth's center from space geodesy, *Geophys. J. Int.,* **180,** 913–960.

Atwater, T. & Mudie, J.D., 1973. Detailed near-bottom geophysical study of the Gorda Rise, *J. geophys. Res.,* **78,** 8665–8686.

Atwater, T. & Stock, J., 1998. Pacific-North America plate tectonics of the Neogene Southwestern United States: an update, *Int. Geol. Rev.,* **40,** 375–402.

Ball, M.M. & Harrison, C.G.A., 1970. Crustal plates in the central Atlantic, *Science,* **167,** 1128–1129.

Bandy, W.L., 1992. Geological and geophysical investigation of the Rivera-Cocos plate boundary: implications for plate fragmentation, *PhD thesis*, Texas A&M Univ., College Station, Texas.

Bandy, W.L., Kostoglodov, V. & Mortera-Gutierrez, C.A., 1998. Southwest migration of the instantaneous Rivera-Pacific Euler pole and Cocos plates since 0.78 Ma, *Geofisica Internacional,* **37,** 153–169.

Beavan, J., Tregoning, P., Bevis, M., Kato, T. & Meertens, C., 2002. Motion and rigidity of the Pacific plate and implications for plate boundary deformation, *J. geophys. Res.,* **107** (B10), doi:10.1029/2001JB000282.

Belderson, R.H., Jones, E.J.W., Gorini, M.A. & Kenyon, N.H., 1984. A long range side-scan sonar (GLORIA) survey of the Romanche active transform in the equatorial Atlantic, *Mar. Geol.,* **56,** 65–78.

Benard, F. *et al.*, 2007. Ocean deformation processes at the Caribbean-North America-South America triple junction: initial results of the 2007 ANTIPLAC marine survey, *Am. Geophys. U.* Fall meeting abstracts, #T23B–1409.

Bennett, R.A., Davis, J.L. & Wernicke, B.P., 1999. Present-day pattern of Cordilleran deformation in the western United States, *Geology,* **27,** 371–374.

Bergman, E.A., 1986. Intraplate earthquakes and the state of stress in oceanic lithosphere, *Tectonophys.,* **132,** 1–35.

Bird, P., 2003. An updated digital model of plate boundaries, *Geochem. Geophys. Geosyst.,* **4,** 1027, doi:10.1029/2001GC000252.

Blewitt, G., 2003. Self-consistency in reference frames, geocenter definition, and surface loading of the solid Earth, *J. geophys. Res.,* **108,** doi:10.1029/2002JB002082.

Blewitt, G. & Lavallée, D., 2002. Effect of annual signals on geodetic velocity, *J. geophys. Res.,* **107** (B7), doi:10.1029/2001JB000570.

Briais, A., 1995. Structural analysis of the segmentation of the Central Indian ridge between 20°30'S and 25°30'S (Rodriguez triple junction), *Mar. geophys. Res.,* **17,** 431–467.

Brozena, J.M., 1986. Temporal and spatial variability of seafloor spreading processes in the northern South Atlantic, *J. geophys. Res.,* **91,** 497–510.

Calais, E., Vergnolle, M., Sankov, V., Lukhnev, A., Miroshnitchenko, A., Amarjargal, S. & Deverchere, J., 2003. GPS measurements of crustal deformation in the Baikal-Mongolia area motions? (1994–2002): implications for the current kinematics of Asia *J. geophys. Res.,* **108,** doi:10.1029/2002JB002373.

Calais, E., Ebinger, C., Hartnady, C. & Nocquet, J.M., 2006a. Kinematics of the East African Rift from GPS and earthquake slip vector data, *Geol. Soc. London, Spec. Pub.,* **259,** 9–22, doi:10.1144/GSL.SP.2006.259.01.03.

Calais, E., Han, J.Y., DeMets, C. & Nocquet, J.M., 2006b. Deformation of the North American plate interior from a decade of continuous GPS measurements, *J. geophys. Res.,* **111,** B06402, doi:10.1029/2005JB004253.

Canales, J.P., Danobeitia, J.J., Detrick, R.S., Hooft, E.E.E., Bartolome, R. & Naar, D.F., 1997. Variations in axial morphology along the Galapagos spreading center and the influence of the Galapagos hotspot, *J. geophys. Res.,* **102,** 27 341–27 354.

Cande, S.C. & Stock, J.M., 2004. Pacific-Antarctic-Australia motion and the formation of the Macquarie plate, *Geophys. J. Int.,* **157,** 399–414.

Cande, S.C., Raymond, C.A., Stock, J. & Haxby, W.F., 1995. Geophysics of the Pitman fracture zone and Pacific-Antarctic plate motions during the Cenozoic, *Science,* **270,** 947–953.

Cannat, M. *et al.*, 1999. Mid-Atlantic Ridge-Azores hotspot interactions: along-axis migration of a hotspot-derived event of enhanced magmatism 10 to 4 Ma ago, *Earth planet Sci. Lett.,* **173,** 257–269.

Carbotte, S. & Macdonald, K., 1992. East Pacific Rise 8°–10°30'N: evolution of ridge segments and discontinuities from SeaMARC II and three-dimensional magnetic studies, *J. geophys. Res.,* **97,** 6959–6982.

Carbotte, S.M., Welch, S.M. & Macdonald, K.C., 1991. Spreading rates, rift propagation, and fracture zone offset histories during the past 5 my on the Mid-Atlantic Ridge: 25°–27°30'S and 31°–3°30'S, *Mar. geophys. Res.,* **13,** 51–80.

Carbotte, S.M. *et al.*, 2004. New integrated data management system for Ridge2000 and MARGINS research, *EOS, Trans. Am. geophys. Un.,* **85,** 553 and 559.

Cardellach, E., Elosegui, P. & Davis, J.L., 2007. Global distortion of GPS networks associated with satellite antenna model errors, *J. geophys. Res.,* **112** (B07405), doi:10292006JB004675.

Chase, C.G., 1972. The *n*-plate problem of plate tectonics, *Geophys. J. R. astr. Soc.,* **29,** 117–122.

Chase, C.G., 1978. Plate kinematics: the Americas, East Africa, and the rest of the world, *Earth planet. Sci. Lett.,* **37,** 355–368.

Chaytor, J.B., Goldfinger, C., Dziak, R.P. & Fox, C.G., 2004. Active deformation of the Gorda plate: constraining deformation models with new geophysical data, *Geology,* **32,** 353–356, doi:10.1130/G20178.2.

Cherkis, N.Z., Fleming, H.S. & Brozena, J.M., 1989. Bathymetry of the South Atlantic Ocean: 3°S to 40°S, Map and Chart Series MCH-069, Geological Society of America, Boulder.

Chu, D. & Gordon, R.G., 1998. Current plate motions across the Red Sea, *Geophys. J. Int.,* **135,** 313–328.

Chu, D. & Gordon, R.G., 1999. Evidence for motion between Nubia and Somalia along the Southwest Indian Ridge, *Nature,* **398,** 64–67.

Collette, B.J., Verhoef, J. & Roest, W.R., 1984. Geophysical investigations of the floor of the Atlantic Ocean between 10°N and 38°N (Kroonvlag Project) Series B, *Proceedings of the Koniklijke Nederlandse Akademie van Wetenschappen,* **87,** 1–76.

Conder, J.A. & Forsyth, D.W., 2001. Seafloor spreading on the Southeast Indian Ridge over the last one million years: a test of the Capricorn plate hypothesis, *Earth planet. Sci. Lett.,* **188,** 91–105.

Conder, J.A., Scheirer, D.S. & Forsyth, D.W., 2000. Seafloor spreading on the Amsterdam-St. Paul hotspot plateau, *J. geophys. Res.,* **105,** 8263–8277.

Crane, K. & Solheim, A. (editors), 1995. Seafloor atlas of the northern Norwegian-Greenland *Norsk Polarinstitutt Meddelelser,* **137,** 172 pp.

Croon, M.B., Cande, S.C. & Stock, J.M., 2008. Revised Pacific-Antarctic plate motions and geophysics of the Menard Fracture Zone, *Geochem. Geophys. Geosyst.,* **9,** Q07001, doi:10.1029/2008GC002019.

d'Acremont, E., Leroy, S., Maia, M., Patriat, P., Bselier, M.-O., Bellahsen, N., Fournier, M. & Gente, P., 2006. Structure and evolution of the eastern Gulf of Aden: insights from magnetic and gravity data (Encens-Sheba MD117 cruise), *Geophys. J. Int.,* **165,** 786–803, doi:10.1111/j.1365-246X.2006.02950.x.

Dauteil, O., Huchon, P., Quemeneur, F. & Souriot, T., 2001. Propagation of an oblique spreading center: the western Gulf of Aden, *Tectonophysics,* **332,** 423–442.

DeMets, C., 1993. Earthquake slip vectors and models of present-day plate motions, *J. geophys. Res.,* **98,** 6703–6714.

DeMets, C., 1995. A reappraisal of seafloor spreading lineations in the Gulf of California: implications for the transfer of Baja California to the Pacific plate and models of Pacific-North America motion, *Geophys. Res. Lett.,* **22,** 365–369.

DeMets, C., 2001. A new estimate for present-day Cocos-Caribbean plate motion: implications for slip along the Central American volcanic arc, *Geophys. Res. Lett.,* **28,** 4043–4046.

DeMets, C. & Dixon, T., 1999. New kinematic models for Pacific-North America motion from 3 Ma to present, 1: evidence for steady motion and biases in the NUVEL-1A model, *Geophys. Res. Lett.,* **26,** 1921–1924.

DeMets, C. & Stein, S., 1990. Present-day kinematics of the Rivera plate and implications for tectonics of southwestern Mexico, *J. geophys. Res.,* **95,** 21,931–21,948.

DeMets, C. & Traylen, S., 2000. Motion of the Rivera plate since 10 Ma relative to the Pacific and North American plates and the mantle, *Tectonophysics,* **318,** 119–159.

DeMets, C. & Wiggins-Grandison, M., 2007. Deformation of Jamaica and motion of the Gonave microplate from GPS and seismic data, *Geophys. J. Int.,* **168** (1), 362–378, doi:10.1111/j.1365-246X.2006.03236.x.

DeMets, C. & Wilson, D.S., 1997. Relative motions of the Pacific, Rivera, North American, and Cocos plates since 0.78 Ma, *J. geophys. Res.,* **102,** 2789–2806.

DeMets, C. & Wilson, D.S., 2008. Toward a minimum change model for recent plate motions: calibrating seafloor spreading rates for outward displacement, *Geophys. J. Int.,* **174,** 825–841, doi:10.1111/j.1365-246X.2008.03836.x.

DeMets, C., Gordon, R.G. & Argus, D.F., 1988. Intraplate deformation and closure of the Australia-Antarctica-Africa plate circuit *J. geophys. Res.,* **93,** 11 877–11 897.

DeMets, C., Gordon, R.G., Argus, D.F. & Stein, S., 1990. Current plate motions, *Geophys. J. Int.* **101,** 425–478.

DeMets, C., Gordon, R.G., Argus, D.F. & Stein, S., 1994a. Effect of recent revisions to the geomagnetic reversal timescale, *Geophys. Res. Lett.,* **21,** 2191–2194.

DeMets, C., Gordon, R.G. & Vogt, P., 1994b. Location of the Africa-Australia-India triple junction and motion between the Australian and Indian plates: results from an aeromagnetic investigation of the Central Indian and Carlsberg ridges, *Geophys. J. Int.,* **119,** 893–930.

DeMets, C., Jansma, P.E., Mattioli, G.S., Dixon, T.H., Farina, F., Bilham, R., Calais, E. & Mann, P., 2000. GPS geodetic constraints on Caribbean-North America plate motion, *Geophys. Res. Lett.,* **27,** 437–440.

DeMets, C., Gordon, R.G. & Royer, J.-Y., 2005. Motion between the Indian, Capricorn, and Somalian plates since 20 Ma: implications for the timing and magnitude of distributed deformation in the equatorial Indian ocean, *Geophys. J. Int.,* **161,** 445–468.

DeMets, C., Mattioli, G., Jansma, P., Rogers, R., Tenorio, C. & Turner, H.L., 2007. Present motion and deformation of the Caribbean plate: constraints from new GPS geodetic measurements from Honduras and Nicaragua, in *Geologic and Tectonic Development of the Caribbean Plate in Northern Central America,* Geol. Soc. Am. Spec. Paper, ed. P. Mann, **428,** 21–36, doi:10.1130/2007.2428(02), The Geological Society of America, Boulder.

Deng, J. & Sykes, L.R., 1995. Determination of Euler pole for contemporary relative motion of Caribbean and North American plates using slip vectors of interplate earthquakes, *Tectonics,* **14,** 39–53.

Detrick, R.S., Needham, H.D. & Renard, V., 1995. Gravity anomalies and crustal thickness variations along the Mid-Atlantic Ridge between 33°N and 40°N, *J. geophys. Res.,* **100,** 3767–3787.

Dick, H.J.B. *et al.*, 1991. Tectonic evolution of the Atlantis II Fracture Zone, ed. Von Herzen, R.P., Robinson, P.T., *et al.*, *Proceedings of the Ocean Drilling Program, Scientific Results,* **118,** 359–398.

Patriat, P., Sloan, H. & Sauter, D., 2008. From slow to ultraslow: a previously undetected event at the Southwest Indian Ridge at ca. 24 Ma, *Geology,* **36,** 207–210, doi:10.1130/G24270A.1.

Dick, H.J.B., Lin, J. & Schouten, H., 2003. An ultraslow-spreading class of ocean ridge, *Nature,* **426,** 405–412.

Dixon, T.H., Farina, F., DeMets, C., Jansma, P., Mann, P. & Calais, E., 1998. Relative motion between the Caribbean and North American plates and related boundary zone deformation from a decade of GPS observations, *J. geophys. Res.,* **103,** 15 157–15 182.

Dixon, T. *et al.*, 2000. New kinematic models for Pacific-North America motion from 3 Ma to present, II: tectonic implications for Baja and Alta California, *Geophys. Res. Lett.,* **27,** 3961–3964.

Douglass, J., Schilling, J.-G. & Fontignie, D., 1999. Plume-ridge interaction of the Discovery and Shona mantle plumes with the southern Mid-Atlantic Ridge (40°–55°S), *J. geophys. Res.,* **104,** 2941–2962.

Drolia, R.K. & DeMets, C., 2005. Deformation in the diffuse India-Capricorn-Somalia triple junction from a multibeam and magnetic survey of the northern Central Indian ridge, 3°S–10°S, *Geochem., Geophys., Geosyst.,* **6,** doi:10.1029/2005GC000950.

Dyment, J. & Arkani-Hamed, J., 1995. Spreading-rate-dependent magnetization of the oceanic lithosphere inferred from the anomalous skewness of marine magnetic anomalies, *Geophys. J. Int.,* **121,** 789–804.

Embley, R.W. & Wilson, D.S., 1992. Morphology of the Blanco transform fault zone—NE Pacific: implications for its tectonic evolution, *Mar. geophys. Res.,* **14,** 25–45.

Escartin, J., Smith, D.K. & Cannat, M., 2003. Parallel bands of seismicity at the Mid-Atlantic Ridge, 12–14°N, *Geophys. Res. Lett.,* **30** (12) 1620, doi:10.1029/2003GL017226.

Feden, R.H., Vogt, P.R. & Fleming, H.S., 1979. Magnetic and bathymetric evidence for the 'Yermak Hot Spot' northwest of Svalbard in the Arctic Basin, *Earth planet. Sci. Lett.,* **44,** 18–38.

Fernandes, R.M.S., Bastos, L., Miranda, J.M., Lourenco, N., Ambrosius, B.A.C., Noomen, R. & Simons, W., 2006. Defining the plate boundaries in the Azores region, *J. Volcan. Geotherm. Res.,* **156,** 1–9.

Fitch, T.J., 1972. Plate convergence, transcurrent faults, and internal deformation adjacent to Southeast Asia and the western Pacific, *J. geophys. Res.,* **77,** 4432–4460.

Fornari, D.J., Gallo, D.G., Edwards, M.H., Madsen, J.A., Perfit, M.R. & Shor, A.N., 1989. Structure and topography of the Siquieros transform fault system: evidence for the development of intra-transform spreading centers, *Mar. geophys. Res.,* **11,** 263–299.

Fournier, M., Patriat, P. & Leroy, S., 2001. Reappraisal of the Arabia-India-Somalia triple junction kinematics, *Earth planet. Sci. Lett.,* **189,** 103–114, doi:10.1016/S0012-82X(01)00371-5.

Fournier, M., Chamot-Rooke, N., Petit, C., Fabbri, O., Huchon, P., Maillot, B. & Lepvrier, C., 2008. *In situ* evidence for dextral active motion at the Arabia-India plate boundary, *Nat. Geosci.,* **1,** 54–58, doi:10.1038/ngeo.2007.24.

Fox, P.J. & Gallo, D.G., 1984. A tectonic model for ridge-transform-ridge plate boundaries: implications for the structure of oceanic lithosphere, *Tectonophysics,* **104,** 205–242.

Fox, P.J., Grindlay, N.R. & Macdonald, K.C., 1991. The Mid-Atlantic Ridge (31°S–34° 30'S): temporal and spatial variations of accretionary processes, *Mar. geophys. Res.,* **13,** 1–20.

Fujiwara, T. *et al.*, 1995. Morphological studies of the Ayu Trough, Philippine Sea-Caroline plate boundary, *Geophys. Res. Lett.,* **22,** 109–112.

Fujiwara, T., Lin, J., Matsumoto, T., Kelemen, P.B., Tucholke, B.E. & Casey, J.F., 2003. Crustal evolution of the Mid-Atlantic Ridge near the Fifteen-Twenty fracture zone in the last 5 Ma, *Geochem. Geophys. Geosyst.,* **4,** 1024, doi:10.1029/2002GC000364.

Gallo, D.G., Fox, P.J. & Macdonald, K.C., 1986. A Seabeam investigation of the Clipperton transform fault: the morphotectonic expression of a fast slipping transform boundary, *J. geophys. Res.,* **91,** 3455–3467.

Gente, P. *et al.*, 1995. Characteristics and evolution of the segmentation of the Mid-Atlantic Ridge between 20°N and 24°N during the last 10 million years, *Earth planet Sci. Lett.,* **129,** 55–71.

Girdler, R.W. & Southren, T.C., 1987. Structure and evolution of the northern Red Sea, *Nature,* **330,** 716–721.

Girdler, R.W., Brown, C., Noy, D.J.M. & Styles, P., 1980. A geophysical survey of the westernmost Gulf of Aden, *Phil. Trans. R. Soc. Lond., A,* **298,** 1–43.

Glebovsky, V.Y. *et al.*, 1995. Mid-oceanic ridges and deep ocean basins: AMF structure, *Anomalous Magnetic Field of the World Ocean,* 67–144, ed. Gorodnitsky, A.M., CRC Press, Boca Raton.

Goff, J.A., Fornari, D.J., Cochran, J.R., Keeley, C. & Malinverno, A., 1993. Wilkes transform system and 'nanoplate', *Geology,* **21,** 623–626.

Gonzales-Garcia, J.J., Prawirodirdjo, L., Bock, Y. & Agnew, D., 2003. Guadalupe Island, Mexico as a new constraint for Pacific plate motion, *Geophys. Res. Lett.,* **30**(16), 1872, doi:10.1029/2003GL017732.

Gordon, R.G., 1998. The plate tectonic approximation: plate nonrigidity, diffuse plate boundaries, and global plate reconstructions, *Annu. Rev. Earth planet. Sci.,* **26,** 615–642.

Gordon, R.G. & DeMets, C., 1989. Present-day motion along the Owen Fracture Zone and Dalrymple Trough in the Arabian Sea, *J. geophys. Res.,* **94,** 5560–5570.

Gordon, R.G. & Stein, S., 1992. Global tectonics and space geodesy, *Science,* **256,** 333–342.

Gordon, R.G., Stein, S., DeMets, C. & Argus, D.F., 1987. Statistical tests for closure of plate motion circuits, *Geophys. Res. Lett.,* **14,** 587–590.

Gordon, R.G., Argus, D.F. & Royer, J.-Y., 2008. Space geodetic test of kinematic models for the Indo-Australian composite plate, *Geology,* **36,** 827–830, doi:10.1130/G25089A.1.

Goslin, J.H. & Triatnord Scientific Party, 1999. Extent of Azores plume influence on the Mid-Atlantic Ridge north of the hotspot, *Geology,* **27,** 991–994.

Grindlay, N.R., Fox, P.J. & Macdonald, K.C., 1991. Second-order ridge axis discontinuities in the south Atlantic: morphology, structure, and evolution, *Mar. geophys. Res.* **13,** 21–49.

Grindlay, N.R., Fox, P.J. & Vogt, P.R., 1992. Morphology and tectonics of the Mid-Atlantic ridge (25° – 27°30'S) from Sea Beam and magnetic data, *J. geophys. Res.,* **97,** 6983–7010.

Grindlay, N.R., Madsen, J.A., Rommevaux-Jestin, C. & Sclater, J., 1998. A different pattern of ridge segmentation and mantle Bouguer gravity anomalies along the ultra-slow spreading Southwest Indian Ridge (15°30'E to 25°E), *Earth planet. Sci. Lett.,* **161,** 243–253.

Hartnady, C.J.H., 2002. Earthquake hazard in Africa: perspectives on the Nubia-Somalia boundary, *S. Afric. J. Sci.,* **98,** 425–428.

Hayward, N., Watts, A.B., Westbrook, G.K. & Collier, J.S., 1999. A seismic reflection and GLORIA study of compressional deformation in the Gorringe Bank region, eastern North Atlantic, *Geophys. J. Int.,* **138,** 831–850.

Heki, K. & Kataoka, T., 2008. On the biannually repeating slow-slip events at the Ryukyu Trench, southwestern Japan, *J. geophys. Res.,* **113,** B11402, doi:10.1029/2008JB005739.

Hey, R., Johnson, G.L. & Lowrie, A., 1977. Recent plate motions in the Galapagos area, *Bull. Geol. Soc. Am.,* **88,** 1385–1403.

Hilgen, F.J., Krijgsman, W., Langereis, C.G., Lourens, L.J., Santarelli, A. & Zachariasse, W.J., 1995. Extending the astronomical (polarity) time scale into the Miocene, *Earth planet. Sci. Lett.,* **136,** 495–510.

Horner-Johnson, B.C., Gordon, R.G., Cowles, S.M. & Argus, D.F., 2005. The angular velocity of Nubia relative to Somalia and the location of the Nubia-Somalia-Antarctica triple junction, *Geophys. J. Int.,* **162,** 221–234, doi:10.1111/j.1365-24X.2005.02608.x.

Horner-Johnson, B.C., Gordon, R.G. & Argus, D.F., 2007. Plate kinematic evidence for the existence of a distinct plate between the Nubian and Somalian plates along the Southwest Indian Ridge, *J. geophys. Res.,* **112,** B05418, doi:10292006JB004519.

Hosford, A., Tivey, M., Matsumoto, T., Dick, H., Schouten, H. & Kinoshita, H., 2003. Crustal magnetization and accretion at the Southwest Indian Ridge near the Atlantis II fracture zone, 0–25 Ma, *J. geophys. Res.,* **108,**(B3), 2169, doi:10.1029/2001JB000604.

Iaffaldano, G., Bunge, H.-P. & Dixon, T.H., 2006. Feedback between mountain belt growth and plate convergence, *Geology,* **34,** 893–896, doi:10.1130/G22661.1.

Izzeldin, A., 1987. Seismic, gravity, and magnetic surveys in the central part of the Red Sea: their interpretation and implications for the structure and evolution of the Red Sea, *Tectonophys.,* **143,** 269–306.

Jarrard, R.D., 1986a. Relations among subduction parameters, *Rev. Geophys.,* **24,** 217–284.

Jarrard, R.D., 1986b. Terrane motion by strike-slip faulting of forearc slivers *Geology,* **14,** 780–783.

Jestin, F., Huchon, P. & Gaulier, J.M., 1994. The Somalia plate and the East African Rift System: present-day kinematics, *Geophys. J. Int.,* **116,** 637–654.

Jin, S., Park, P.-H. & Zhu, W., 2007. Micro-plate tectonics and kinematics in Northeast Asia inferred from a dense set of GPS observations, *Earth planet. Sci. Lett.,* **257,** 486–496, doi:10.1016j.epsl.2007.03.011.

Karsten, J. *et al.*, 1999. The northern Chile Ridge revealed: preliminary cruise report of PANORAMA Expedition Leg 04, *InterRidge News,* **8,** 15–21.

Kato, T., Beavan, J., Matsushima, T., Kotake, Y., Camacho, J.T. & Nakao, S., 2003. Geodetic evidence of backarc spreading in the Mariana Trough, *Geophys. Res. Lett.,* **30** (12), doi:10.1029/2002GL016757.

King, R.W. & Bock, Y., 2000. Documentation for the GAMIT GPS analysis software, release 10.0, Mass. Inst. of Technol. Cambridge.

Klein, E.M., Smith, D.K., Williams, C.M. & Schouten, H., 2005. Counter-rotating microplates at the Galapagos triple junction, *Nature,* **433,** 855–858.

Kleinrock, M.C. & Bird, R.T., 1994. Southeastern boundary of the Juan Fernandez microplate: braking microplate rotation and deforming the Antarctic plate, *J. geophys. Res.,* **99,** 9237–9261.

Kogan, M.G. & Steblov, G.M., 2008. Current global plate kinematics from GPS (1995–2007) with the plate-consistent reference frame, *J. geophys. Res.,* **113,** B04416, doi:10.1029/2007JB005353.

Korenaga, J. & Hey, R.N., 1996. Recent dueling propagation history at the fastest spreading center, the East Pacific Rise, 26°S–32°S, *J. geophys. Res.,* **101,** 18 023–18 041.

Kovacs, L.C., Bernero, C., Johnson, G.L., Pilger, R.H. Jr., Taylor, P.T. & Vogt, P.R., 1982. *Residual Magnetic Anomaly Chart of the Arctic Ocean Region,* Naval Research Laboratory, and Naval Ocean Research and Development Activity.

Kreemer, C., Holt, W.E. & Haines, A.J., 2003. An integrated global model of present-day plate motions and plate boundary deformation, *Geophys. J. Int.,* **154,** 8–34.

Kumar, R.V. & Gordon, R.G., 2009. Horizontal thermal contraction of oceanic lithosphere: the ultimate limit to the rigid plate approximation, *J. geophys. Res.,* **114,** B01403, doi:10.1029/2007JB005473.

Larson, R.L. *et al.*, H., 1992. Roller-bearing tectonic evolution of the Juan Fernandez microplate, *Nature,* **356,** 571–576.

Larson, K.M., Freymueller, J.T. & Philipsen, S., 1997. Global plate velocities from the Global Positioning System, *J. geophys. Res.,* **102,** 9962–9982.

Laughton, A.S., Whitmarsh, R.B. & Jones, M.T., 1970. The evolution of the Gulf of Aden *Phil. Trans. R. Soc. Lond., A,* **267,** 227–266.

Laughton, A.S., Whitmarsh, R.B., Rusby, J.S.M., Somers, M.L., Revie, J., McCartney, B.S. & Nafe, J.E., 1972. A continuous east-west fault of the Azores-Gibraltar Ridge, *Nature,* **327,** 217–220.

Lee, S.-M. & Kim, S.-S., 2004. Vector magnetic analysis within the southern Ayu Trough, equatorial western Pacific, *Geophys. J. Int.,* **156,** 213–221, doi:10.1111/j.1365-246X.2003.02125.x.

Lemaux, J., Gordon, R.G. & Royer, J.-Y., 2002. Location of the Nubia-Somalia boundary along the Southwest Indian Ridge, *Geology,* **30,** 339–342.

Leroy, S., Gente, P., Fournier, M. & many others, 2004. From rifting to spreading in the Gulf of Aden: a geophysical survey of a young ocean basin from margin to margin, *Terra Nova,* **16,** 185–192.

Ligi, M. *et al.*, 1999. Bouvet triple junction in the South Atlantic: geology and evolution, *J. geophys. Res.,* **104,** 29 365–29 386.

Livermore, R., Eagles, G., Morris, P. & Maldonado, A., 2004. Shackleton Fracture Zone: no barrier to early circumpolar ocean circulation, *Geology,* **32,** 797–800, doi:10.1130/G20537.1.

Lodolo, E. & Coren, F., 1997. A late Miocene plate boundary reorganization along the westernmost Pacific-Antarctic Ridge, *Tectonophysics,* **274,** 295–305.

Lonsdale, P., 1988. Structural pattern of the Galapagos microplate and evolution of the Galapagos triple junctions, *J. geophys. Res.,* **93,** 13 551–13 574.

Lonsdale, P., 1989. Segmentation of the Pacific-Nazca spreading center, 1°N–20°S, *J. geophys. Res.,* **94** 12 197–12 225.

Lonsdale, P., 1994. Structural geomorphology of the Eltanin fault system and adjacent transform faults of the Pacific-Antarctic plate boundary, *Mar. Geophys. Res.,* **16,** 105–143.

Lonsdale, P., 1995. Segmentation and disruption of the East Pacific rise in the mouth of the Gulf of California, *Mar. geophys. Res.,* **17,** 323–359.

Lothian, A.M., 1995. An investigation of the subduction of the Chile Ridge and the Louisville Ridge using GLORIA side-scan sonar and other marine geophysical data, *Unpublished thesis,* University of Birmingham, 148 pp.

Lourens, L., Hilgen, F.J., Laskar, J., Shackleton, N.J. & Wilson, D., 2004. The Neogene Period, in *A Geologic Time Scale,* pp. 409–440, eds Gradstein, F., Ogg, J., and Smith, A., Cambridge University Press, London.

Luis, J.F., Miranda, J., Galdeano, A., Patriat, P., Rossignol, J. & Victor-Mendes, L., 1994. The Azores Triple Junction evolution since 10 Ma from an aeromagnetic survey of the Mid-Atlantic ridge, *Earth planet. Sci. Lett.,* **125,** 439–459.

Ma, Y. & Cochran, J.R., 1997. Bathymetric roughness of the Southeast Indian Ridge: implications for crustal accretion at intermediate spreading rate mid-ocean ridges, *J. geophys. Res.,* **102,** 17 697–17 711.

Macdonald, K.C., Castillo, D., Miller, S., Fox, P.J., Kastens, K. & Bonatti, E., 1986. Deep-tow studies of the Vema fracture zone, 1, tectonics of a major slow slipping transform fault and its intersection with the Mid-Atlantic ridge, *J. geophys. Res.,* **91,** 3334–3354.

Macdonald, K.C. *et al.*, 1992. The East Pacific Rise and its flanks 8°–18°N: history of segmentation, propagation and spreading direction based on SeaMARC II and Sea Beam studies, *Mar. geophys. Res.,* **14,** 299–344.

Madsen, J.A., Macdonald, K.C. & Fox, P.J., 1986. Morphotectonic fabric of the Orozco Fracture Zone: results from a sea beam investigation, *J. geophys. Res.,* **891,** 3439–3454.

Madsen, J.A., Fornari, D.J., Edwards, M.H., Gallo, D.G. & Perfit, M.R., 1992. Kinematic framework of the Cocos-Pacific plate boundary from 13°N to the Orozco transform fault: results from an extensive magnetic and SeaMARC II survey, *J. geophys. Res.,* **97,** 7011–7024.

Mackey, K.G., Fujita, K., Gunbina, L.V., Kovalev, V.N., Imaev, V.S., Koz'min, B.M. & Imaeva, L.P., 1997. Seismicity of the Bering Strait region: evidence for a Bering block, *Geology,* **25,** 979–982.

Mann, P., Taylor, F.W., Edwards, R.L. & Ku, T., 1995. Actively evolving microplate formation by oblique collision and sideways motion along strike-slip faults: an example from the northeastern Caribbean plate margin, *Tectonophysics,* **246,** 1–69.

Mann, P., Calais, E., Ruegg, J.-C., DeMets, C., Jansma, P. & Mattioli, G.S., 2002. Oblique collision in the northeastern Caribbean from GPS measurements and geological observations, *Tectonics,* **37,** doi:10.1029/2001TC001304.

Marquez-Azua, B. & DeMets, C., 2003. Crustal velocity field of Mexico from continuous GPS measurements, 1993 to June, 2001: implications for the neotectonics of Mexico, *J. geophys. Res.,* **108**(B9), doi:10.1029/2002JB002241.

Marquez-Azua, B., Cabral-Cano, E., Correa-Mora, F. & DeMets, C., 2004. A model for Mexican neotectonics based on nationwide GPS measurements, 1993–2001, *Geofisica Internacional,* **43,** 319–330.

Maschenkov, S. & Pogrebitsky, Y., 1992. Preliminary results of Canary-Bahamas Project, *EOS, Trans. Am. geophys. Un.,* **73,** 393–397.

Mazarovich, A.O., Sokolov, S.Y., Turko, N.N. & Dobrolyubova, K.O., 2001. Seafloor topography and structure of the rift zone of the Mid-Atlanti Seafloor topography and structure of the rift zone of the Mid-Atlantic Ridge between 5°N and 7° 18'N, *Russ. J. Earth Sci.,* **3,** 353–350.

McCaffrey, R., 1991. Slip vectors and stretching of the Sumatran fore arc, *Geology,* **19,** 881–884.

McCaffrey, R., 1992. Oblique plate convergence, slip vectors, and forearc deformation, *J. geophys. Res.,* **97,** 8905–8915.

Mendel, V., Sauter, D., Parson, L.M. & Vanney, J.R., 1997. Segmentation and morphotectonic variations along a super slow-spreading centre: the Southwest Indian Ridge (57°E–70°E), *Mar. geophys. Res.,* **19,** 503–531.

Merkouriev, S. & DeMets, C., 2006. Constraints on Indian plate motion since 20 Ma from dense Russian magnetic data: implications for Indian plate dynamics, *Geochem. Geophys. Geosyst.,* **7,** Q02002, doi:10.1029/2005GC001079.

Merkouriev, S. & DeMets, C., 2008. A high-resolution model for Eurasia-North America plate kinematics since 20 Ma, *Geophys. J. Int.,* **173,** 1064–1083, doi:10.1111/j.1365-246X.2008.03761.x.

Merkouriev, S.A. & Sotchevanova, N.A., 2003. Structure and evolution of the Carlsberg Ridge: evidence for non-stationary spreading on old and modern spreading centers, *Curr. Sci.,* **85,** 334–338.

Michaud, F., Royer, J.-Y., Bourgois, J., Mercier de Lepinay, B. & Liaudon, G.P., 1997. The Rivera fracture zone revisited, *Mar. Geol.,* **137,** 207–225.

Michaud, F. *et al.*, 2004. Motion partitioning between the Pacific plate, Baja California, and the North America plate: the Tosco-Abreojos fault revisited, *Geophys. Res. Lett.,* **31,** L08604, doi:10.10292004GL019665.

Minster, J.B. & Jordan, T.H., 1978. Present-day plate motions, *J. geophys. Res.,* **83,** 5331–5354.

Minster, J.B., Jordan, T.H., Molnar, P. & Haines, E., 1974. Numerical modeling of instantaneous plate tectonics, *Geophys. J. R. astr. Soc.,* **36,** 541–576.

Mitchell, N.C., Livermore, R.A., Fabretti, P. & Carrara, C., 2000. The Bouvet triple junction, 20 to 10 Ma, and extensive transtensional deformation adjacent to the Bouvet and Conrad transforms, *J. geophys. Res.,* **105,** 8279–8296.

Morgan, W.J., Vogt, P.R. & Falls, D.F., 1969. Magnetic anomalies and sea floor spreading on the Chile Rise, *Nature,* **222,** 137–142.

Müller, R.D. & Smith, W.H.F., 1993. Deformation of the oceanic crust between the North American and South American plates, *J. geophys. Res.,* **98,** 8275–8291.

Müller, R.D., Roest, W.R., Royer, J.-Y., Gahagan, L.M. & Sclater, J.G., 1997. Digital isochrons of the world's ocean floor, *J. geophys. Res.,* **102,** 3211–3214.

Müller, R.D., Royer, J.-Y., Cande, S.C., Roest, W.R. & Maschenkov, S., 1999. New constraints on the Late Cretaceous/Tertiary plate tectonic evolution of the Caribbean, in *Caribbean Basins, Sedimentary Basins of the World 4,* pp. 39–55, ed. Mann, P., Elsevier Science, B.V., Amsterdam.

Munguia, L., Gonzalez, M., Mayer, S. & Aguirre, A., 2006. Seismicity and state of stress in the La Paz-Los Cabos region, Baja California Sur, Mexico, *Bull. seism. Soc. Am.,* **96,** 624–636, doi:10.1785/0120050114.

Naar, D.F. & Hey, R.N., 1991. Tectonic evolution of the Easter microplate, *J. geophys. Res.,* **96,** 7961–7993.

Nishimura, S., Hashimoto, M. & Ando, M., 2004. A rigid block rotation model for the GPS derived velocity field along the Ryukyu arc, *Phys. Earth planet. Int.,* **142,** 185–203.

Norabuena, E., Dixon, T.H., Stein, S. & Harrison, C.G.A., 1999. Decelerating Nazca-South America and Nazca-Pacific plate motion, *Geophys. Res. Lett.,* **26,** 3405–3408.

Ondreas, H., Aslanian, D., Geli, L. & Olivet, J.-L., 2001. Variations in axial morphology, segmentation, and seafloor roughness along the Pacific-Antarctic Ridge between 56°S and 66°S, *J. geophys. Res.,* **106,** 8521–8546.

Palmer, J., Sempere, J.-C., Christie, D. & Morgan, J.P., 1993. Morphology and tectonics of the Australian-Antarctic discordance between 123°E and 128°E, *Mar. geophys. Res.,* **15,** 121–152.

Parson, L.M., Patriat, P., Searle, R.C. & Briais, A.R., 1993. Segmentation of the Central Indian Ridge between 12°12'S and the Indian Ocean triple junction, *Mar. geophys. Res.,* **15,** 265–282.

Patriat, P., Sauter, D., Munschy, M. & Parson, L., 1997. A survey of the Southwest Indian ridge axis between Atlantis II fracture zone and the Indian Ocean triple junction: regional setting and large scale segmentation, *Mar. geophys. Res.,* **19,** 457–480.

Pelayo, A.M. & Wiens, D.A., 1989. Seismotectonics and relative plate motions in the Scotia Sea region, *J. geophys. Res.,* **94,** 7293–7320.

Perez, O.J., Bilham, R., Bendick, R., Velandia, J.R., Hernandez, N., Moncayo, C., Hoyer, M. & Kozuch, M., 2001. Velocity field across the southern Caribbean plate boundary and estimates of Caribbean/South-American plate motion using GPS geodesy 1994–2000, *Geophys. Res. Lett.,* **28,** 2987–2990.

Perram, L.J. & Macdonald, K.C., 1990. A one-million-year history of the 11°45'N East Pacific Rise discontinuity, *J. geophys. Res.,* **95,** 21363–21381.

Perry, R.K., Fleming, H.S., Cherkis, N.Z., Feden, R.H. & Vogt, P.R., 1978. Bathymetry of the Norwegian-Greenland and western Barents Seas, Map, Naval Research Laboratory—Acoustics Division, Washington, DC.

Perry, R.K., Fleming, H.S., Vogt, P.R., Cherkis, N.Z., Feden, R.H., Thiede, J., Strand, J.E. & Collette, B.J., 1981. North Atlantic Ocean: bathymetry and plate tectonic evolution, *Geol. Soc. Am. Map Chart Series,* MC-35.

Petit, C. & Fournier, M., 2005. Present-day velocity and stress fields of the Amurian plate from thin-shell finite-element modelling, *Geophys. J. Int.,* **160,** 357–369, doi:10.1111/j.1365-246X.2004.02486.x.

Petroy, D.E. & Wiens, D.A., 1989. Historical seismicity and implications for diffuse plate convergence in the northeast Indian Ocean, *J. geophys. Res.,* **94,** 12 301–12 319.

Plattner, C., Malservisi, R., Dixon, T.H., LaFemina, P., Sella, G., Fletcher, J. & Suarez-Vidal, F., 2007. New constraints on relative motion between the Pacific plate and Baja California microplate (Mexico) from GPS measurements, *Geophys. J. Int.,* **170,** 1373–1380, doi:10.1111/j.1365-246X.2007.03494.x.

Pockalny, R.A., 1997. Evidence of transpression along the Clipperton Transform: implications for processes of plate boundary reorganization, *Earth planet. Sci. Lett.,* **146,** 449–464.

Pockalny, R.A., Detrick, R.S. & Fox, P.J., 1988. The morphology and tectonics of the Kane transform from Sea Beam bathymetry data, *J. geophys. Res.,* **94,** 3179–3194.

Pollitz, F.F., Burgmann, R. & Romanowicz, B., 1998. Viscosity of oceanic asthenosphere inferred from remote triggering of earthquakes, *Science,* **280,** 1245–1249.

Ranken, B., Cardwell, R.K. & Karig, D.E., 1984. Kinematics of the Philippine Sea plate, *Tectonophys.,* **3,** 555–575.

Reilinger, R., McClusky, S., Vernant, P., Lawrence, S. & many others, 2006. GPS constraints on continental deformation in the Africa-Arabia-Eurasia continental collision zone and implications for the dynamics of plate interactions, *J. geophys. Res.,* **111,** B05411, doi:10.10292005JB004051.

Riegel, S.A., Fujita, K., Koz'min, B.M., Imaev, V.S. & Cook, D.B., 1993. Extrusion tectonics of the Okhotsk plate, northeast Asia, *Geophys. Res. Lett.,* **20,** 607–610.

Roeser, H.A., 1975. A detailed magnetic survey of the southern Red Sea, *Geol. Jahrb.,* **D13,** 131–153.

Roest, W., R. & Collette, B.J., 1986. The Fifteen-Twenty Fracture Zone and the North American-South American plate boundary, *J. Geol. Soc. Lond.,* **143,** 833–844.

Roest, W.R., Searle, R.C. & Collette, B.J., 1984. Fanning of fracture zones and a three-dimensional model of the Mid-Atlantic Ridge, *Nature,* **308,** 527–531.

Rosencrantz, E. & Mann, P., 1991. SeaMARC II mapping of transform faults in the Cayman Trough, Caribbean Sea, *Geology,* **19,** 690–693.

Royer, J.Y. & Gordon, R.G., 1997. The motion and boundary between the Capricorn and Australian plates, *Science,* **277,** 1268–1274.

Royer, J.-Y., Gordon, R.G. & Horner-Johnson, B.C., 2006. Motion of Nubia relative to Antarctica since 11 Ma: implications for Nubia-Somalia, Pacific-North America, and India-Eurasia motion, *Geology,* **34,** 501–504, doi:10.1130G22463.1.

Sauter, D. *et al.*, 2001. The Southwest Indian Ridge between 49°15'E and 57°E: focused accretion and magma redistribution, *Earth planet Sci. Lett.,* **192,** 303–317.

Scheirer, D.S., Forsyth, D.W., Conder, J.A., Eberle, M.A., Hung, S.-H., Johnson, K.T.M. & Graham, D.W., 2000. Anomalous seafloor spreading of the Southeast Indian Ridge near the Amsterdam-St. Paul Plateau, *J. geophys. Res.,* **105,** 8243–8262.

Sclater, J.G., Munschy, M., Fisher, R.L., Weatherall, P., Cande, S.C., Patriat, P., Bergh, H. & Schlich, R., 1997. *Geophysical Synthesis of the Indian/Southern Oceans. Part 1: the Southwest Indian Ocean, v. 97-6*, Scripps Institution of Oceanography, La Jolla, California, USA.

Sclater, J.G., Grindlay, N.R., Madsen, J.A. & Rommevaux-Jestin, C., 2005. Tectonic interpretation of the Andrew Bain transform fault, southwest Indian Ocean, *Geochem., Geophys., Geosyst.,* **6,** Q09K10, doi:10.1029/2005GC000951.

Searle, R., 1980. Tectonic pattern of the Azores spreading centre and triple junction, *Earth planet. Sci. Lett.,* **51,** 415–434.

Searle, R., 1981. The active part of Charlie-Gibbs Fracture Zone: a study using sonar other geophysical techniques, *J. geophys. Res.,* **86,** 243–262.

Searle, R.C., 1983. Multiple, closely spaced transform faults in fast-slipping fracture zones, *Geology,* **11,** 607–610.

Searle, R.C., 1986. GLORIA investigations of oceanic fracture zones: comparative study of the transform fault zone, *J. Geol. Soc. Lond.,* **143,** 743–756.

Searle, R.C., 1989. Location and segmentation of the Cocos-Nazca spreading centre west of 95°W, *Mar. geophys. Res.,* **11,** 15–26.

Searle, R.C., Bird, R.T., Rusby, R.I. & Naar, D.F., 1993. The development of two oceanic microplates: easter and Juan Fernandez microplates, East Pacific Rise, *J. Geol. Soc. Lond.,* **150,** 965–976.

Searle, R.C., Thomas, M.V. & Jones, E.J.W., 1994. Morphology and tectonics of the Romanche Transform and its environs, *Mar. geophys. Res.,* **16,** 427–453.

Searle, R.C., Keeton, J.A., Owens, R.B., White, R.S., Mecklenburgh, R., Parson, B. & Lee, S.M., 1998. The Reykjanes Ridge: structure and tectonics of a hot-spot-influenced, slow-spreading ridge, from multibeam bathymetry, gravity, and magnetic investigations, *Earth planet. Sci. Lett.,* **160,** 463–478.

Sella, G.F., Dixon, T.H. & Mao, A., 2002. REVEL: a model for recent plate velocities from space geodesy, *J. geophys. Res.,* **107** (B4), doi:10.1029/2000JB000033.

Sella, G.F., Stein, S., Dixon, T.H., Craymer, M., James, S., Mazzotti, S. & Dokka, R.K., 2007. Observation of glacial isostatic adjustment in 'stable' North America with GPS, *Geophys. Res. Lett.,* **34** (L02306), doi:10.10292006GL027081.

Sempere, J.-C., Macdonald, K.C. & Miller, S.P., 1987. Detailed study of the Brunhes/Matuyama reversal boundary on the East Pacific Rise at 19°30'S: implications for crustal emplacement processes at an ultra fast spreading center, *Mar. geophys. Res.,* **9,** 1–23.

Sempere, J.-C., Palmer, J., Christie, D.M., Morgan, J.P. & Shor, A.N., 1991. Australian-Antarctic discordance, *Geology,* **19,** 429–432.

Sempere, J.-C. *et al.*, 1995. The Mid-Atlantic Ridge between 29°N and 31°30'N in the last 10 Ma, *Earth planet Sci. Lett.,* **130,** 45–55.

Sempere, J.C. *et al.*, 1997. The Southeast Indian Ridge between 88°E and 118°E: variations in crustal accretion at constant spreading rate, *J. geophys. Res.,* **102,** 14 489–15 505.

Seno, T., Stein, S. & Gripp, A.E., 1993. A model for the motion of the Philippine Sea plate consistent with NUVEL-1 and geological data, *J. geophys. Res.,* **98,** 17 941–17 948.

Shah, A. & Sempere, J.-C., 1998. Morphology of the transition from an axial high to an axial valley at the Southeast Indian Ridge and the relation to variations in mantle temperature, *J. geophys. Res.,* **103,** 5203–5223.

Shen, Z.K., Lu, J., Wang, M. & Burgmann, R., 2005. Contemporary crustal deformation around the southeast borderland of the Tibetan Plateau, *J. geophys. Res.,* **110,** B11409, doi:10.1029/2004JB003421.

Simons, W.J.F. *et al.*, 2007. A decade of GPS in Southeast Asia: resolving Sundaland motion and boundaries, *J. geophys. Res.,* **112,** B6, B06420, doi:10.10292005JB003868.

Sinton, J., Detrick, R., Canales, J.P., Ito, G. & Behn, M., 2003. Morphology and segmentation of the western Galapagos spreading center: Plume-ridge interaction at intermediate spreading, *Geochem., Geophys., Geosyst.,* **4**(12), 8515, doi:10.1029/2003GC000609.

Smalley, R., Kendrick, E., Bevis, M.G., Dalziel, I.W.D., Casassa, G., Olivero, E. & Piana, E., 2003. Geodetic determination of relative plate motion and crustal deformation across the Scotia-South America plate boundary in eastern Tierra del Fuego, *Geochem. Geophys. Geosyst.,* **4**(9), 1070–1074, doi:10.1029/2002GC000446.

Smalley, R. *et al.*, 2007. Scotia arc kinematics from GPS geodesy, *Geophys. Res. Lett.,* **34,** L21308, doi:10.1029/2007GL031699.

Smith, W.H.F. & Sandwell, D.T., 1997. Global sea floor topography from satellite altimetry and ship depth soundings, *Science,* **277,** 1956–1962.

Smith, D.K., Escartin, J., Schouten, H. & Cann, J.R., 2008. Fault rotation and core complex formation: significant processes in seafloor formation at slow-spreading mid-ocean ridges (Mid-Atlantic Ridge, 13°–15°N), *Geochem. Geophys. Geosyst.,* **9**(3), Q03003, doi:10.1029/2007GC001699.

Spitzak, S. & DeMets, C., 1996. Constraints on present-day plate motions south of 30°S from satellite altimetry, *Tectonophysics,* **253,** 167–208.

Stein, S. & Gordon, R.G., 1984. Statistical tests of additional plate boundaries from plate motion inversions *Earth planet. Sci. Lett.,* **69,** 401–412.

Stein, C.A., Cloetingh, S.A.P.L. & Wortel, M.J.R., 1989. Seasat-derived gravity constraints on stress and deformation in the northeastern Indian Ocean, *Geophys. Res. Lett.,* **16,** 823–826.

Suarez, G., Escobedo, D., Bandy, W. & Pacheco, J.F., 1999. The 11 December, 1995 earthquake (M_w=6.4): implications for the present-day relative motion on the Rivera-Cocos plate boundary, *Geophys. Res. Lett.,* **26,** 1957–1960.

Takahashi, H. *et al.*, 1999. Velocity field around the Sea of Okhotsk and Sea of Japan regions determined from a new continuous GPS network data, *Geophys. Res. Lett.,* **26,** 2533–2535.

Tamsett, D. & Searle, R.C., 1988. Structure and development of the mid-ocean ridge plate boundary in the Gulf of Aden: evidence from GLORIA side scan sonar, *J. geophys. Res.,* **94,** 3157–3178.

Tamsett, D. & Searle, R., 1990. Structure of the Alula-Fartak fracture zone, Gulf of Aden, *J. geophys. Res.,* **95,** 1239–1254.

Taylor, B., Klaus, A., Brown, G.R., Moore, G.F., Okamura, Y. & Murakami, F., 1991. Structural development of the Sumisu Rift, Izu-Bonin arc, *J. geophys. Res.,* **96,** 16 113–16 129.

Tebbens, S.F., Westbrook, G.K., Cande, S.C., Lewis, S.D. & Bangs, N., 1990. Preliminary interpretation of combined GLORIA and SeaBeam imagery in the vicinity of the Chile margin triple junction, *Am. Assoc. Petrol. Geol.,* **74,** 776.

Tebbens, S.F., Cande, S.C., Kovacs, L., Parra, J.C., LaBrecque, J.L. & Vergara, H., 1997. The Chile Ridge: a tectonic framework, *J. geophys. Res.,* **102,** 12 035–12 059.

Thibaud, R., Gente, P. & Maia, M., 1998. A systematic analysis of the Mid-Atlantic Ridge morphology and gravity between 15°N and 40°N: constraints of the thermal structure, *J. geophys. Res.,* **103,** 24 223–24 243.

Thomas, C., Livermore, R. & Pollitz, F., 2003. Motion of the Scotia Sea plates, *Geophys. J. Int.,* **155,** 789–804.

Valenzuela, R.W. & Wysession, M.E., 1993. Intraplate earthquakes in the southwest Pacific ocean basin and the seismotectonics of the southern Tasman sea, *Geophys. Res. Lett.,* **20,** 2467–2470.

Vogt, P.R. & Jung, W.Y., 2004. The Terceira Rift as hyper-slow, hotspot dominated oblique spreading axis: a comparison with other slow-spreading plate boundaries, *Earth planet. Sci. Lett.,* **218,** 77–90, doi:10.1016S0012-821X(03)00627-7.

Vogt, P.R., Taylor, P.T., Kovacs, L.C. & Johnson, G.L., 1979. Detailed aeromagnetic investigation of the Arctic Basin, *J. geophys. Res.,* **84** 1071–1089.

Vogt, P.R., Johnson, G.L. & Kristjansson, L., 1980. Morphology and magnetic anomalies north of Iceland, *J. Geol.,* **47,** 67–80.

Vogt, P.R., Cherkis, N.Z. & Morgan, G.A., 1983. Project Investigator. I: evolution of the Australia-Antarctic Discordance deduced from a detailed aeromagnetic study, in *Antarctic Earth Science,* pp. 608–613, eds Oliver, R.L., James, P.R. & Jago, J.B., Australian Academy of Sciences, Canberra.

Wang, Q. *et al.*, 2001. Present-day crustal deformation in China constrained by Global Positioning System measurements *Science,* **294,** 574–577.

Ward, S.N., 1990. Pacific-North America plate motions: new results from very long baseline interferometry, *J. geophys. Res.,* **95,** 21 965–21 981.

Wdowinski, S., Bock, Y., Zhang, J., Fang, P. & Genrich, J., 1997. Southern California Permanent GPS Geodetic Array: spatial filtering of daily positions for estimating coseismic and postseismic displacements induced by the 1992 Landers earthquake, *J. geophys. Res.,* **102,** 18 057–18 070.

Weber, J.C. *et al.*, 2001. GPS estimate of relative motion between the Caribbean and South American plates, and geologic implications for Trinidad and Venezuela, *Geology,* **29,** 75–78.

Weiland, C., Wilson, D.S. & Macdonald, K., 1995. High-resolution plate reconstruction of the southern Mid-Atlantic ridge, *Mar. geophys. Res.,* **17,** 143–166.

Weissel, J.K. & Anderson, R.N., 1978. Is there a Caroline plate? *Earth planet. Sci. Lett.,* **41,** 143–158.

Wessel, P. & Smith, W.H.F., 1991. Free software helps map and display data, *EOS, Trans. Am. geophys. Un.,* **72,** 441–446.

White, R.S., 1984. Active and passive plate boundaries around the Gulf of Oman, northwest Indian Ocean, in Marine Science of the north-west Indian Ocean and adjacent waters. *Deep-Sea Res., Part A: Oceanogr. Res. Papers,* **31** (6-8A), 731–745.

White, R.A. & Harlow, D.H., 1993. Destructive upper-crustal earthquakes of Central America since 1900, *Bull. seism. Soc. Am.,* **83,** 1115–1142.

Wilson, D.S., 1993. Confidence intervals for motion and deformation of the Juan de Fuca plate, *J. geophys. Res.,* **98** 16 053–16 071.

Wilson, D.S. & DeMets, C., 1998. Reply to Comment on 'Relative motions of the Pacific, Rivera, North American, and Cocos plates since 0.78 Ma', *J. geophys. Res.,* **103,** 24 251–24 256.

Wilson, D.S. & Hey, R.N., 1995. History of rift propagation and magnetization intensity for the Cocos-Nazca spreading center, *J. geophys. Res.,* **100,** 10 041–10 056.

Wilson, D.S., McCrory, P.A. & Stanley, R.G., 2005. Implications of volcanism in coastal California for the Neogene deformation history of western North America, *Tectonics,* **24,** TC3008, doi:10.1029/2003TC001621.

Wysession, M.E., Wilson, J., Bartko, L. & Sakata, R., 1995. Intraplate seismicity in the Atlantic ocean basin: a teleseismic catalog, *Bull. seism. Soc. Am.,* **85,** 755–774.

Zang, S.X., Chen, Q.Y., Ning, J.Y., Shen, Z.K. & Liu, Y.G., 2002. Motion of the Philippine Sea plate consistent with the NUVEL-1A model, *Geophys. J. Int.,* **150,** 809–819, doi:10.1046j.1365-246X.2002.01744.x.

Zatman, S., Gordon, R.G. & Richards, M.A., 2001. Analytic models for the dynamics of diffuse oceanic plate boundaries, *Geophys. J. Int.,* **145,** 145–156, doi:10.1111/j.1365-246X.2001.00357.x.

Zatman, S., Gordon, R.G. & Mutnuri, K., 2005. Dynamics of diffuse oceanic plate boundaries: insensitivity to rheology, *Geophys. J. Int.,* **162,** 239–248, doi:10.1111/j.1365-246X.2005.02622.x.

Zumberge, J.F., Heflin, M.B., Jefferson, D.C., Watkins, M.M. & Webb, F.H., 1997. Precise point positioning for the efficient and robust analysis of GPS data from large networks, *J. geophys. Res.,* **102,** 5005–5017.

SUPPORTING INFORMATION

Additional Supporting Information may be found in the online version of this article:

Tables S1–S5. Five tables that document all the MORVEL plate kinematic data and fits of the MORVEL angular velocities are presented in this supplement. Separate tables are included for the 1696 seafloor spreading rates, 163 fault azimuths, 56 earthquake slip directions, 144 GPS station velocities for plates whose motions are estimated with GPS, and 498 additional GPS station velocities that are used to establish the motions of three geodetic reference plates linked to MORVEL. Selected spreading rates and transform fault azimuths from deforming zones along the mid-ocean ridges are also given for data shown in the manuscript figures. All information necessary for reproducing the MORVEL angular velocities is included. Footnotes that accompany each table give further specific information. All references cited in the tables and table footnotes are included. Many additional references that describe the data denoted in these tables are given in the paper. Readers are also referred to the following URL for extensive graphical documentation of the original data underlying MORVEL and assistance with calculating MORVEL plate velocities: http://www.geology.wisc.edu/∼chuck/MORVEL.